DESIGN ATTRIBUTES OF SPINAL FUSION CAGES AND A SURGICAL INSTRUMENT TO AID THEIR SCREW FIXATION

by

FARNAZ JABBARY ASLANI

A thesis submitted to
University of Birmingham
for the degree of
DOCTOR OF PHILOSOPHY

School of Mechanical Engineering
University of Birmingham
May 2011

ABSTRACT

Spinal fusion cages are used to aid spinal fusion where the joint between the vertebrae is fused by bone graft. The design and material of these cages are of great importance to the fusion process. Methods such as screw fixation are sometimes used to secure these cages *in vivo*. However, access to the cage screw holes is partially obscured by the vertebral bodies. This study aimed to evaluate the effect of side-holes on the design of a cage, assess the feasibility of a bioactive/biodegradable composite as a cage material and develop an instrument to aid screw access to the cage screw holes. Computer models of cages with between 0 and 10 side-holes were produced to model compression between adjacent vertebrae. The bioactive/biodegradable composite as a cage material was analysed using a range of Young's modulus values for the composite. The results suggested that the number of side-holes had a negligible effect on the stress distribution within the cage and the bioactive/biodegradable composite as a cervical cage material is unlikely to fail in static compression. A cutter instrument was developed in compliance with regulatory standards. It neatly removed the targeted vertebral edge adjacent to the cage screw holes allowing screw insertion.

To my wonderful beloved Maman and Baba

ACKNOWLEDGMENTS

The work presented in this thesis would not have been possible without the help and invaluable guidance of Professor David Hukins and Dr Duncan Shepherd. I would like to thank them for their outstanding supervision and support throughout my PhD.

I would like to thank Mr Carl Hingley, Mr Lee Gauntlett, Mr Peter Thornton, Mr Simon Payne-Rowan, Mr Hossein Ostadi, Dr Mike Keeble, Mr David Cunningham (University of Strathclyde) and Mr Steve Lambell (Finsbury Surgical Ltd.) for their technical support which made the experimental aspects of this thesis possible. I would also like to thank Surgicraft Ltd. for funding part of this project, providing technical advice and supplying implants, specially Mr Tony Fennell and Mr Jeffrey Johnson.

I am grateful to my friends who are my chosen family. Special thanks to, *in no particular order* (!), Mahtab, Sahar, Maryam H, Daniel, Eirini, Maryam NF, Parshia, Jugal and Jyothi, Aziza, Theodoros and Nadia, Stergio and Helen, Golnar, Purvi, Anish, Jin and Lei, Markus, Hua, Naomi, Pauliena and Francesca for their continuous encouragement and love.

My thanks are also due to my grandparents for their support and encouragement as well as to my aunt Frida.

A very special thank you must go to Behrang for always being there for me and reminding me that life should never be taken too seriously. This work would have been impossible without you.

Finally, from the bottom of my heart, I would like to thank my dear mother, my dear father and my brothers, Shahrad and Fardad, for their unconditional love, support and encouragement. Without you I would not have achieved what I have.

TABLE OF CONTENTS

LIST OF FIGURES

LIST OF TABLES

1. INTRODUCTION

Degeneration of the human intervertebral disc, because of aging, disease or mechanical damage often requires stabilization of the spinal segment (Cho *et al.*, 2004; Kumar *et al.*, 2005; Tsuang *et al.*, 2009; Zhang and Teo, 2008; Zhong *et al.*, 2006). Interbody spinal fusion involves excising the intervertebral disc and replacing it with bone fragments to encourage bone growth into the intervertebral space to fuse adjacent vertebrae together (Zhang and Teo, 2008). The aim of spinal fusion is to provide structural stability and reduce pain. A fusion cage is often used to retain the bone fragments (Adam *et al.*, 2003; Axelsson *et al.*, 2009; Cho *et al.*, 2002; Mastronardi *et al.*, 2006; McAfee and Maryland, 1999; Smit *et al.*, 2006; Zhang and Teo, 2008; Zhong *et al.*, 2006). These cages act as axial load-bearing devices and should provide immediate structural stability post-operation as well as maintain the intervertebral height while fusion takes place (Adam *et al.*, 2003; Cho *et al.*, 2008; Epari *et al.*, 2005; Hee and Kundnani, 2010; Kandziora *et al.*, 2001; Steffen *et al.*, 2000; Zhang and Teo, 2008; Zhong *et al.*, 2006). Hence, the design and material of spinal fusion cages can be of great importance to the clinical success of the overall fusion operation. Commercially available fusion cages come in many designs and materials (Abu Bakar *et al.*, 2003; Adam *et al.*, 2003; Cho *et al.*, 2002; Cho *et al.*, 2004; Cho *et al.*, 2008; Chou *et al.*, 2008; Epari *et al.,* 2005; Hee and Kundnani, 2010; Kandziora *et al.,* 2001; Mastronardi *et al.,* 2006; Steffen *et al.,* 2000; Toth *et al.,* 2006; Tsuang *et al.,* 2009; Zhang and Teo, 2008; Zhong *et al.,* 2006). Finite element analysis (FEA), which is a design process tool (explained in detail in §2.2.1), is often used to evaluate a newly proposed design and material for a fusion cage.

There are several FEA studies available on the biomechanical behaviour of cervical and lumbar fusion cages which are explained in detail in §2.5.2.1. However, there are no studies available that have addressed the problems of how many side-holes can be accommodated on the cage lateral walls and the effect of the side-holes (and hole number) on the cage strength in compression. Also, the mechanical suitability of a bioactive/biodegradable composite material for a fusion cage has not been analysed.

Some fusion cages are designed such that fixation screws are used to secure them in between adjacent vertebrae (Cho *et al.,* 2004; Galbusera *et al.,* 2008; Pitzen *et al.,* 2002b; Steffen *et al.,* 2000;Vadapalli *et al.,* 2006). However, problems arising during surgery such as accessing screw holes which are situated at awkward angles have not been addressed.

The aim of this thesis was to investigate the design and material of a fusion cage (using FEA) as well as to develop a surgical instrument to aid its implantation. The specific objectives were to:

- determine the extent to which side-holes can be incorporated into the design of a cervical spinal fusion cage without it failing mechanically;

- evaluate the feasibility of using a bioactive/biodegradable composite as the material for a cervical spinal fusion cage;
- develop a surgical instrument to facilitate implantation of a range of lumbar spinal fusion cages; specifically, the instrument was intended to remove parts of the vertebrae that obscure the holes for screw insertion.

These objectives were proposed by and agreed upon with Surgicraft Ltd. who partially sponsored this research. The evaluation of design and material of a fusion cage in addition to the development of a new surgical instrument were of interest to Surgicraft Ltd. because they wanted to stay ahead of the trend and gain a competitive advantage in the market place.

Chapter 2 presents the background information required to understand this thesis. The chapter begins with a description of the design process and its required tools. An explanation of the anatomical terms used for the spine then follows. The chapter continues by describing the need for spinal fusion and fusion cages.

Chapter 3 starts by introducing a cage model for cervical spinal fusion. Side-holes whose numbers vary between 0 and 10 are incorporated into the cage model. The effect of side-holes on the predicted stress levels in the cages subjected to compressive loading is investigated using FEA. The analyses are then validated by experimental tests. This chapter also provides a general discussion of the results followed by a comparison with other published studies.

In Chapter 4, the feasibility of using a bioactive/biodegradable composite as a potential cervical spinal fusion cage material is evaluated. A range of possible Young's modulus values for the composite is calculated. The cage model (with 10 side-holes) defined in Chapter 3 is then used to determine the stress levels within the cage, using FEA. This chapter includes a detailed background literature on the material and mechanical properties of bioactive/biodegradable composite and its individual components. The chapter ends with the main conclusions of the study.

Chapter 5 describes the development of a surgical instrument to facilitate implantation of a range of lumbar spinal fusion cages. In this chapter the design process for the instrument is explained in detail. The development and evaluation of concept designs are presented and discussed. The final design for an instrument is described and the prototype instrument is presented. The instrument is tested and compared with other available devices. The chapter ends with a brief discussion of the study.

Chapter 6 summarises the thesis by presenting the overall conclusions with regard to the original aims of the research. Following Chapter 6 are Appendices A to K, which provide further information on a range of subjects; the reader is referred to the relevant appendix in the text.

2. BACKGROUND

2.1. Chapter overview

This chapter aims to provide the general information required to understand the subsequent chapters. Section 2.2 introduces the medical device design process and its tools. The anatomical terms are presented in §2.3. The human spine is described in §2.4 followed by a description of spinal fusion and fusion cages in §2.5. Detailed background information on each specific part of the study is given in the relevant chapter.

2.2. Design

2.2.1. Process

In order to ensure the safety of healthcare workers and patients, the design process of medical devices is highly regulated (Aitchison *et al.*, 2009). Design developers are required to ensure that the entire design process is carried out in a systematic and repeatable manner in order to comply with regulations (Leahy *et al.,* 2000). The design of the device has to meet certain requirements directed by legislations such as the Medical Device Directive for Europe and the Food and Drug Administration for the USA. A record has to be kept of the design process which describes the design history of the product. This is known as the Design History File (also referred to as a Technical File or Design Dossier), which needs to be maintained after the product is released to include any subsequent modifications (Aitchison *et al.,* 2009). This document needs to show compliance with regulatory requirements and evidence that the device achieves the performance intended by the manufacturer.

The design process can be divided into six stages: market research, design specification, development of concept designs, detail design, manufacturing and sales (Aitchison *et al.*, 2009). In this thesis, depending on the objective of the chapter, different stages of this process have been applied. For example, Chapters 3 and 4 develop and analyse the concept design of an implantable medical device while Chapter 5 includes a broader use of the design process. There are different tools used during the design process such as finite element analysis (FEA). The advantages of FEA are discussed in §2.2.2.

2.2.2. FEA

The initial concept designs may constantly be altered during the design process. Hence, mechanical testing of these concepts may not be economical and would be time consuming. Thus, there is a need to use other methods to design and test medical devices. FEA is a method that has been used widely to analyse surgical implants (Galbusera *et al.,* 2008; Pitzen *et al.,* 2002b; Zhong *et al.,* 2006). A major advantage of this method is that it allows different designs to be assessed and optimized without the need to build unnecessary and expensive prototypes. Parameters in the finite element model can be changed repeatedly and quickly to evaluate the effect and influence of a single component before the concept design is manufactured (Pitzen *et al.,* 2002b). FEA also has the advantage of mimicking *in vitro* conditions (i.e. experimental procedures). However, FEA should not replace mechanical *in vitro* testing, but rather complement it. The operation of FEA is explained in detail in §2.2.3.

2.2.3. How FEA works

FEA is a computer method that is used to produce three-dimensional models (Figure 2.1 a) and simulate the effect of applying loads to them. It characterizes a complex structure by dividing it into distinct homogeneous parts, called elements (Figure 2.1 b). The individual elements are interconnected at nodes (Figure 2.1 c). The size and shape of the elements can be controlled and need to be specified accurately in order to produce a reliable model (Pitzen *et al.,* 2002b). Usually the shape of the elements depends on the geometry of the model under analysis. Several commercial software packages which perform FEA are available. SolidWorks (SolidWorks 2009, Santa Monica, USA) was used in this thesis to produce the models which were analysed using COSMOS (in SolidWorks). The information provided in this section on operation of FEA is taken from COSMOSWorks Designer 2007 Training Manual (Document number: PMT0140-ENG, SolidWorks, Santa Monica, USA). Analysis of a model using FEA can be divided into three phases.

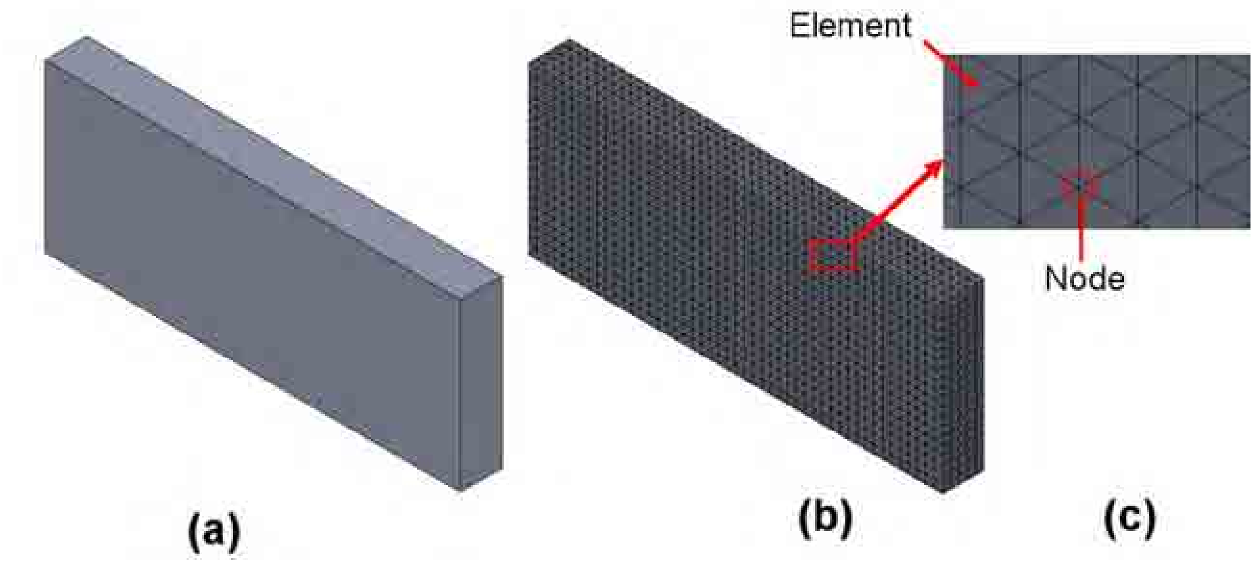

Figure 2. 1. (a) Three-dimensional view of a model. (b) Three-dimensional view of a meshed model. (c) Two-dimensional illustration of elements connected by nodes.

In the first phase SolidWorks is used to produce the model (Figure 2.1 a). The structure of the model can then be divided into small elements; this process is called meshing (Figure 2.1 b). Elements with different sizes can be defined on the same model in order to obtain a suitable mesh for analysing a specific component of the model in more detail. The duration of the analysis can be affected by the mesh size; coarser sizes usually reduce the analysis time and can be suitable in areas of low anticipated stress, whereas finer mesh sizes usually increase the analysis time and can be used in areas where high stress is expected. Tetrahedral-shaped elements are one of the shapes used to analyse linear problems. This shape is used in the analyses of this thesis (Chapters 3 and 4). Tetrahedral-shaped elements have a total of four nodes (one in each corner) and each node has three degrees of freedom (DOF). The DOF of a node allows it to translate or rotate. Each DOF of each node contains an unknown. In analysis, a DOF can be referred to as a nodal displacement. Displacements are primary unknowns and are always calculated first. Once meshing is complete, loads and constraints (boundary conditions) as well as material properties are applied to the model (Figure 2.2 a).

In the second phase COSMOS is used to analyse the model by finding nodal displacements. Stresses and strains (other aspects of the analysis) are calculated based on the nodal displacements. The results of the analysis can be viewed in the final phase and are shown by colour plots either in the form of displacements, stresses (von Mises stress and stresses in different directions) or strains (Figures 2.2 b, c and d). In Chapters 3 and 4 of this thesis, the models are analysed using FEA and the results in terms of displacement, von Mises and normal compressive stresses are determined. The von Mises stress is explained in §2.2.4. The information provided in this section on the definition of von Mises stress is taken from Benham and Crawford (1987).

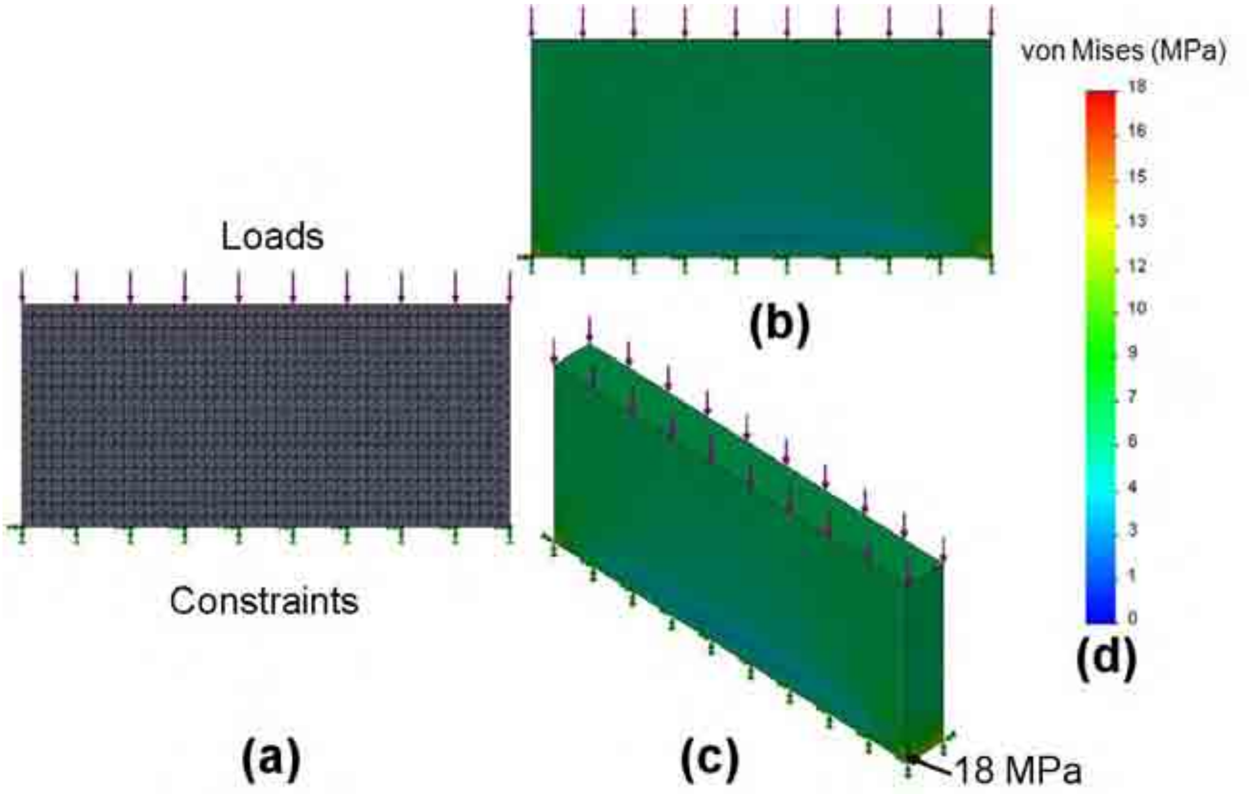

Figure 2. 2. (a) Two-dimensional view of a meshed model when loads and constraints are applied on the model. (b) and (c) Two-dimensional and three-dimensional views of the analysed model, respectively. The colours show the distribution pattern of the von Mises stress within the model. (d) Colour scale showing von Mises stresses corresponding to the colours in (b) and (c).

2.2.4. von Mises stress

Chapters 3 and 4 of this thesis consider the possibility of the cage material yielding as well as investigate the normal compressive stress and displacement for the cage models. Yielding will occur when the material is stressed beyond a certain point, which results in a disproportionate stress-strain relationship. For example, in a uni-axial tensile test, yielding will occur when the axial stress exceeds the material's yield stress. When there is only one principal stress, yielding is easy to predict because fracture occurs perpendicular to the direction of tensile stress (Benham and Crawford, 1987).

In many load-bearing structures, the stresses are not uni-axial and yielding is more difficult to predict. It has been suggested that one way to approach this problem is to consider the strain energy within the material. A material will yield if the strain energy exceeds the value required to initiate fracture (Benham and Crawford, 1987). This concept of considering the strain energy in a material has been used to develop a yield criterion, known as the shear strain energy criterion (von Mises), whereby the three principal stresses can be used to calculate the von Mises stress. Determining the principal stresses at any point within a structure will give an indication as to whether the material will yield at that point. By comparing the von Mises and yield stresses of the material, the likelihood of a structure yielding for a given load and deflection can be determined (Benham and Crawford, 1987). Such analyses typically use the von Mises stress distribution.

2.2.5. Validation

FEA can be a very useful tool to quickly and rapidly investigate the influence of different loading conditions on a component. However, predictions of FEA have to be validated to ensure that they are reliable to use (Ng *et al.,* 2003; Pitzen *et al.,* 2002a; Pitzen *et al.,* 2002b). There are different strategies used to validate models. In general, validation is either qualitative or quantitative. Qualitative validation involves comparison of the general results (e.g. positions of high stress) without estimating quantitatively how well the model approximates the truth. Estimating the accuracy of the model requires quantitative validation. This usually involves comparisons with either mathematical or experimental results. Mathematical methods may be either analytical or numerical (i.e. comparing the FEA results to those of other FEA studies) models. In these methods, the obtained results are usually compared to those of other available studies which may involve drawbacks such as the reliability of the other studies and how conditions and methods of the studies compare. In the experimental approach, the finite element (FE) predictions are compared to the results from the corresponding experiments. These methods allow a complete control of the experimental procedure and its consistency with the FE study. The accuracy of the FE model can be evaluated by calculating the average percentage difference between the FE predictions and the experimental results. Once the results of this comparison are close together, the FE model may be reliable to use for further analysis (Pitzen *et al.*, 2002b). Experimental validation of an FE model is presented in Chapter 3, §3.3.5.

2.3. Anatomical terminology

2.3.1. Planes of the human body

There are three reference planes in the human body (Figure 2.3 a): the sagittal, coronal and transverse planes (Middleditch and Oliver, 2005). These planes are mutually perpendicular. The sagittal plane vertically divides the body into left and right sides. The coronal plane divides the body into front and back sides. The transverse plane horizontally divides the body into upper and lower portions.

2.3.2. Anatomical directions

Positions of the anatomical features are referred to by their relevant anatomical directions (Kurtz and Edidin, 2006) (Figure 2.3 b). The upward and downward directions are referred to as superior and inferior, respectively. The anterior describes the front of the body while the posterior describes the back of the body. The lateral direction points away from the middle of the body and the medial direction points towards the middle of the body.

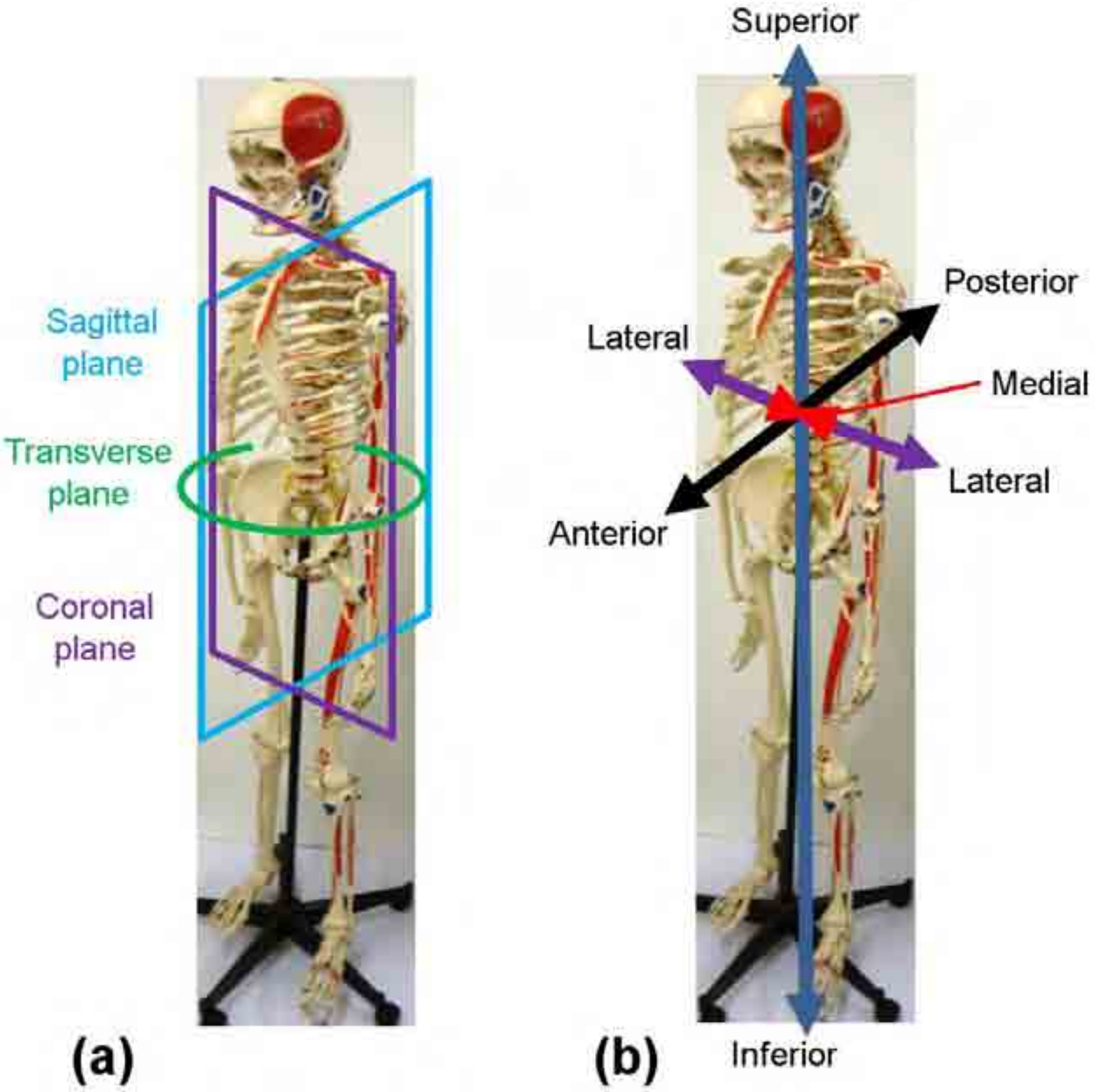

Figure 2. 3. (a) Anatomical planes through the body. (b) Anatomical reference direction through the body.

2.4. The human spine

2.4.1. Regions of the spine

As shown in Figure 2.4 the spine is divided into four regions (Kurtz and Edidin, 2006). The cervical vertebrae (C1-C7) provide flexibility and range of motion for the head. The thoracic vertebrae (T1-T12) support the ribs and are responsible for structural support and some flexibility. The lumbar vertebrae (L1-L5) have the largest and strongest of the vertebral bodies because they are subjected to the highest forces and moments in the spine. Sacral vertebrae (sacrum) (S1-S5) attach the spine (at L5-S1) to the iliac bones of the pelvis. A series of four fused vertebrae, called the coccyx, follows the sacral region. In a healthy human body, the cervical, thoracic and lumbar regions consist of individual vertebrae (Kurtz and Edidin, 2006; Middleditch and Oliver, 2005). In many text books it is stated that the vertebrae of the sacral region are fused together. However, magnetic imaging of the region shows that there is some cartilage between S1 and S2 (Wicke, 1998).

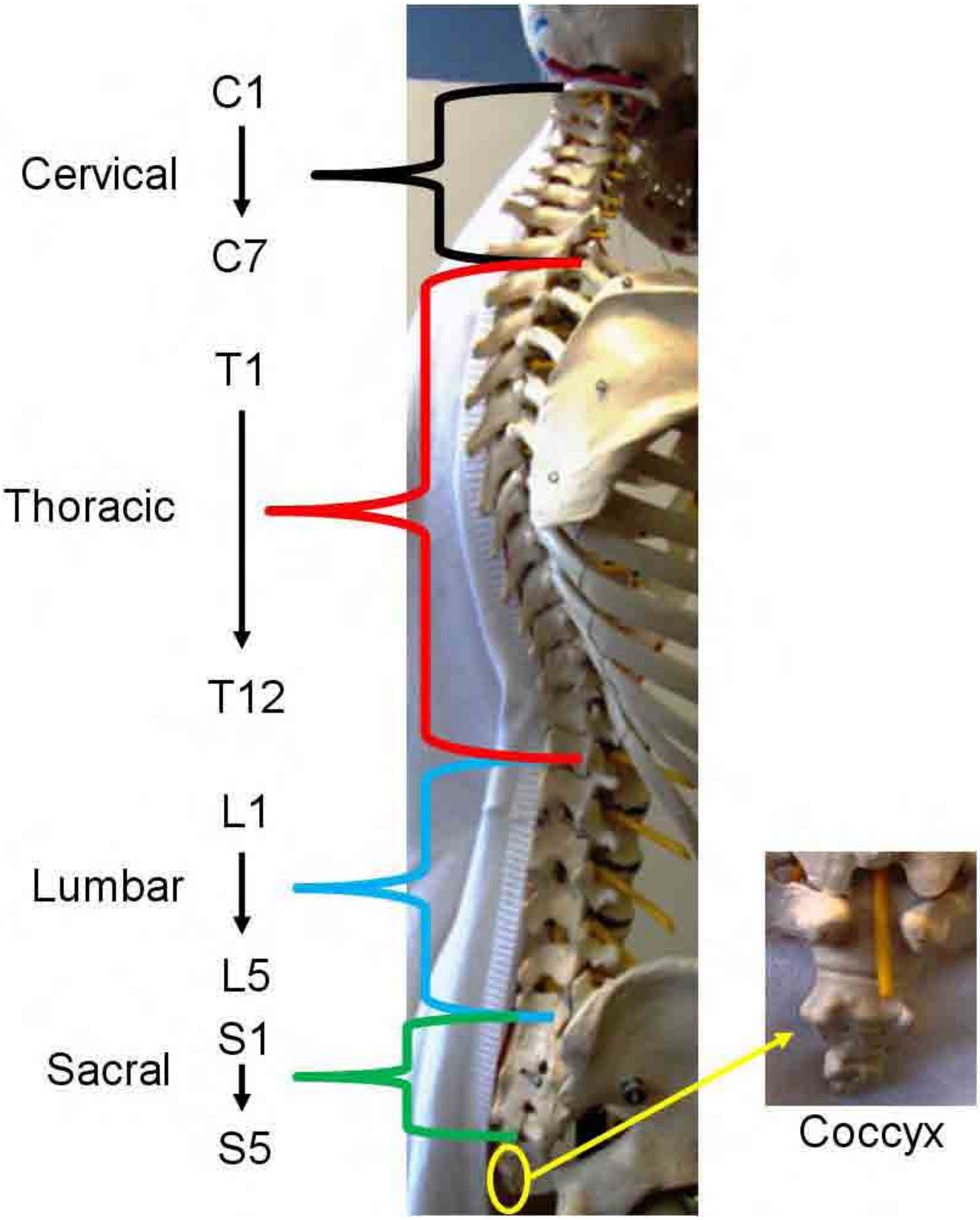

Figure 2. 4. Model of the vertebral column. From the top of the column going down: cervical vertebrae (C1 to C7), thoracic vertebrae (T1 to T 12), lumbar vertebrae (L1 to L5), sacral vertebrae (S1 to S5) and coccyx.

2.4.2. Motions of the spine

Figures 2.5 to 2.7 illustrate the motions of the spine in terms of segments which are considered to consist (in this chapter) of an intervertebral disc in between two adjacent vertebrae (Kurtz and Edidin, 2006; Middleditch and Oliver, 2005). Axial compression is caused by the vertical loads applied on the spine; a combination of the weight of the body above the segment and the forces from the surrounding muscles (Figure 2.5) (Kurtz and Edidin, 2006). The terms flexion and extension convey the meaning of anterior and posterior bending, respectively (Figure 2.6). Axial rotation (or torsion) refers to rotation of the spine along its axis and involves twisting of the intervertebral discs (Figure 2.7). Lateral bending is a sideways bending movement which is a combination of lateral bending and rotation of the intervertebral discs.

The loads experienced by the spine arise from a combination of compressive forces and various movements i.e. shear, torsion and bending (Kurtz and Edidin, 2006; Middleditch and Oliver, 2005). These movements arise because the surrounding muscles contract, resulting in additional compressive forces to the spine. Depending on the nature of the research, a particular load in a particular direction is applied to the concept design. For example in Chapters 3 and 4 of this thesis a compressive load is applied.

Different methods such as computational models (e.g. FEA), experimental procedures (e.g. measurement of the pressure within intervertebral discs) and a combination of the two (e.g. linked segment models with electromyographic data) have been used to determine spinal loading (Kurtz and Edidin, 2006). The calculated compressive forces applied to the neck predicted by a mathematical model (Moroney *et al.*, 1988) range from 122 N (relaxed posture) to 1164 N (extension posture). Hattori *et al.* (1981) measured the pressure in human cervical discs and the corresponding calculated forces ranged from 53 N (lying on the back) to 155 N (extension) (Kurtz and Edidin, 2006).

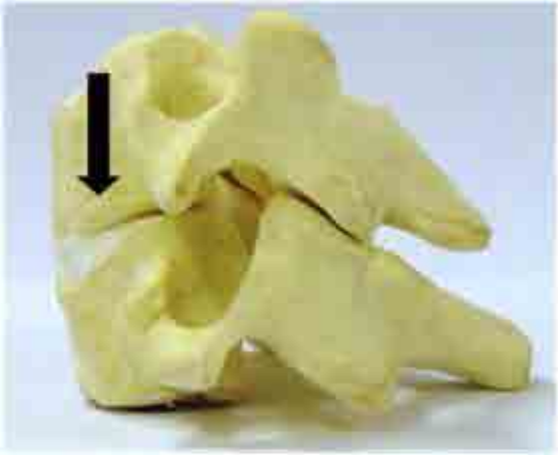

Figure 2. 5. Axial compression; the direction of compression is shown by the arrow.

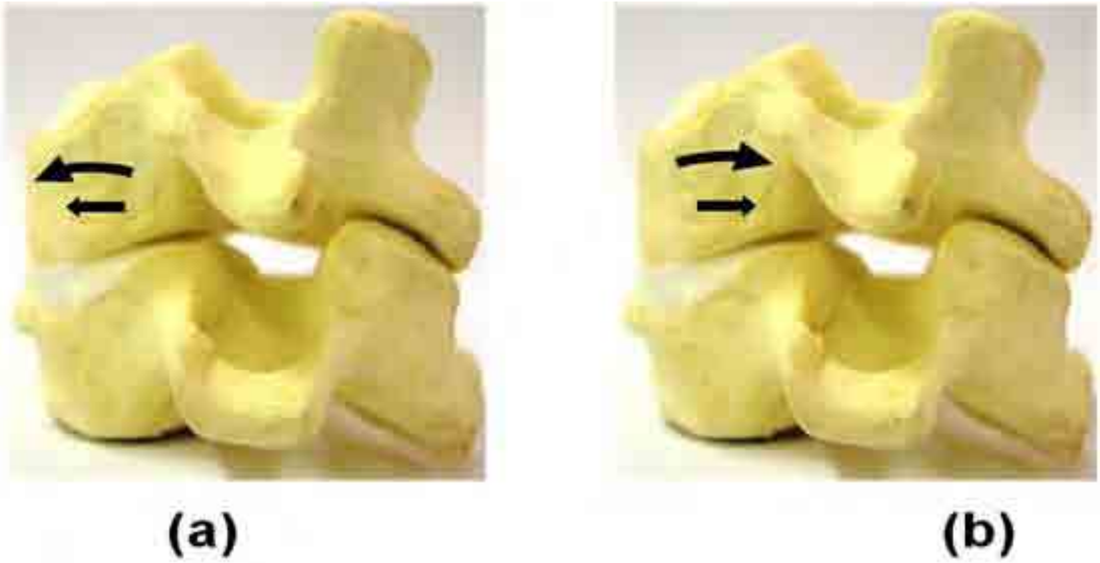

Figure 2. 6. (a) Forward flexion; the curved arrow shows the direction of flexion and the straight arrow the direction of the anterior translation. (b) Backward extension; the curved arrow shows the direction of extension and the straight arrow the direction of the posterior translation.

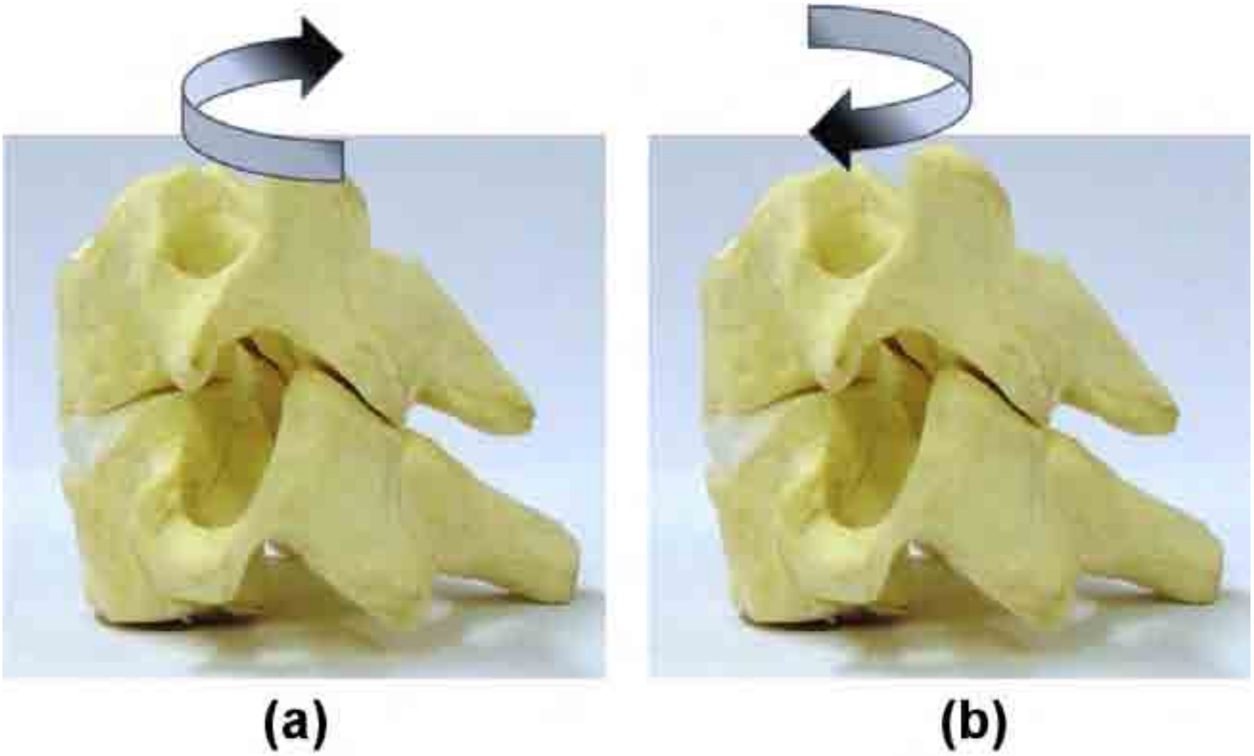

Figure 2. 7. (a) Axial rotation to the right; arrow is showing a clockwise direction. (b) Axial rotation to the left; arrow is showing an anti-clockwise direction.

2.4.3. Vertebrae

The vertebrae are the bones in the spine. Figures 2.8 and 2.9 illustrate the anatomy of a typical C7 vertebra (Middleditch and Oliver, 2005). Each can be divided into three functional components: the vertebral body, the pedicles and the posterior elements (Joseph, 1986) (Figure 2.10).

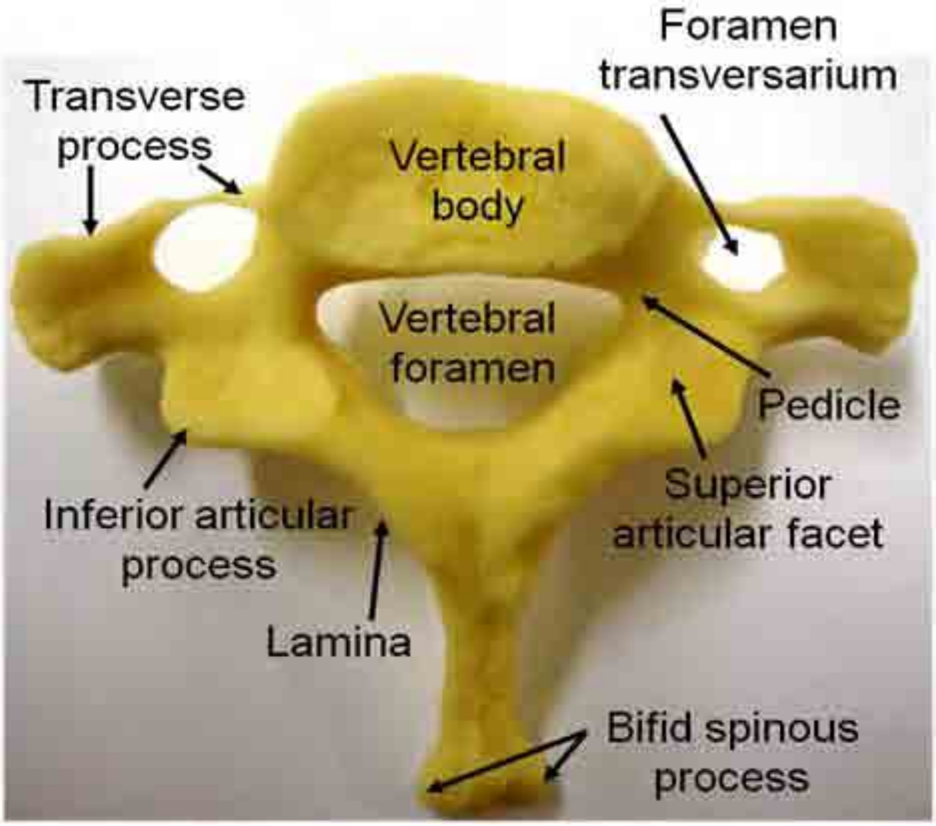

Figure 2. 8. Top (transverse) view of a model of cervical vertebra (C7).

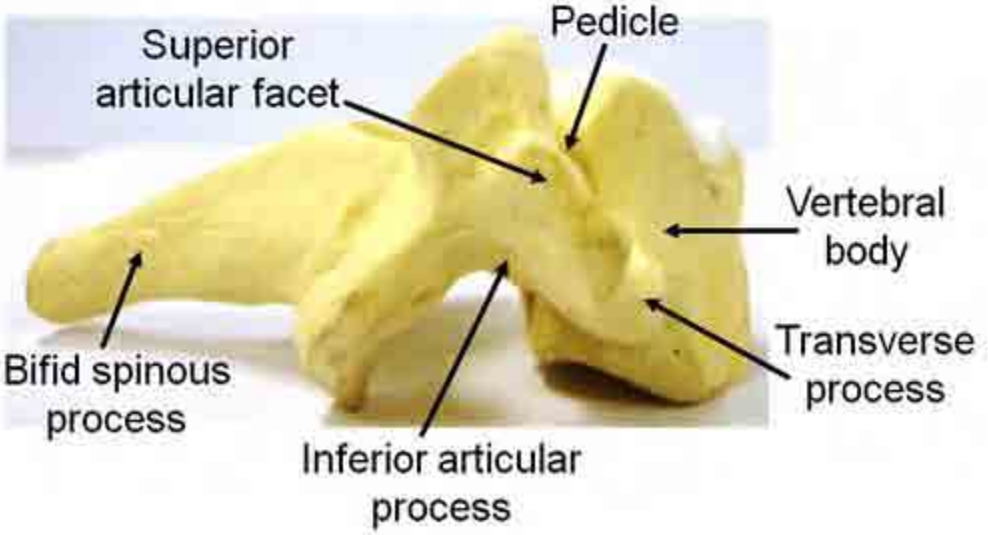

Figure 2. 9. Side (right lateral) view of a model of cervical vertebra (C7).

The vertebral body has roughly flat superior and inferior surfaces and is the main weight-bearing component of a vertebra. It sustains the compressive loads applied to the spine and transmits them to the vertebra below. In the vertebral body a thin cortical shell surrounds an inner cancellous bone cavity (Bryce *et al.*, 1995; Kurtz and Edidin, 2006). The cortical shell consists of densely packed layers of bone. The cancellous bone (also referred to as trabecular bone) consists of many small pores or cavities within its matrix. Its structure extends into the posterior elements via the pedicle (Bogduk, 2005). There are cartilage layers at the top and bottom surfaces of the vertebral body called end-plates. Their thickness varies with spinal level, for example, the lower lumbar vertebrae have the thickest end-plates (Edwards *et al.*, 2001).

The pedicles are two columns of bone which are situated between the posterior elements and the vertebral body and transmit tension and bending forces between the two (Denman, 1992; Middleditch and Oliver, 2005). They are usually hollow and are surrounded by a thick wall of cortical bone (Bogduk, 2005).

The posterior elements protect the spinal cord as well as facilitate the spinal motion (Joseph, 1986). The posterior elements receive the different applied forces on the vertebra through its various ligament (and associated muscle) attachments and then transmit them to the vertebral body via the pedicles (Bogduk, 2005).

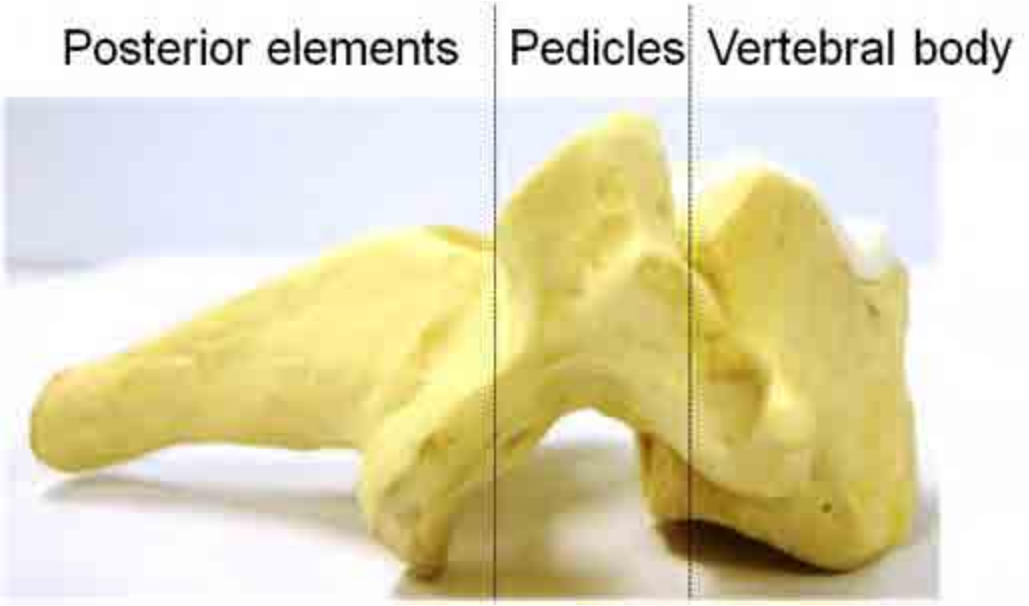

Figure 2. 10. The division of a cervical vertebra into its three functional components.

In some FEA studies, the cortical shell has been modelled as a thin layer that is bonded to the surface of the inner cancellous bone (Liebschner *et al.,* 2003; Silva *et al.,* 1997). This model creates two independent load paths: the cortical shell and the cancellous bone. However, in a study by Bayraktar *et al.* (2004), it was shown that these load paths are not independent and there is a mechanical interaction between the two. An experimental study by Rockoff *et al.* (1969) has shown that the cortical shell carries between 45 and 75% of the applied axial compressive load to the vertebra. Also, it has been shown that in the vertebrae, the cortical shell around the cancellous bone enhances its stiffness and strength (Bryce *et al.,* 1995). Hence, vertebral models used in Chapters 3 and 4 of this thesis are modelled as cortical bone and assumed to have homogeneous and isotropic material properties.

2.4.4. Intervertebral disc

The intervertebral discs are the soft segments of the spine and are located in between most vertebrae (Hukins, 1988). They provide the spine with the necessary flexibility by allowing movement of the vertebrae relative to each other. Loads applied to the spinal column are transmitted to the intervertebral discs from the vertebral bodies. The intervertebral discs then transmit the loads from one vertebral body to the next. The size and shape of the intervertebral discs vary along the spinal column. They are small and have an elliptical cross-sectional shape in the cervical region and become larger with a more kidney-like cross-sectional shape in the lumbar region (Hukins, 1988; Kurtz and Edidin, 2006). The change in size and shape is to fulfil the mechanical requirements at different spinal regions. The intervertebral discs are loaded in combinations of compression, torsion and bending (Hukins, 1988).

Approximately a third of the total length of the spinal column is made up of the intervertebral discs (Hukins, 1988). The intervertebral disc has a soft inner region, nucleus pulposus, which is surrounded by a tough outer region, annulus fibrosus. The two parts, although quite different in texture, have no clear boundary between them; the outer parts of the nucleus pulposus merge with the inner parts of the annulus fibrosus (Hukins, 1988) (Figure 2.11). The intervertebral discs are separated from the vertebral bodies by the end-plates. The articulation between vertebral bodies is allowed by the intervertebral discs and the end-plates (Kurtz and Edidin, 2006).

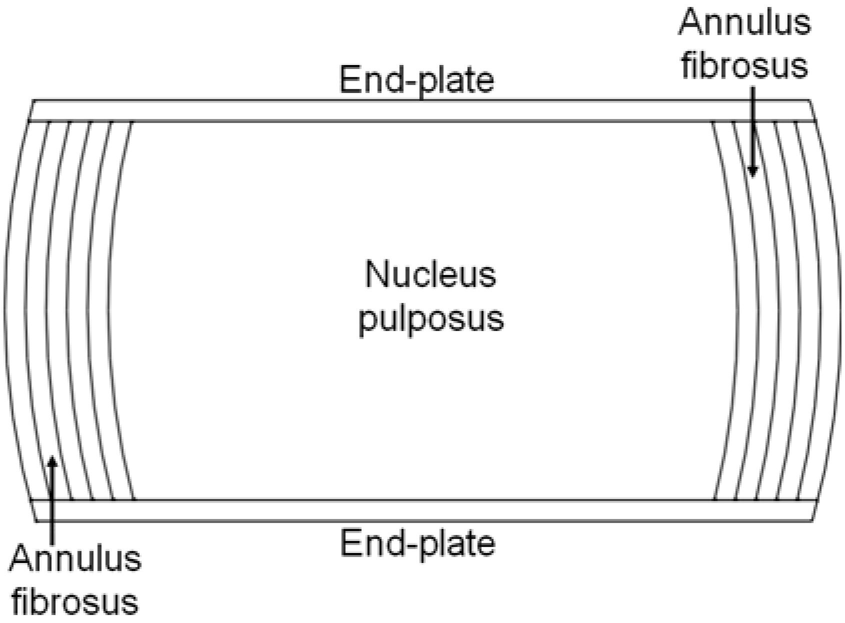

Figure 2. 11. An intervertebral disc schematic image; illustrating a vertical section. Note, in a healthy human spine the end-plates merge with the annulus fibrosus (Aspden *et al.*, 1981).

The mechanical properties and physiological functions of the intervertebral discs are directly influenced by their components (Kurtz and Edidin, 2006). The nucleus pulposus of a healthy disc contains water (approximately 80% by weight), a small percentage of collagen fibrils and proteoglycans (proteins bonded to polysaccharides which draw water into the nucleus pulposus) (Hukins, 1988; Kurtz and Edidin, 2006). Axial load in a healthy disc is converted by the nucleus pulposus into radial pressure which is then resisted by the tensile properties of the annulus fibrosus (Hukins, 1988). The annulus fibrosus consists of between 60 and 70% water (by weight) and multiple layers of collagen fibres (Hickey and Hukins, 1980; Markolf and Morris, 1974).

The structure of the intervertebral disc changes with age (Kurtz and Edidin, 2006). Age-related disc degeneration may lead to mechanical disruption of its components (Porter, 1993) which may cause back pain, laxity or immobility (Zhang and Teo, 2008). Surgical treatment of this condition is discussed in §2.5.1.

2.5. Spinal fusion and fusion cages

2.5.1. Introduction

Age and degenerative disc disease can result in changes in the structure, composition and mechanical function of the intervertebral discs (Kurtz and Edidin, 2006). These changes may cause chronic pain, laxity or immobility (Zhang and Teo, 2008) which may lead to changes in the normal pattern of movements (§2.4.2). Spinal fusion has been used to treat degenerative discs after conservative treatments have failed (Mastronardi *et al.*, 2006; Toth *et al.*, 2006; Zhang and Teo, 2008). As stated in Chapter 1, interbody spinal fusion is a surgical treatment where the intervertebral disc is excised and replaced with bone fragments to encourage bone growth into the intervertebral space to fuse adjacent vertebrae together (Adam *et al.*, 2003; Axelsson *et al.*, 2009; Cho *et al.*, 2002; Mastronardi *et al.*, 2006; McAfee and Maryland, 1999; Zhang and Teo, 2008; Zhong *et al.*, 2006).

2.5.2. Fusion cages

2.5.2.1. *What they do*

Fusion cages are usually used in spinal fusion to retain the bone fragments (Adam *et al.*, 2003; Axelsson *et al.*, 2009; Cho *et al.*, 2002; Mastronardi *et al.*, 2006; McAfee and Maryland, 1999; Smit *et al.*, 2006; Zhang and Teo, 2008; Zhong *et al.*, 2006). These cages act as axial load-bearing devices and should provide immediate structural stability post-operation as well as maintain the intervertebral height while fusion takes place (Adam *et al.*, 2003; Cho *et al.*, 2008; Epari *et al.*, 2005; Hee and Kundnani, 2010; Kandziora *et al.*, 2001; Steffen *et al.*, 2000; Zhang and Teo, 2008; Zhong *et al.*, 2006). Commercially available fusion cages come in many designs (Adam *et al.*, 2003; Cho *et al.*, 2002; Cho *et al.*, 2008; Chou *et al.*, 2008; Epari *et al.*, 2005; Hee and Kundnani, 2010; Kandziora *et al.*, 2001; Steffen *et al.*, 2000; Tsuang *et al.*, 2009; Zhang and Teo, 2008; Zhong *et al.*, 2006). Typical cervical and lumbar fusion cages are shown in Figures 2.12 and 2.13, respectively. Some cage designs have toothed surfaces to aid fixation (Cho *et al.*, 2002; Cho *et al.*, 2004; Chou *et al.*, 2008; Epari *et al.*, 2005; Mastronardi *et al.*, 2006; Steffen *et al.*, 2000) while others are fixed by screws or plates (Cho *et al.*, 2004; Galbusera *et al.*, 2008; Pitzen *et al.*, 2002b; Steffen *et al.*, 2000; Vadapalli *et al.*, 2006). Also, there are fusion cages that have both toothed surfaces and screws to aid fixation (Figures 2.12 and 2.13). The cage models analysed in Chapters 3 and 4 of this thesis have toothed surfaces. Design of some fusion cages is such that access to the screw holes, to insert fixation screws, is partially obscured by the vertebral body (Figures 2.12 and 2.13). An instrument is developed and explained in Chapter 5 to overcome this problem.

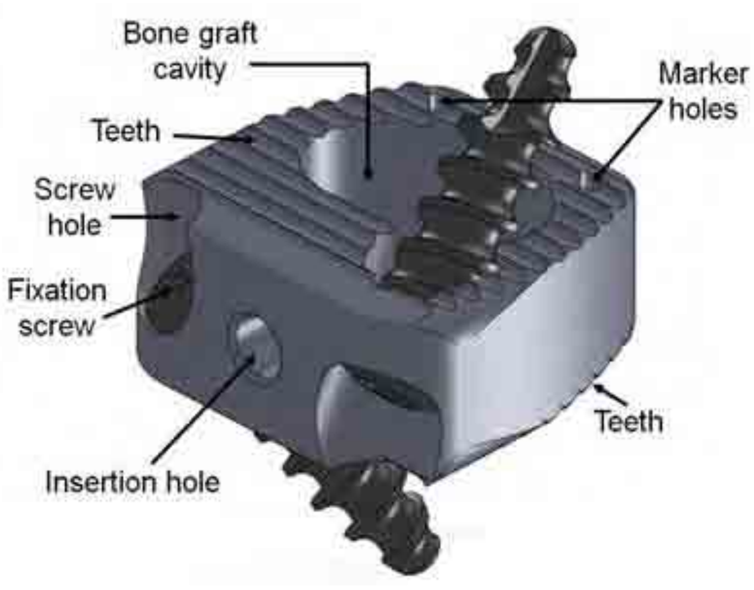

Figure 2. 12. Commercially available cervical fusion cage (STALIF^{TM} C, C147561-2T) made from PEEK with titanium alloy fixation screws (CSP4017) (Surgicraft Ltd., Redditch, UK).

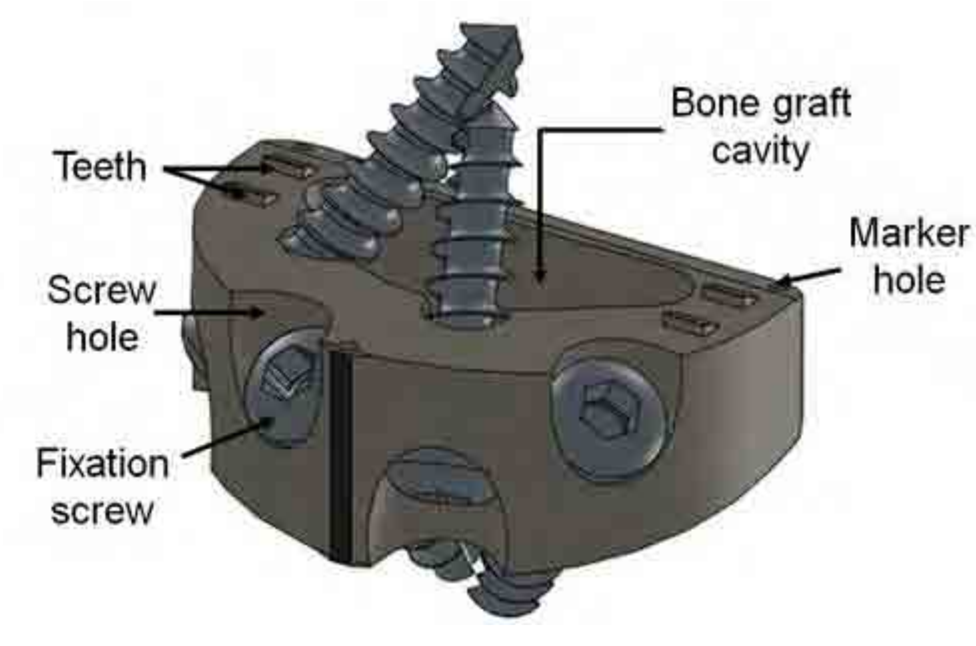

Figure 2. 13. Commercially available lumbar fusion cage (STALIF^{TM} TT, STT39130-12LT) made from PEEK with titanium alloy fixation screws (STT5525 and STT5530) (Surgicraft Ltd., Redditch, UK).

There are several previous FEA studies on the mechanical behaviour of lumbar fusion cages that have investigated the following: cage number (single or coupled cage use), cage shape (box or cylinder), cage size and position, hollow or solid cage, stress distribution on (end-plates) bone-cage interface, cage designs in range of motion and cage material (Adam *et al.*, 2003; Tsuang *et al.*, 2009; Vadapalli *et al.*, 2006; Zhong *et al.*, 2006). However, there are only a few published FEA studies on cervical cages which mainly concentrate on comparing current surgical methods (Galbusera *et al.*, 2008), analyzing the performance of new implants and investigating different implant designs on the segmental range of motion (Pitzen *et al.*, 2002b). Side-holes are a common feature in many commercial fusion cages (Cho *et al.*, 2008; Epari *et al.*, 2005; Kandziora *et al.*, 2001; Steffen *et al.*, 2000; Tsuang *et al.*, 2009; Zhang and Teo, 2008). These holes may enable fluid to flow into and out of the cage interior which can aid the transportation of nutrients and removal of waste products. Studies of lumbar and cervical cages have not addressed the problems of how many side-holes can be accommodated on the cage lateral walls and the effect of the side-holes (and hole number) on the cage strength in compression. In Chapter 3 of this thesis the influence of side-holes and their number on cervical cage models under compressive loading is evaluated using FEA.

2.5.2.2. Fusion cage materials

Fusion cage materials should provide high mechanical strength and increase the rate of fusion (Hee and Kundnani, 2010; van Dijk *et al.*, 2002) by discouraging stress shielding. Commercially available fusion cages are made from titanium alloy (Chou *et al.*, 2008; Kandziora *et al.*, 2001), polyetheretherketone (PEEK) (Cho *et al.*, 2002; Mastronardi *et al.*, 2006; Toth *et al.*, 2006) or composites (e.g. carbon–fibre reinforced PEEK) (Abu Bakar *et al.*, 2003). In Chapter 4 of this thesis, the feasibility of using a bioactive/biodegradable composite as the material for a cervical spinal fusion cage is evaluated.

PEEK is the most common and favoured material for fusion cages because it is a highly biocompatible, non-toxic, non-resorbable polymer (Abu Bakar *et al.*, 2003; Cho *et al.*, 2002; Chou *et al.*, 2008; Ferguson *et al.*, 2006; Hee and Kundnani, 2010; Kurtz and Devine, 2007; Mastronardi *et al.*, 2006; Sagomonyants 2008; Toth *et al.*, 2006). Compared to other current fusion cage materials (e.g. titanium alloy with a Young's modulus of 110 GPa, Hee and Kundnani, 2010; Vadapalli *et al.*, 2006), PEEK has a Young's modulus of 3.6 GPa (Chou *et al.*, 2008; Hee and Kundnani, 2010; Vadapalli *et al.*, 2006). This is much closer to that of cortical bone (Cho *et al.*, 2008; Chou *et al.*, 2008; Mastronardi *et al.*, 2006) which has a typical Young's modulus of 12 GPa (Hee and Kundnani, 2010; Vadapalli *et al.*, 2006). This better match of Young's modulus results in less stress shielding and potentially encourages bone growth (Cho *et al.*, 2002; Chou *et al.*, 2008; Ferguson *et al.*, 2006; Hee and Kundnani, 2010). PEEK has good sterilization resistance (e.g. using steam, gamma irradiation and ethylene oxide processes) and can be fabricated using extrusion, injection molding and machining (Abu Bakar *et al.*, 2003; Ferguson *et al.*, 2006; Sagomonyants *et al.*, 2008; Toth *et al.*, 2006). It is also transparent to X-rays (Cho *et al.*, 2002; Cho *et al.*, 2008; Ferguson *et al.*, 2006; Hee and Kundnani, 2010; Kurtz *et al.*, 2007; Mastronardi *et al.*, 2006; Sagomonyants *et al.*, 2008; Toth *et al.*, 2006) which allows the bone within the cage to be seen on radiographs; usually two titanium markers (pins) are embedded on the upper and lower frames of the cage to identify the cage position during the post-operative follow-up X-rays (Cho *et al.*, 2002). PEEK is considered as the fusion cage material in Chapter 3 of this thesis.

3. EFFECT OF SIDE-HOLES IN CERVICAL FUSION CAGES

3.1. Chapter overview

This chapter uses finite element analysis (FEA) to investigate the extent to which side-holes can be incorporated into the design of a cervical spinal fusion cage without it failing mechanically. Section 3.2 introduces the study and states its aim. The cage model used in this study is developed and analysed in §3.3. Experimental set-up for FEA validation is also included in this section. The validation and FEA results obtained are shown in §3.4. The FEA results are discussed and compared with those of other FEA studies in §3.5 and the conclusions from this study are presented in §3.6.

3.2. Introduction

As mentioned in Chapter 2 (§2.5.2.1), there are no previous studies of cervical and lumbar cages that have addressed the effect of side-holes (and hole number) on the cage strength in compression. These holes can be important as they may enable fluid to flow into and out of the cage interior which can aid the transportation of nutrients and removal of waste products. In this study, the influence of side-holes and their numbers on cervical cage models under compressive loading was evaluated using FEA. A generic cervical fusion cage model based on commercially available designs is produced in §3.3.1 and analysed in §3.3.4.

3.3. Materials and methods

3.3.1. Cage model development

The finite element (FE) fusion cage model used in this study is based on two commercially available designs made from polyetheretherketone (PEEK) for the cervical spine: STALIF^{TM} C (Figure 3.1) and RABEA (Figure 3.2) (Surgicraft Ltd., Redditch, UK). STALIF^{TM} C cages are available in two types: domed and tapered and are offered in multiple heights (5.5, 6.5, 7.5, 8.5 and 9.5 mm) and widths (16, 14 and 12 mm). RABEA cages are also available in multiple heights (4, 5, 6, 7, 8 and 9 mm) and widths (14 and 16 mm). These cages have no side-holes. In this study the height and shape of the cage model, insertion hole size and position along with the number and dimensions of the teeth (Figure 3.3) were obtained from the mid-range tapered STALIF^{TM} C (C147561-2T). The cage model overall dimensions are means of the two cages: mid-range tapered STALIF^{TM} C (16.5 mm × 14 mm × 7.5 mm) and RABEA (CPPK081214) (14 mm × 12 mm × 8 mm). The dimensions of the cage model are shown in Figure 3.4. The cage material was chosen to be PEEK and modelled as a linear elastic isotropic material (Table 3.1).

Table 3. 1. Material properties used for FEA. Note that the Poisson's ratio for PEEK is taken from the data sheet (Victrex PLC, Thornton Cleveleys, UK).

Material	Young's Modulus (GPa)	Poisson's ratio	Reference
PEEK	3.6	0.4	Chen and Lee, 2006; Hee and Kundnani, 2010; Vadapalli *et al.*, 2006
Cortical bone	12 - 30	0.3	Hee and Kundnani, 2010; Hench, 1998; Vadapalli *et al.,* 2006; Zhong *et al.,* 2006
Stainless steel	200	0.3	Pietrzak *et al.,* 1996; Pitzen *et al.,* 2002a; Zhang and Teo, 2008

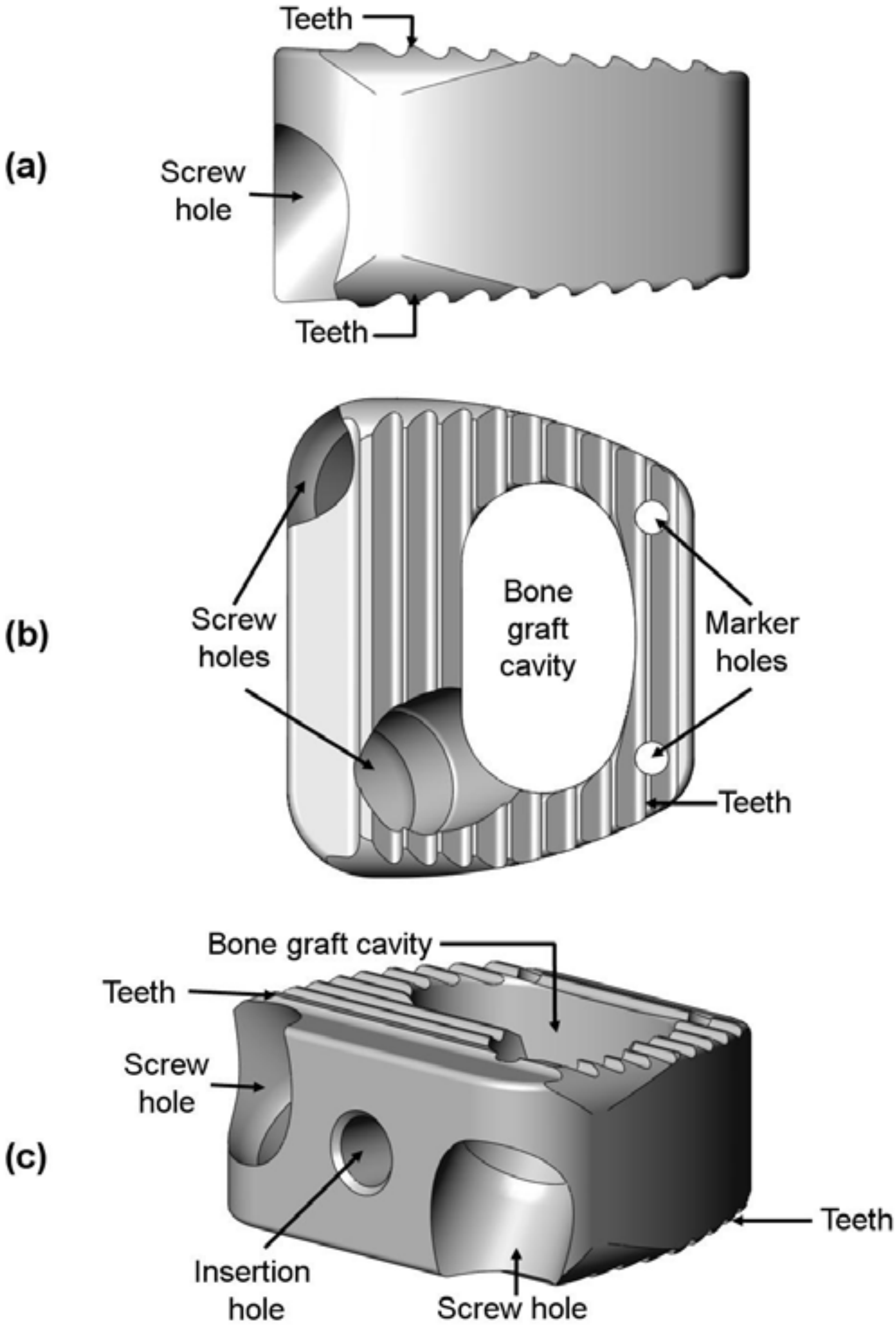

Figure 3. 1. Mid-range tapered STALIF^{TM} C (C147561-2T) made from PEEK (Surgicraft Ltd., Redditch, UK). The insertion hole enables a rod-shaped surgical instrument to be used to position the cage between the adjacent vertebrae. (a) Side view, (b) top view and (c) three-dimensional view.

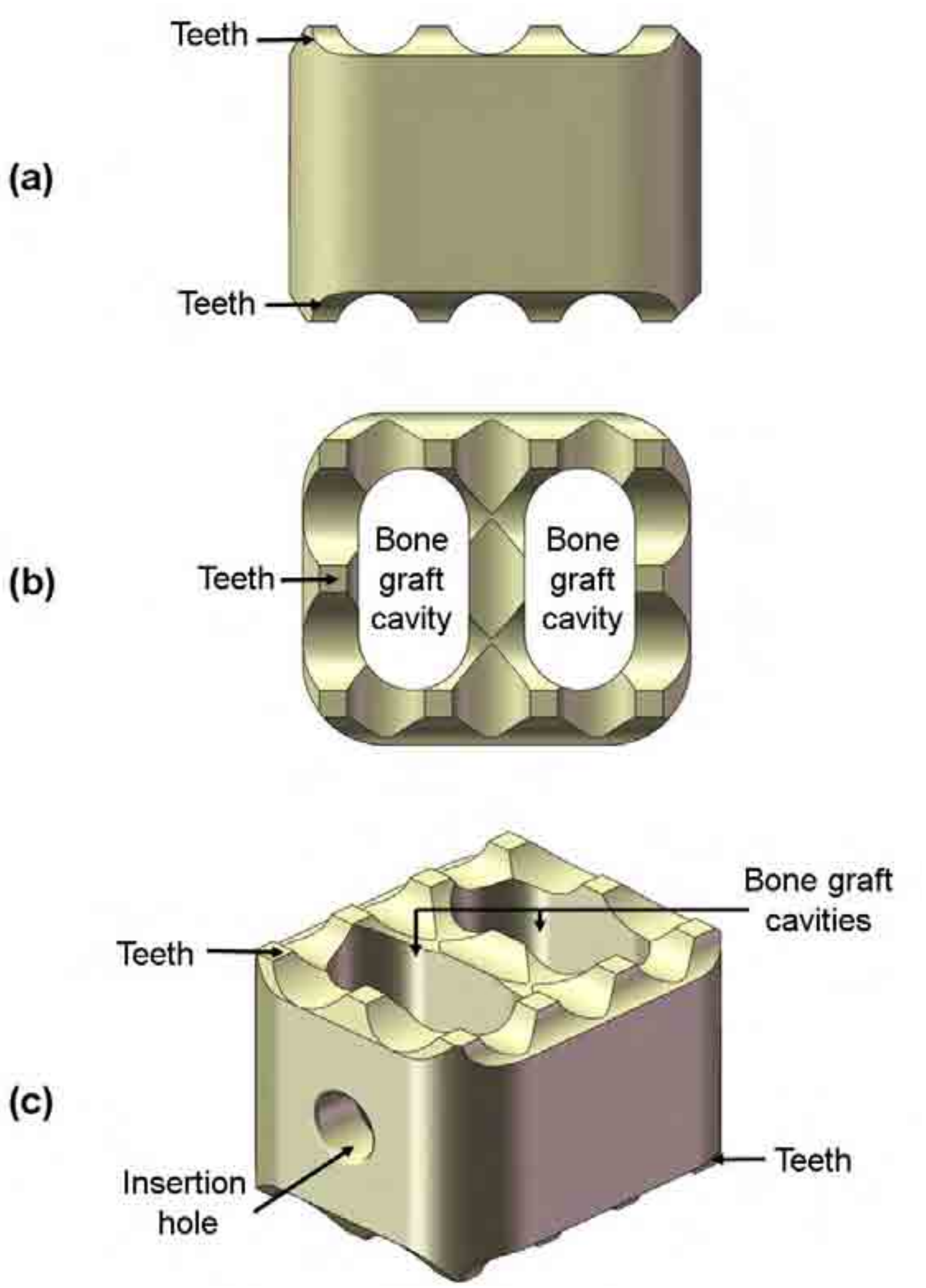

Figure 3. 2. RABEA cervical fusion cage (CPPK081214) made from PEEK (Surgicraft Ltd., Redditch, UK). (a) Side view, (b) top view and (c) three-dimensional view.

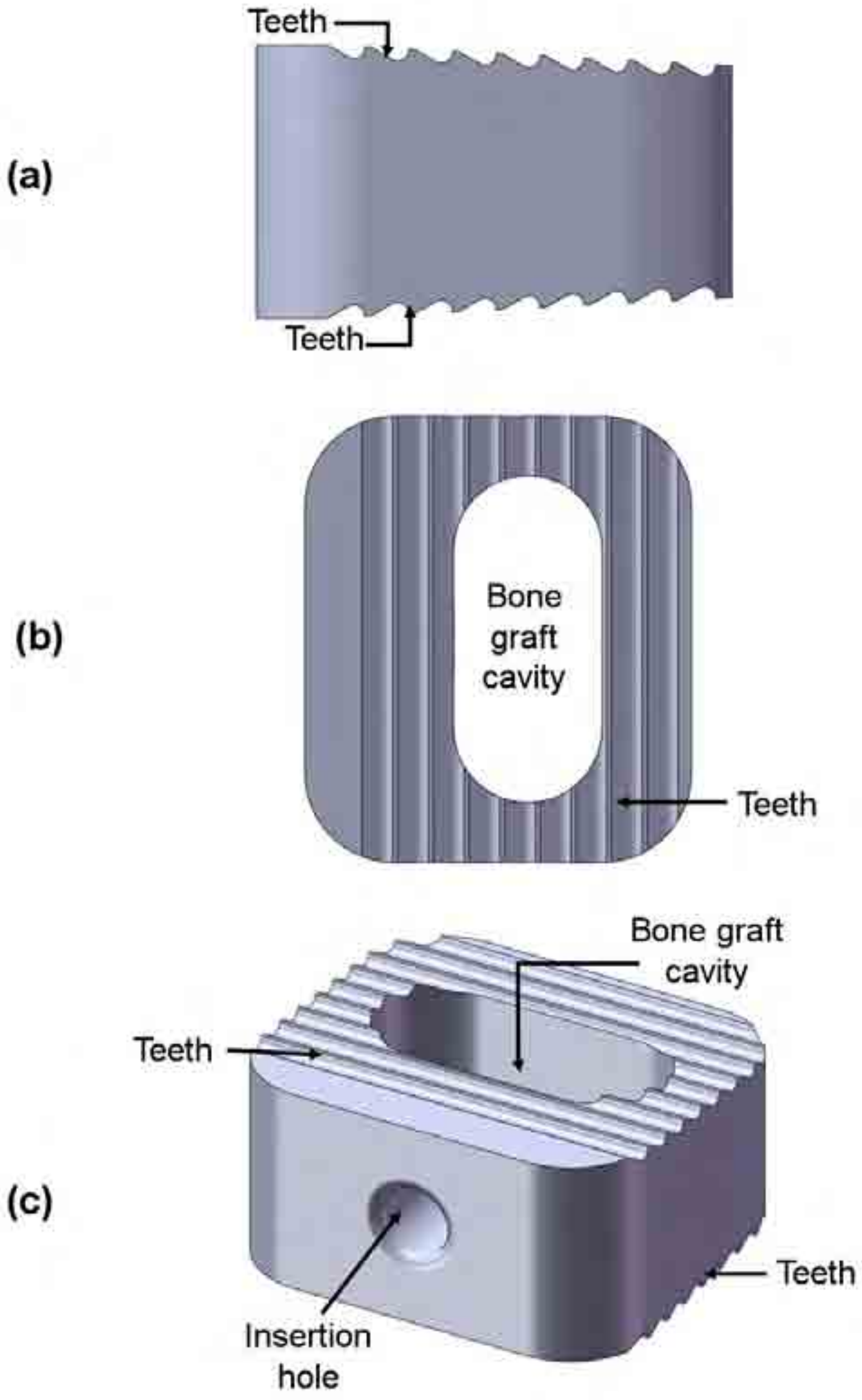

Figure 3. 3. Fusion cage model. There are teeth at the top and bottom of the cage that may enable the cage to grip the vertebrae, in order to retain the cage in place. (a) Side view, (b) top view and (c) three-dimensional view. Model dimensions are given in Figure 3.4.

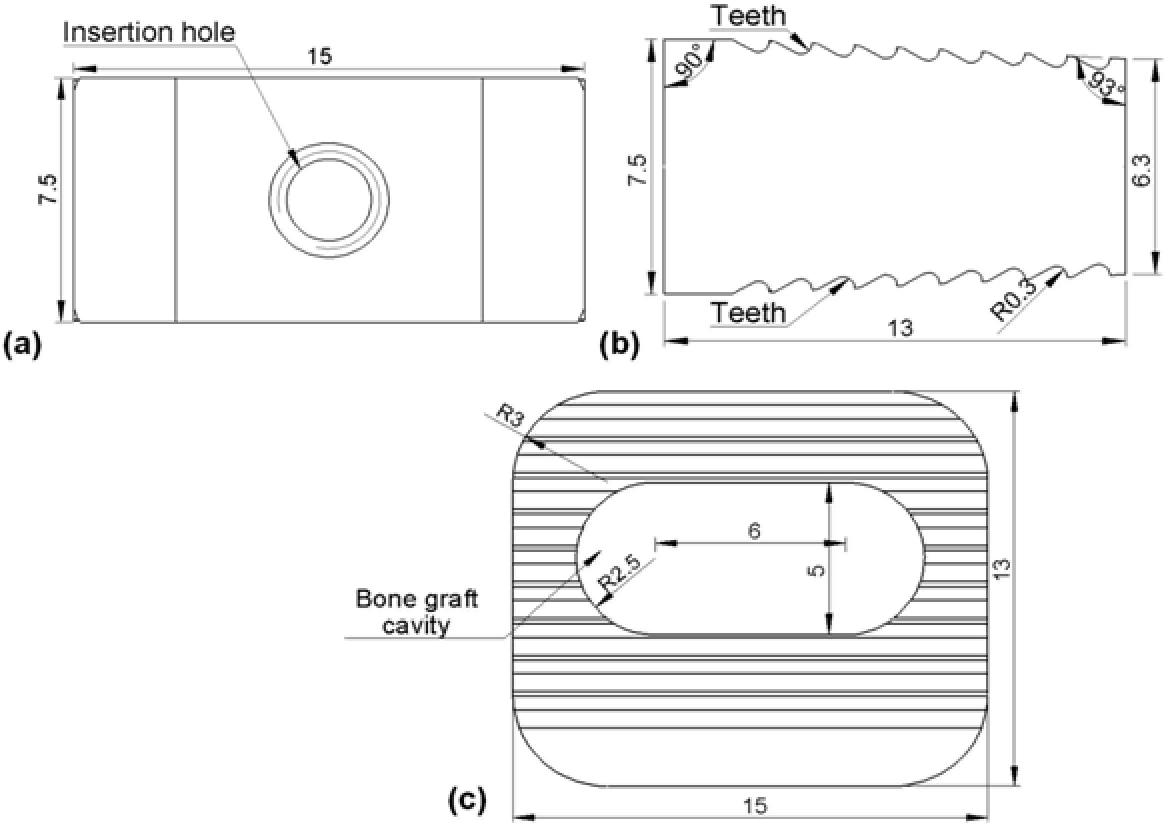

Figure 3. 4. Dimensions of the cage model shown in Figure 3.3. (a) Front view, (b) side view and (c) top view. All dimensions are in millimetres.

3.3.2. Side-holes

One model was developed with no side-holes (Figures 3.3 and 3.4); other models were identical but included between 1 and 10 side-holes. In order to position the holes, a rectangle (5.6 mm × 3.2 mm) was constructed on one side of the cage (Figures 3.5 a). The height corresponded to the height of the cage and the width corresponded to the anterior-posterior (AP) dimensions of the graft cavity. Initially, a single side-hole of diameter 2.9854 mm was cut in the centre of the rectangle, on the model's lateral side (Figure 3.5 b). This diameter was the biggest that could be defined within the confines of the rectangle while allowing for 0.1073 mm of clearance between the side-hole and the heights of the rectangle. Additional side-holes were introduced in a honeycomb pattern, with a maximum of 10 holes on each cage lateral side (Figure 3.5 c). In all the models, corresponding holes were cut on the opposite lateral side of the cage. On each cage, holes were spaced in such a way that their centres were positioned at a 60° angle from their immediate neighbouring holes. The total area of the side-holes on each lateral side of the cage was kept constant at 7.00 mm^2. This is the area determined from a single side-hole cage. The side-holes are circular to reduce stress concentrations. Appendix A, Figure A.1 provides further details of side-holes and their positions for each cage model.

3.3.3. Modelling vertebrae

The adjacent vertebrae were modelled as blocks (Figure 3.6) whose transverse sections correspond to the dimensions of the cage in Figures 3.4 b and c. The upper surface of the superior and the lower surface of the inferior vertebrae were parallel to each other (i.e. the furthermost surfaces of the two vertebrae). However, the surfaces in contact with the cage were angled. The angle matched that of the surface of the cage on which they (cage and vertebra) made contact, but not the indentations of the teeth (Figure 3.7). The height of the vertebral block was 10.00 mm posterior and 9.42 mm anterior (Figure 3.6). As described in detail in §2.4.3, the vertebrae were modelled as cortical bone with homogeneous and isotropic material properties. The Young's modulus of the cortical bone, in this study referred to as $E_{Cortical}$, was assumed to be in the range of 12 to 30 GPa (Hee and Kundnani, 2010; Hench, 1998; Vadapalli *et al.*, 2006; Zhong *et al.*, 2006). The cortical bone material properties are shown in Table 3.1.

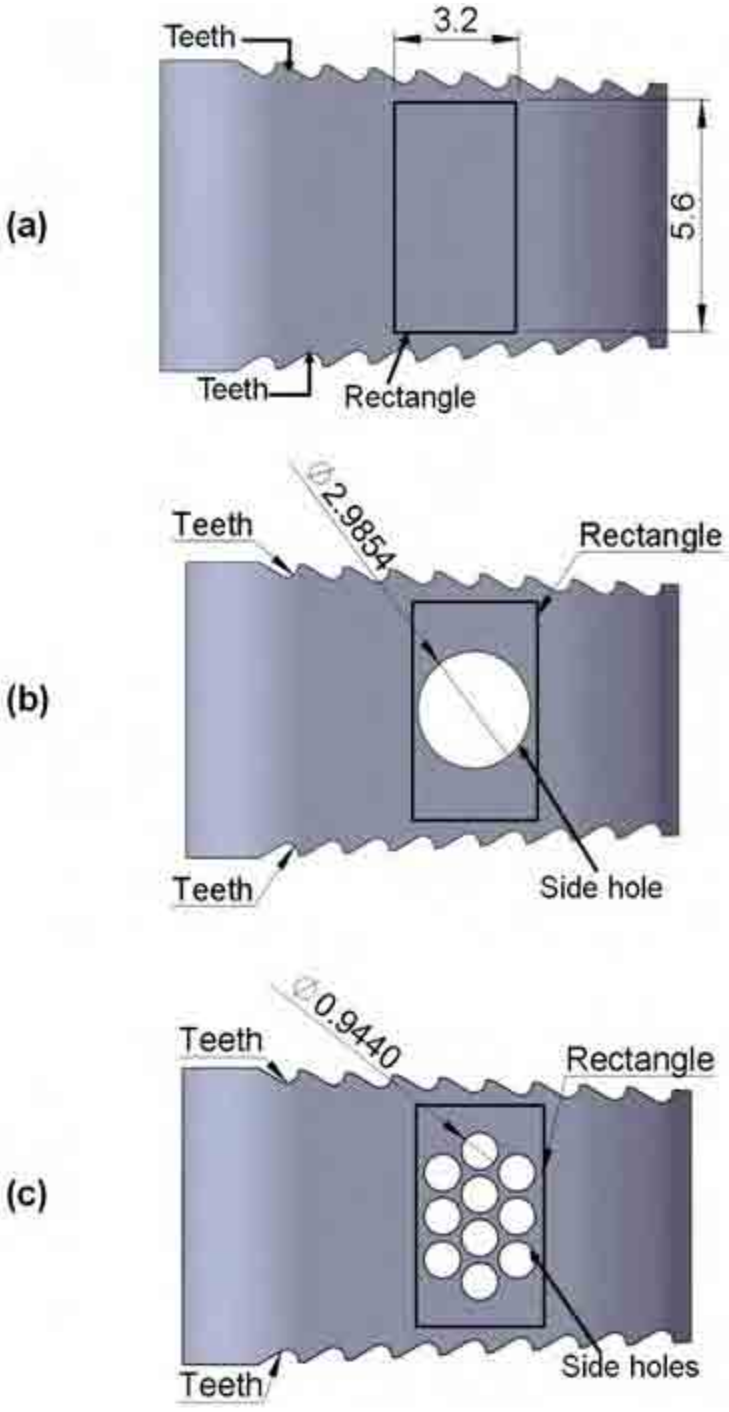

Figure 3. 5. In this study the number of side-holes was varied. Side-holes appear on both sides of the cage in equal numbers. (a) A rectangle was constructed for positioning the side-holes. The width of the rectangle corresponds to the anterior-posterior dimension of the graft cavity and its height corresponds to the posterior cage height below the level of the teeth. Positions of (b) single and (c) ten holes within the confines of the rectangle.

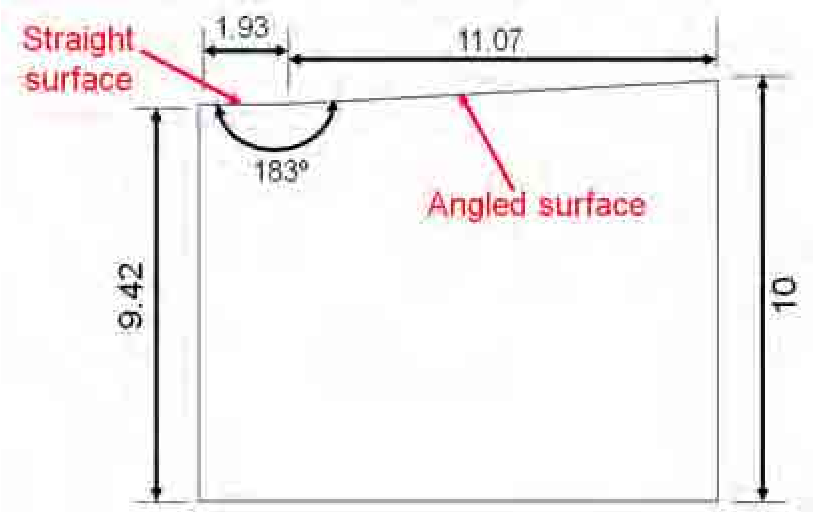

Figure 3. 6. Dimensions of the vertebra model; all dimensions are in millimetres. The depth of the model is 15 mm.

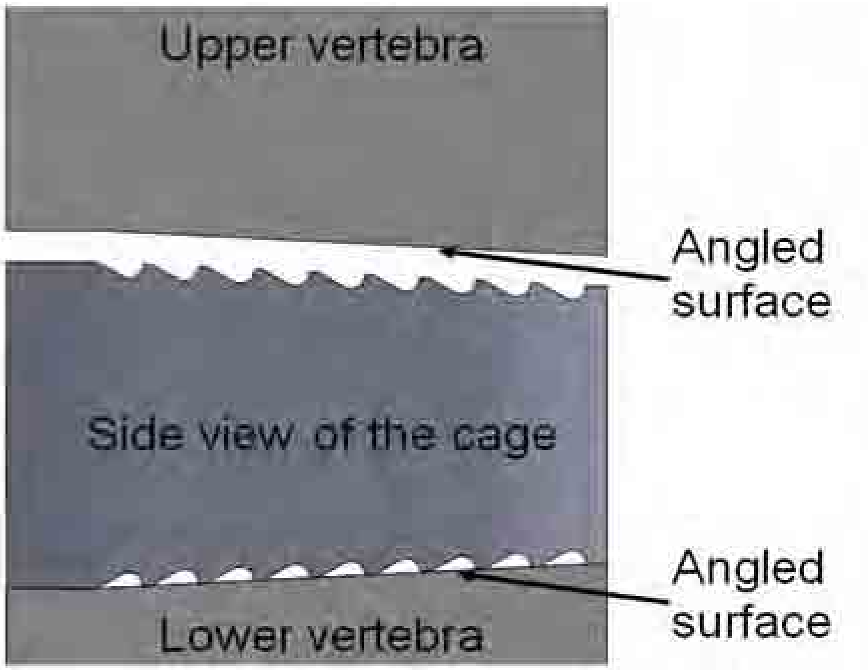

Figure 3. 7. A cage model with no side-hole in between adjacent vertebrae. The vertebrae surfaces in contact with the cage are angled. The angles match those of the surfaces of the cage on which they make contact, but not the indentations of the teeth. The upper vertebra has been separated for viewing only; in the FE model both vertebrae were in contact with the cage teeth.

3.3.4. FEA on cage models

The vertebrae and cage models were assembled and joined together (bonded) with no clearance (Figure 3.8). Simulations did not include bone graft or any other soft tissue that would be associated with fusion *in vivo*. They also did not include newly formed bone as the models were designed to simulate the stage immediately post-operation. To mimic the load experienced by the cervical spine, a uniform axial compressive load of 150 N suggested by the British Standard, BS ISO 18192-1:2011, was applied on the top surface of the superior vertebral block in the assembly. In previous cervical FE studies a range of axial compressive loads including 100 N (Galbusera *et al.,* 2008), 110 N (Yang *et al.,* 2007) and 130 N (Epari *et al.,* 2005) have been applied. Hence, it was assumed that a load of 150 N is a reasonable load to be used in this study. The bottom surface of the inferior vertebral block in the assembly was fully restrained in all directions (Figure 3.9).

As explained in §2.2.3, mesh size (the size of the elements) can be controlled and needs to be specified accurately in order to produce a reliable model (Pitzen *et al.,* 2002b). In this study, convergence tests were used to determine a suitable mesh size for the cage model (Appendix B, Figure B.1). To ensure convergence was unaffected by the design of the cage, four models were analysed with different design features. The four models included a cage with: (i) no teeth and no side-hole; (ii) teeth and no side-hole; (iii) no teeth and one side-hole; (iv) teeth and one side-hole. All the models were analysed with a mesh size of between 0.3 and 0.6 mm in intervals of 0.05 mm. Although convergence occurred before the finest allowed mesh, the difference in solution time was negligible. Thus, the finest mesh (0.3 mm) was selected for all the subsequent cage models. The vertebrae in all the subsequent assembled models were analysed using a mesh size of 0.6 mm (the finest mesh size allowed). Since the focus of the study is the cage, convergence tests for the vertebrae blocks were not carried out. A meshed cage model with 10 side-holes between adjacent meshed vertebrae models is shown in Figure 3.9. All the cage models were meshed using tetrahedral-shaped elements. Table 3.2 provides further details of node and element numbers for each cage model.

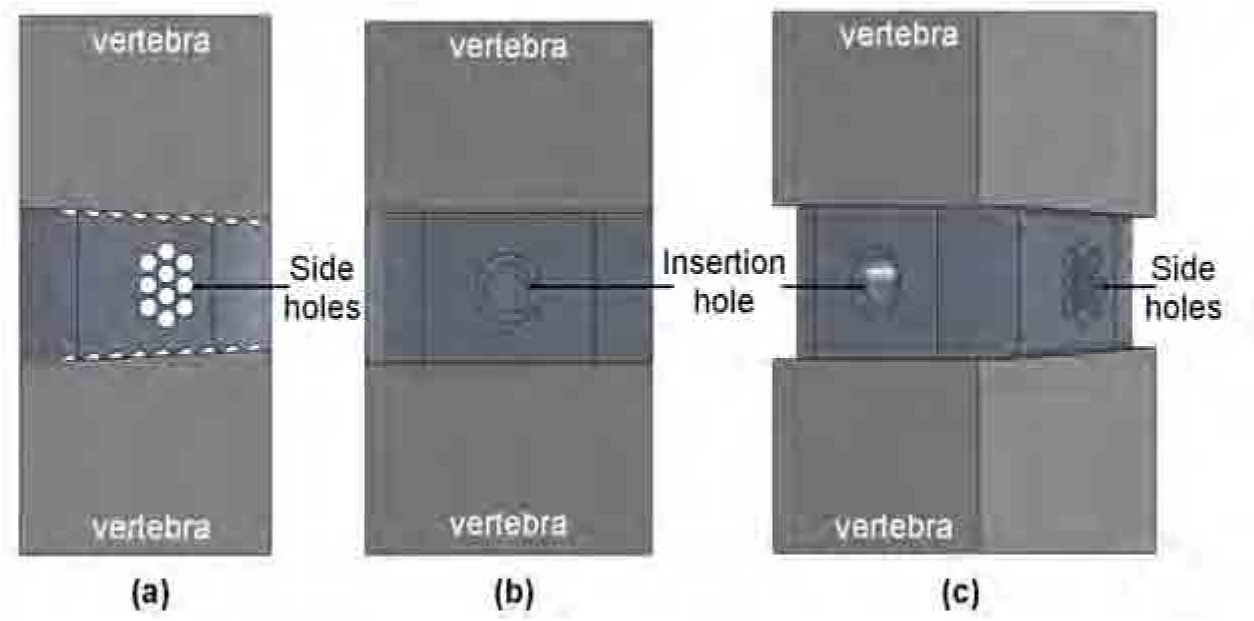

Figure 3. 8. The vertebrae and cage models were assembled and bonded with no clearance. A 10 side-hole cage model was placed between adjacent vertebrae. (a) Side view, (b) front view and (c) three-dimensional view.

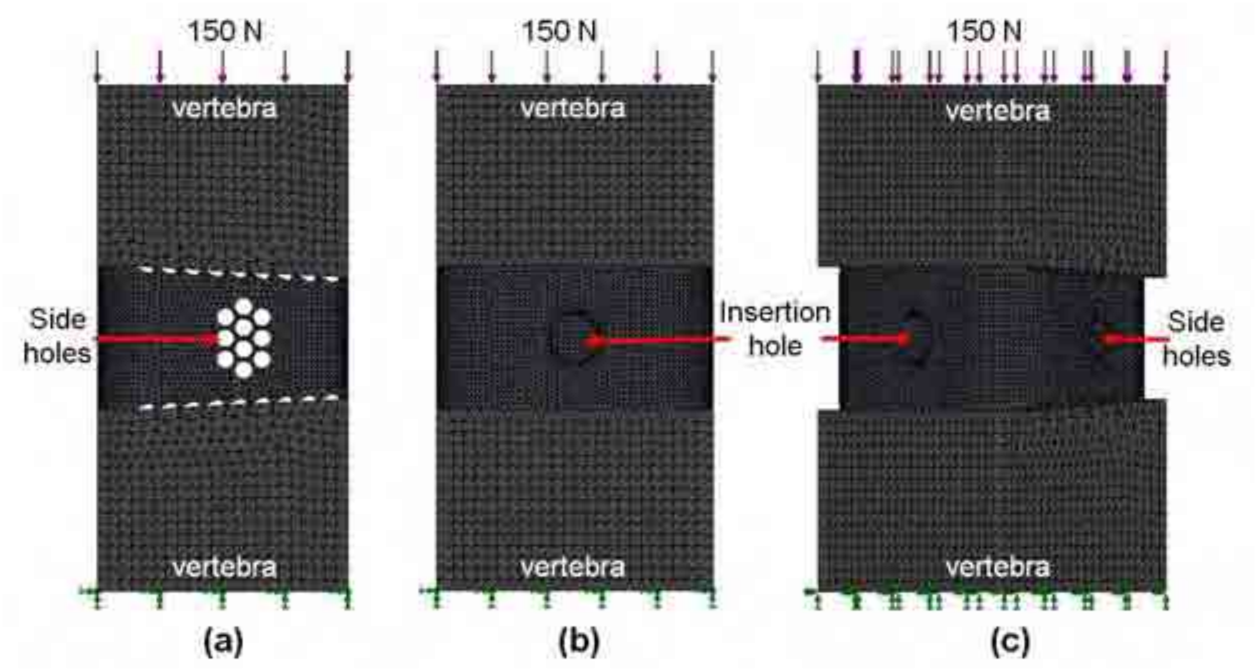

Figure 3. 9. Tetrahedral-shaped elements were used to mesh the vertebrae and cage models with sizes of 0.6 and 0.3 mm, respectively. A 10 side-hole cage model was placed between adjacent vertebrae; (a) side view, (b) front view and (c) three-dimensional view. A uniform axial compressive load was applied on the top surface of the superior vertebral block (purple arrows). The bottom surface of the inferior vertebral block was restrained in all directions (green arrows).

Table 3. 2. Total number of nodes and elements for the cage models with different number of side-holes.

Number of side-holes	Total number of nodes	Total number of elements
0	442,384	310,218
1	434,649	304,121
2	436,916	305,517
3	440,000	307,574
4	438,498	306,288
5	442,243	308,753
6	440,231	307,218
7	441,068	307,768
8	443,606	309,414
9	439,125	306,265
10	441,350	307,722

3.3.5. Validation

As explained in §2.2.5, validation is an important aspect of FEA (Pitzen *et al.*, 2002a; Pitzen *et al.*, 2002b) and this was achieved by comparing experimental results of mechanical testing on a cage model with the FEA predictions. ABS (acrylonitrile butadiene styrene) cage models (Figure 3.10) with a single side-hole, no teeth and horizontal inferior and superior surfaces were made by fused deposition modelling (FDM) (University of Strathclyde, Glasgow, UK); two identical models were produced. In order to compare the results of mechanical testing with the FEA predictions, the Young's modulus of ABS (E_{ABS}) had to be measured. Hence, a block of ABS (15 mm × 13 mm × 7.5 mm) was also made by FDM (Figure 3.11). The outer dimensions of the block match those of the ABS cages.

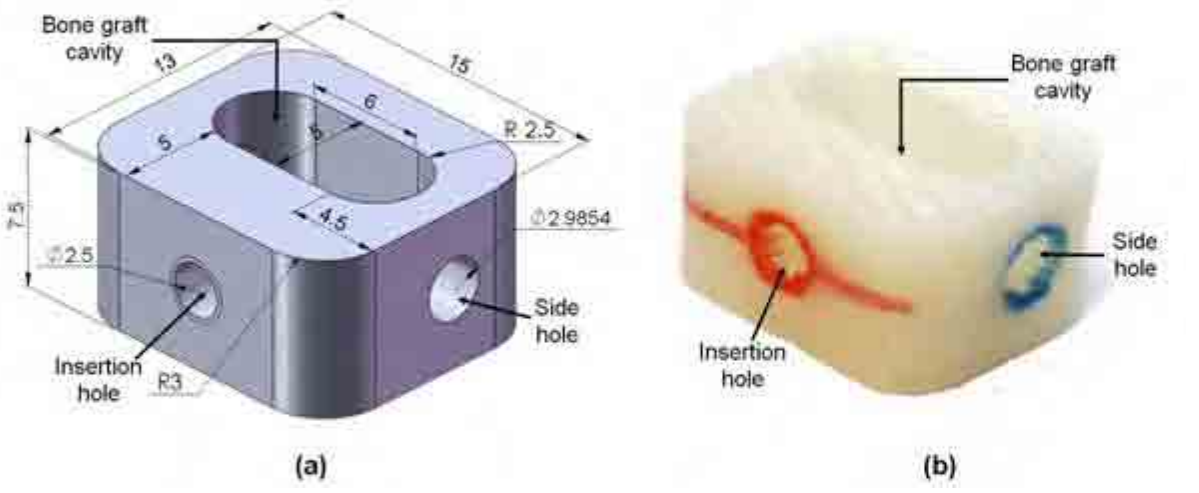

Figure 3. 10. ABS cage model with a single side-hole, no teeth and horizontal inferior and superior surfaces; (a) SolidWorks model and (b) specimen made by FDM. Note, red and blue marks are shown on the cage for picture clarity.

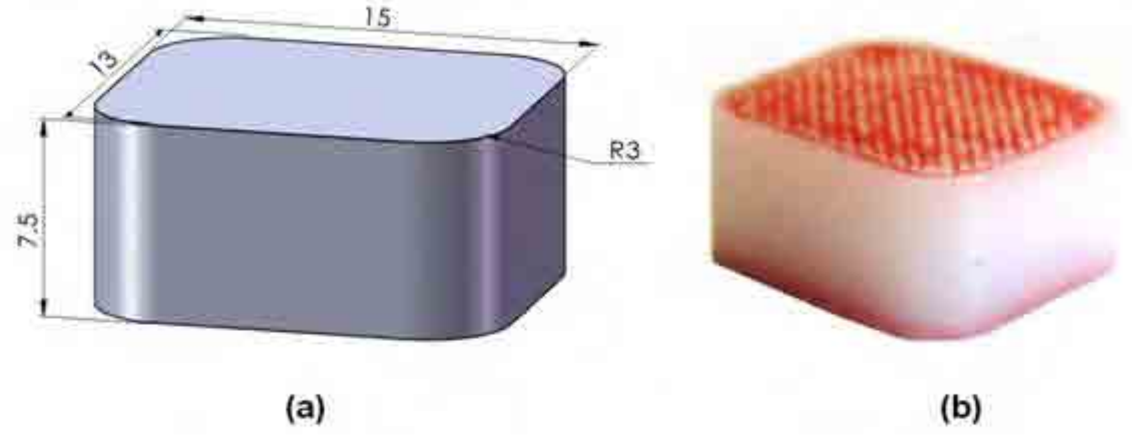

Figure 3. 11. An ABS block with no side-holes, no insertion hole and no graft cavity was made to measure the E_{ABS} for use in FEA. (a) SolidWorks model and (b) specimen made by FDM. Note, red marks are shown on the block for picture clarity.

The ABS cage models (n=2) and the ABS block (n=1) were compressed between 2 mm thick stainless steel plates (material properties shown in Table 3.1) to a maximum load of 150 N under displacement control (0.02 mm.s^{-1}, Chen and Lee, 2006; Ferguson *et al.*, 2006) using a BOSE ELF3300 materials testing machine (Bose Corporation, ElectroForce Systems Group, Minnesota, USA) fitted with a 2.5 kN load cell (Figure 3.12). Each compression test was repeated three times. The loads and displacements were recorded; 100 points were taken at 0.05 s intervals over 5 s duration. In order to determine the E_{ABS}, stress and strain values were calculated from the ABS block experimental results using equations 3.1 and 3.2, respectively (Hibbeler, 2004).

$$\sigma = \frac{F}{A} \tag{3.1}$$

where σ, F and A are the stress, load and cross-sectional area of the block, respectively.

$$\varepsilon = \frac{\Delta x}{dl} \tag{3.2}$$

where ε, Δx and l are the strain, displacement and original height of the block, respectively.

Stress against strain curves were plotted and second-order polynomials were fitted through the data points, in the form of $\sigma = A\varepsilon^2 + B\varepsilon$. The equation was then differentiated with respect to strain to calculate values for E_{ABS}:

$$E_{ABS} = \frac{d\sigma}{d\varepsilon} = \frac{d}{d\varepsilon}(A\varepsilon^2 + B\varepsilon) \qquad (3.3)$$

$$E_{ABS} = 2A\varepsilon + B \qquad (3.4)$$

where the parameters are as defined for equations 3.1 and 3.2.

The E_{ABS} values were determined between 0 and 150 N at approximately 10 N intervals. These load values were approximate because the tests were run under displacement control.

FEA was carried out on the ABS cage model (with a single side-hole, no teeth and horizontal inferior and superior surfaces) compressed between stainless steel blocks (Figure 3.13), using the E_{ABS} values determined experimentally. The transverse section of the stainless steel blocks corresponded to the dimensions of the ABS model, and the height of each block was 10.00 mm (Figure 3.13). Because the blocks were made from stainless steel, the difference in thickness of the test plates (2 mm) and the FE blocks (10 mm) is not likely to be a problem as the Young's modulus of stainless steel is about 30 times that of ABS. The plates were firmly attached to the load cell and the base of the machine which are also stainless steel. The ABS cage model was meshed with the finest mesh size possible (0.35 mm) and the stainless steel blocks were meshed with a coarser mesh size (0.6 mm). All the assembled models were analysed with total nodes of 371,672 and total elements of 264,437. The same loads applied to the ABS block by the machine were also applied to the FEA models (0 N to 150 N at approximately 10 N intervals) with the corresponding E_{ABS} values and the resulting displacements were determined.

Load against displacement curves for the ABS cages were plotted for both experimental and FEA results. Second-order polynomials were fitted to all the curves in the form of $F = Ax^2 + Bx$ (where F is load and x is displacement). The equations were then differentiated with respect to displacement, using equations 3.5 and 3.6, in order to calculate values for stiffness at displacements of 0.04 and 0.07 mm:

$$k = \frac{dF}{dx} = \frac{d}{dx}(Ax^2 + Bx) \tag{3.5}$$

$$k = 2Ax + B \tag{3.6}$$

where k is the stiffness.

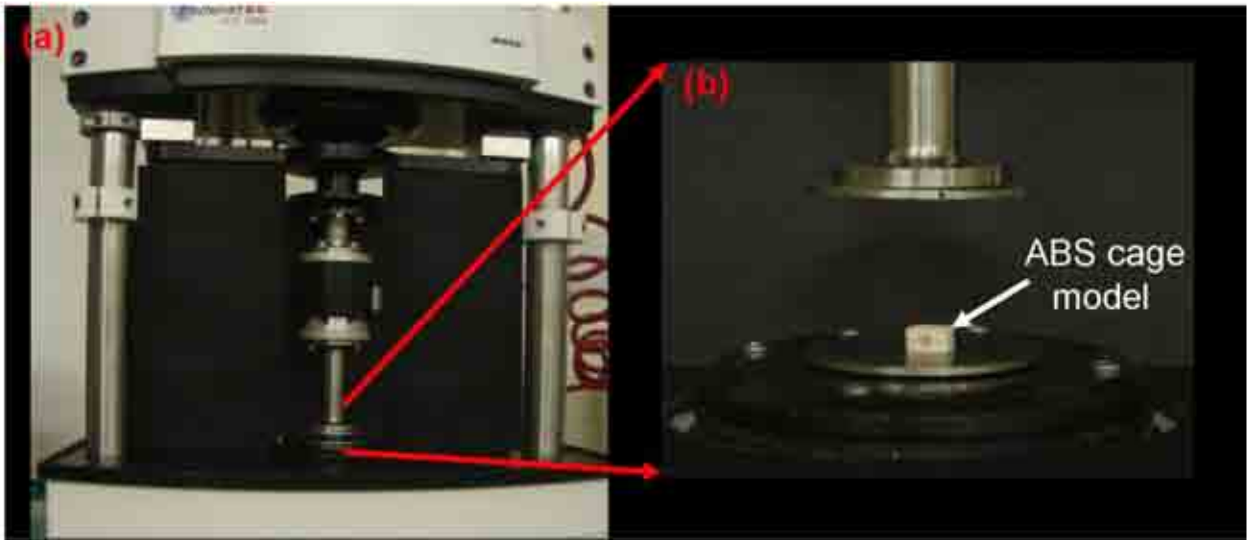

Figure 3. 12. ABS cage model and the ABS block compression test set-up using the (a) ELF3300 materials testing machine, with (b) a close-up of an ABS cage (with single side-hole) that was compressed between two stainless steel plates.

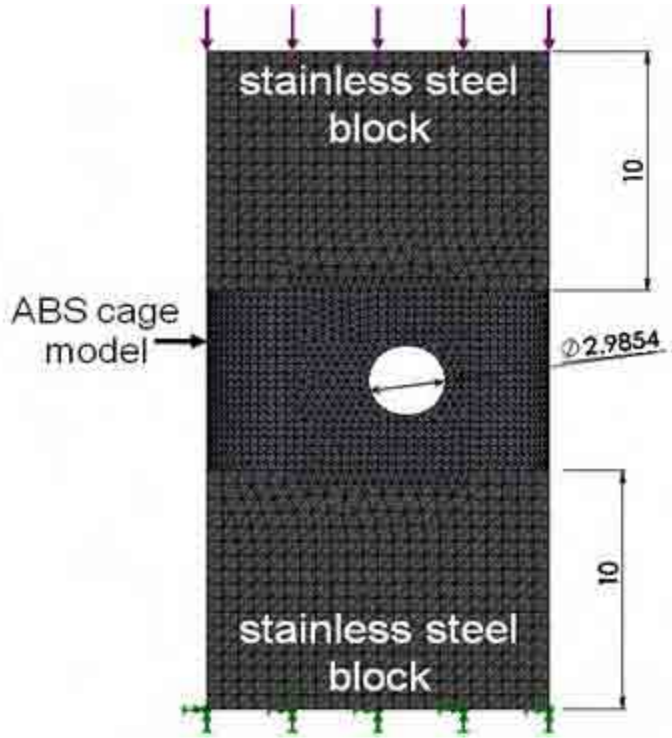

Figure 3. 13. Side view of the ABS cage model and stainless steel blocks in FE. Tetrahedral-shaped elements were used to mesh the models with sizes of 0.35 and 0.6 mm for the ABS cage and the stainless steel blocks, respectively. All dimensions are in millimetres.

3.4. Results

3.4.1. Validation

Figure 3.14 shows the stress against strain curves from the ABS block experimental tests. The range of E_{ABS} values determined using the second-order polynomials for each test is shown in Appendix C, Tables C.1 to C.3. The load against displacement curves from FEA on ABS cage models using the resultant E_{ABS} values are shown in Figure 3.15. The experimental load against displacement curves from tests on ABS cages are shown in Figure 3.16.

Figure 3.17 shows the load against displacement curves from FEA and experimental tests on the ABS cage models. As can be seen, all the curves show a similar trend. Note, for clarity, this figure only shows some of the experimental curves. Appendix D, Figure D.1 shows all the load against displacement curves from FEA and experimental tests. The FE validation results in terms of load against displacement are in good agreement with the conducted experimental test. Hence, FEA carried out in this study appears to be reasonable. The stiffness was determined at displacements of 0.04 and 0.07 mm for each curve because it was assumed that they are good representations of the lower and higher values of displacement. The stiffness values for each curve are shown in Table 3.3. The difference between FEA and experimental results was (on average) 5 and 3% for 0.04 and 0.07 mm displacements, respectively.

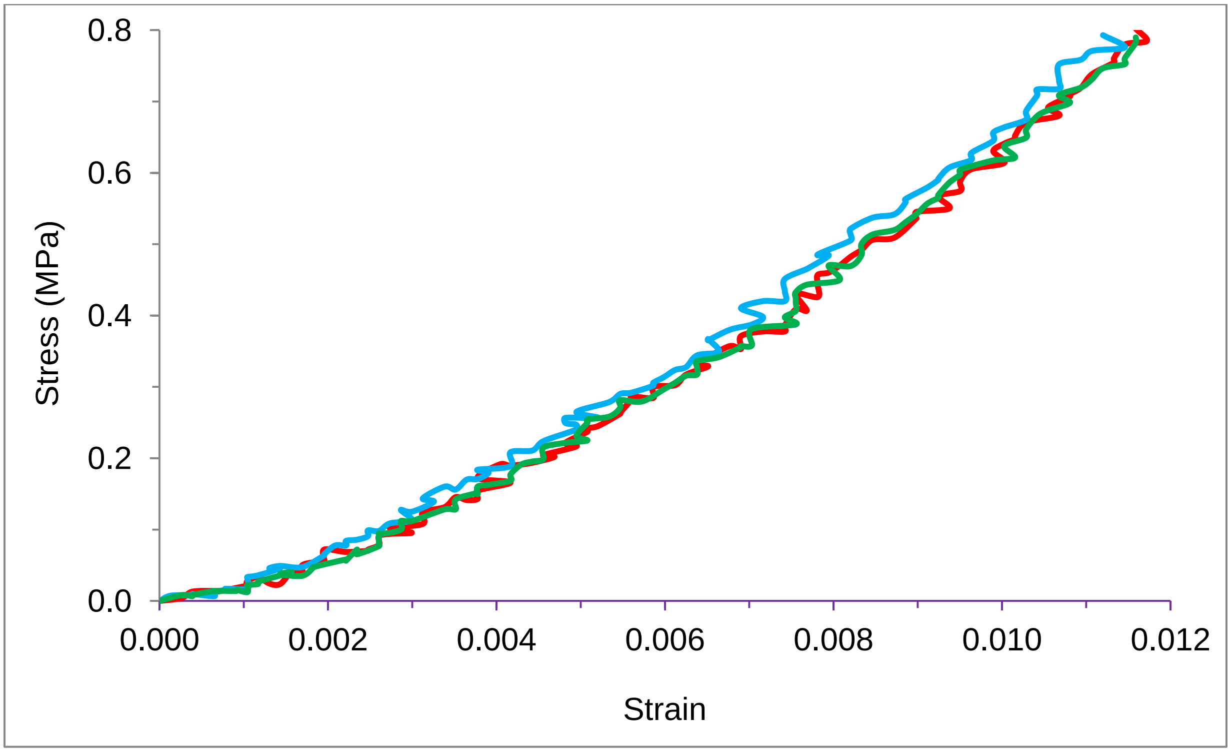

Figure 3. 14. Stress against strain curves from experimental tests on the ABS block, repeated three times: first, second and third tests are shown in blue, red and green, respectively. In order to calculate the E_{ABS}, a second-order polynomial was fitted to each set of test results; the resulting equations were $\sigma = 3262.5\varepsilon^2 + 33.843\varepsilon$, $\sigma = 3478.5\varepsilon^2 + 28.324\varepsilon$ and $\sigma = 3462\varepsilon^2 + 28.515\varepsilon$, respectively (see Appendix C, Tables C.1 to C.3 for results). For clarity, the second-order polynomials are hidden and only the data points are shown. FEA was performed on the ABS cage models using the E_{ABS} values and the resultant maximum von Mises stress levels and displacements were determined (Appendix C, Tables C.1 to C.3). The load against displacement curves are shown in Figure 3.15.

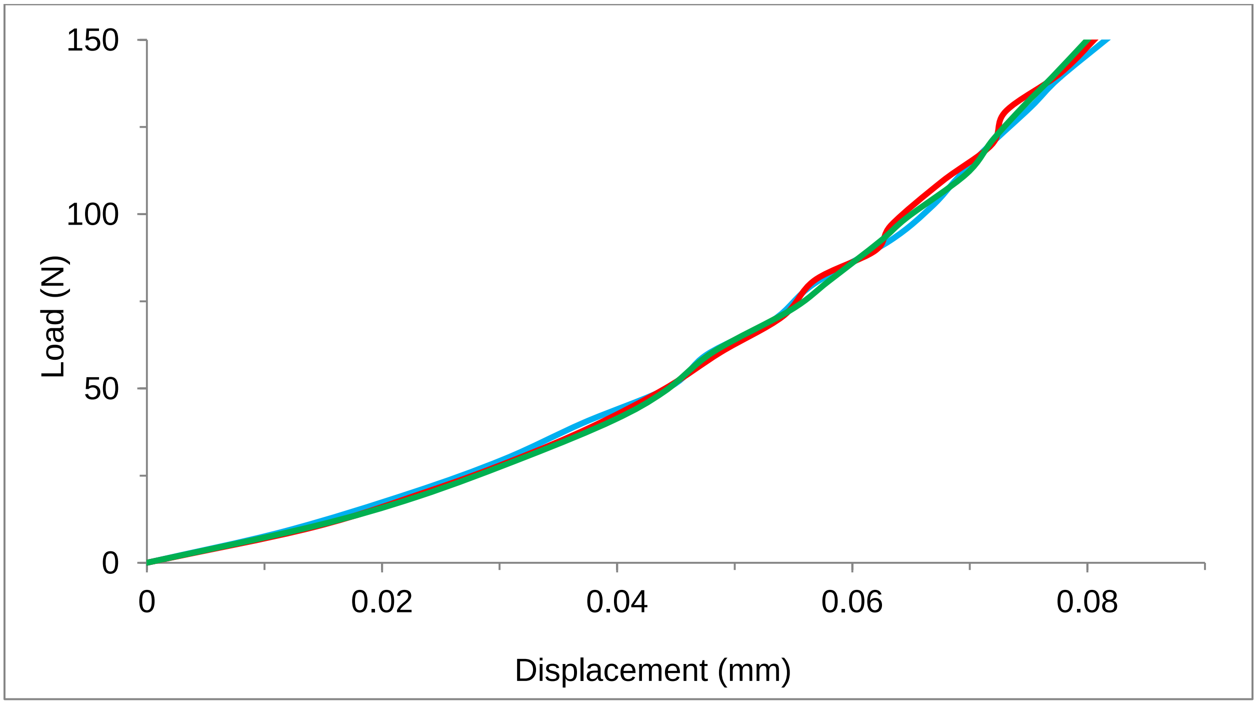

Figure 3. 15. Load against displacement curves from FEA on the ABS cage models when analysed using the E_{ABS} values from equations in Figure 3.14. The colours of the curves in this figure are in accordance with those in Figure 3.14.

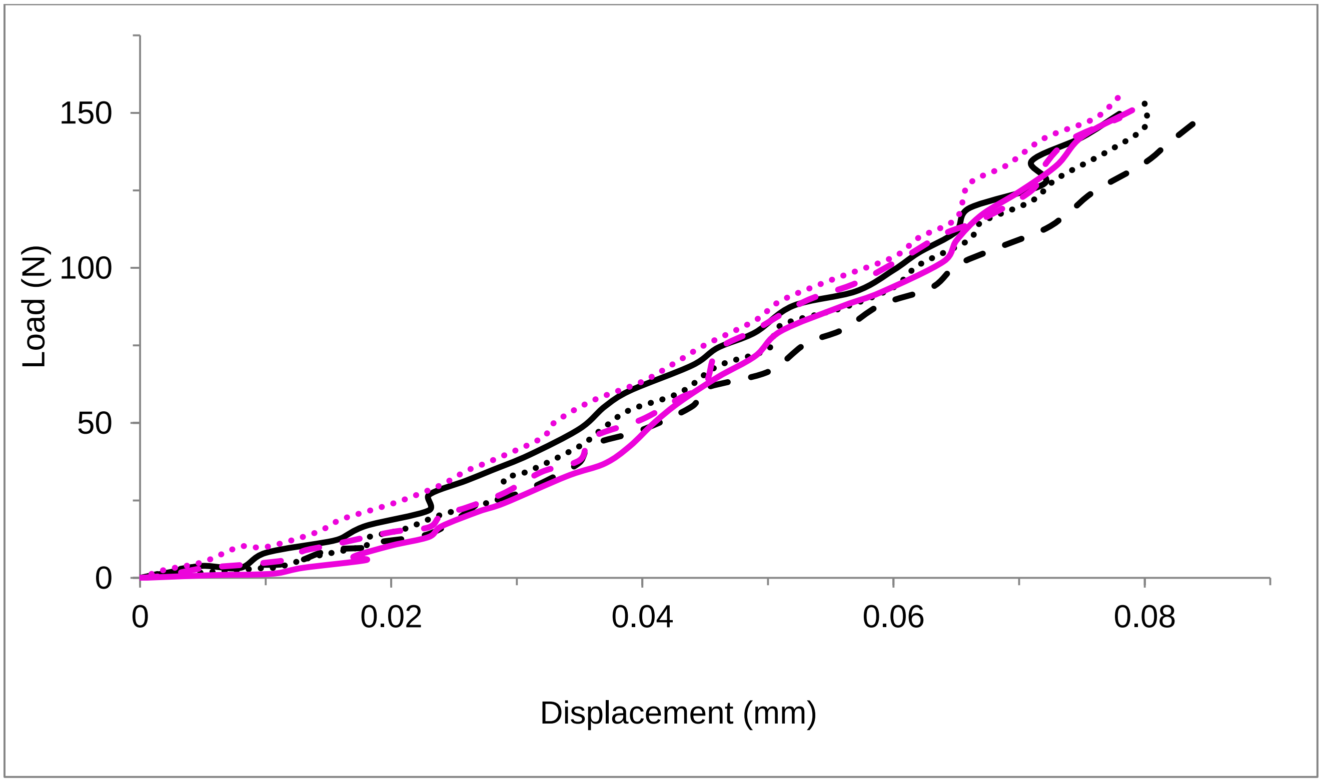

Figure 3. 16. Load against displacement curves from experimental tests on ABS cages (n=2), each test was repeated three times. For clarity, the black curves are from the first and the pink curves from the second ABS cages; dotted, dashed and continuous lines are from the first, second and third tests, respectively.

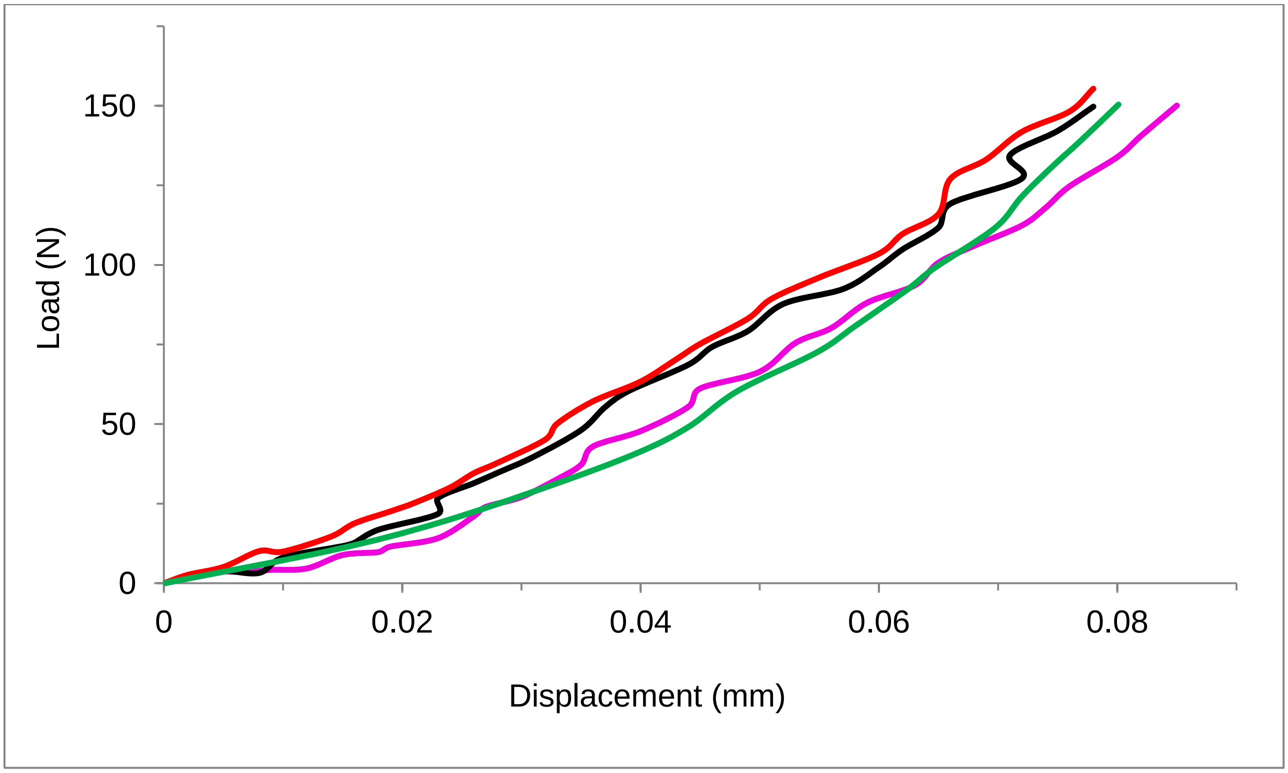

Figure 3. 17. Load against displacement curves from FEA and experimental tests on ABS cages. This figure is a combination of some of the curves from Figures 3.15 and 3.16 to show how the FEA and experimental results compare. The middle line of Figure 3.15 (FEA test three, green) and highest line (ABS cage 2, test one, red), middle line (ABS cage 2, test three, black) and lowest line (ABS cage 1, test two, purple) of Figure 3.16 are shown. In order to calculate the stiffness, second-order polynomials were fitted to all the curves. The equations derived from second-order polynomials were then differentiated and the stiffness at displacements of 0.04 and 0.07 mm were determined for both FEA and experimental results (Table 3.3).

Table 3. 3. The stiffness values for each of the curves in Figures 3.15 and 3.16, where F, x and k are the load, displacement and stiffness.

Specimen	Test number	Equation	Differentiated equation	x (mm)	k (N/mm)
ABS cage 1 (experimental)	Test one	$F = 15296x^2 + 657.96x$	$k = 30592x + 657.96$	0.04	1,882
				0.07	2,799
	Test two	$F = 14038x^2 + 587.19x$	$k = 28076x + 587.19$	0.04	1,710
				0.07	2,553
	Test three	$F = 13264x^2 + 898.52x$	$k = 26528x + 898.52$	0.04	1,960
				0.07	2,755
ABS cage 2 (experimental)	Test one	$F = 12034x^2 + 1068.70x$	$k = 24068x + 1068.70$	0.04	2,031
				0.07	2,753
	Test two	$F = 17972x^2 + 566.71x$	$k = 35944x + 566.71$	0.04	2,004
				0.07	3,083
	Test three	$F = 21680x^2 + 271.09x$	$k = 43360x + 271.09$	0.04	2,005
				0.07	3,306
ABS cage (FEA)	Test one	$F = 17556x^2 + 400.45x$	$k = 35112x + 400.45$	0.04	1,805
				0.07	2,858
	Test two	$F = 19313x^2 + 305.36x$	$k = 38626x + 305.36$	0.04	1,850
				0.07	3,009
	Test three	$F = 19769x^2 + 266.65x$	$k = 39538x + 266.65$	0.04	1,848
				0.07	3,034

3.4.2. FEA results on cage models

Table 3.4 shows the maximum von Mises stress, displacement and normal compressive stress under compression for all the models (side-holes ranging from 0 to 10) determined from FEA. Figures 3.18 to 3.20 illustrate the von Mises stress distribution in the cage with 10 side-holes. In all the models the stress distribution was highest at the cage-vertebrae interface (the tip of the cage teeth). The presence and number of side-holes had a negligible effect on the stress (von Mises and normal compressive stresses) distribution within the cage; the stress magnitudes were fairly constant for all the models and did not change substantially with the number of holes (Table 3.4).

FEA was carried out for $E_{Cortical}$ values of 12 and 30 GPa. The maximum von Mises stress for all the models (side-holes of 0 to 10) when analysed with $E_{Cortical}$ = 12 GPa was 14 MPa (Figure 3.18) with maximum displacement between 10.9 and 11.2 μm. The maximum von Mises stress for the same models when analysed with $E_{Cortical}$ = 30 GPa was between 17 and 18 MPa (Figure 3.19 shows the maximum stress obtained in this group) with maximum displacement between 9.4 and 9.6 μm. The average normal compressive stress for all the models analysed in this study was 4 MPa (Table 3.4). Figure 3.21 shows the normal compressive stress for the model with 10 side-holes when analysed with $E_{Cortical}$ = 12 GPa. Increasing the value of $E_{Cortical}$ from 12 to 30 GPa increases the maximum von Mises stress predicted on average by 29% and decreases the maximum displacement on average by 14%. In all the models, the maximum von Mises stress levels within each side-hole were between 1 and 4 MPa and between 1 and 5 MPa within the insertion hole (Figure 3.20).

Table 3. 4. Maximum von Mises stress, maximum displacement and normal compressive stress for the cage models when analysed with different number of side-holes. Analyses were performed with mesh sizes of 0.3 and 0.6 mm for the cage models and vertebrae models, respectively.

Number of side-holes	$E_{Cortical}$ = 12 GPa			$E_{Cortical}$ = 30 GPa		
	Maximum von Mises stress (MPa)	Maximum displacement (µm)	Normal compressive stress (MPa)	Maximum von Mises stress (MPa)	Maximum displacement (µm)	Normal compressive stress (MPa)
0	14	11.2	3	17	9.6	4
1	14	11.1	4	18	9.5	4
2	14	10.9	4	18	9.4	4
3	14	11.2	4	18	9.6	4
4	14	11.1	4	18	9.5	4
5	14	11.1	4	17	9.5	4
6	14	11.0	4	17	9.4	4
7	14	11.2	4	18	9.6	4
8	14	11.1	4	18	9.6	4
9	14	11.1	4	17	9.5	4
10	14	11.1	5	18	9.5	5
Mean	**14**	**11.1**	**4**	**18**	**9.5**	**4**

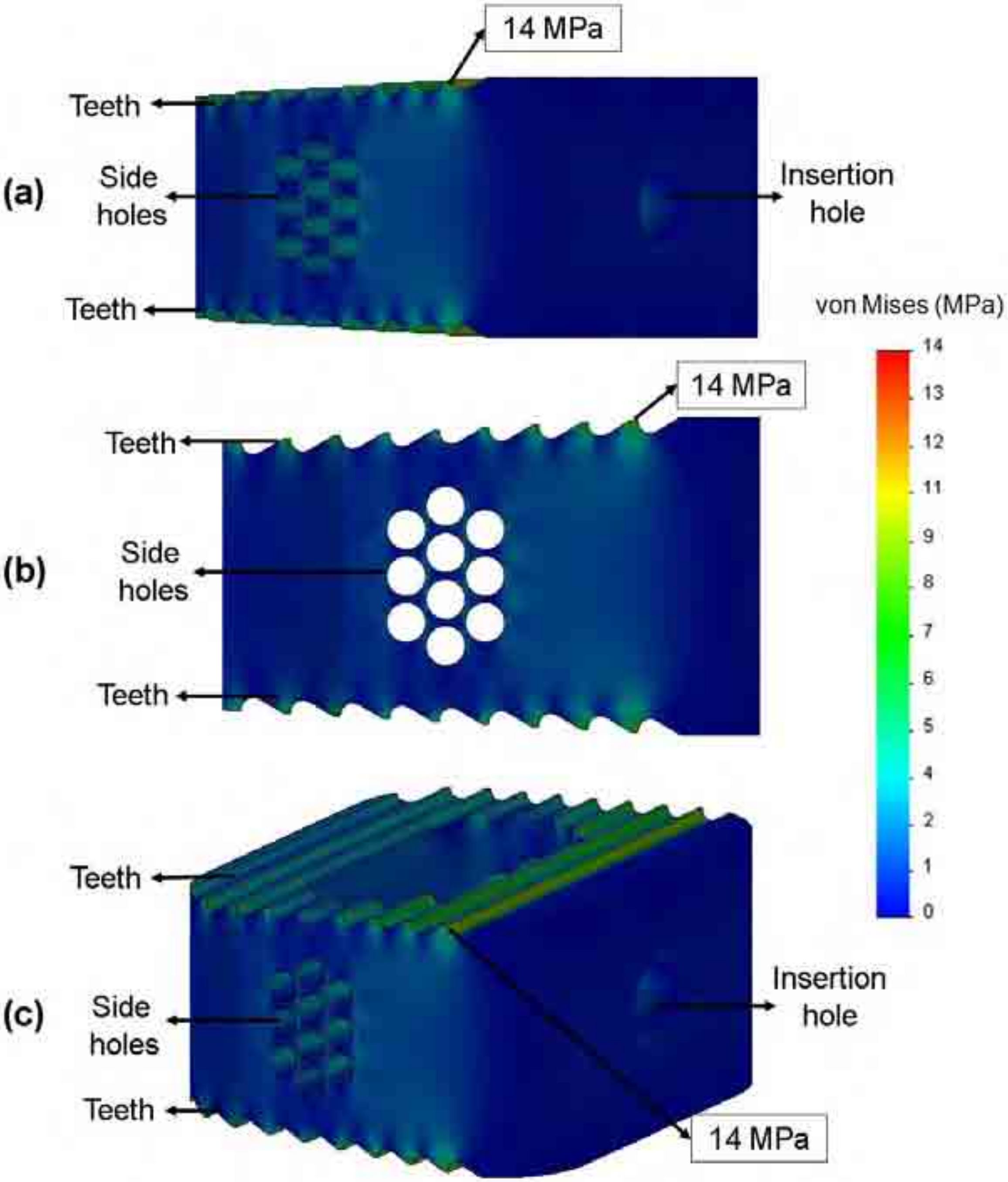

Figure 3. 18. von Mises stress distribution in the 10 side-hole cage model with $E_{Cortical}$ = 12 GPa, maximum stress is seen on the tip of the teeth. (a) Three-dimensional view not showing the top, (b) side view, (c) three-dimensional view showing the top.

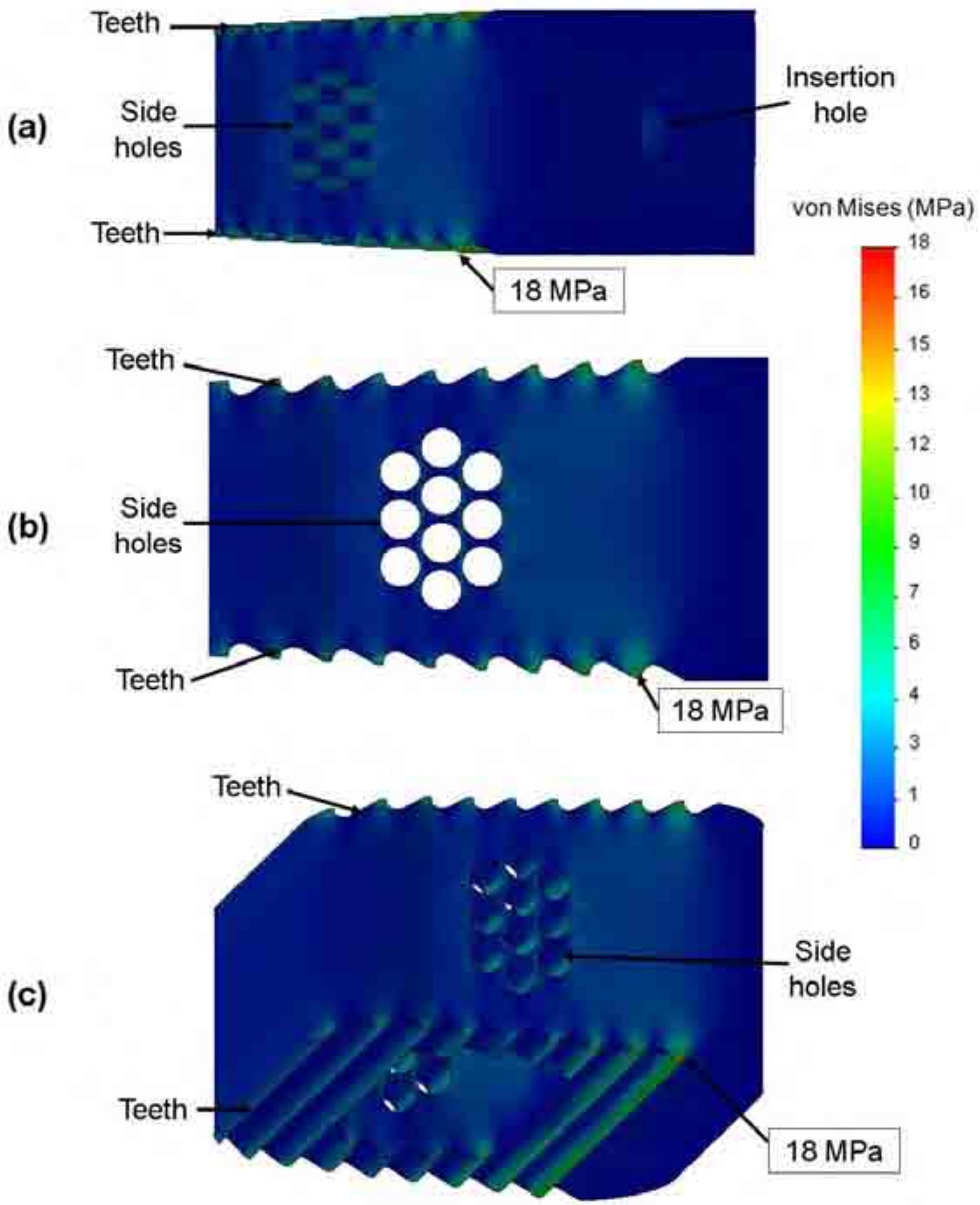

Figure 3. 19. von Mises stress distribution in the 10 side-hole cage model with $E_{Cortical}$ = 30 GPa, maximum stress is seen on the tip of the teeth. (a) Three-dimensional view not showing the bottom, (b) side view, (c) three-dimensional view showing the bottom.

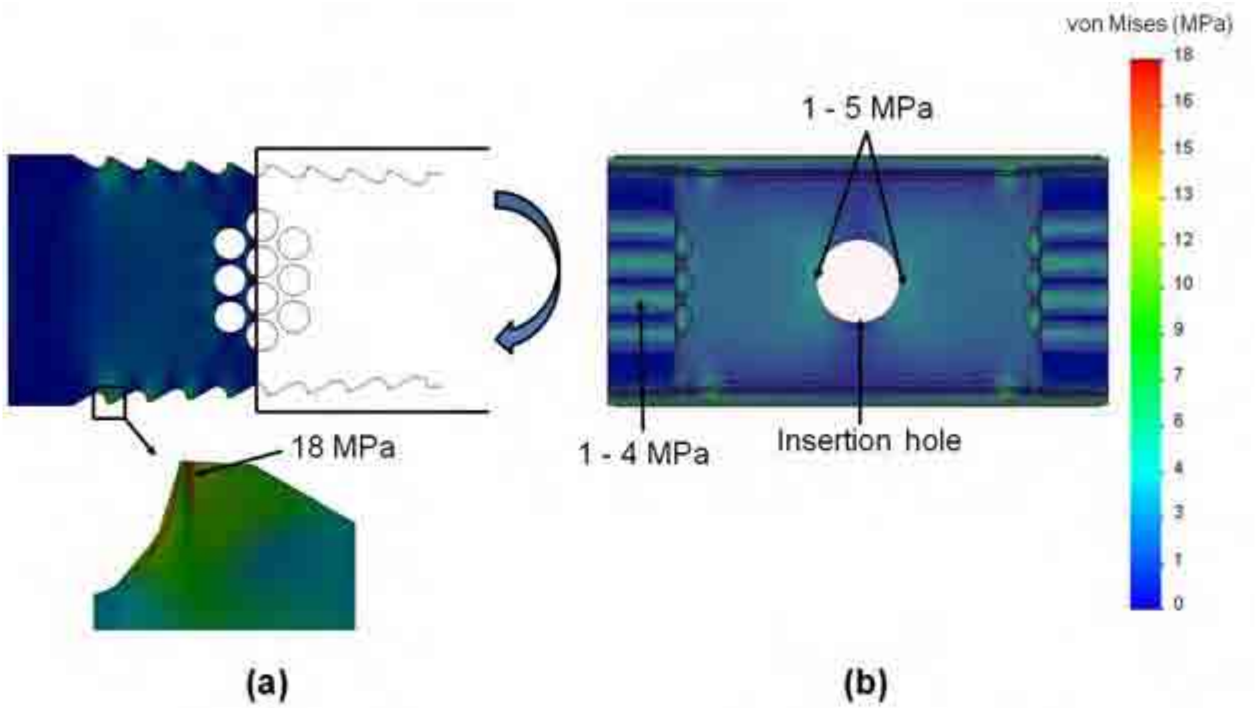

Figure 3. 20. von Mises stress distribution in the 10 side-hole cage model with $E_{Cortical}$ = 30 GPa, (a) maximum stress is seen on the tip of the teeth, (b) the cage is cut and rotated to show stress concentration in the holes.

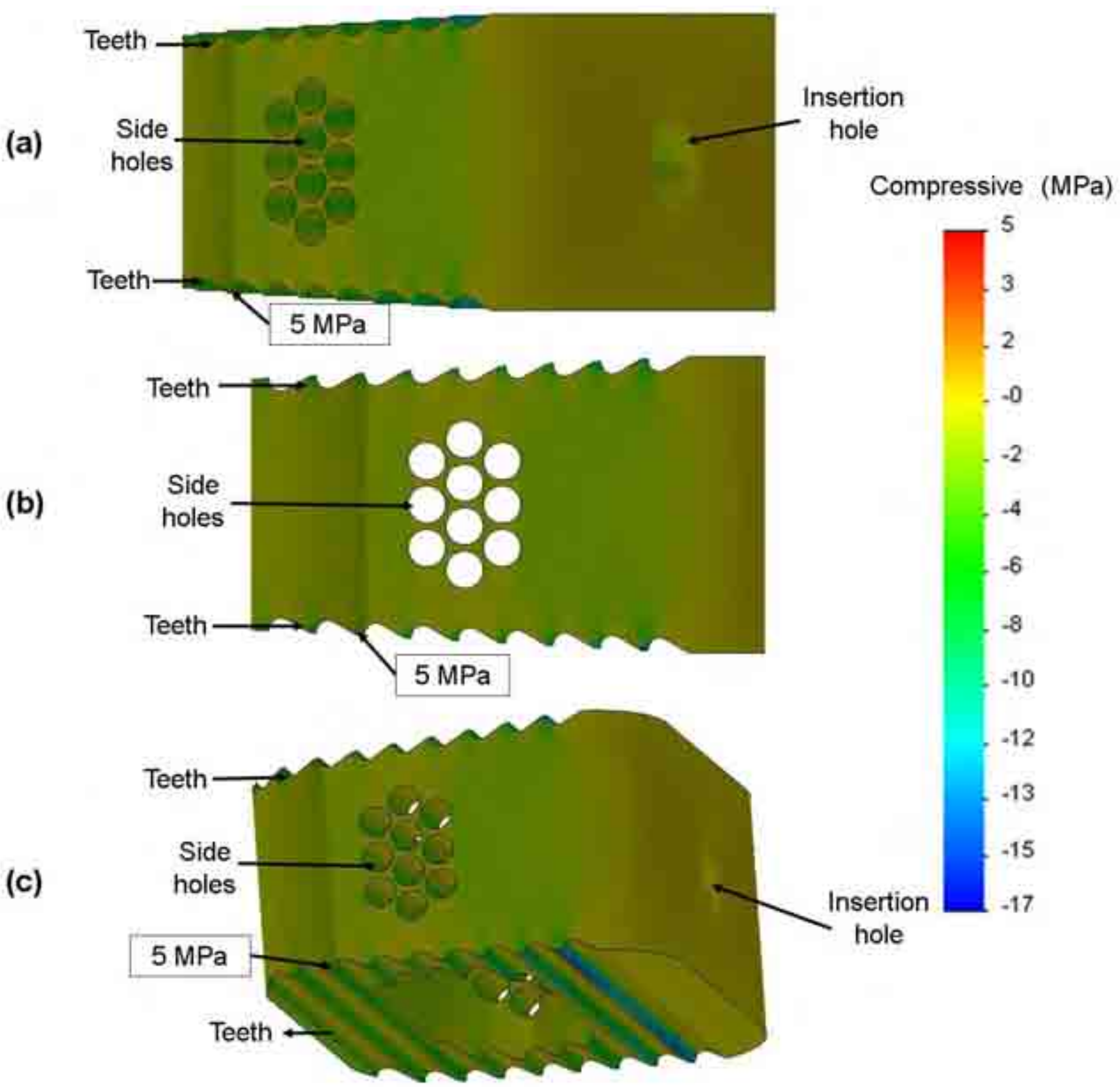

Figure 3. 21. Normal compressive stress distribution in the 10 side-hole cage model with $E_{Cortical}$ = 12 GPa, maximum stress is seen on the tip of the teeth. (a) Three-dimensional view not showing the bottom, (b) side view, (c) three-dimensional view showing the bottom.

3.5. Discussion

FE models of a cervical fusion cage with various numbers of side-holes were developed, analysed and the stress distribution in the models was evaluated. In this study, the mechanical behaviour of the cage was evaluated under axial compressive load as in previous FE studies (Epari *et al.,* 2005; Ferguson *et al.,* 2006; Kumar *et al.,* 2005). The vertebrae in the current study were modelled as cortical bone. This was in agreement with Bryce *et al.* (1995) who concluded that the stiffness and strength of the cancellous bone in the vertebrae increases because of the surrounding cortical shell.

The maximum von Mises stress levels of the models were between 14 and 18 MPa when analysed with $E_{Cortical}$ values in the range of 12 and 30 GPa. Increasing the $E_{Cortical}$ from 12 to 30 GPa increases the maximum von Mises stress predicted on average by 29%. This shows that a change in material properties of the cortical bone can influence the results. However, this value is still much lower than the compressive strength of PEEK (118 MPa, Chen and Lee, 2006). Natarajan *et al.* (2000) evaluated the mechanical responses to external loads with loose-fitting and tight-fitting fusion grafts. They found that the compressive stress in the graft was highest for tight-fitting graft in flexion and lateral bending (10 MPa). Considering that they used different material properties in their models ($E_{Cortical}$ = 10 GPa and E = 3.5 GPa for the graft) and different loading conditions (compressive pre-load of 105 N and moment of 0.5 N.m), their maximum stresses are comparable to the results of this study.

In all the models, the maximum von Mises stress was always seen at the cage-vertebrae interface and this result is similar to the results of Galbusera *et al.* (2008). They found that a stand-alone cage induced a higher value of peak contact stress at the cage-endplate interface compared to the cages supplemented by an anterior locking or dynamic plates. The FEA results in this study suggest that a cervical cage with side-holes is unlikely to fail in static compression.

Fatigue testing to 5 million cycles is recommended for cervical cages by the American Society for Testing and Materials (ASTM) standard for test methods for intervertebral body fusion devices (ASTM F 2077-03). The STALIF^{TM} C cage (manufactured from PEEK) was cyclically loaded at 3000 N at a frequency of 5 Hz and reached the endurance value of 5 million cycles without evidence of failure (internal report, Surgicraft Ltd., Redditch, UK). According to the data sheet for PEEK (Victrex PLC, Thornton Cleveleys, UK), the tensile fatigue strength of the material is approximately 60 MPa at 10 million cycles. This fatigue strength value is in accordance with measured data obtained by Nisitani *et al.* (1992). Another PEEK cervical cage study (Cho *et al.*, 2002) demonstrated that the cage could withstand a static axial load of 4170 N and a cyclic load for 5 million cycles, with a maximum load of 2160 N. These values are higher than the compressive axial load applied to the cervical spine (Panjabi *et al.*, 1998). Abu Bakar *et al.* (2003) showed in a tension-tension fatigue study that PEEK has a fatigue strength of 58.72 MPa (75% of the ultimate tensile strength of PEEK) at one million cycles. The highest stresses in the FE models of this study are well within the fatigue strength reported of 60 MPa at 10 million cycles (Victrex PLC, Thornton Cleveleys, UK).

3.6. Conclusions

In all the models the maximum von Mises stress showed highest values at the cage-vertebrae interface and had a value of between 14 and 18 MPa (and on average 4 MPa for normal compressive stress) with maximum displacements of between 9.4 and 11.2 μm. The stress values obtained are much lower than the compressive strength of PEEK which has a value of 118 MPa. The presence and number of side-holes had a negligible effect on the von Mises stress distribution within the cage; the stress level was fairly constant for all the models and did not change substantially with the number of holes. The fatigue strength of PEEK is approximately 60 MPa at 10 million cycles (Victrex PLC, Thornton Cleveleys, UK). This implies that a PEEK cervical cage can resist fatigue failure. The investigation of this study suggests that a cervical cage with side-holes is unlikely to fail in static compression or as a result of fatigue.

4. SUITABILITY OF BIOACTIVE/BIODEGRADABLE COMPOSITE IN CERVICAL FUSION CAGES

4.1. Chapter overview

The aim of this chapter is to evaluate a bioactive/biodegradable composite as a potential cervical spinal fusion cage material using finite element analysis (FEA). Section 4.2 describes the aim of the study and introduces each composite material in detail. It also provides information and possible drawbacks on the currently used materials for fusion cages. A range of possible Young’s modulus values for the composite is calculated in §4.3 and used in the FEA in §4.4. The resultant stress distribution within the cage using these Young’s modulus values is also shown in this section. The findings of this study are discussed in §4.5 and summarised in §4.6.

4.2. Introduction

Conventional cages made from permanent materials may have some shortcomings. Permanent materials (polymer or metal, e.g. polyetheretherketone (PEEK) or titanium alloy) may restrict the localized growth of surrounding tissues (Pietrzak and Eppley, 2000) and there may be long-term complications associated with a retained foreign body (Jiya *et al.,* 2009; Lippman *et al.,* 2004). These complications include implant loosening, migration, breakage or tissue irritation, which may require a removal operation (Hojo *et al.,* 2005; Pietrzak, 2000; Pietrzak and Eppley, 2000; Thomas *et al.,* 2008). Some permanent materials such as metallic implants may cause stress shielding due to the difference between the Young's modulus of metals and cortical bone (Hojo *et al.,* 2005; Kandziora *et al.,* 2004; van Dijk *et al.,* 2002). These limitations have led to the development of cages that degrade in the body (Jiya *et al.,* 2009; Kandziora *et al.,* 2004; Kuklo *et al.,* 2004; Lowe and Coe, 2002).

The biodegradable polymers that have been used include poly(lactide) (PLA) which exists in two forms: poly(L-lactide) (PLLA) and poly(D-lactide) (PDLA) (Wuisman and Smit, 2006). HYDROSORB (Medtronic Sofamor Danek, Memphis, USA) is an example of a degradable fusion cage (Jiya *et al.,* 2009; Kuklo *et al.,* 2004; Lowe and Coe, 2002). It is manufactured from a material called MacroPore (MacroPore Biosurgery Inc., San Diego, USA), which has a 70:30 ratio of poly(L-lactide) to poly(D,L lactide); in this study, this is referred to as PLDLA.

Biodegradable cages, after providing initial stability required for spinal fusion, degrade over time to natural metabolic compounds (Lowe and Coe, 2002; Rezwan *et al.,* 2006; Wuisman and Smit, 2006). Hence, the potential long-term risks associated with permanent cages are eliminated (Kandziora *et al.,* 2004; Wuisman and Smit, 2006). As they degrade, the load is gradually transferred to the healing bone resulting in a higher fusion rate (Kandziora *et al.,* 2004; Lippman *et al.,* 2004; Smit *et al.,* 2006; Wuisman and Smit, 2006). Reduced stiffness of these cages compared with those made from metallic materials may eliminate stress shielding (Kandziora *et al.,* 2004; Wuisman and Smit, 2006). It was shown by van Dijk *et al.* (2002) that PLLA cages had a higher fusion rate when compared with titanium alloy cages. However, these biodegradable materials are weak; microcracks and failures with plastic deformation in PLDLA cages were observed by Smit *et al.* (2006) in an animal (goat) study. Furthermore, subsidence of HYDROSORB (PLDLA) cages in patients undergoing lumbar spinal fusion was reported by Jiya *et al.* (2009).

Bioactive materials are another group of biomaterials which include hydroxyapatite (HA), bioactive glasses (e.g. 45S5 Bioglass) and selected compositions of glass-ceramics (Hench, 1998; Rezwan *et al.,* 2006; Yang *et al.,* 2006; Zhang *et al.,* 2009). These materials are brittle, stiff and are not easily fabricated into complicated shapes (Blaker *et al.,* 2003; Zhang *et al.,* 2009). Hence, recent studies have evaluated the use of bioactive/biodegradable composites as fusion cage materials, e.g. composites of HA and PLLA (Hojo *et al.,* 2005; Totoribe *et al.,* 2003). Previous literature has shown that the addition of a bioactive phase to a biodegradable polymer introduces a bioactive composite with enhanced mechanical properties relative to a pure polymer and improved structural integrity and flexibility compared with brittle glass (Hong *et al.,* 2008; Maquet *et al.,* 2003; Maquet *et al.,* 2004; Rezwan *et al.,* 2006; Zhang *et al.,* 2009).

A 45S5 Bioglass/PLDLA composite is evaluated in this study as a potential fusion cage material. In order to carry out the analysis, a range of possible Young's modulus values for the composite is calculated (§4.3.3) and the stress distribution within the cage is determined using FEA (§4.4.1.3).

4.3. Properties of the composite material

4.3.1. Introduction

45S5 Bioglass was chosen as the additive bioactive material in this study because it is a Class A bioactive material; it induces bone formation (osteoinductive) and is a material around which bone can grow (osteoconductive) (Rezwan *et al.,* 2006; Stamboulis *et al.,* 2002; Yang *et al.,* 2006). PLDLA was the biodegradable polymer selected in this study since it has already been used as a material for fusion cages (Kuklo *et al.,* 2004; Lowe and Coe, 2002) and also causes less tissue reaction when compared with other biodegradable materials such as crystalline PLLA or copolymers containing glycolide (Maquet *et al.,* 2003; Thomas *et al.,* 2008). However, investigation of these properties is not the focus of this study. Enhanced mechanical properties of 45S5 Bioglass/PLDLA composite compared with pure PLDLA have been reported (Maquet *et al.,* 2003; Maquet *et al.,* 2004).

4.3.2. Composite mechanical properties

In order to carry out FEA on the fusion cage model with the 45S5 Bioglass/PLDLA composite, Reuss and Voigt models (Hukins *et al.,* 1999) were used to determine a range of values for the composite Young's modulus ($E_{Composite}$). Several Young's modulus values have been suggested for PLDLA in the literature (Kuklo *et al.,* 2004; Middleton and Tipton, 2000; Toth *et al.,* 2002; Yang *et al.,* 2001). Hence, to cover the full range, the lowest (1.4 GPa, Yang *et al.,* 2001) and the highest (3.15 GPa, Kuklo *et al.,* 2004; Toth *et al.,* 2002) suggested PLDLA Young's modulus values were taken into consideration when calculating the $E_{Composite}$. Thus, the Young's modulus of 45S5 Bioglass (35 GPa) (Hench, 1998; Rezwan *et al.,* 2006) along with the two Young's modulus values for the PLDLA (1.4 and 3.15 GPa) (Kuklo *et al.,* 2004; Toth *et al.,* 2002; Yang *et al.,* 2001) were used in the Reuss and Voigt models. The mechanical properties of 45S5 Bioglass and PLDLA are shown in Table 4.1.

The lower value of the $E_{Composite}$ was determined using the Reuss model from equation 4.1.

$$\frac{1}{E_{Composite}} = \frac{V_B}{E_B} + \frac{V_P}{E_P} \qquad (4.1)$$

where E_B and E_P are the Young's modulus values and V_B and V_P are the volume fractions of 45S5 Bioglass and PLDLA, respectively. Note that $V_B + V_P = 1$. The lowest suggested PLDLA Young's modulus (1.4 GPa) was used in this model.

The upper value of the $E_{Composite}$ was determined using the Voigt model from equation 4.2.

$$E_{Composite} = E_B V_B + E_P V_P \tag{4.2}$$

where the parameters are as defined in equation 4.1. The highest suggested PLDLA Young's modulus (3.15 GPa) was used in this model.

A study by Zhang *et al.* (2009) showed that the addition of bioactive glass and increasing its volume fraction increases the Young's modulus of the bioactive glass/poly(D,L-lactide) composite while decreasing its tensile strength. However, their study showed that the decrease in the tensile strength of the bioactive glass/poly(D,L-lactide) composite is much greater when the volume fraction of the additive is increased from 0.2 (27 MPa) to 0.4 (15 MPa) as opposed to 0.3 (23 MPa). Volume fractions of between 0.2 and 0.3 of 45S5 Bioglass were used to determine the lower and upper limits for the $E_{Composite}$, respectively.

Table 4. 1. Material properties. Cortical bone Young's modulus was presented in Table 3.1.

Material	Young's Modulus (GPa)	Compressive strength (MPa)	Reference
PLDLA (HYDROSORB)	3.15	100	Kuklo *et al.,* 2004; Toth *et al.,* 2002
PLDLA	1.4	-	Yang *et al.,* 2001
45S5 Bioglass	35	~ 500	Hench, 1998; Rezwan *et al.,* 2006

4.3.3. Results

Figure 4.1 shows the lower and upper limits for the $E_{Composite}$. The $E_{Composite}$ with between 0.2 and 0.3 volume fractions of 45S5 Bioglass is between 2 and 13 GPa. This range of values was used in the subsequent FEA of the fusion cage.

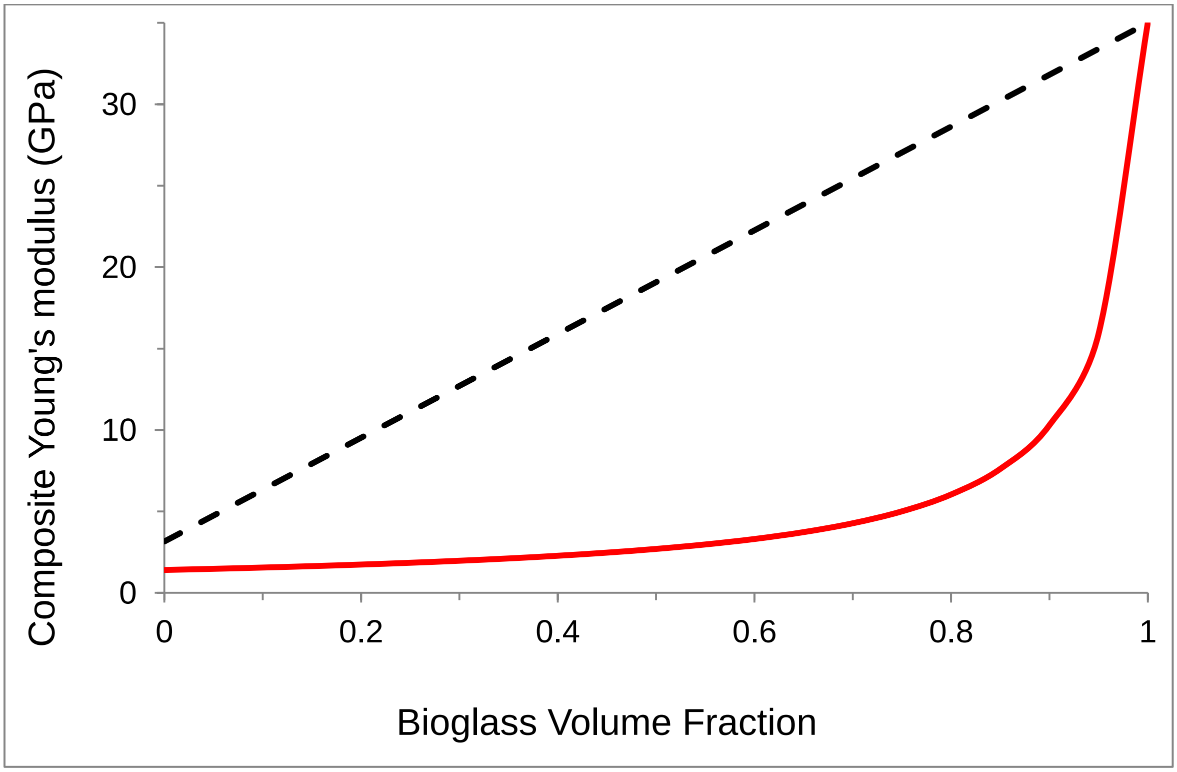

Figure 4. 1. Lower (Reuss) and upper (Voigt) limits of the $E_{Composite}$ were determined using two Young's modulus values for PLDLA. The lines shown are: lower limit (red line) and upper limit (dashed black line). The two different Young's modulus values for PLDLA result in different initial points for the lower and the upper limits of the $E_{Composite}$.

4.4. Analysis

4.4.1. Materials and methods

4.4.1.1. Cage model

A cage model with 10 side-holes was used in this study (Figure 4.2). The dimensions of the cage model (Figure 4.3) and the details of the side-holes and their positions were described in §3.3.1 and §3.3.2, respectively. The experimental validation of the cage model was explained in §3.3.5.

4.4.1.2. Vertebrae model

The shape and dimensions of the vertebrae models used in this study were described in §3.3.3 and illustrated in Figure 3.6. The vertebrae were modelled as cortical bone with homogeneous and isotropic material properties (described in detail in §2.4.3 and §3.3.3). The Young's modulus of the cortical bone, in this study referred to as $E_{Cortical}$, was assumed to be in the range of 12 to 30 GPa (Hee and Kundnani, 2010; Hench, 1998; Vadapalli *et al.*, 2006; Zhong *et al.*, 2006). The cortical bone material properties were shown in Table 3.1. The vertebrae and the cage assembly were shown in Figure 3.7.

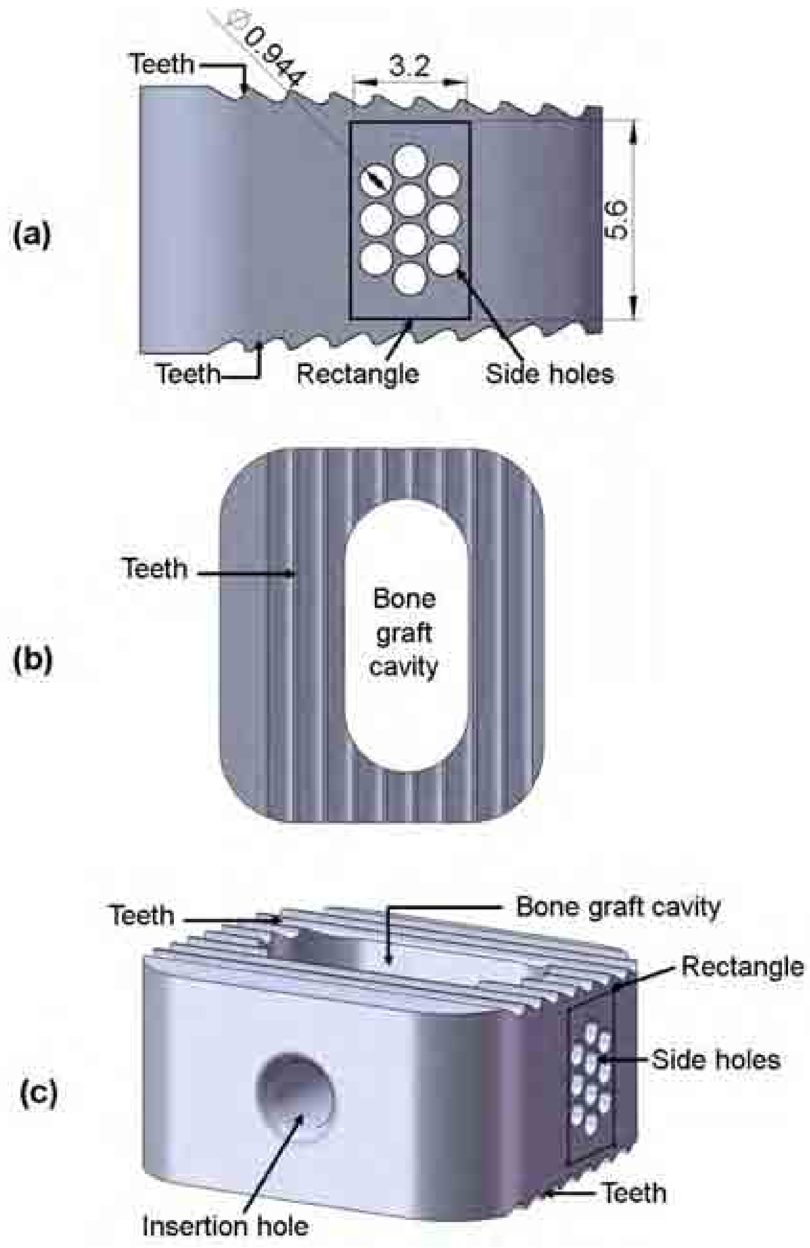

Figure 4. 2. The cage analysed in this study has 10 side-holes on each lateral side. The side-holes are positioned within a rectangle. The width of the rectangle corresponds to the anterior-posterior dimension of the graft cavity and its height corresponds to the posterior cage height below the level of the teeth. The insertion hole enables a rod-shaped surgical instrument to be used to position the cage between the adjacent vertebrae. There are teeth at the top and bottom of the cage that may enable the cage to grip the vertebrae, hence retaining the cage in place. (a) Side view (dimensions are in millimetres), (b) top view and (c) three-dimensional view. Model dimensions are given in Figure 4.3.

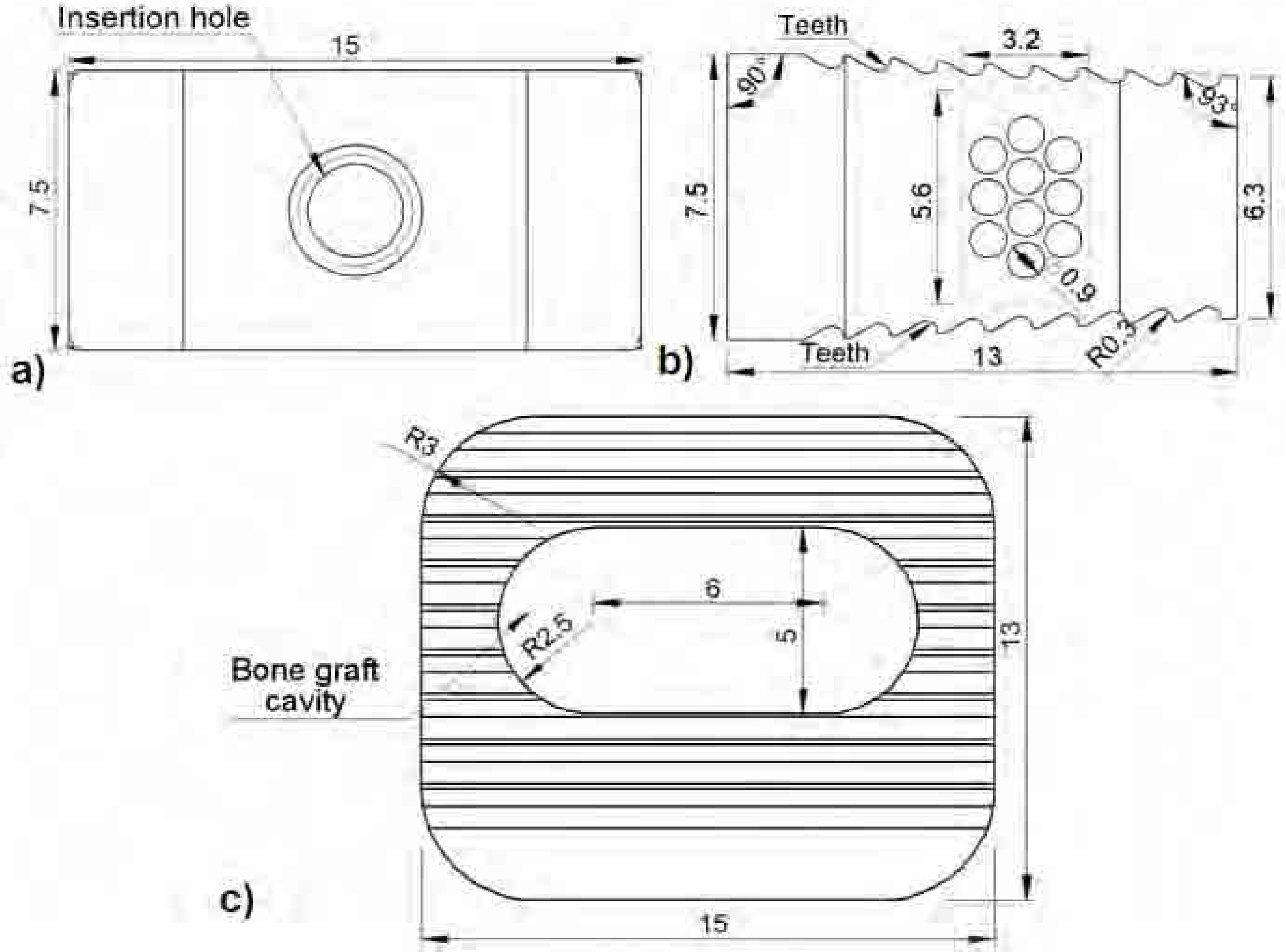

Figure 4. 3. Dimensions of the cage model shown in Figure 4.2. (a) Front view, (b) side view and (c) top view. All dimensions are in millimetres.

4.4.1.3. FEA on the cage models

In this study, no clearance was applied when assembling and bonding the vertebrae and cage models (as described in §3.3.4, Figure 3.8). The simulations did not include bone graft, any other soft tissue or newly formed bone. A uniform axial compressive load of 150 N (BS ISO 18192-1:2011) was applied on the superior surface of the assembly to mimic the axial load experienced by the cervical spine. The inferior of the assembly was fully restrained in all directions (Figure 3.9).

The cage mesh size (0.3 mm) used in this study was described in §3.3.4 and is shown in Appendix B, Figure B.1. The finest possible mesh size (0.6 mm) was used for the vertebrae models. This was also described in §3.3.4. All the assembled models were analysed with total nodes of 441,350, total elements of 307,722 and were meshed with tetrahedral-shaped elements.

Since the Poisson's ratio of the composite is not known, all the models were analysed with a Poisson's ratio of between 0.3 and 0.49 (the largest Poisson's ratio allowed) in intervals of 0.05 to determine an optimum Poisson's ratio for this study. The results (maximum von Mises stress and displacement) are shown in Table 4.2 and Appendix E, Tables E.1 to E.4. Increasing the Poisson's ratio from 0.3 to 0.49, when analysed with $E_{Cortical}$ of 12 and 30 GPa, decreased the maximum von Mises stress on average by 13 and 29%, respectively. The same increase in the Poisson's ratio, decreased the maximum displacement on average by 9 and 12% when analysed with $E_{Cortical}$ of 12 and 30 GPa, respectively. Hence, to take the worst case into consideration, the lowest Poisson's ratio (0.3) was used in this study, which corresponded to the highest von Mises stress and displacement levels achieved.

4.4.2. Results

Table 4.2 shows the maximum von Mises stress, displacement and normal compressive stress determined for each $E_{Composite}$ value. Figures 4.4 and 4.5 illustrate typical examples of a von Mises stress distribution in the cage resulting from the compressive load. Models showed stress distribution peaks at the cage-vertebrae interface (the tip of the cage teeth) (Figures 4.4 to 4.6).

FEA was carried out for $E_{Cortical}$ values of both 12 and 30 GPa (Hee and Kundnani, 2010; Hench, 1998; Vadapalli *et al.,* 2006; Zhong *et al.,* 2006). The maximum von Mises stress for all the models (when the $E_{Composite}$ ranged between 2 and 13 GPa) when analysed with $E_{Cortical}$ = 12 GPa was between 14 and 18 MPa (Figure 4.4) with maximum displacement between 5.1 and 18.7 µm. The maximum von Mises stress for the same models when analysed with $E_{Cortical}$ = 30 GPa was between 14 and 20 MPa (Figure 4.5) with maximum displacement between 3.5 and 17.1 µm. The average normal compressive stress for all the models analysed in this study was 4.5 MPa. Figure 4.7 shows the normal compressive stress when $E_{Composite}$ = 2 GPa and $E_{Cortical}$ = 30 GPa. Increasing the value of $E_{Cortical}$ from 12 to 30 GPa increases the maximum von Mises stress predicted by 13% and decreases the maximum displacement by 19%. In all the models, the maximum von Mises stress levels within each side-hole were between 1 and 4 MPa and between 1 and 6 MPa within the insertion hole (Figure 4.6).

Table 4. 2. Maximum von Mises stress, maximum displacement and normal compressive stress of the cage model when analysed with the $E_{Composite}$ ranging between 2 and 13 GPa and Poisson's ratio of 0.3. The assembled model had a total of 441,350 nodes and 307,722 elements.

$E_{Composite}$ (GPa)	$E_{Cortical}$ = 12 GPa			$E_{Cortical}$ = 30 GPa		
	Maximum von Mises stress (MPa)	Maximum displacement (μm)	Normal compressive stress (MPa)	Maximum von Mises stress (MPa)	Maximum displacement (μm)	Normal compressive stress (MPa)
2	18	18.7	5	20	17.1	5
3	16	13.4	5	19	11.8	5
4	15	10.7	4	18	9.1	5
5	14	9.1	4	18	7.5	5
6	14	8.0	4	17	6.4	5
7	14	7.2	4	16	5.7	5
8	14	6.6	4	16	5.1	5
9	14	6.2	4	16	4.6	5
10	15	5.8	4	15	4.3	4
11	15	5.5	4	15	4.0	4
12	16	5.3	4	14	3.7	4
13	16	5.1	4	14	3.5	4
Mean	**15**	**8.5**	**4**	**17**	**6.9**	**5**

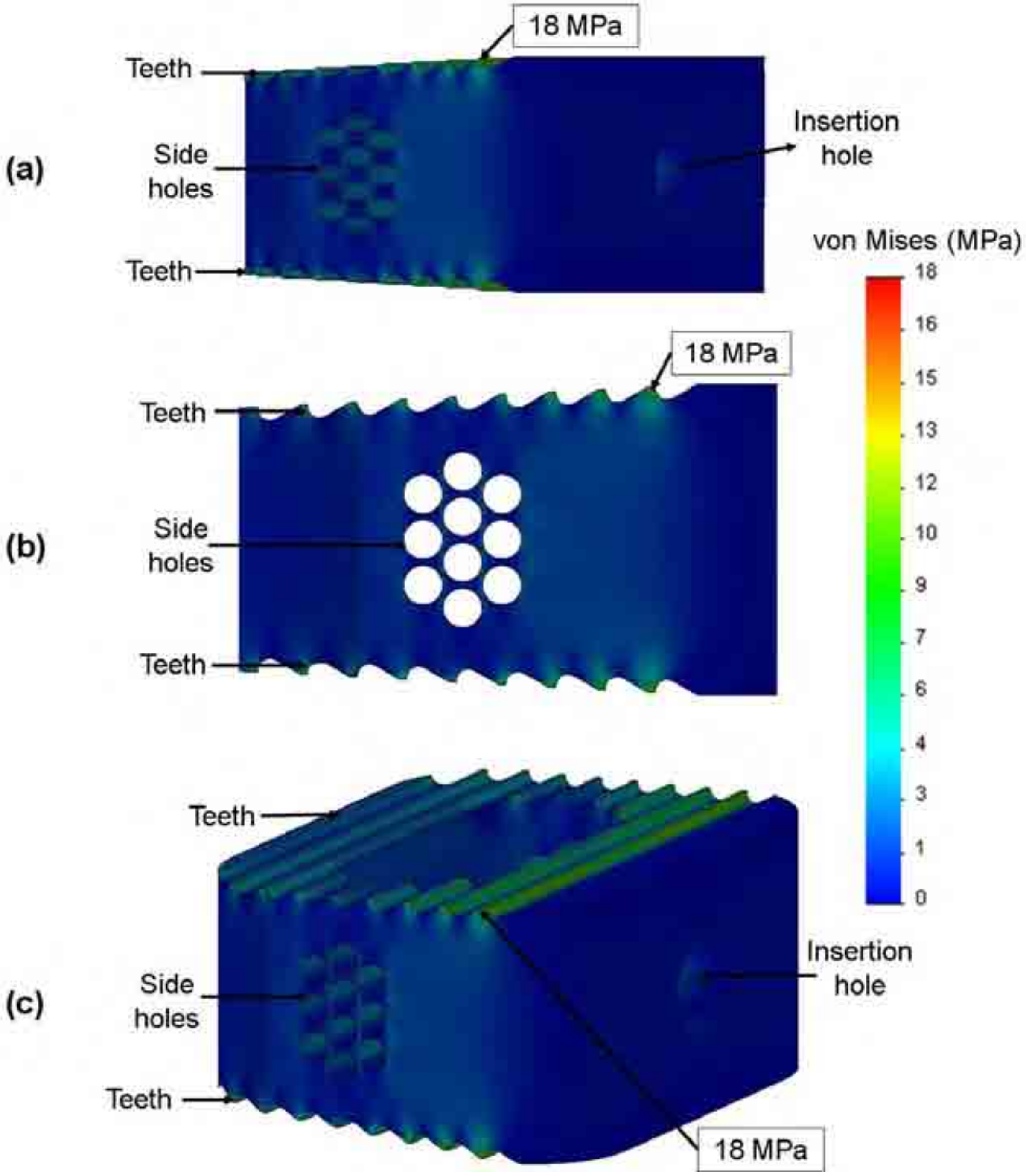

Figure 4. 4. von Mises stress distribution in the cage model with $E_{Composite}$ = 2 GPa and $E_{Cortical}$ = 12 GPa. Maximum stress is seen on the tip of the teeth. (a) Three-dimensional view not showing the top, (b) side view, (c) three-dimensional view showing the top.

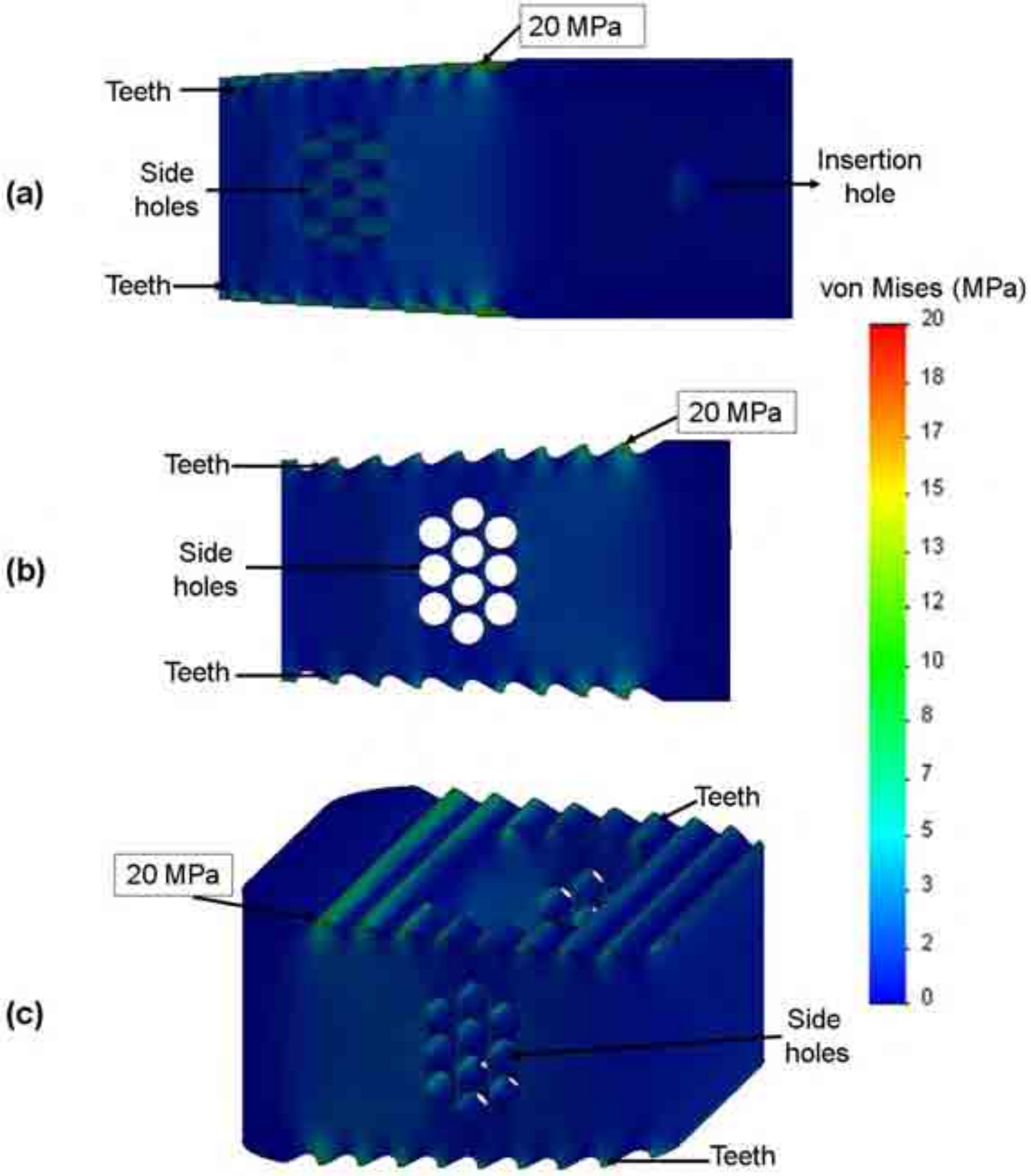

Figure 4. 5. von Mises stress distribution in the cage model with $E_{Composite}$ = 2 GPa and $E_{Cortical}$ = 30 GPa. Maximum stress is seen on the tip of the teeth. (a) Three-dimensional view not showing the top, (b) side view, (c) three-dimensional view showing the top.

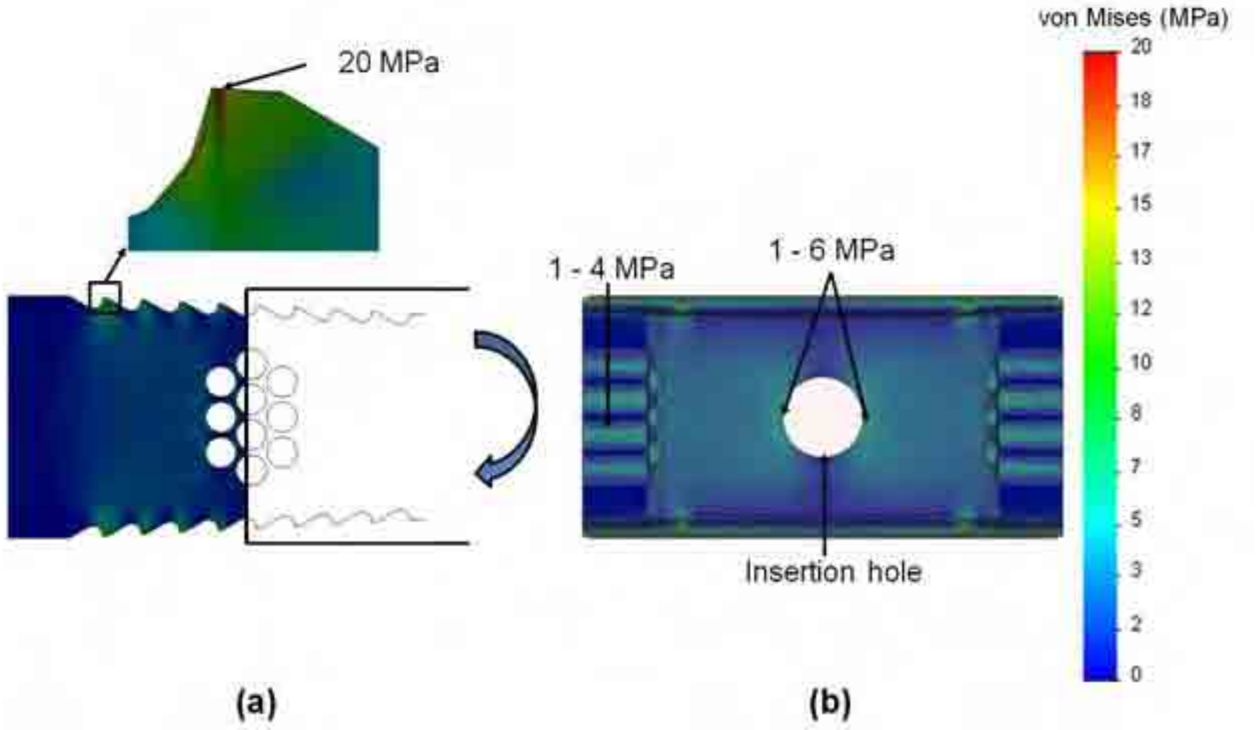

Figure 4. 6. von Mises stress distribution in the cage model with $E_{Composite}$ = 2 GPa and $E_{Cortical}$ = 30 GPa. In (a) maximum stress is seen on the tip of the teeth, in (b) the cage is cut and rotated to show stress concentration in the side-holes.

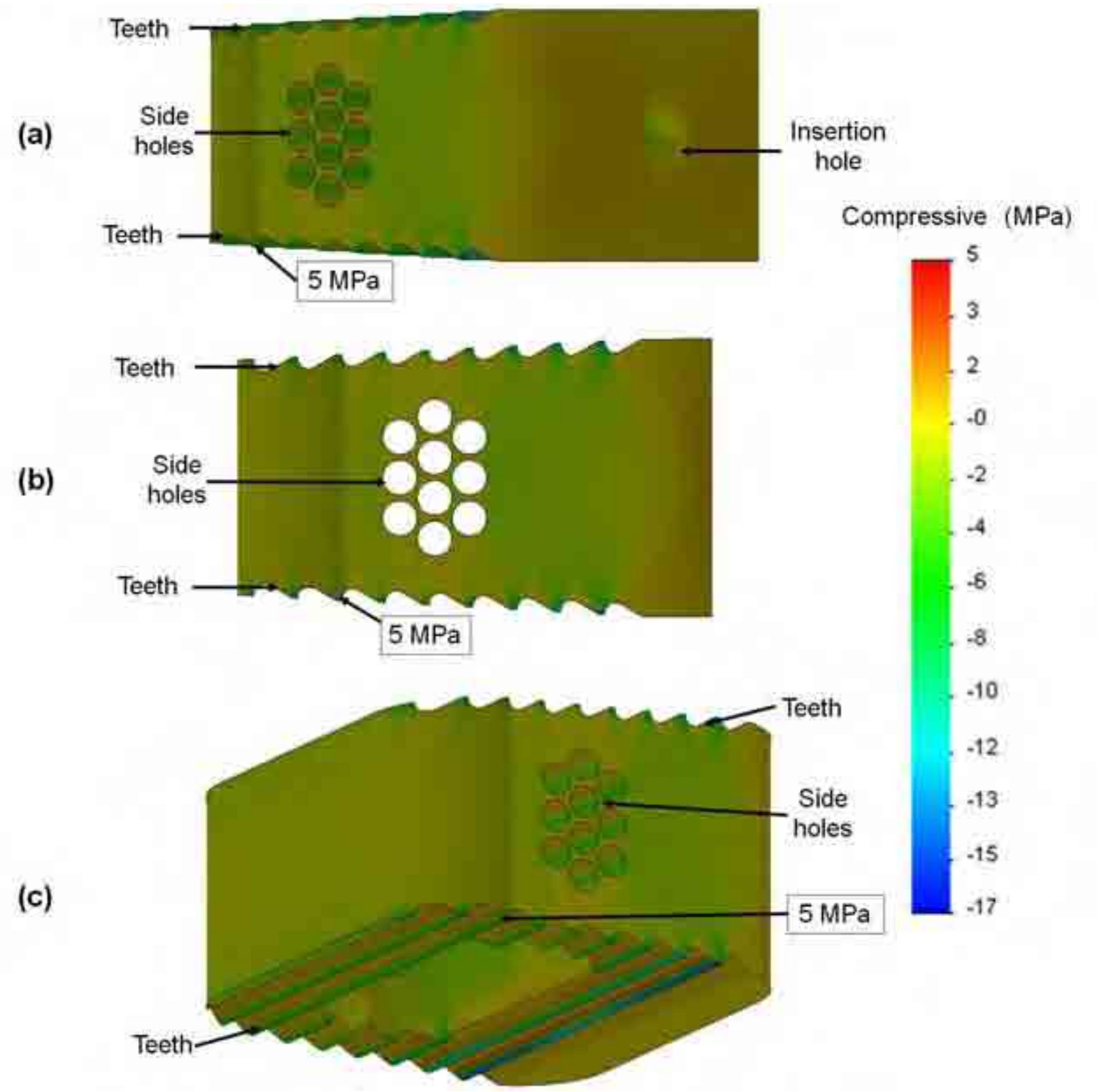

Figure 4. 7. Normal compressive stress distribution in the cage model with $E_{Composite}$ = 2 GPa and $E_{Cortical}$ = 30 GPa. Maximum stress is seen on the tip of the teeth. (a) Three-dimensional view not showing the bottom, (b) side view, (c) three-dimensional view showing the bottom.

4.5. Discussion

All the models were analysed with both 12 and 30 GPa for $E_{Cortical}$ and the maximum von Mises stress levels obtained ranged between 14 and 20 MPa. Increasing the $E_{Cortical}$ from 12 to 30 GPa increases the maximum stress predicted by 13%. This shows that a change in material properties of the cortical bone can influence the results. However, this value is still lower than the compressive strength of pure PLDLA (100 MPa, Kuklo *et al.,* 2004; Toth *et al.,* 2002). As the von Mises stress values predicted by the FEA model were always less than the compressive strength of pure PLDLA, it can then be concluded that the 45S5 Bioglass/PLDLA composite is unlikely to fail in static compression when used as a cervical fusion cage material. The maximum von Mises stress determined in this study was compared to the compressive strength of pure PLDLA because the compressive strength of the 45S5 Bioglass/PLDLA composite has not been reported.

There is currently no literature available on the fatigue strength of the 45S5 Bioglass/PLDLA composite. However, the maximum von Mises stress determined in this study is 20 MPa which is five times lower than the compressive strength of pure PLDLA (100 MPa); hence, the device is unlikely to fail due to fatigue, but mechanical testing would be required to confirm this assumption. The conclusion of this study is consistent with those of some clinical studies (Kuklo *et al.,* 2004; Lowe and Coe, 2002) which have found no mechanical failures of cages made from PLDLA *in vivo*.

The lack of testing standards for biodegradable materials has led to the use of testing standards for permanent materials (Smit *et al.*, 2008; Smit *et al.*, 2010). However, biodegradable implants differ from permanent ones; biodegradable implants are only required to withstand *in vivo* conditions without failure for as long as necessary (e.g. complete bone formation) whilst permanent implants are needed for as long as possible. The material properties of the biodegradable implants change over time. Many factors such as design of the implant, manufacturing process, sterilization method, material properties, loading, temperature, humidity and chemical environment (e.g. pH) have an effect on their degradation process and rate (thus on their strength) (Smit *et al.*, 2006; Smit *et al.*, 2008; Smutz *et al.*, 1991). Therefore, in order to employ experimental test results, the detailed processing methods and parameters should be known as they can have a bearing on the test outcome.

4.6. Conclusions

In all the models, the maximum von Mises stress showed peaks at the cage-vertebrae interface and had a value of between 14 and 20 MPa (and on average 4.5 MPa for normal compressive stress) with maximum displacements of between 3.5 and 18.7 µm. These stress values are much lower than the compressive strength of pure PLDLA (100 MPa). The peak von Mises stress determined in this study is 20 MPa, which is five times lower than the compressive strength of pure PLDLA. The FE results of this study suggest that 45S5 Bioglass/PLDLA composite as a cervical cage material is unlikely to fail in static compression or as a result of fatigue.

5. DESIGN OF A SURGICAL INSTRUMENT FOR REMOVING VERTEBRAL EDGES TO PROVIDE SCREW ACCESS TO A SPINAL FUSION CAGE

5.1. Chapter overview

This chapter describes the design and development of a surgical instrument which facilitates implantation of lumbar spinal fusion cages. Section 5.2 describes the aim of the study and drawbacks associated with the currently used instruments. The design requirements are outlined in §5.3. Initial and secondary concept designs are described, shown and analysed in §5.4 and §5.5, respectively. The final design is presented in §5.6. This section also includes the risk assessment, tests and validation of the final design. The study is discussed in §5.7.

5.2. Introduction

The surgical instrument developed in this study is intended to be used to aid implantation of polyetheretherketone (PEEK) lumbar fusion cages (STALIF^{TM} TT, Surgicraft Ltd., Redditch, UK, Figure 2.13); specifically, the instrument is required to remove parts of the vertebrae that obscure the holes for screw insertion (Figure 5.1). Screw fixation is used to secure the cage between the vertebrae (Figure 5.1). However, once the cage is in position, the surgeon may find the entrance to a screw hole partially blocked by the edge of the vertebral body (VB) (Figure 5.1). Currently rongeurs (Figure 5.2) are used to nibble the VB edge adjacent to the screw holes in a cage. However, some of the holes in the fusion cage are positioned at an awkward angle (Figure 5.1), which may make the use of rongeurs difficult. Also, rongeurs can take away more bone than is necessary and may cause damage to the PEEK cage (discussed and shown in §5.6.9.3). To avoid these problems a VB edge cutter instrument was designed. This instrument removes enough VB edge adjacent to all screw holes in a cage to enable screw access. This study defines the design requirements, describes the concept designs and concludes with a final design for the instrument. As described in §2.2.1, the stages form part of the sequence of events in the development of a surgical instrument (Aitchison *et al.*, 2009) that must be completed in accordance with the relevant standards (Leahy *et al.*, 2000).

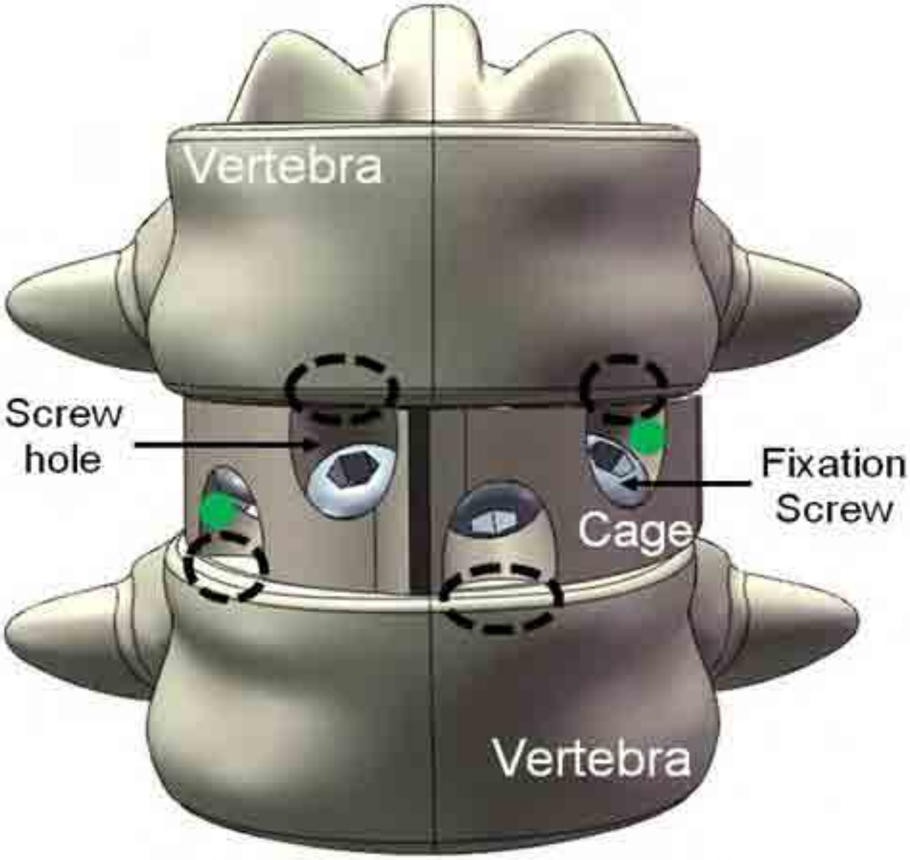

Figure 5. 1. STALIF^{TM} TT spinal fusion cage. Fixation screws are used to stabilize the fusion cage between the adjacent vertebrae. The screw holes with awkward angles are the two holes farthest from the centre of the cage (green circles). The VB edges are blocking the access to all the screw holes (dashed black circles).

Figure 5. 2. Rongeurs.

5.3. Instrument design requirements

The design requirements for the VB edge cutter instrument are listed below. These characteristics were produced in accordance with British Standards and the requirements of the Food and Drug Administration (USA) (BS EN ISO 9001:2008, BS EN ISO 13485:2003 and Quality System Regulation 21 CFR 820). Note, some of the points listed below were included in the instrument design requirements during the design process. These include: points 5, 6, 7, 8 and 15. Reasons for adding these additional requirements are given at each point.

1. The instrument had to be compatible with the STALIF^{TM} TT fusion cage range: height (11, 13, 15 and 17 mm) and width (36, 39, 42 and 45 mm).
2. The instrument had to remove sufficient VB edge adjacent to all screw holes in a cage to enable screw access.
3. The instrument had to reduce the duration of the surgery and be easy to use.
4. The instrument had to promote good visibility of the operative site.
5. The instrument had to be compatible with an existing Surgicraft Ltd. handle which has a universal joint at its end (Figure 5.3). This handle allows continuous 360˚ clockwise and anti-clockwise motions so that the VB edge cutter can reach the fusion cage side holes which are located at awkward angles. These holes are located at the far end of the cage (Figure 5.1). This design requirement was added because of its commercial and marketing benefits. This is because the users are already familiar with the Surgicraft Ltd. universal joint handle.

6. The instrument had to facilitate minimally invasive surgery, be sufficiently small to fit easily into the wound and avoid obstructing the surgeon’s view; the length of the cutter should not exceed 47 mm. This design requirement was added so the final design of the instrument would comply with point 5.
7. The instrument had to be capable of being positioned correctly within the cage screw holes. Hence, it was required to have a feature as a guide (instrument head) with sufficient dimensions to cover all cage sizes. This design requirement was added to ease the use of the instrument which would improve its marketability.
8. The instrument had to be designed so that it would connect to the (universal joint) handle in such a way that it would minimise the risk of it becoming detached while in use. This design requirement was added to make the instrument safer to use and so the final design of the instrument would comply with point 5.
9. The instrument had to operate without causing any damage to the PEEK fusion cage.
10. The instrument had to avoid damage to the patient’s soft tissues during insertion and removal.
11. The instrument had to be hand operated.
12. The instrument had to be able to withstand the forces to which it was subjected during surgery.
13. The instrument had to be able to be easily cleaned and sterilised without complications.
14. The instrument had to have teeth (or sharp edges) that are sufficiently sharp to penetrate and to easily and neatly remove the targeted VB edge.
15. The instrument teeth had to remain sufficiently sharp to aid implantation of at least 25 cages; each cage requires four VB edges to be removed. Hence, at least 100 neat cuts

were required from the instrument. This design requirement was added to improve the instrument's marketability.

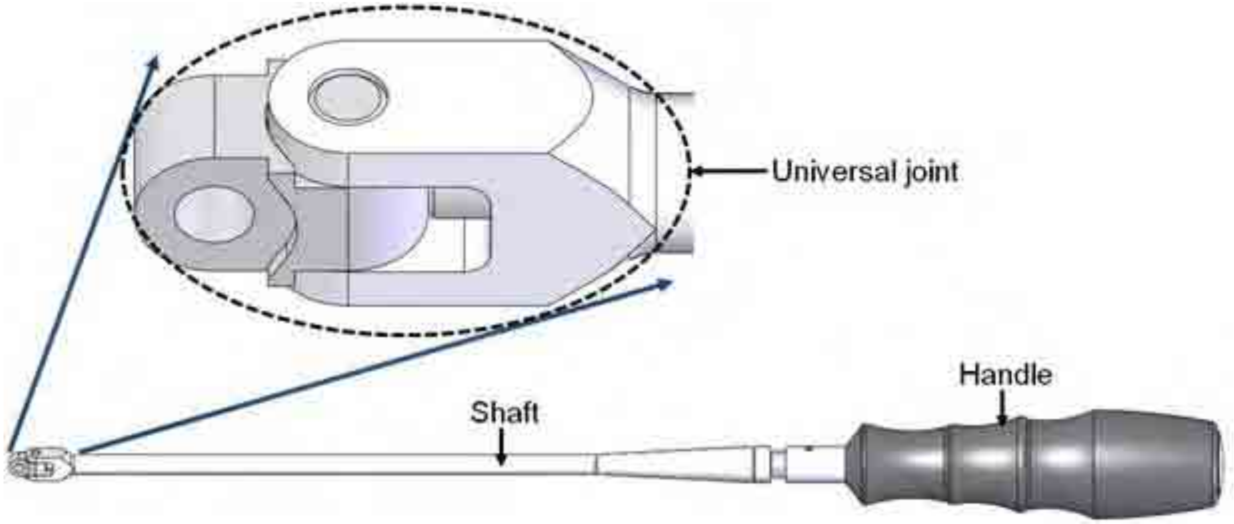

Figure 5. 3. Surgicraft Ltd. universal joint handle which has a flexible neck. This handle allows continuous 360° clockwise and anti-clockwise motions.

5.4. Initial concept designs

5.4.1. Introduction

Initially 11 concept designs were produced. Some of these concepts are designed to be assembled on the tip of a screw driver (Surgicraft Ltd.) with a universal joint (Figure 5.4). The concepts are the: angular chisel, screw driver chisel (SDC), pull-up chisel, screw driver scoop (SDS), angular scoop, angular bone file (ABF), T-handle rotating cutter (TRC), angular rotating cutter (ARC), rotating shaver, screw threaded concept (STC) and universal burr (Figures 5.5 to 5.28). The analysis of each concept is shown in the relevant section.

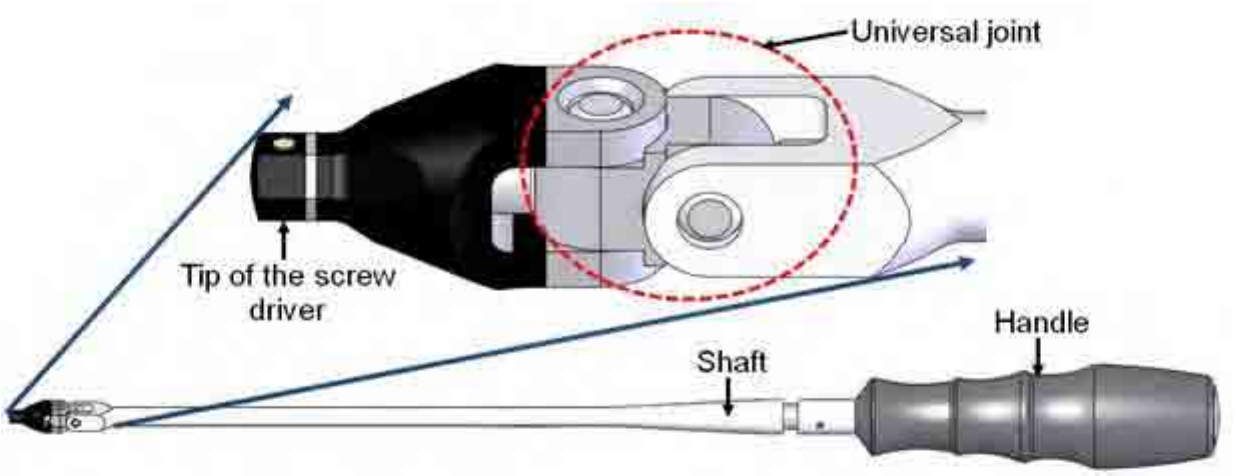

Figure 5. 4. Surgicraft Ltd. screw driver with a universal joint which has a flexible neck. It is used in some of the initial concepts.The universal joint allows continuous 360˚ clockwise and anti-clockwise motions.

5.4.2. Angular chisel

5.4.2.1. Concept introduction

The angular chisel consists of two parts: a shaft and a blade. Figure 5.5 shows the concept and its features. Figure 5.6 shows the operation of the concept (cutting away the VB edge). The shaft is the static part of the angular chisel which forms the instrument head and the guide at one end and is attached to the Surgicraft Ltd. handle at the other end (Figure 5.5). The shaft has an angular neck (Figure 5.5) which enables access to the side holes (with an awkward angle). The instrument head dimensions correspond with those of the cage screw holes. The blade (indicated in green in Figures 5.5 and 5.6) is the mobile part of the angular chisel which consists of a sharp edge and an area A. The sharp edge cuts away the targeted VB edge when a force is applied to area A (shown by blue arrow in Figures 5.5 and 5.6). The guide protects the cage as it controls how far the green component (hence the sharp edge) can travel (Figure 5.6).

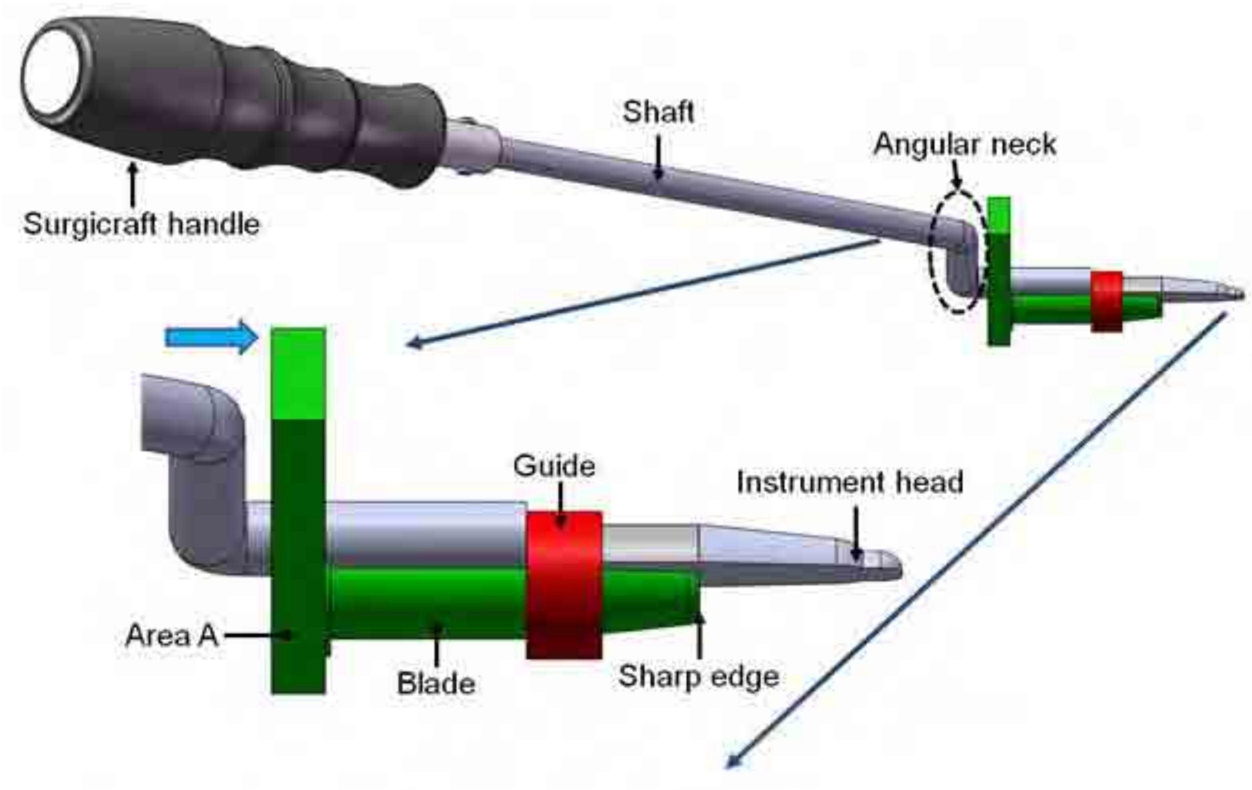

Figure 5. 5. The angular chisel concept and its features.

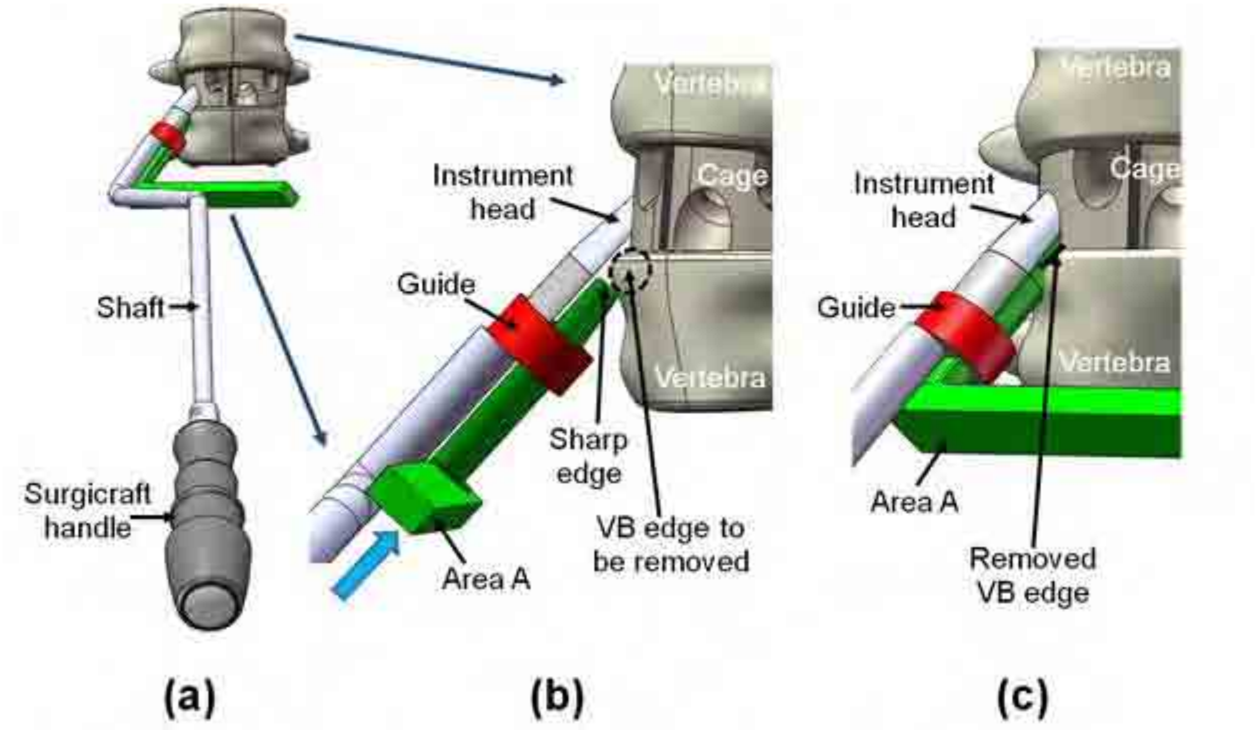

Figure 5. 6. Operation of the angular chisel. (a) and (b) The instrument head is placed in the screw hole and rests against the screw hole wall to provide an appropriate angle for the sharp edge. The instrument head holds the instrument in place (inside the screw hole) and prevents any undesired movements. (b) Force has to be applied to area A in the direction of the blue arrow to enable the sharp edge to remove the targeted VB edge. (c) The guide stops the green component and the targeted VB edge has been removed.

5.4.2.2. Concept analysis

The main advantage of the angular chisel concept is that it can remove the targeted VB edge in a single action (by the force applied to area A) (Figure 5.6). Also, it is safe to use because there are no sharp teeth or edges on the instrument head. However, the angular chisel may require a large space in which to function because of the angular neck (Figures 5.5 and 5.6).

5.4.3. Screw driver chisel (SDC)

5.4.3.1. Concept introduction

The SDC is assembled on the tip of the screw driver with a universal joint (Figure 5.4) and consists of three parts: an instrument head, a guide and a blade. Figure 5.7 shows the concept and its features. Figure 5.8 shows the operation of the concept (cutting away the VB edge). The universal joint provides a flexible neck which allows the desired angle to be achieved in order to place the instrument head in the cage screw hole. The instrument head dimensions correspond with those of the cage screw holes. The blade (shown in green in Figures 5.7 and 5.8) consists of a sharp edge and an area A. The sharp edge cuts away the targeted VB edge when a force is applied to area A (shown by blue arrow in Figures 5.7 and 5.8). The guide protects the cage as it controls how far the green component (hence the sharp edge) can travel (Figure 5.8).

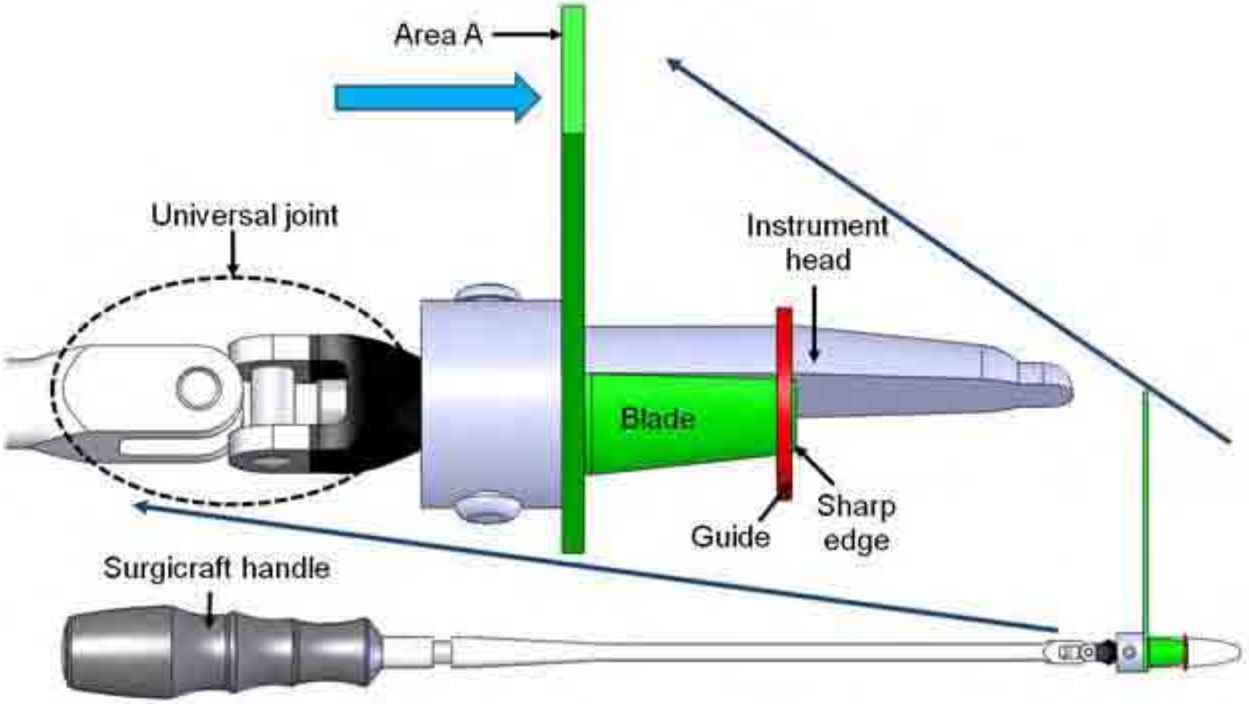

Figure 5. 7. The SDC and its features.

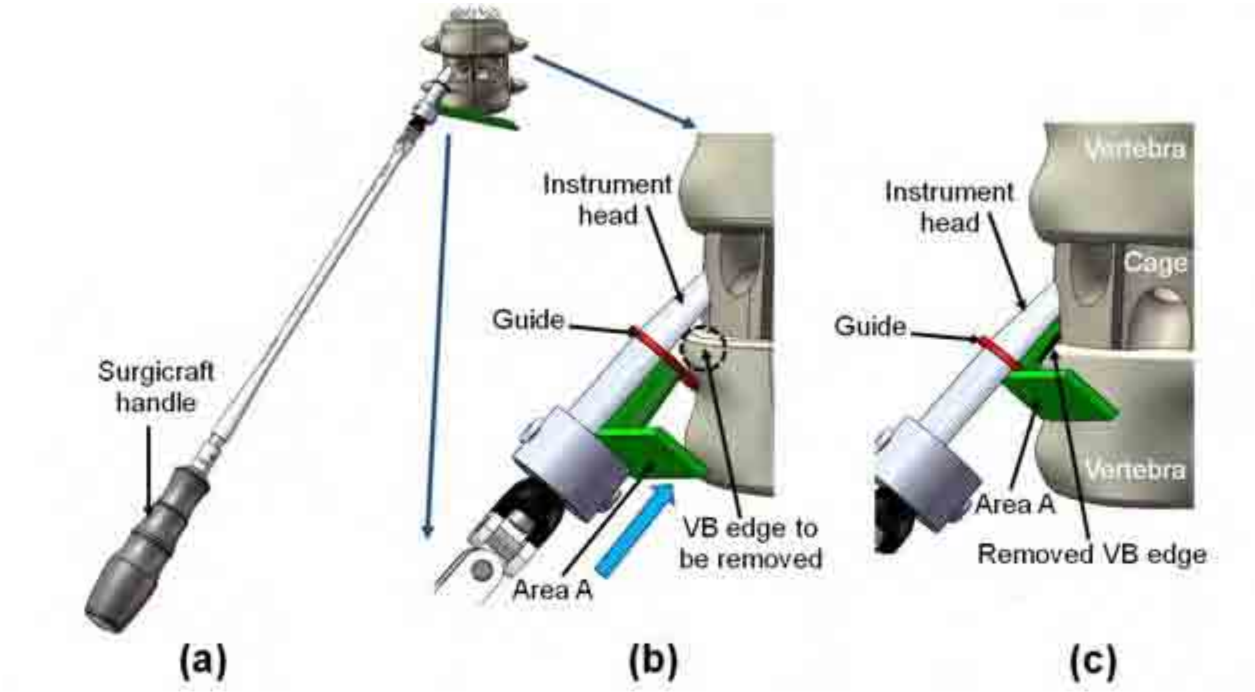

Figure 5. 8. Operation of the SDC. (a) and (b) The instrument head is placed in the screw hole and rests against the screw hole wall to provide an appropriate angle for the sharp edge. The instrument head holds the instrument in place (inside the screw hole) and prevents any undesired movements. (b) Force has to be applied to area A in the direction of the blue arrow to enable the sharp edge to remove the targeted VB edge. (c) The guide stops the green component and the targeted VB edge has been removed.

5.4.3.2. Concept analysis

The main advantage of the SDC concept is that it can remove the targeted VB edge in a single action (by the force applied to area A) (Figure 5.8). Also, it is safe to use because there are no sharp teeth or edges on the instrument head. However, applying a sudden force to area A may not be desirable since it will be inside the wound during surgery and may cause trauma to the surrounding soft tissues.

5.4.4. Pull-up chisel

5.4.4.1. Concept introduction

The pull-up chisel is a single part instrument. It has a sharp cone-shaped head with dimensions which correspond with those of the cage screw holes. Figure 5.9 shows the concept and its features. Figure 5.10 shows the operation of the concept (cutting away the VB edge). The shaft of the pull-up chisel has an angular neck (Figure 5.9) which enables access to the side holes (with an awkward angle). The shaft is attached to Surgicraft Ltd. handle (Figure 5.9).

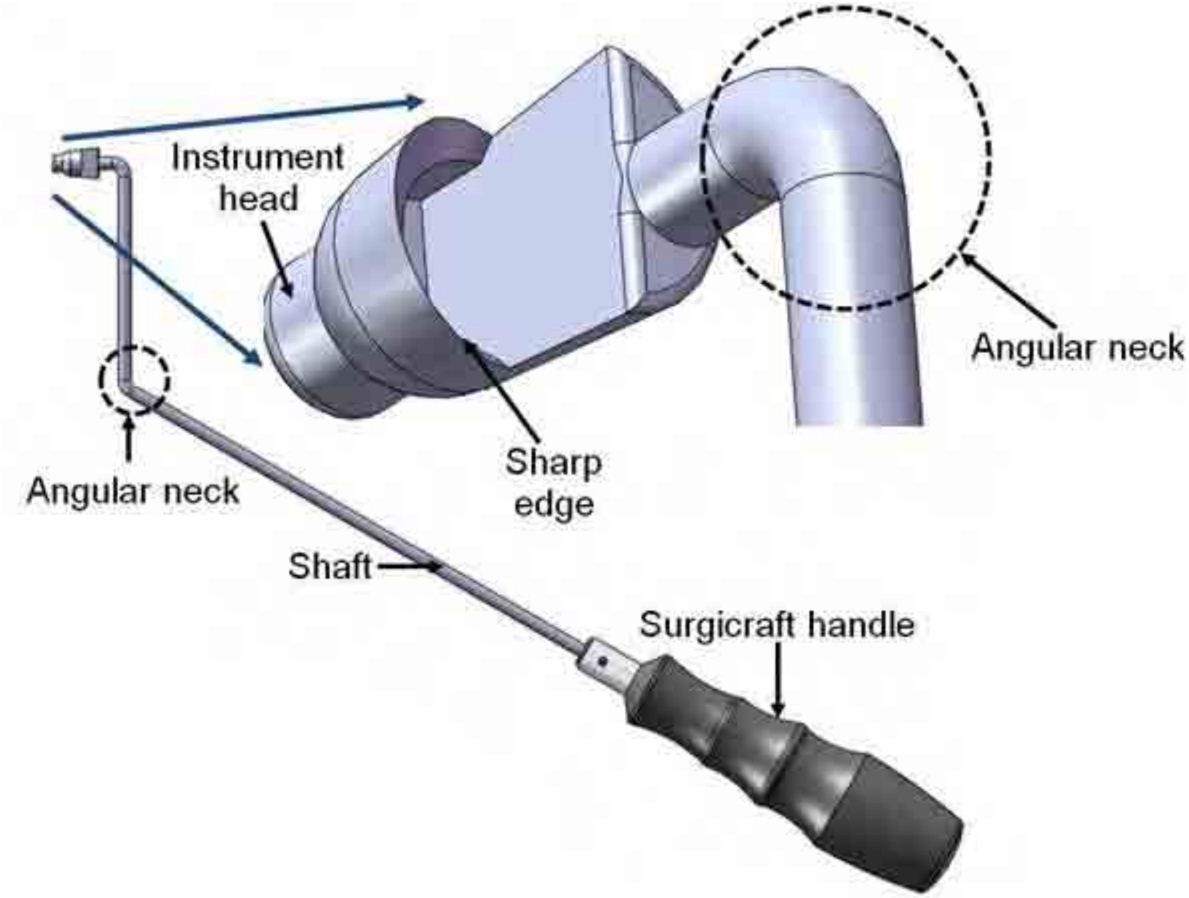

Figure 5. 9. The pull-up chisel and its features.

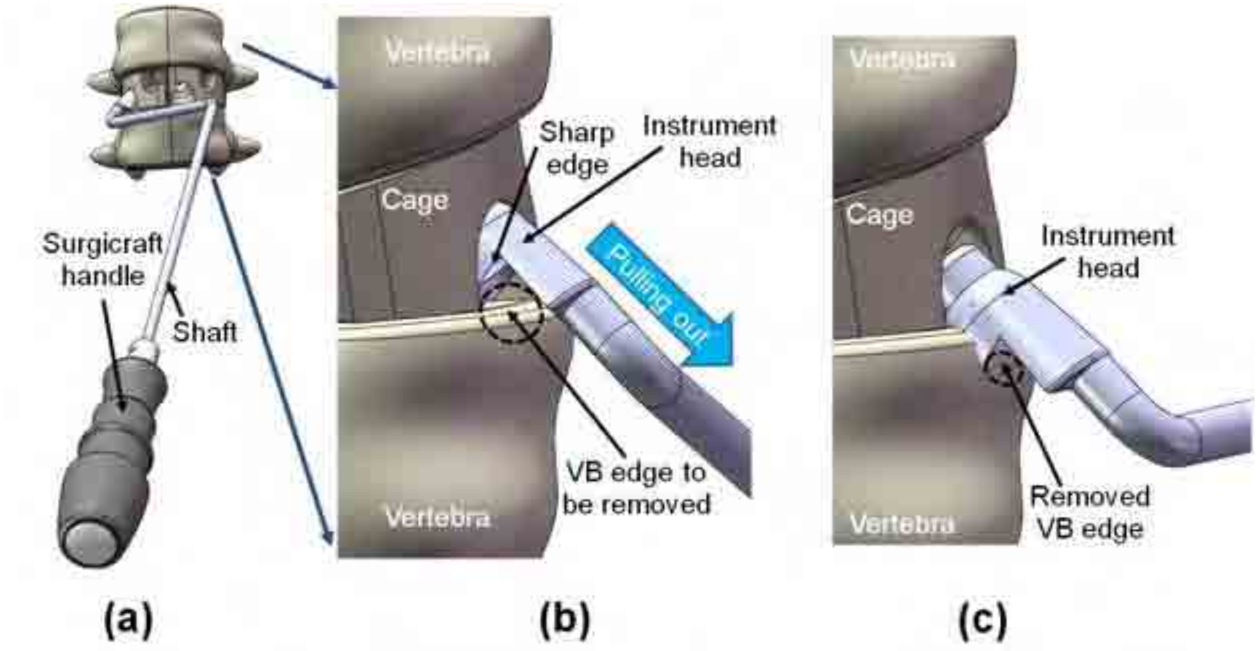

Figure 5. 10. Operation of the pull-up chisel. (a) and (b) The instrument head is placed in the screw hole, while its sharp edge is facing towards the targeted VB edge. The instrument cuts away the targeted VB edge whilst being pulled out (direction is shown by the blue arrow). (c) The targeted VB edge has been removed.

5.4.4.2. Concept analysis

The main advantage of the pull-up chisel concept is that it can be easy to use. However, the diameter of the sharp edge has to be small enough so the instrument head can be fitted into the partially blocked screw hole. This may result in a repeated pulling action to completely remove the targeted VB edge. The pull-up chisel may require a large space in which to function because of the angular neck (Figures 5.9 and 5.10). There is also a risk that it may cause trauma to the surrounding soft tissues when being pulled out.

5.4.5. Screw driver scoop (SDS)

5.4.5.1. Concept introduction

The SDS is a single part instrument that is assembled on the tip of the screw driver with a universal joint (Figure 5.4). Figure 5.11 shows the concept and its features. Figure 5.12 shows the operation of the concept (cutting away the VB edge). The SDS has a sharp edge on its cone-shaped head (Figure 5.11). The dimensions of the cone-shaped head correspond with those of the cage screw holes. The universal joint provides a flexible neck which allows the desired angle to be achieved in order to place the instrument head in the cage screw hole (Figure 5.12). The SDS cuts away the targeted VB edge by the rotation action applied to its handle (Figure 5.12). Protection for the cage is provided by the guide surface (Figure 5.12).

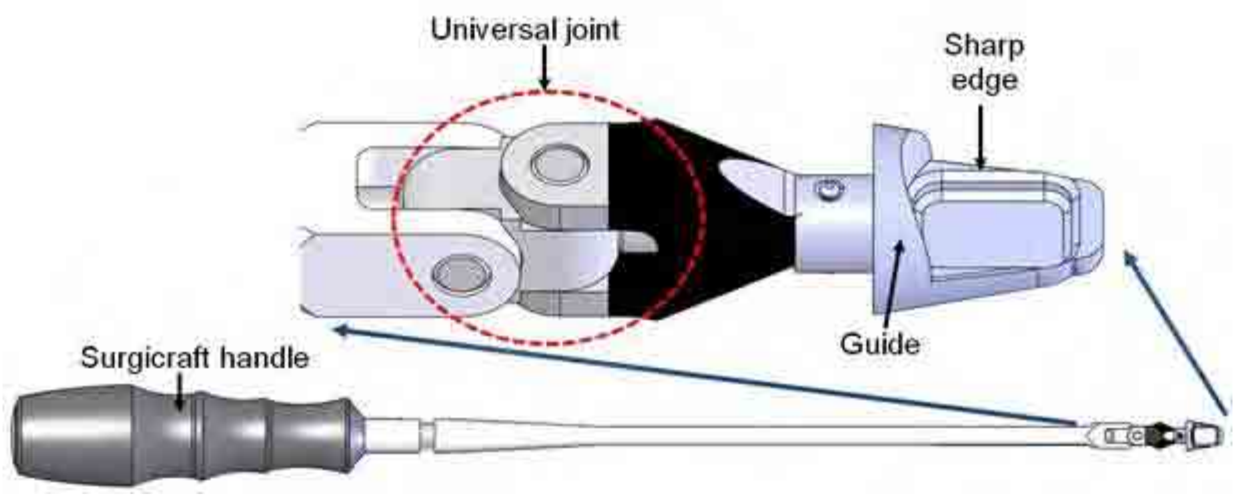

Figure 5. 11. The SDS and its features.

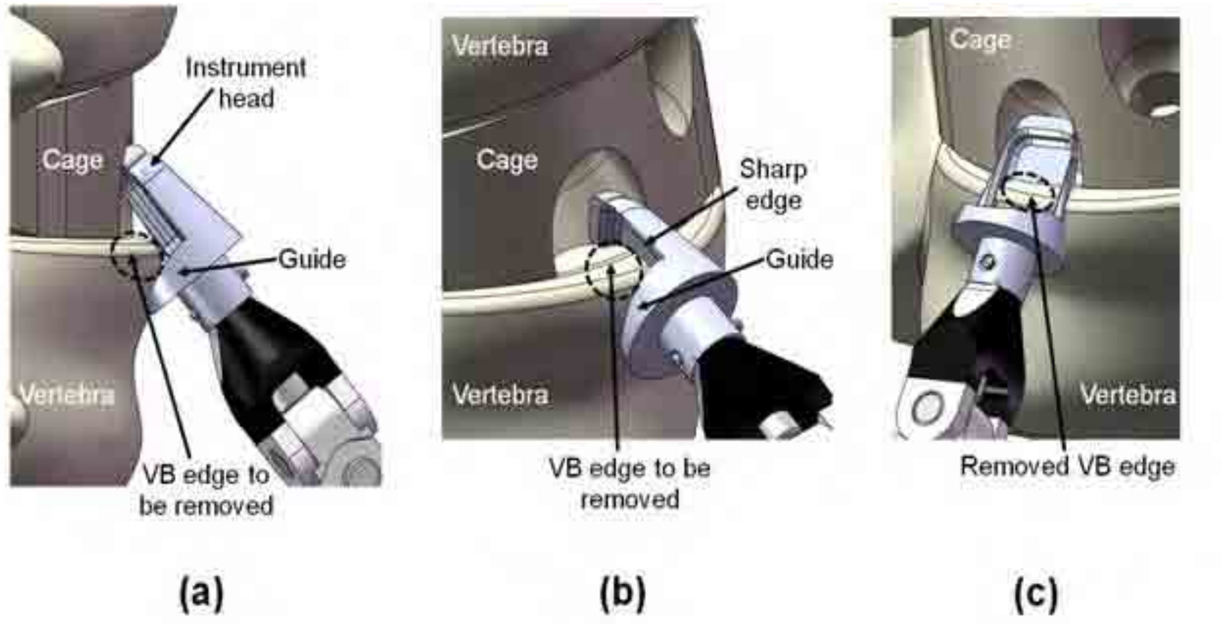

Figure 5. 12. Operation of the SDS. (a) The instrument head is placed in the screw hole, while its sharp edge is facing towards the targeted VB edge. (b) The instrument has to be rotated to cut away the target VB edge. The cage is being protected by the instrument head and the guide. (c) The targeted VB edge is removed once the rotation action applied to the handle is complete.

5.4.5.2. Concept analysis

The main advantages of the SDS concept are that it can be easy to use and it may remove the targeted VB edge in a single rotational action. However, damage to the fusion cage may occur because of the sharp edge on the instrument head.

5.4.6. Angular scoop

5.4.6.1. Concept introduction

The angular scoop is a single part instrument with a sharp edge on its cone-shaped head (Figure 5.13). Figure 5.13 shows the concept and its features. Figures 5.14 and 5.15 show the operation of the concept (cutting away the VB edge). The dimensions of the cone-shaped head correspond with those of the cage screw holes. The shaft of the instrument has an angular neck (Figure 5.13) which enables access to the side holes (with an awkward angle) and is attached to the Surgicraft Ltd. handle. The cage is protected by the guide surface (Figures 5.14 and 5.15).

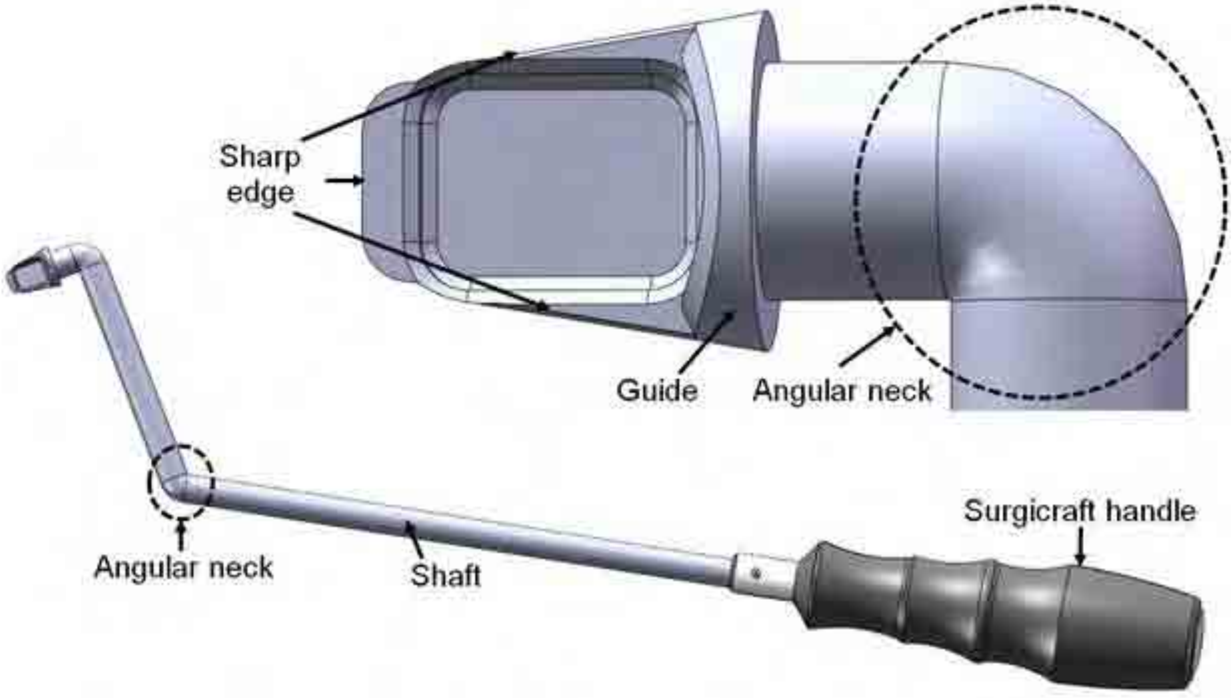

Figure 5. 13. The angular scoop and its features.

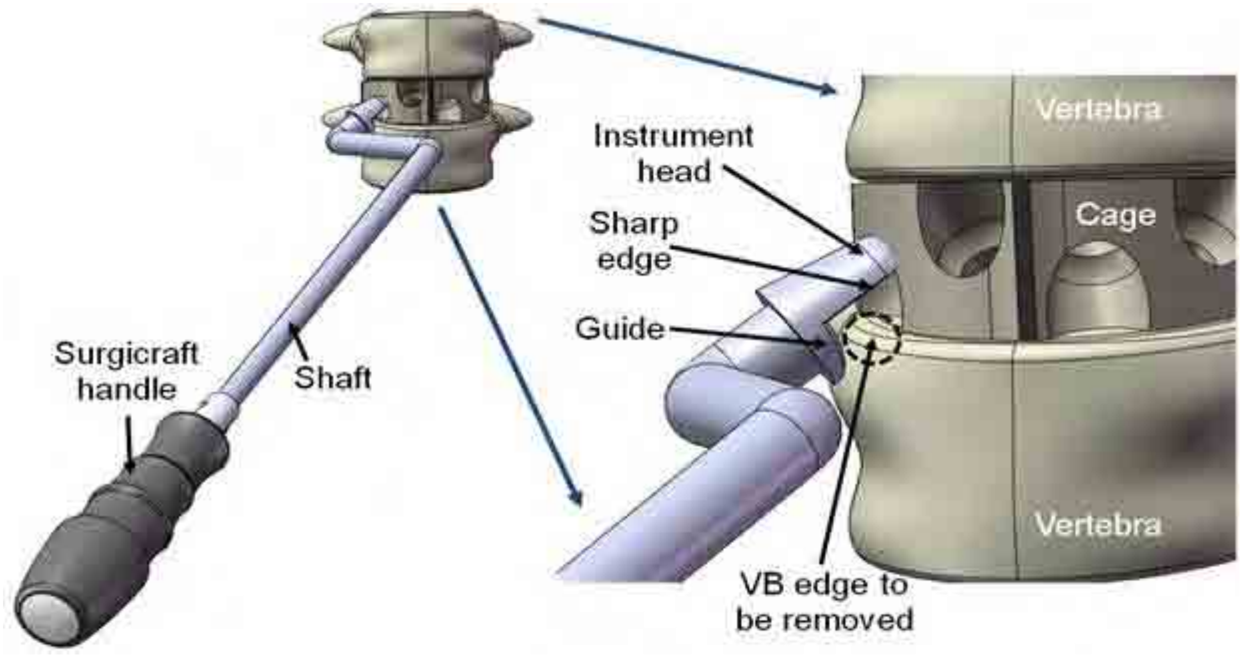

Figure 5. 14. Operation of the angular scoop. The instrument head is placed in the cage screw hole, while its sharp edge is facing towards the targeted VB edge.

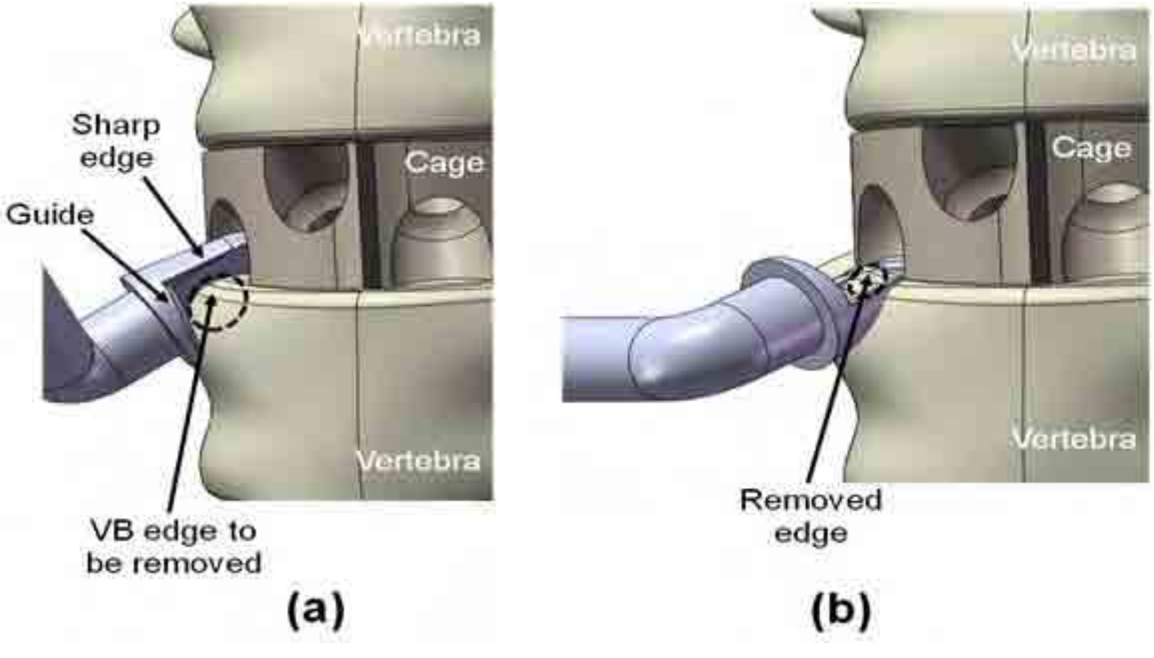

Figure 5. 15. Operation of the angular scoop. (a) The instrument has to be rotated to cut away the targeted VB edge. The cage is protected by the instrument head and the guide. (b) The targeted VB edge is removed once the rotation action applied to the handle is complete.

5.4.6.2. *Concept analysis*

The main advantages of the angular scoop concept are that it can be easy to use and it may remove the targeted VB edge in a single rotational action. However, damage to the cage may occur because of the sharp edge on the instrument head. Also, the angular scoop may require a large space in which to function because of its angular neck (Figures 5.13 and 5.14).

5.4.7. Angular bone file (ABF)

5.4.7.1. *Concept introduction*

The ABF consists of two parts: a static handle and a file handle. Figure 5.16 shows the concept and its features. Figure 5.17 shows the operation of the concept (cutting away the VB edge). The static handle forms the instrument head at one end and is attached to the Surgicraft Ltd. handle at the other end (Figure 5.16). The instrument head dimensions correspond with those of the cage screw holes. The guide is attached to the static handle. Both the static and file handles have angular necks (Figure 5.16) which enable access to the side holes (with an awkward angle). The file handle is the mobile part of the concept and has sharp teeth at its end (Figures 5.16 and 5.17).

5.4.7.2. *Concept analysis*

The main advantage of the ABF concept is that it is safe to use because there are no sharp teeth or edges on the instrument head. However, controlling the two long parts of the instrument during surgery may be difficult. Also, the ABF may require a large space in which to function (Figures 5.16 and 5.17).

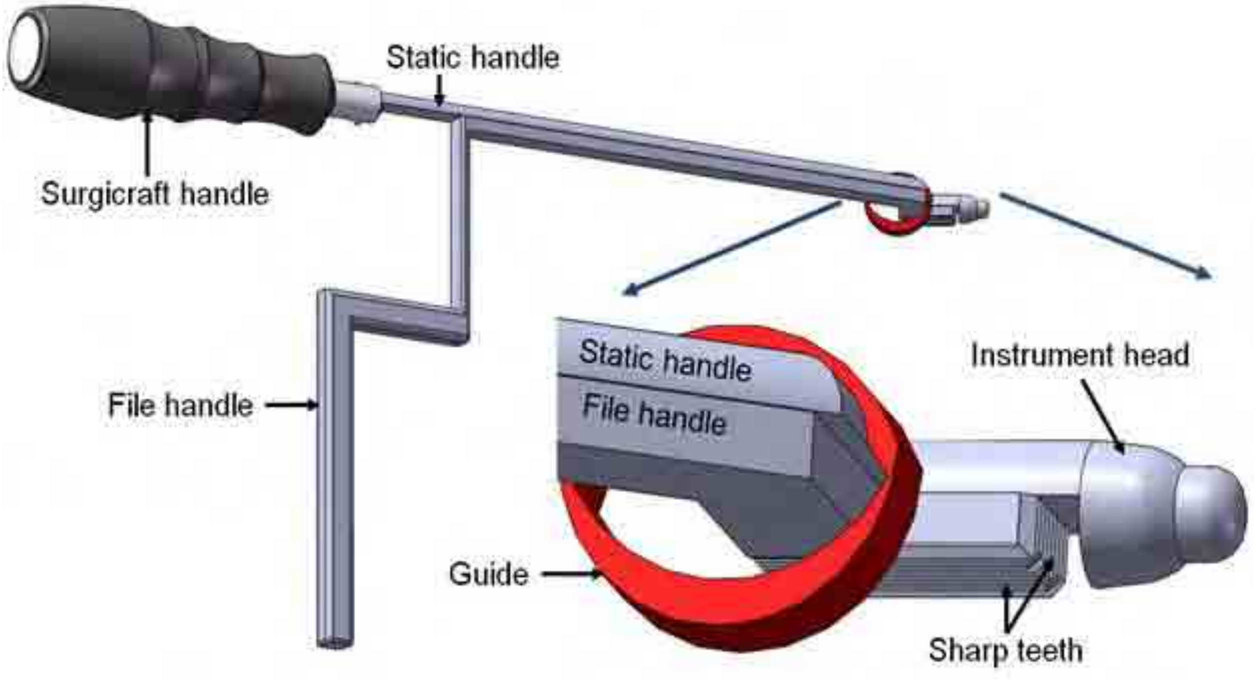

Figure 5. 16. The ABF and its features.

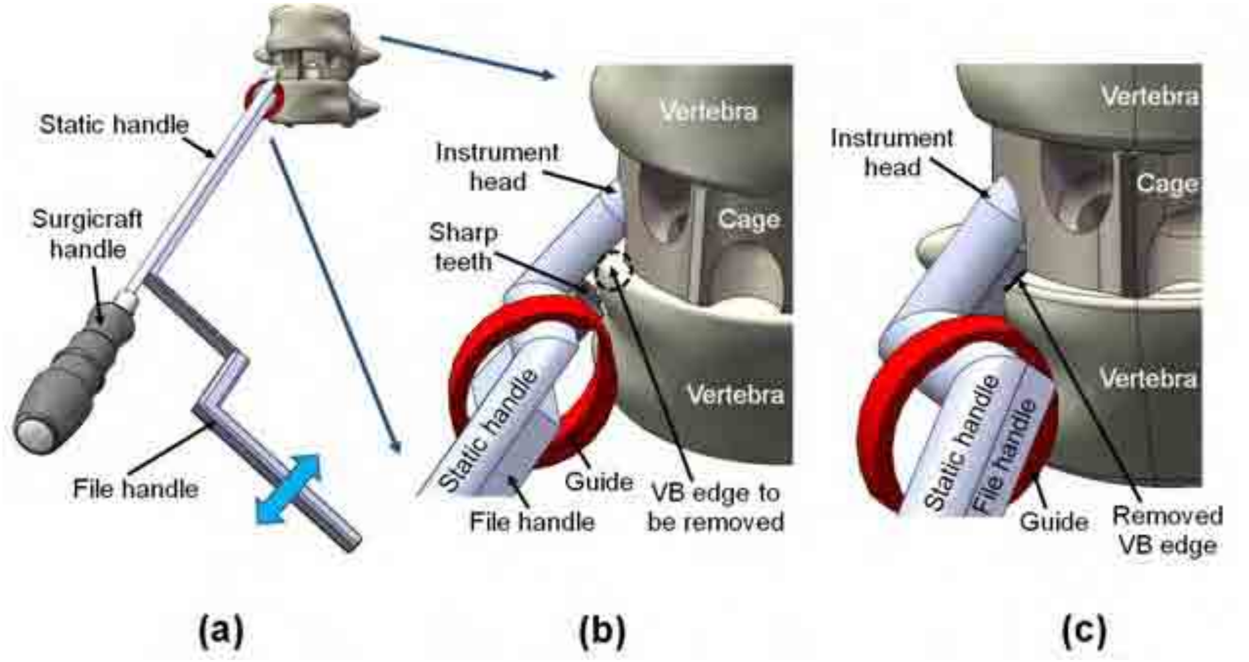

Figure 5. 17. Operation of the ABF. (a) and (b) The instrument head is placed in the cage screw hole and rests against the screw hole wall to provide an appropriate angle for the sharp teeth to remove the targeted VB edge. The instrument head holds the instrument in place (inside the screw hole) and prevents any undesired movements. The filing action (forwards and backwards action, shown by blue arrow) applied on the file handle would result in removal of the targeted VB edge. (c) The guide stops the file handle and the targeted VB edge has been removed.

5.4.8. T-handle rotating cutter (TRC)

5.4.8.1. Concept introduction

The TRC consists of two parts: a static handle and a T-handle. Figure 5.18 shows the concept and its features. Figures 5.19 and 5.20 show the operation of the concept (cutting away the VB edge). The static handle forms the instrument head at one end and is attached to the Surgicraft Ltd.

handle at the other end (Figure 5.18 a). The instrument head dimensions correspond with those of the cage screw holes. The T-handle has sharp teeth at its end (Figure 5.18). In order to remove the targeted VB edge, semi-circular actions have to be applied to the T-handle which results in rotation of the teeth (shown by blue arrows in Figures 5.18 and 5.19).

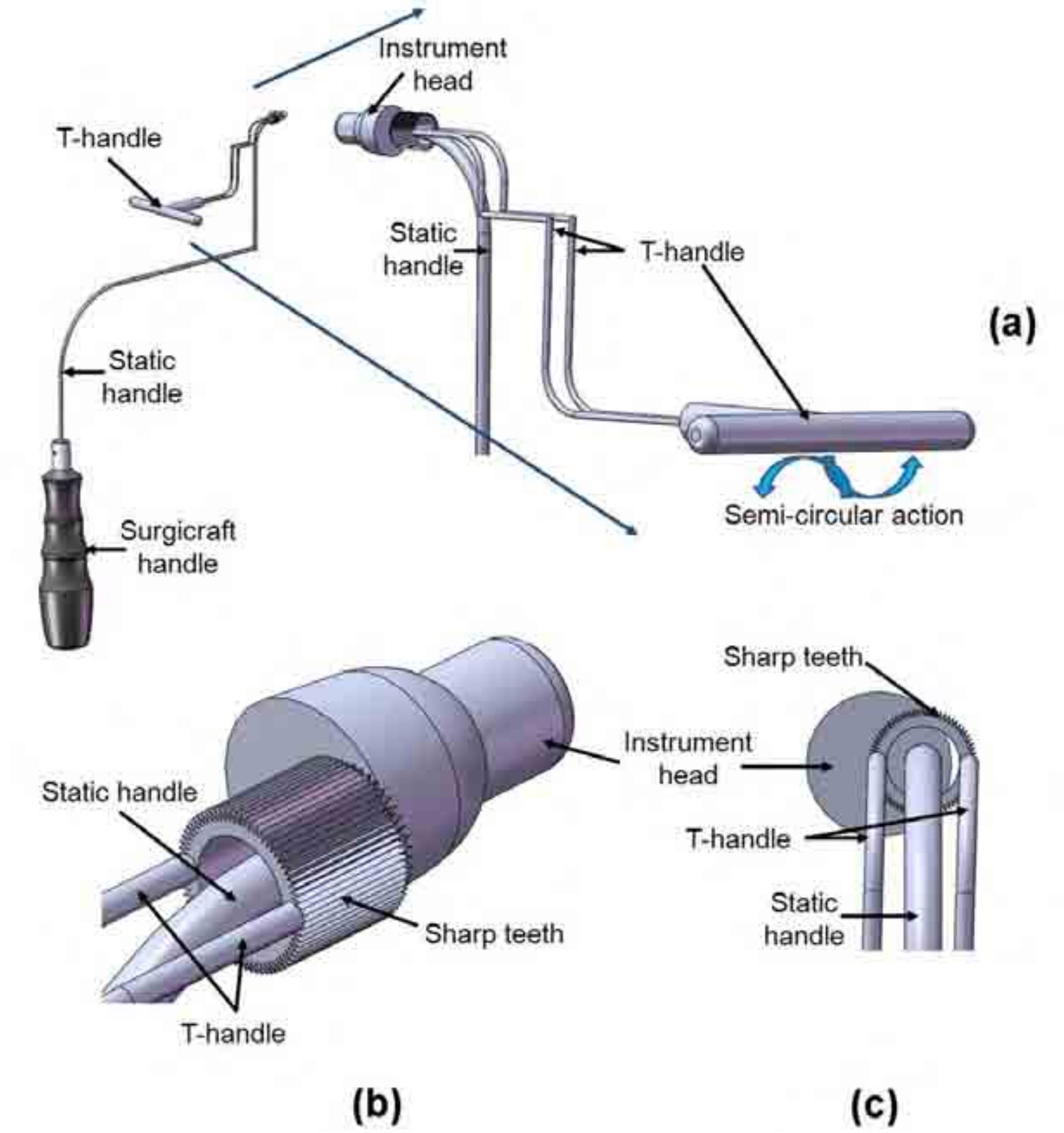

Figure 5. 18. The TRC and its features. (a) Three-dimensional view of the TRC, (b) side view of the instrument head and teeth and (c) back view of the instrument head and teeth.

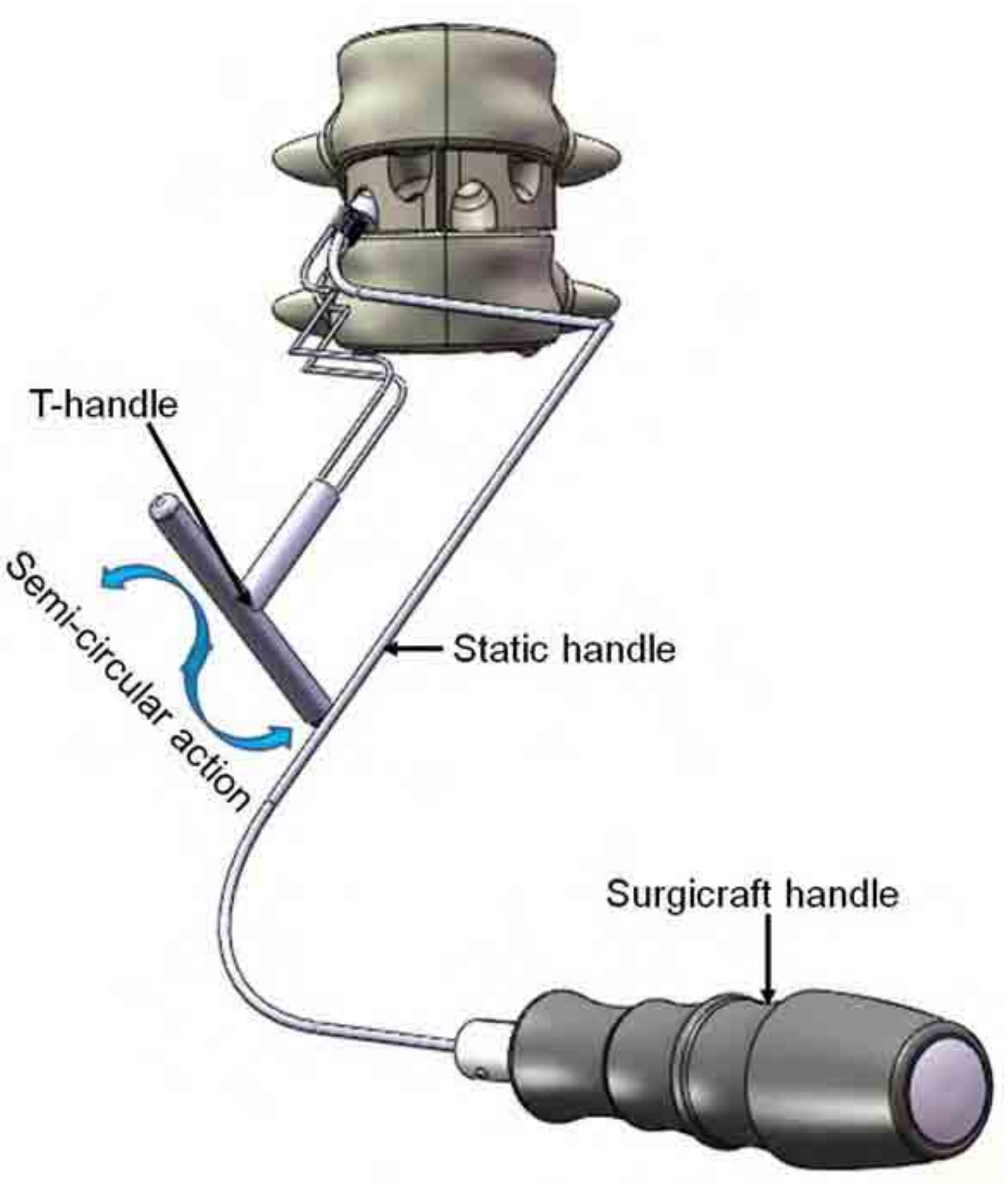

Figure 5. 19. Operation of the TRC. The instrument head is placed in the cage screw hole and rests against the screw hole wall to provide an appropriate angle for the sharp teeth to remove the targeted VB edge. The instrument head holds the instrument in place (inside the screw hole) and prevents any undesired movements of the instrument. The teeth cut away the targeted VB edge by the semi-circular actions applied to the T-handle (blue arrows).

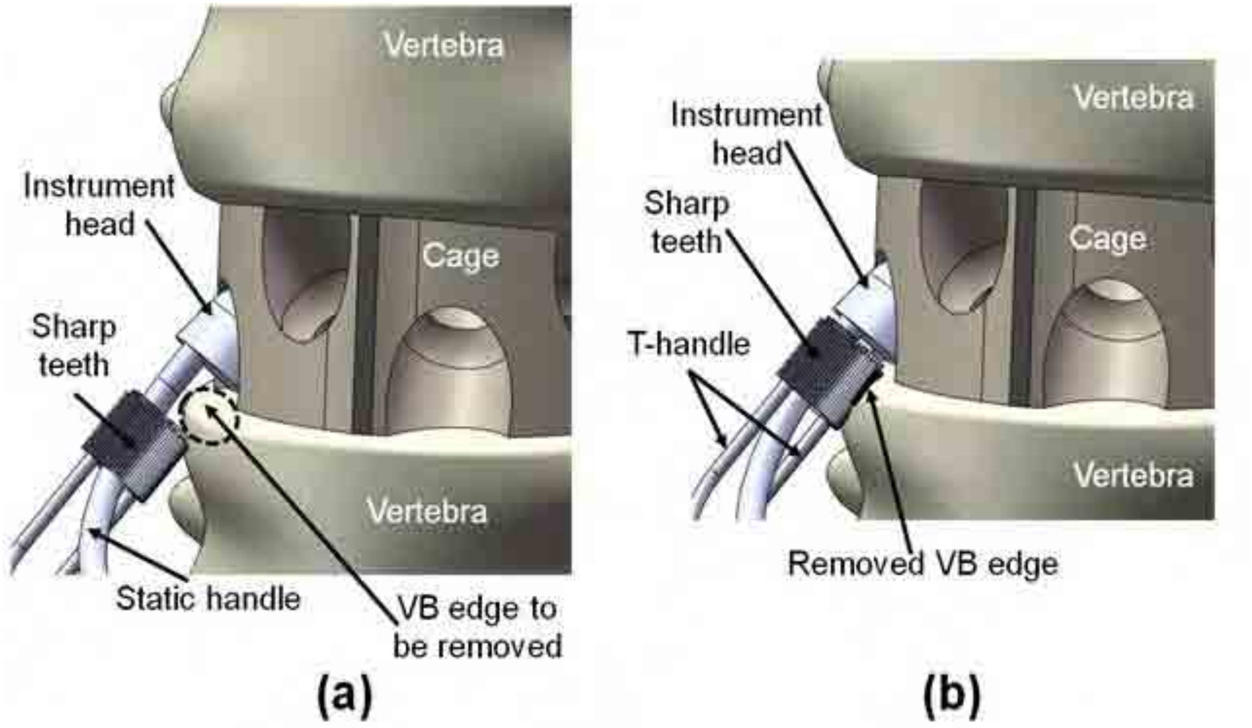

Figure 5. 20. Operation of the TRC. (a) Side view of the instrument head being placed in the screw hole. Whilst semi-circular actions are applied to the T-handle (Figure 5.19), the targeted VB edge is being removed by the sharp teeth. (b) The targeted VB edge has been removed.

5.4.8.2. Concept analysis

The main advantage of the TCR concept is that it is safe to use because there are no sharp teeth or edges on the instrument head. However, controlling the two long parts of the instrument during surgery may be difficult. Also, the TCR may require a large space in which to function (Figures 5.18 and 5.19).

5.4.9. Angular rotating cutter (ARC)

5.4.9.1. Concept introduction

The ARC consists of three parts: an instrument head, sharp teeth and a handle. Figure 5.21 shows the concept and its features. Figure 5.22 shows the operation of the concept (cutting away the VB edge). The instrument head dimensions correspond with those of the cage screw holes. The teeth are attached to the shaft of the handle (Figure 5.21). The end of the shaft is inserted in to the free space within the instrument head (Figure 5.21 b). The shaft has an angular neck (Figure 5.21 a) which enables access to the side holes (with an awkward angle).

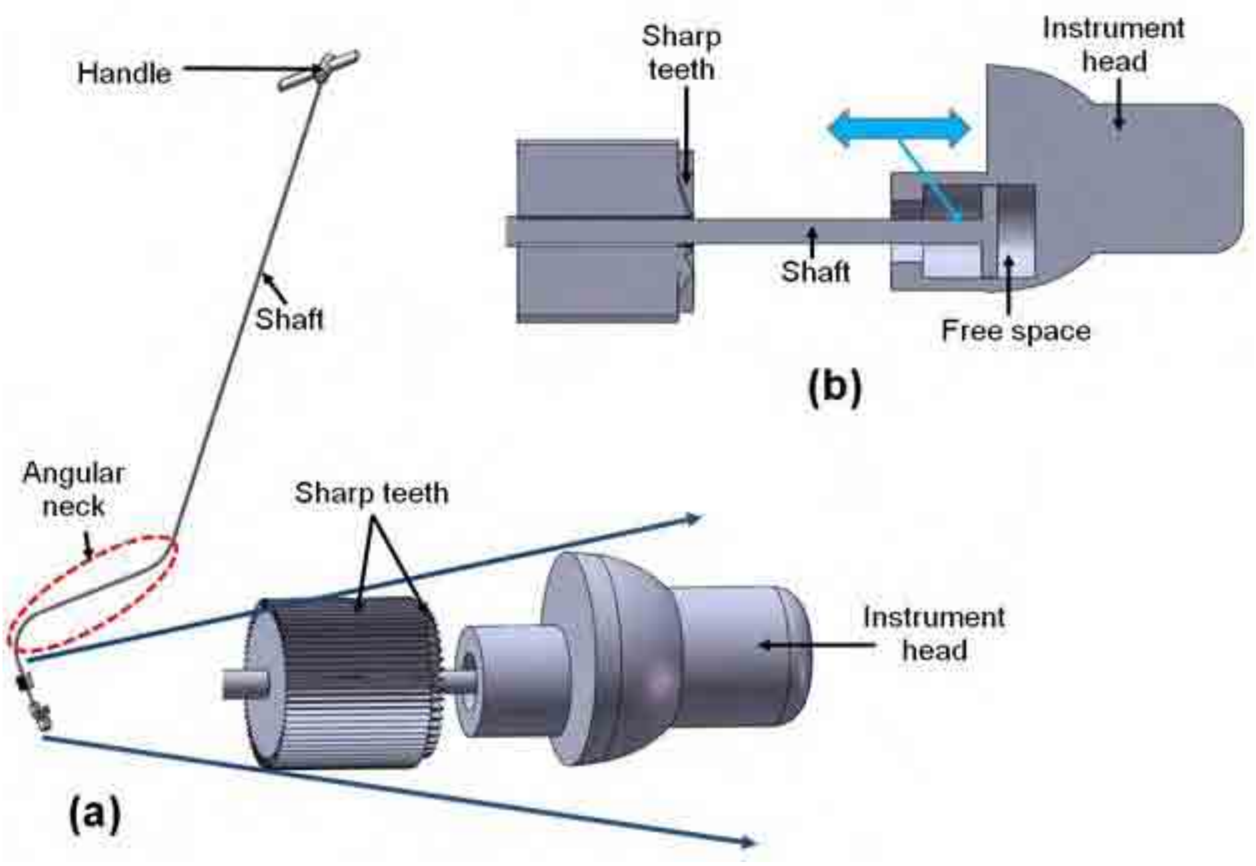

Figure 5. 21. The ARC and its features.

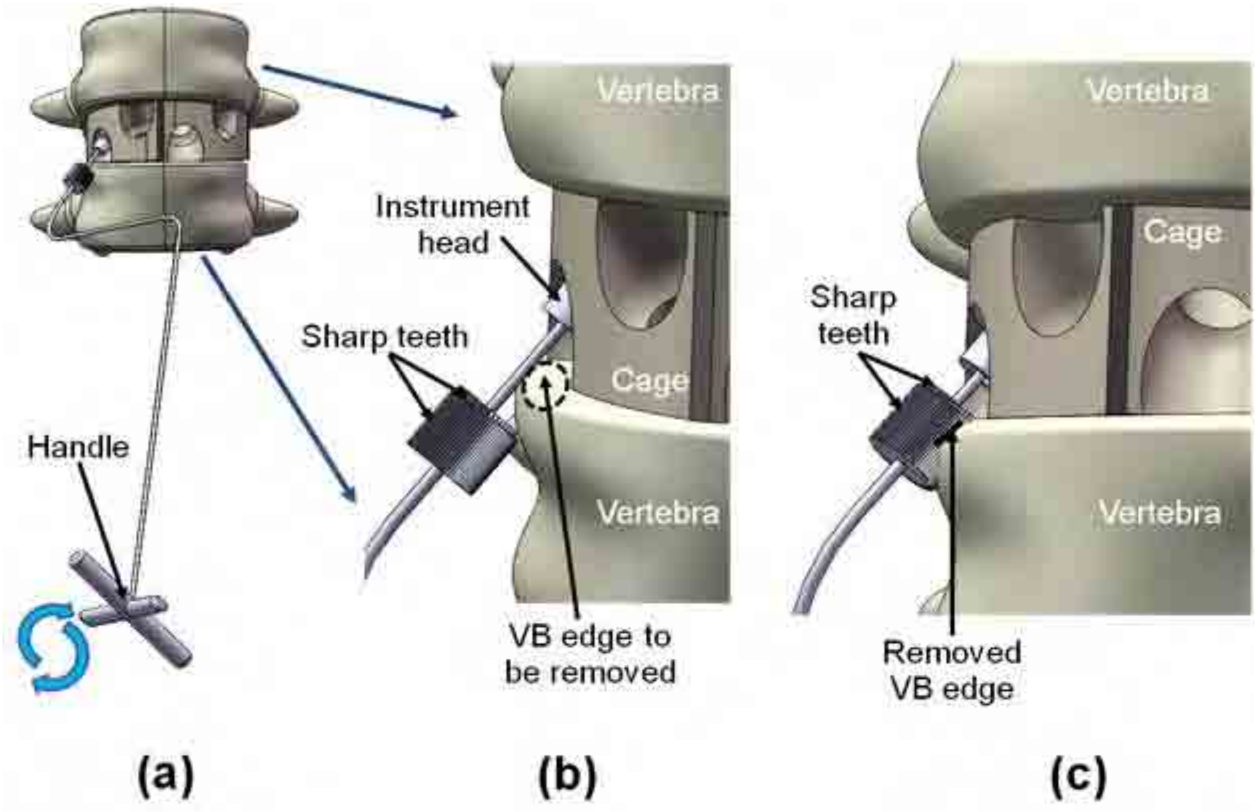

Figure 5. 22. Operation of the ARC. (a) and (b) The instrument head is placed in the screw hole and rests against the screw hole wall to provide an appropriate angle for the sharp teeth to remove the targeted VB edge. The instrument head holds the instrument in place (inside the screw hole) and prevents any undesired movements of the instrument. (b) The handle has to be pushed down whilst rotating (blue arrows) to allow the teeth to remove the targeted VB edge by their rotating action. This is possible due to the free space within the instrument head, since this space is limited, it also prevents the teeth from damaging the cage (Figure 5.21 b). (c) The targeted VB edge has been removed.

5.4.9.2. Concept analysis

The main advantage of the ARC concept is that it is safe to use because there are no sharp teeth or edges on the instrument head. However, the ARC may require a large space in which to function (Figures 5.21 and 5.22).

5.4.10.Rotating shaver

5.4.10.1. Concept introduction

The rotating shaver is a single part instrument. Figure 5.23 shows the concept and its features. Figure 5.24 shows the operation of the concept (cutting away the VB edge). Its shaft has an angular neck (Figure 5.23) which enables access to the side holes (with an awkward angle). The shaft forms a cylindrical-shaped end which continues to be the instrument head (Figure 5.23). The cylindrical-shaped end also forms the sharp teeth (Figure 5.23). The rotating shaver removes the targeted VB edge when the component with the teeth rotates. This rotation is applied by the semi-circular actions via the T-handle (shown by blue arrows, Figures 5.23 and 5.24). The instrument head dimensions correspond with those of the cage screw holes.

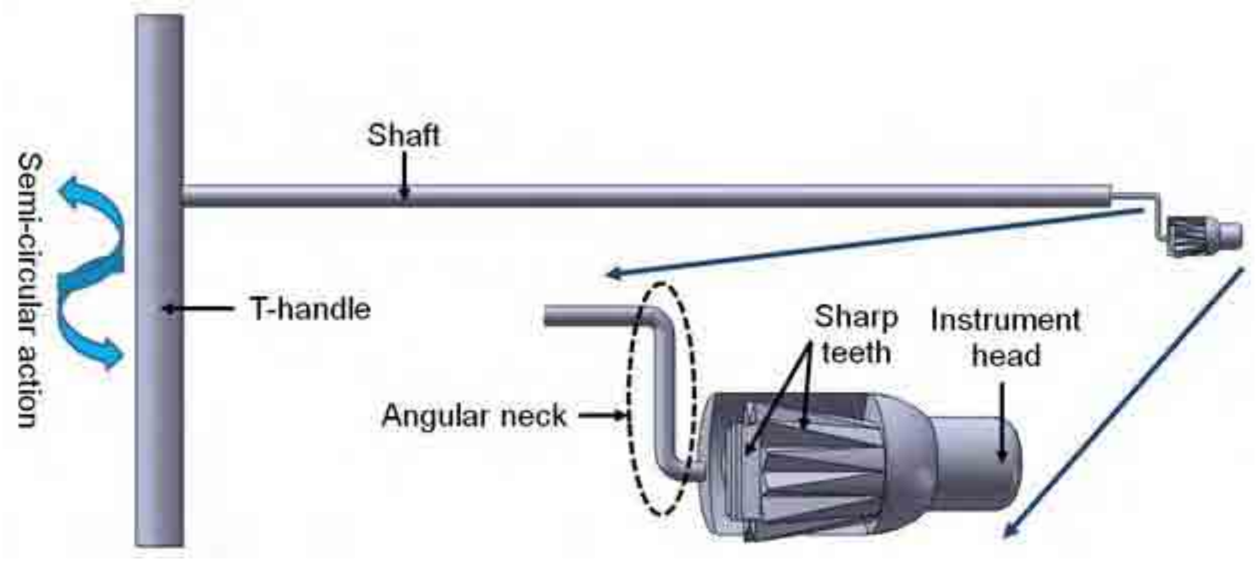

Figure 5. 23. The rotating shaver and its features.

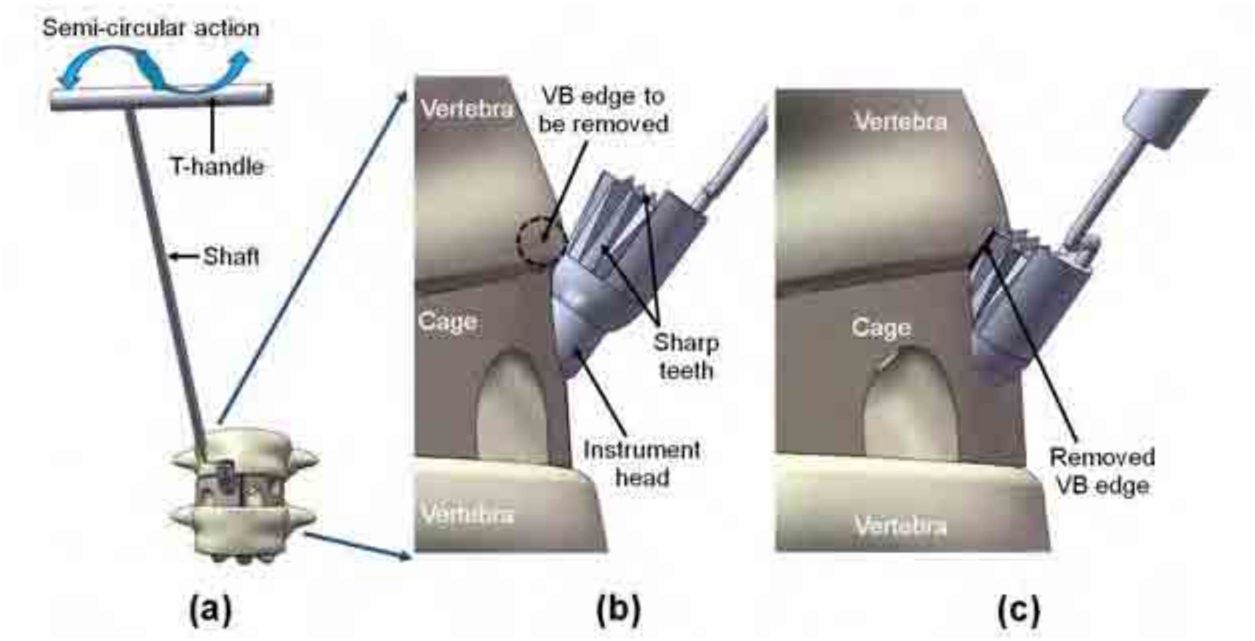

Figure 5. 24. Operation of the rotating shaver. (a) and (b) The instrument head is placed in the screw hole and rests against the screw hole wall to provide an appropriate angle for the sharp teeth to remove the targeted VB edge. The instrument head holds the instrument in place (inside the screw hole) and prevents any undesired movements of the instrument. (b) The semi-circular actions applied to the T-handle (blue arrows) rotate the sharp teeth resulting in the removal of the targeted VB edge. (c) The instrument head is completely inside the screw hole and the targeted VB edge has been removed.

5.4.10.2. Concept analysis

The main advantage of the rotating shaver concept is that it is easy to use. However, the sharp teeth on the instrument head may cause damage to the cage (Figure 5.23).

5.4.11.Screw threaded concept (STC)

5.4.11.1. Concept introduction

The STC is assembled on the tip of the screw driver with a universal joint (Figure 5.4) and consists of two parts: an instrument head and a cutter. Figure 5.25 shows the concept and its features. Figure 5.26 shows the operation of the concept (cutting away the VB edge). The universal joint provides a flexible neck which allows the desired angle to be achieved in order to place the instrument head in the cage screw hole. The instrument head dimensions correspond with those of the cage screw holes. There are sharp teeth on the cutter (Figure 5.25 a), which remove the targeted VB edge when rotation action is applied to the universal joint handle (Figure 5.26). The cutter has a shaft with a threaded end which screws into the threaded hole of the instrument head (Figure 5.25 b).

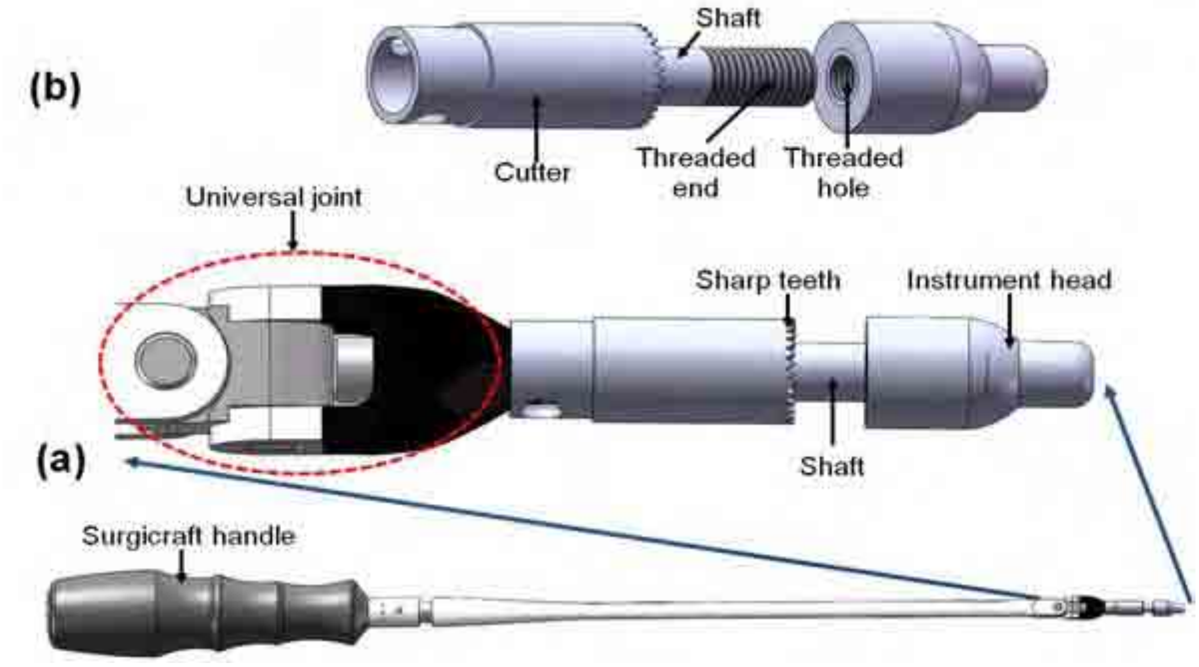

Figure 5. 25. The STC and its features. (a) Side view of the STC concept. (b) Exploded view of the STC concept.

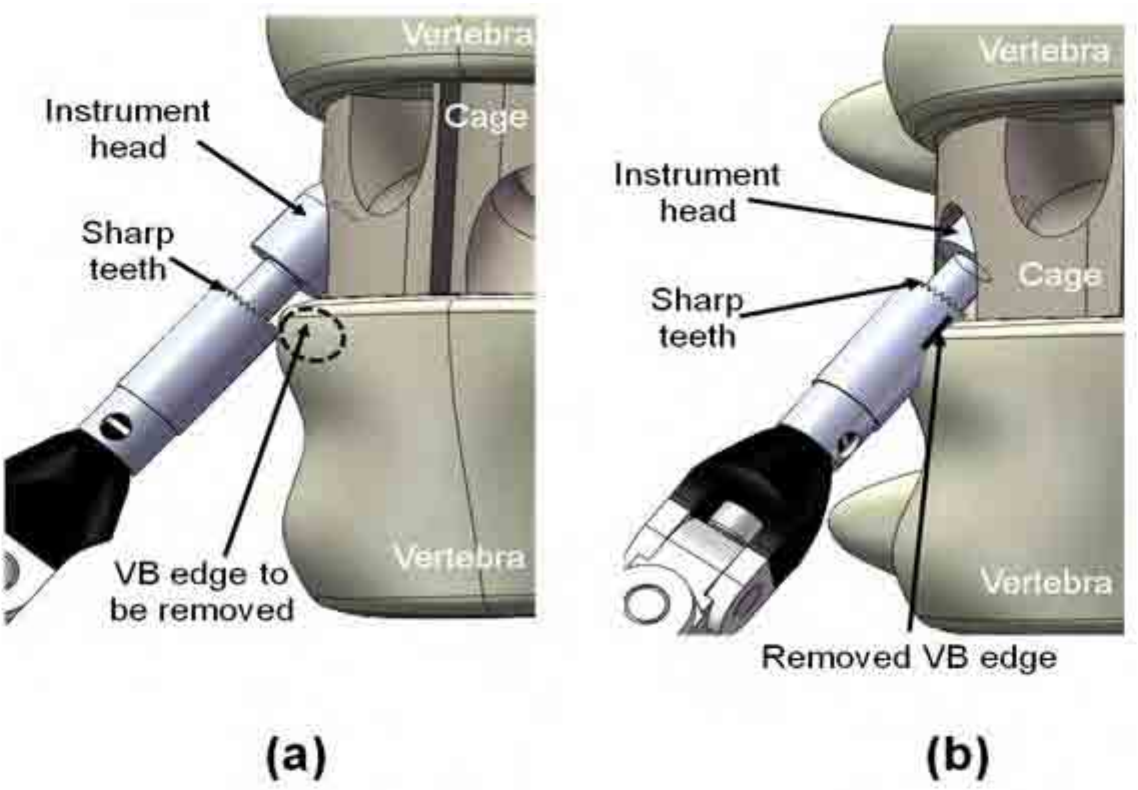

Figure 5. 26. Operation of the STC. (a) The instrument head is placed in the screw hole and rests against the screw hole wall to provide an appropriate angle for the sharp teeth to remove the targeted VB edge. The instrument head holds the instrument in place (inside the screw hole) and prevents any undesired movements of the instrument. (b) The targeted VB edge is removed by the rotation action applied to the universal joint handle which rotates the sharp teeth. (c) The instrument head is completely inside the screw hole and the targeted VB edge has been removed.

5.4.11.2. Concept analysis

The main advantages of the STC concept are that it is safe to use because there are no sharp teeth or edges on the instrument head and it may be easy to use. However, the assembly method is not safe as the STC instrument head may become unscrewed.

5.4.12. Universal burr

5.4.12.1. Concept introduction

The universal burr is assembled on the tip of the screw driver with a universal joint (Figure 5.4) and consists of one part: sharp teeth with an instrument head at their end (Figure 5.27). Figure 5.27 shows the concept and its features. Figure 5.28 shows the operation of the concept (cutting away the VB edge). The universal joint provides a flexible neck which allows the desired angle to be achieved in order to place the instrument head in the cage screw hole. The instrument head dimensions correspond with those of the cage screw holes. The sharp teeth remove the targeted VB edge when rotation action is applied to the universal joint handle (Figure 5.28).

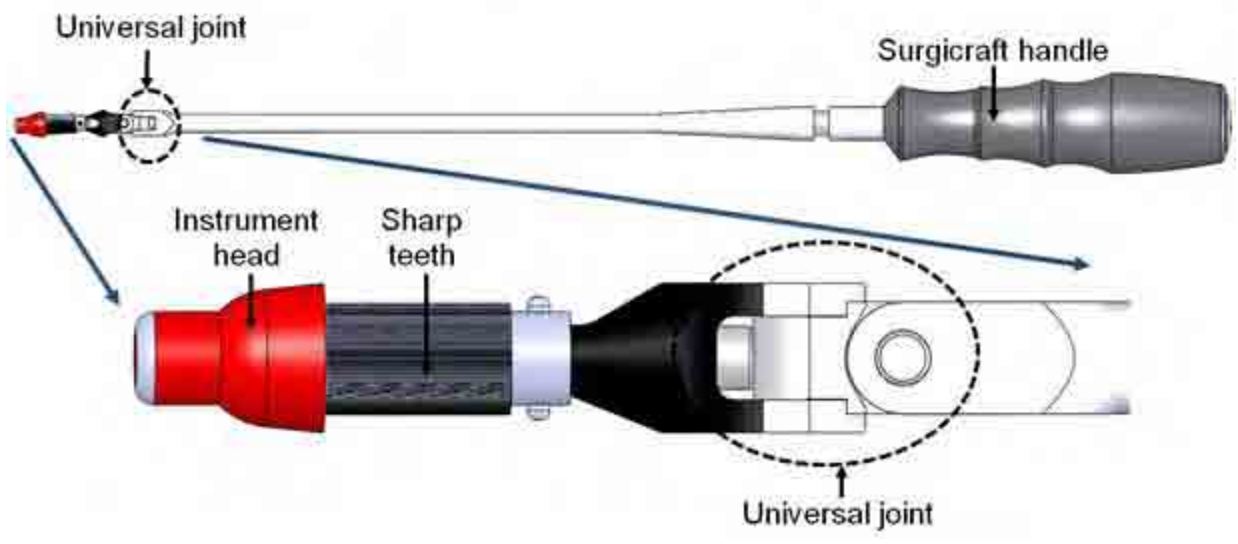

Figure 5. 27. The universal burr and its features.

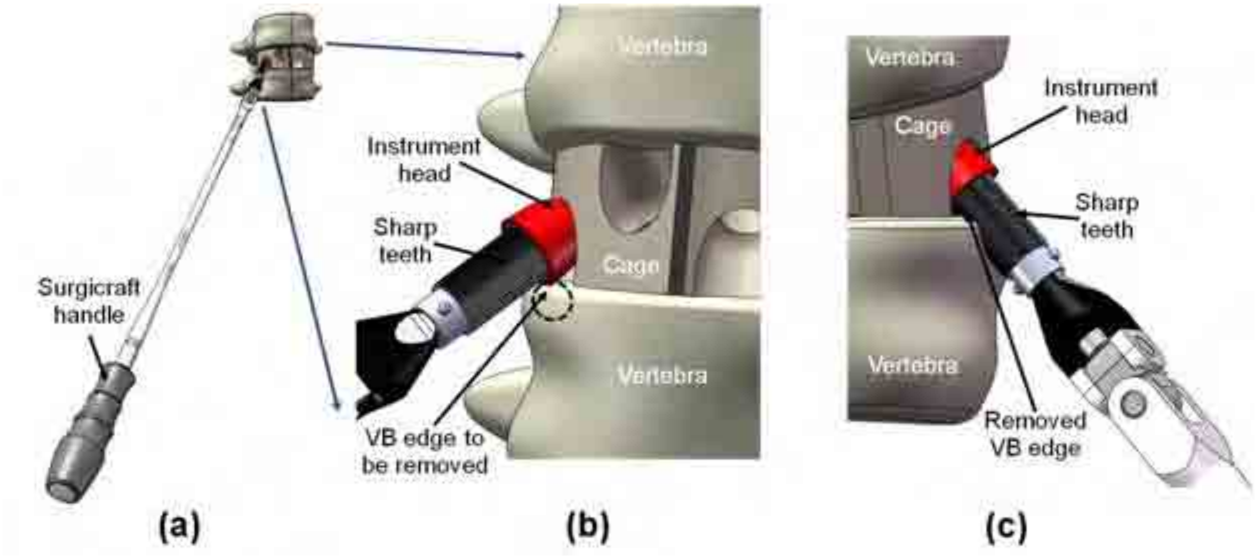

Figure 5. 28. Operation of the universal burr. (a) and (b) The instrument head is placed in the screw hole and rests against the screw hole wall to provide an appropriate angle for the sharp teeth to remove the targeted VB edge. The instrument head holds the instrument in place (inside the screw hole) and prevents any undesired movements of the instrument. (b) The targeted VB edge is removed by the rotation action applied to the universal joint handle which rotates the sharp teeth. (c) The instrument head is completely inside the screw hole and the targeted VB edge has been removed.

5.4.12.2. Concept analysis

The main advantage of the universal burr concept is that it is easy to use. However the sharp teeth, which are very close to the instrument head, may damage the cage (Figures 5.27 and 5.28).

5.5. Secondary concepts

5.5.1. Introduction

After analysing the initial concepts in detail (discussed in each sub-section of §5.4), it was decided that a concept with a universal joint would be more suitable for a minimally invasive surgery. This is because it requires less space in which to operate and promotes better visibility of the operative site for the surgeon. Also, access to the side holes with an awkward angle is made possible by the continuous 360° clockwise and anti-clockwise motions of the universal joint. Additionally, the concept should have a minimum required number of teeth or sharp edges to prevent trauma (as much as possible) whilst being inserted or taken out of the wound. The initial concept analyses also showed that there is a need for a guide in order to position the instrument correctly within the screw hole as well as to fully protect the cage. The instrument head in all the subsequent concepts acts as this guide. The instrument head dimensions need to correspond with those of the cage screw holes. The diameter of the screw holes for the cages with widths of 36 and 39 mm is 5.6 mm and for the cages with widths of 42 and 45 mm is 6.6 mm (Figure 5.29). Note, STALIF^{TM} TT cages with widths of 36 and 39 mm are more commonly in use than the other two cages (personal communication, Mr A. J. Fennell, International Marketing Director, Surgicraft Ltd., Redditch, UK). The diameter of the instrument head was taken to be 5.55 mm in all the subsequent concepts. The clearances (0.05 mm for the 36 and 39 mm cage widths and 1.05 mm for the 42 and 45 mm cage widths) between the diameters of the screw holes and that of the instrument head allow free rotation of the instrument. Furthermore, the concept had to be designed so that it would make full use of the available inner space of the instrument (e.g. similar to the instrument head of the ARC initial concept, §5.4.9 and Figure 5.21). This may aid in meeting the requirements of minimally invasive surgery.

These points were taken into consideration, modifications were carried out accordingly and three secondary concepts were produced: the split ring cutter, the screw threaded cutter and the spring cutter (Figures 5.30 to 5.32). All of these concepts were compatible with the Surgicraft Ltd. screw driver (with a universal joint, Figure 5.4) and were to be assembled on its tip. Hence, for simplification, only the instrument cutter concepts are shown in the figures.

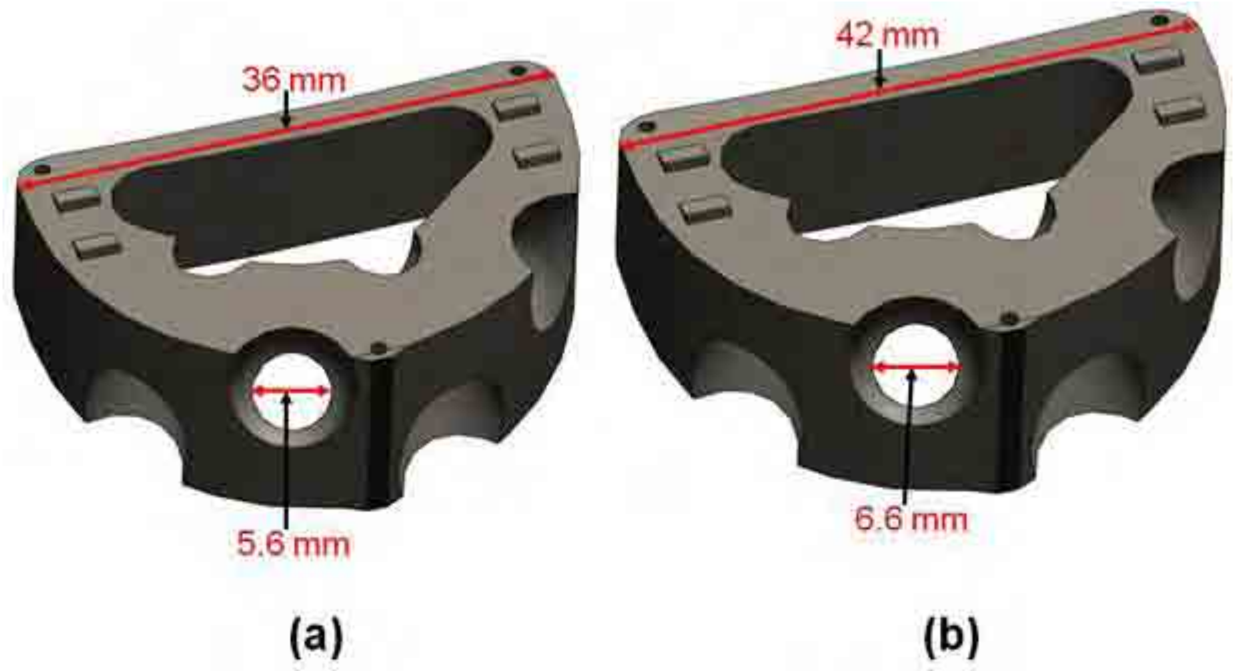

Figure 5. 29. STALIF^{TM} TT cages (Surgicraft Ltd.). (a) Screw hole diameter for the cages with widths of 36 and 39 mm. (b) Screw hole diameter for the cages with widths of 42 and 45 mm.

There are common features in all three secondary concepts: parts A and B. Part A consists of an instrument head and a shaft (Figures 5.30 to 5.32). The instrument head in all three secondary concepts acts as the guide and may aid in fully protecting the cage. The instrument head sits in the cage screw hole and holds the instrument in place. This ensures that the instrument can only follow the desired direction along its centre-line. The shaft is a rod connected to the instrument head which allows part A to be attached to part B by inserting it into the bone cutter (Figures 5.30 to 5.32).

Part B is the bone cutter for each of the secondary concepts. It is a hollow cylinder that consists of sharp teeth and an attachment neck (Figures 5.30 to 5.32). The sharp teeth are at one end of part B. When the instrument head is placed within the cage screw hole the sharp teeth cut away the targeted VB edge (explained in detail in §5.5.2 to §5.5.5 and shown in Figures 5.33 and 5.34). The attachment neck is at the other end of part B opposite to the sharp teeth. It joins the instrument to the screw driver with the universal joint. The attachment neck has a hexagonal cross-section and has the same dimensions as the screw driver tip. There is a ring belt inside part B next to the sharp teeth. This is a common feature between the split ring cutter and the screw threaded cutter (Figures 5.30 and 5.31). It eliminates disassembly of parts A and B.

5.5.2. Split ring cutter

5.5.2.1. Concept introduction

The split ring cutter consists of three parts: part A, part B and a split ring (Figure 5.30). A groove has been made at the end of the shaft to allow the placement of the split ring which, when compressed, fits the diameter of the shaft (Figure 5.30 d). When the shaft is inserted into part B, the split ring recoils to its original diameter. The diameter of the ring belt on part B is smaller than that of the split ring which eliminates separation of the two parts (Figure 5.30 b). Once the instrument head is placed within the cage screw hole (Figure 5.33), the targeted VB edge is removed by the sharp teeth when part B is pushed down whilst rotating the handle (Figure 5.34). The axial movement of the shaft is possible because of the free space in part B (Figures 5.30 b and c).

5.5.2.2. Concept analysis

The main advantages of the split ring cutter concept is that it is safe to use because there are no sharp teeth or edges on the instrument head and it appears to be easy to use. However, the assembly of the concept can be difficult and time consuming. The instrument may easily become detached and be difficult to completely clean as bone debris and other soft tissues can become stuck in the groove of the shaft. If this concept were to become the final design the following modifications would have to be carried out:

- the instrument head has to be modified to allow its insertion into the partially blocked screw hole;
- the design of the instrument attachment neck has to be modified so it forms a universal joint with the Surgicraft Ltd. universal joint handle (Figure 5.3);
- the number of teeth needs to be justified and tested.

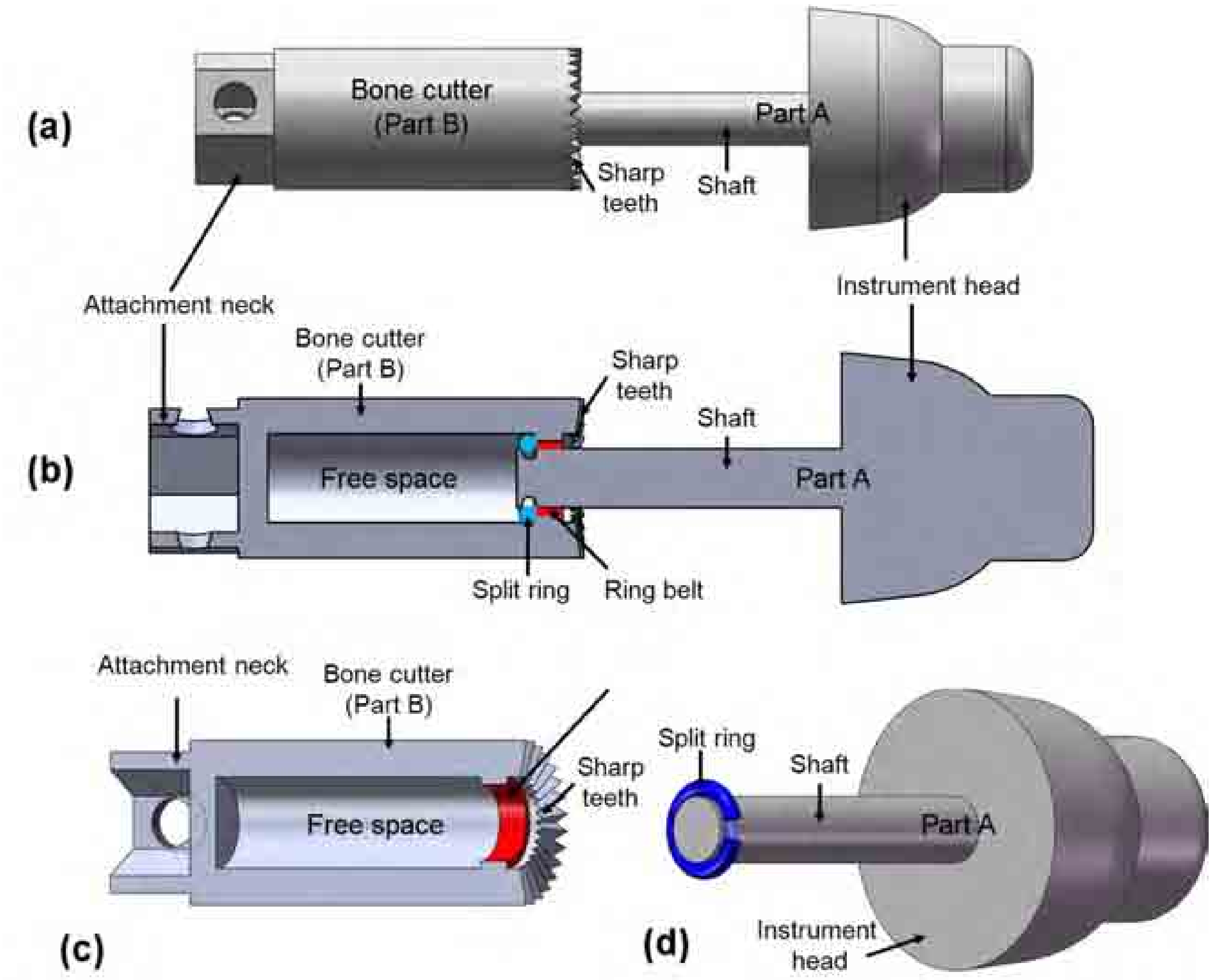

Figure 5. 30. (a) The split ring cutter concept. (b) The cross-section of the concept. Once the shaft is inserted into the bone cutter and the split ring recoils to its original diameter, the separation of the two parts is eliminated because of the diameter of the ring belt (the diameter of the split ring is greater than that of the ring belt). (c) The cross-section of the bone cutter. (d) The split ring on the groove at the end of the shaft of part A.

5.5.3. Screw threaded cutter

5.5.3.1. Concept introduction

The screw threaded cutter consists of three parts: part A, part B and a screw (Figure 5.31). In this concept the shaft has a screw thread at its end (Figure 5.31 d). The instrument is assembled such that the shaft is inserted into part B (Figure 5.31 b). A screw is then inserted into the shaft (Figure 5.31 b). The head of the screw has a greater diameter than that of the ring belt which eliminates separation of the two parts (Figure 5.31 b). Once the instrument head is seated within the cage screw hole (Figure 5.33), the sharp teeth can then remove the targeted VB edge when part B is pushed down whilst rotating the handle (Figure 5.34). The axial movement of the shaft is possible because of the free space in part B (Figures 5.31 b and c).

5.5.3.2. Concept analysis

The main advantages of the screw threaded cutter concept is that it is safe to use because there are no sharp teeth or edges on the instrument head and it appears to be easy to use. However, the assembly of the concept can be difficult. Also, the screw may become loose and parts A and B may detach. In addition, complete cleaning of the instrument may be difficult to achieve as bone debris and other soft tissues can become stuck around the screw. If this concept were to become the final design the following modifications would have to be carried out:

- the instrument head has to be modified to allow its insertion into the partially blocked screw hole;

- the design of the instrument attachment neck has to be modified so it forms a universal joint with the Surgicraft Ltd. universal joint handle (Figure 5.3);
- the number of teeth needs to be justified and tested.

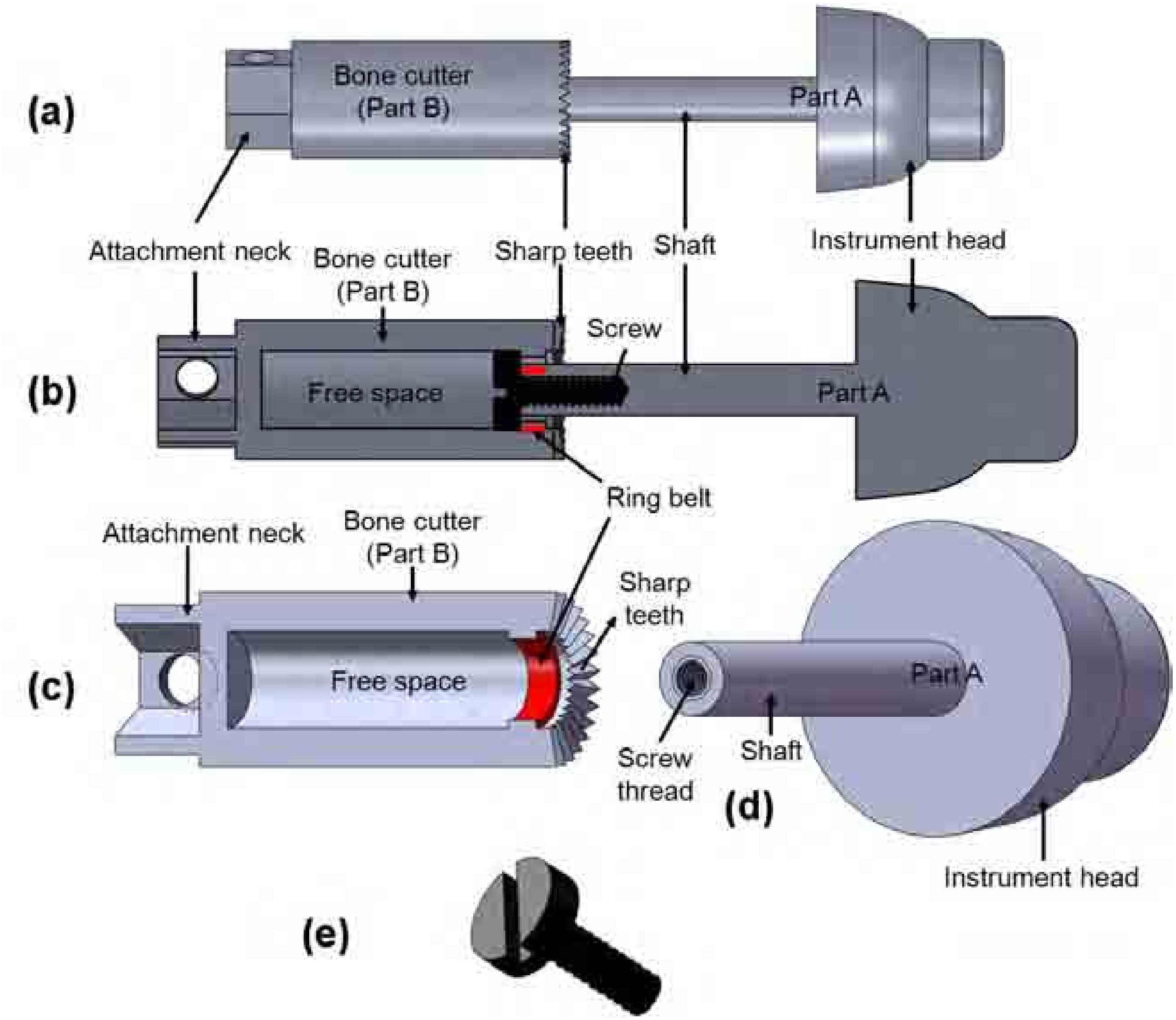

Figure 5. 31. (a) The screw threaded cutter concept. (b) The cross-section of the concept. The shaft is inserted into the bone cutter and a screw is then inserted into the shaft. The separation of the two parts is eliminated because of the diameter of the ring belt (the diameter of the screw head is greater than that of the ring belt). (c) The cross-section of the bone cutter. (d) Part A with a screw thread at the end of the shaft. (e) Screw.

5.5.4. Spring cutter

5.5.4.1. Concept introduction

The spring cutter consists of three parts: part A, part B and a spring (Figure 5.32). The instrument is assembled such that a spring is attached to the shaft (Figure 5.32 d) and then inserted into part B (Figure 5.32 b). A stopping hole is made at the end of part B next to the attachment neck (Figure 5.32 c). A pin is then inserted into this stopping hole through the spring to eliminate separation of the spring and part B (Figures 5.32 a and b). After placing the instrument head in the cage screw hole (Figure 5.33), part B has to be pushed down whilst rotating the handle to allow the sharp teeth to cut away the targeted VB edge (Figure 5.34). This is possible because of the free space in part B and the length of the spring (Figures 5.32 b and c).

5.5.4.2. Concept analysis

The main advantages of the spring cutter concept are that it is safe to use because there are no sharp teeth or edges on the instrument head and it is easy to use and assemble. If this concept were to become the final design the following modifications would have to be carried out:

- the instrument head has to be modified to allow its insertion into the partially blocked screw hole;
- the design of the instrument attachment neck has to be modified so it forms a universal joint with the Surgicraft Ltd. universal joint handle (Figure 5.3);
- the number of teeth needs to be justified and tested;

- the instrument bone cutter design has to be modified to ensure complete cleaning of the inner space of the instrument as well as the spring.

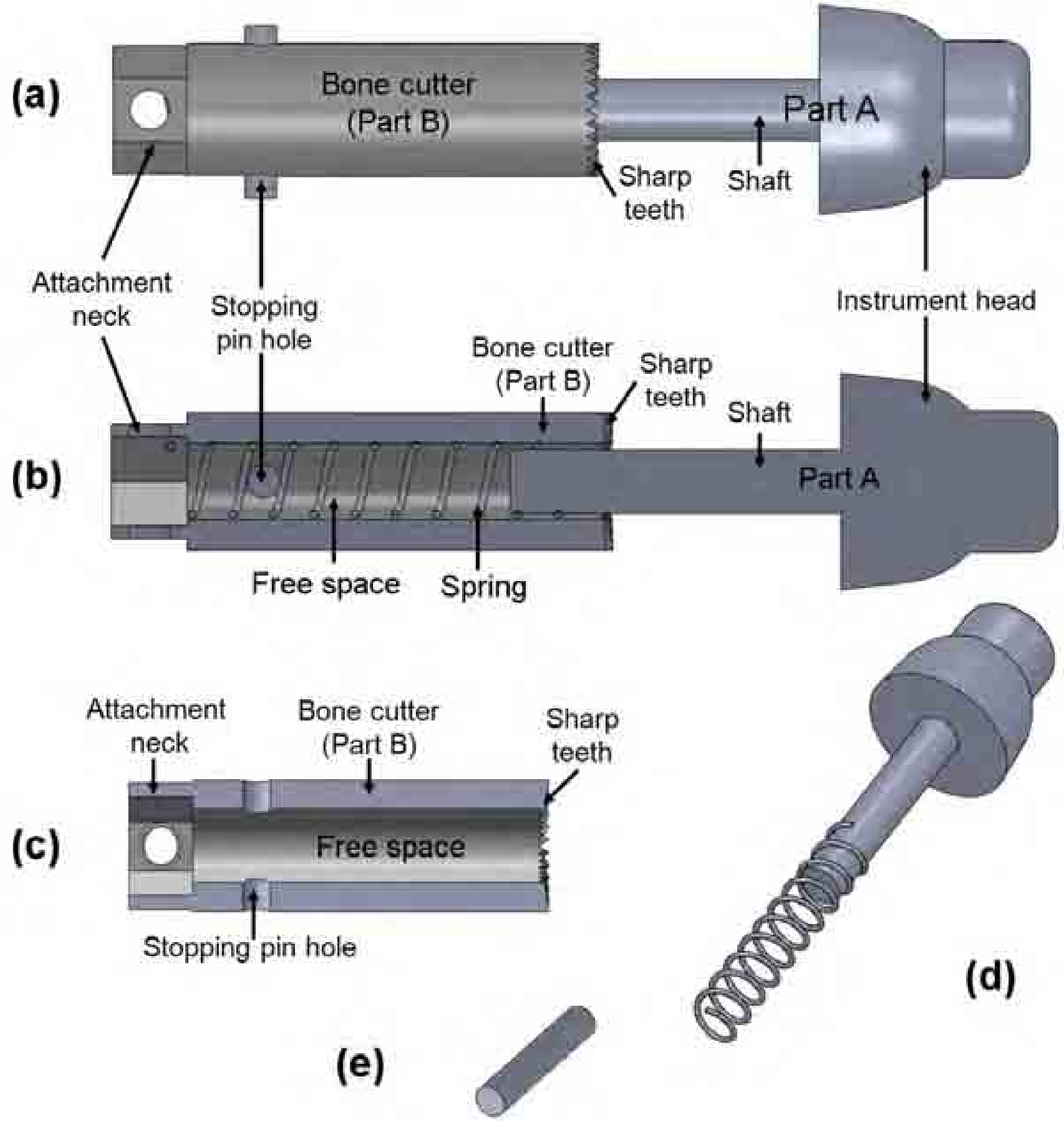

Figure 5. 32. (a) The spring cutter concept. (b) The cross-section of the concept. The shaft is attached to a spring and then inserted into the bone cutter. The separation of the spring and the bone cutter is eliminated when the pin is inserted through the stopping hole and the spring. (c) The cross-section of the bone cutter. (d) The spring is attached to the end of the shaft of part A. (e) Stopping pin.

5.5.5. Operation of the secondary concepts

When the instrument head is placed within the cage screw hole (Figure 5.33), the instrument handle has to be rotated and pushed down to allow the sharp teeth to cut away the targeted VB edge (Figure 5.34). This is possible because of the free space in the instrument bone cutter.

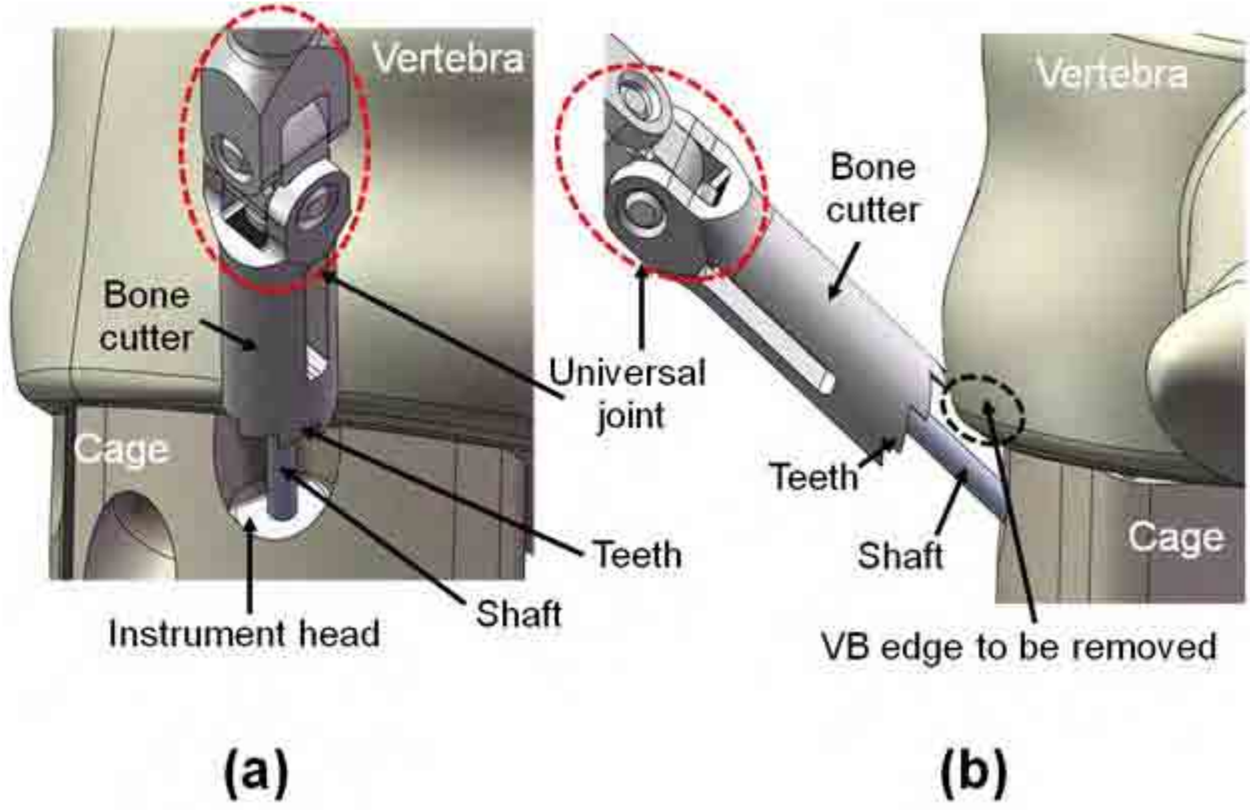

Figure 5. 33. Operation of the secondary concepts. The instrument head is placed in the screw hole. (a) Front view of the instrument once placed in the screw hole, (b) side view of the instrument once placed in the screw hole.

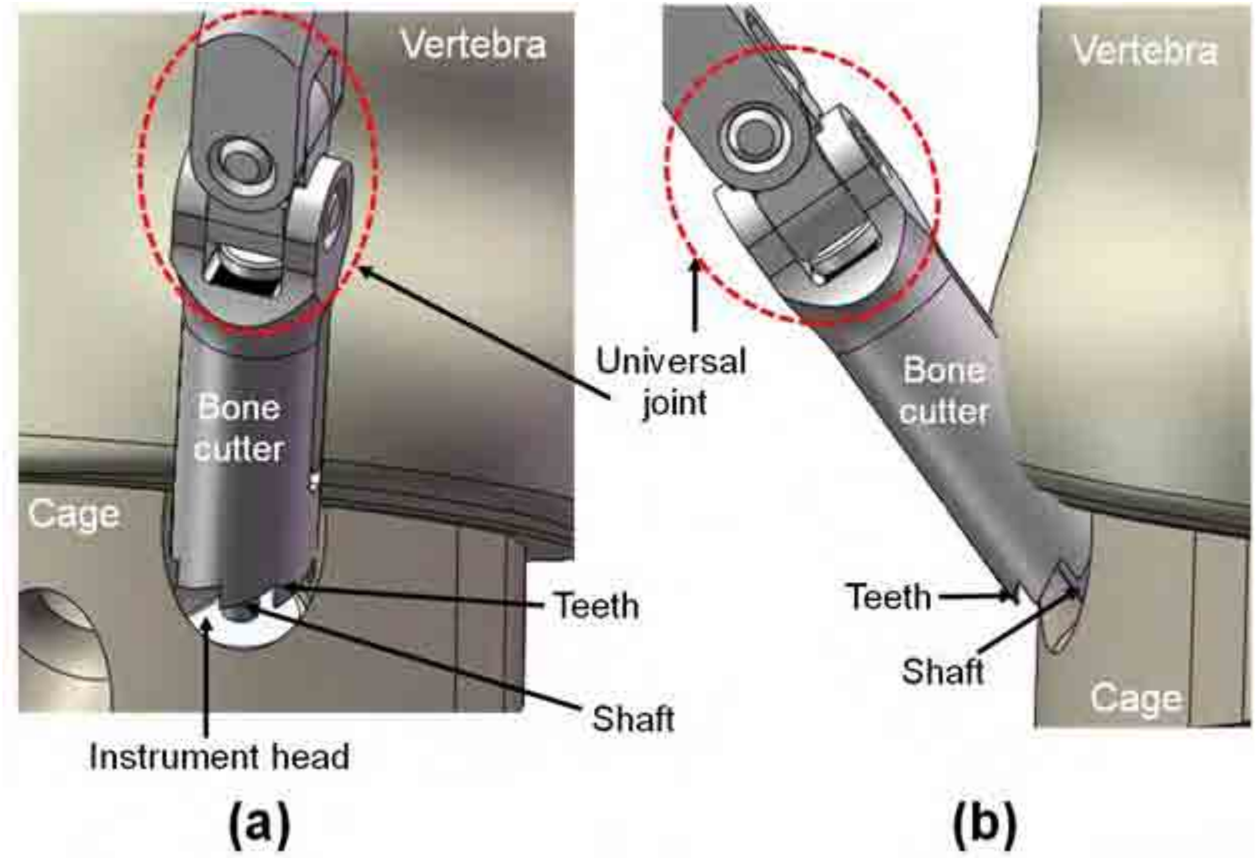

Figure 5. 34. Operation of the secondary concepts. As the instrument handle is pushed down and rotated, the targeted VB edge is cut away by the sharp teeth. (a) Front view of the instrument once the VB edge is removed, (b) side view of the instrument once the VB edge is removed.

5.6. Final design

5.6.1. Introduction

The final design was derived after analysing the three secondary concept designs in detail (discussed in each sub-section of §5.5). The spring cutter concept was chosen because it was believed that it may be more user friendly than the other two concepts and is the easiest to assemble. A few modifications (stated below) were then carried out to produce the final design:

- the instrument head was modified to allow its insertion into the partially blocked screw hole (discussed in §5.6.3);
- the design of the instrument attachment neck was modified so it formed a universal joint with the Surgicraft Ltd. universal joint handle (discussed in §5.6.4);
- the bone cutter was modified to allow complete cleaning and sterilization of the inner space of the instrument as well as the spring (discussed in §5.6.4);
- modifications and justifications were carried out on the teeth and their numbers (discussed in §5.6.5).

5.6.2. Description

The final design consists of an instrument head, a shaft, a spring, a bone cutter, a universal joint and a handle (Figures 5.35 and 5.36). Appendices F to I provide engineering drawings of the whole instrument (with the universal joint handle), the instrument head, the shaft and the bone cutter, respectively. A training guide was produced to provide instructions on how to use the instrument (Appendix J). The VB edge cutter instrument was manufactured from heat treated 17-4 grade stainless steel on a sliding head machine (Finsbury Surgical Ltd., Sheffield, UK). The instrument head, bone cutter, teeth and spring are explained in more detail in §5.6.3 to §5.6.6, respectively.

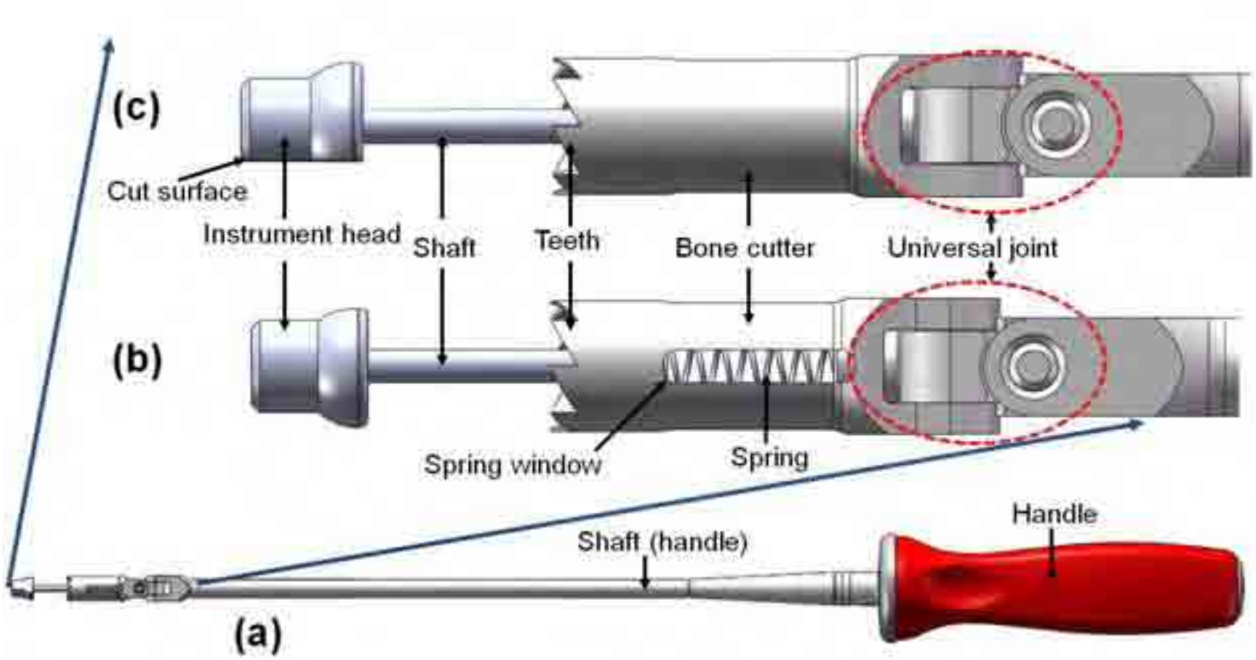

Figure 5. 35. Final design of the VB edge cutter instrument. (a) Instrument is attached to the universal joint handle (Surgicraft Ltd.). (b) Side view of the VB edge cutter instrument showing the spring window. (c) Side view of the VB edge cutter instrument showing the cut surface of the instrument head.

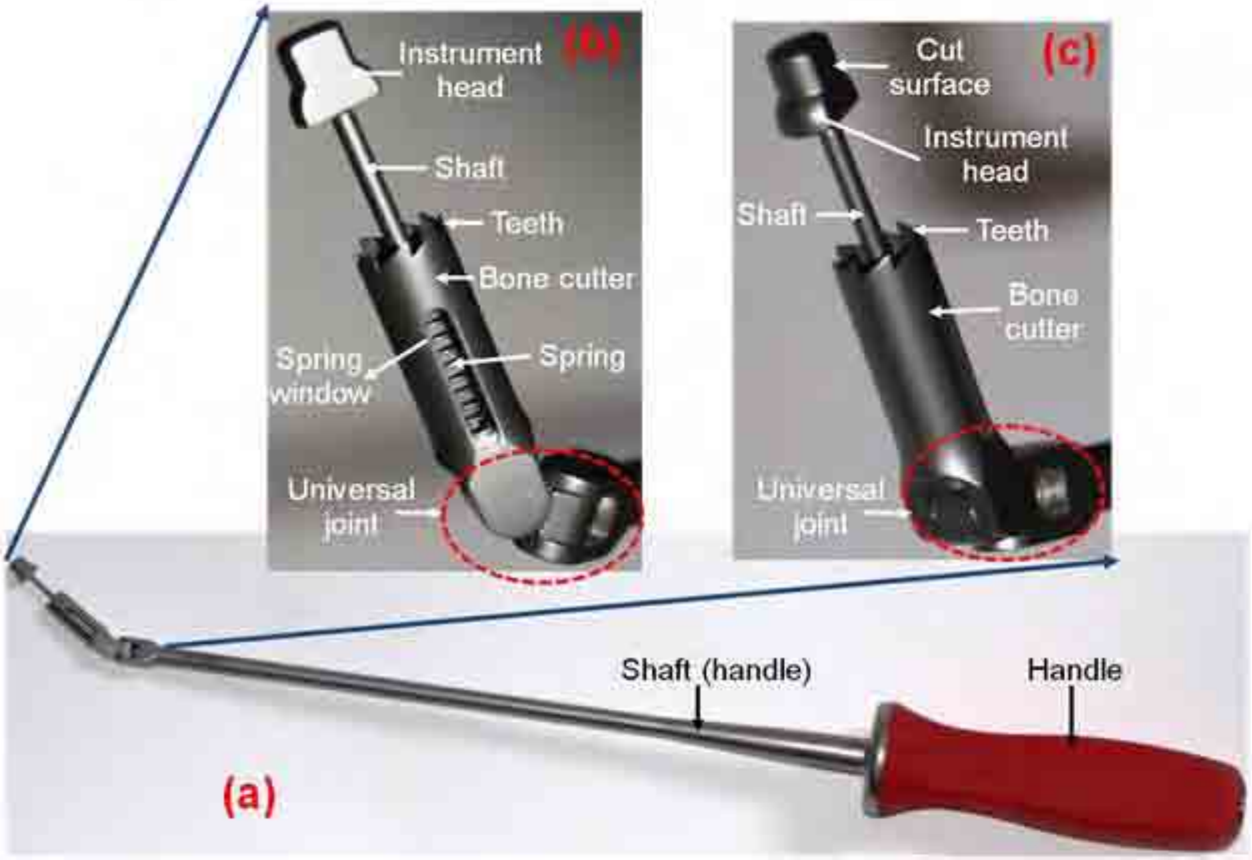

Figure 5. 36. Manufactured VB edge cutter instrument. (a) Instrument is attached to the universal joint handle (Surgicraft Ltd.). (b) Side view of the VB edge cutter instrument showing the spring window. (c) Side view of the VB edge cutter instrument showing the cut surface of the instrument head.

5.6.3. Instrument head dimensions

As described earlier in §5.5.1, there are clearances between the diameter of the instrument head and those of the cage screw holes (0.05 mm for the 36 and 39 mm cage widths and 1.05 mm for the 42 and 45 mm cage widths). These clearances allow the instrument head to be inserted into the cage screw hole and rotate along its axis. Dimensions of the instrument head are shown in Figure 5.37. Part of the instrument head has been cut away (Figures 5.35 and 5.36) so that the head can be placed in the screw hole when it is partially blocked by the VB edge.

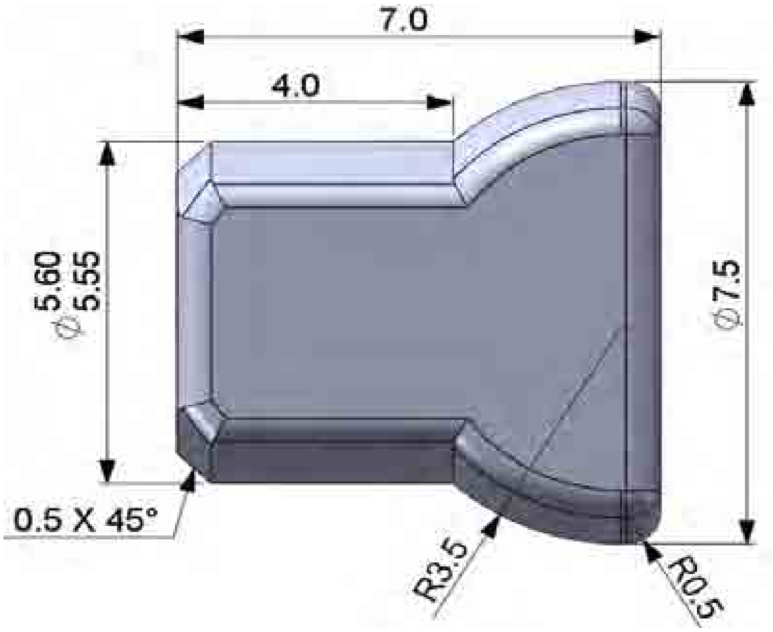

Figure 5. 37. Instrument head dimensions. All dimensions are in millimetres.

5.6.4. Bone cutter

At one end of the bone cutter there are sharp teeth. The other end of the bone cutter is designed (attachment fork) so that it attaches to the universal joint which in turn is connected to the handle (Figure 5.38). There are two parallel spring windows cut on the bone cutter (Figures 5.35, 5.36 and 5.38). These windows aid in cleaning the inside of the bone cutter.

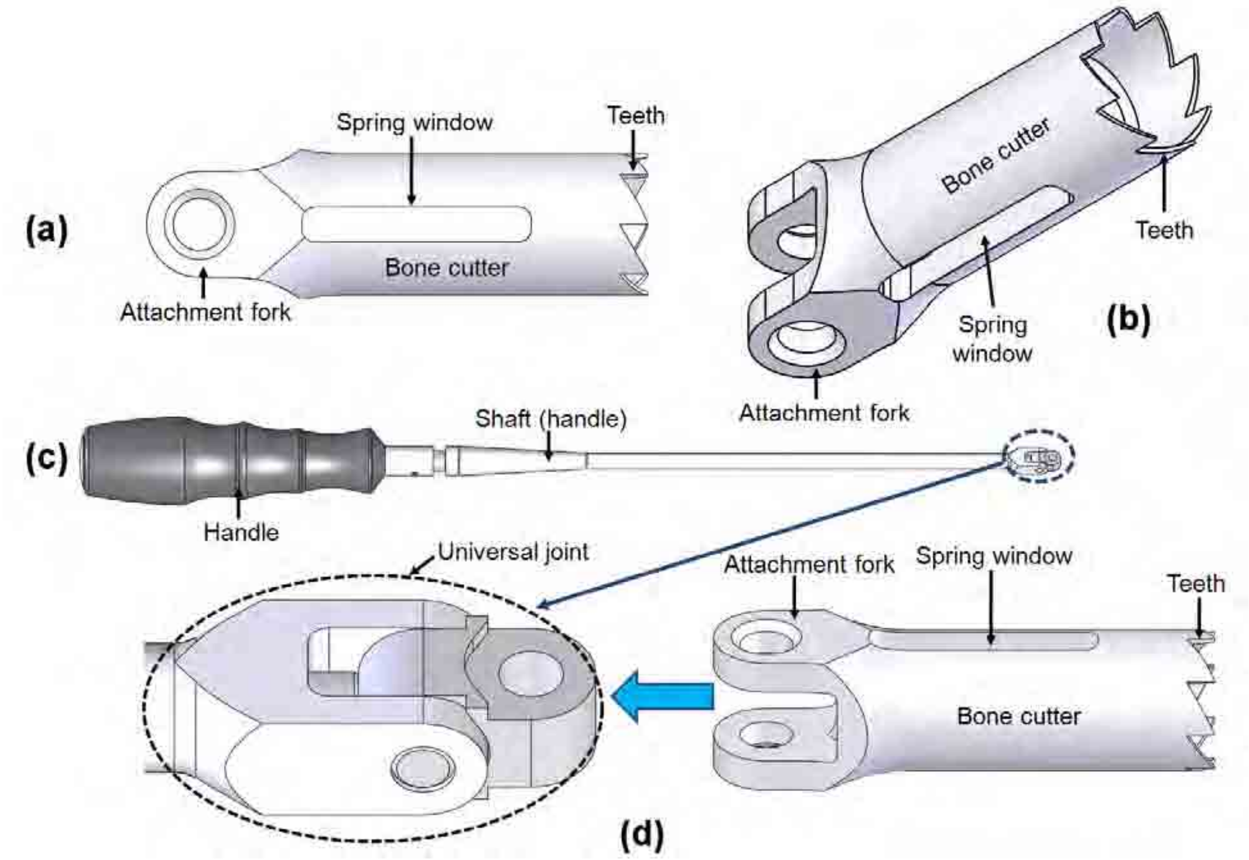

Figure 5. 38. (a) and (b) Side and three-dimensional views of the bone cutter. (c) Universal joint handle. (d) The fork attachment at one end of the bone cutter allows attachment of the bone cutter to the universal joint.

5.6.5. Number of teeth

To determine the optimum number of teeth, two functional concepts with 8 and 16 teeth were manufactured (Figure 5.39). These were suggested by Mr S. Lambell (Technical Manager, Finsbury Surgical Ltd., Sheffield, UK) based on his experience of manufacturing instruments for cutting bone. Tests were carried out on sheep lumbar vertebrae and the resultant cuts were compared. The details of the test specimen and the test set-up are provided in §5.6.9.1 and §5.6.9.2, respectively. The comparison showed that the concept with 8 teeth removed the VB edge more easily and neatly than the concept with 16 teeth (Figure 5.40). Hence, the final design has 8 teeth and the dimensions of the teeth are shown in Figure 5.41. A 6 ° angle taper was added to the inside of the bone cutter to produce the sharp teeth (Finsbury Surgical Ltd., Sheffield, UK).

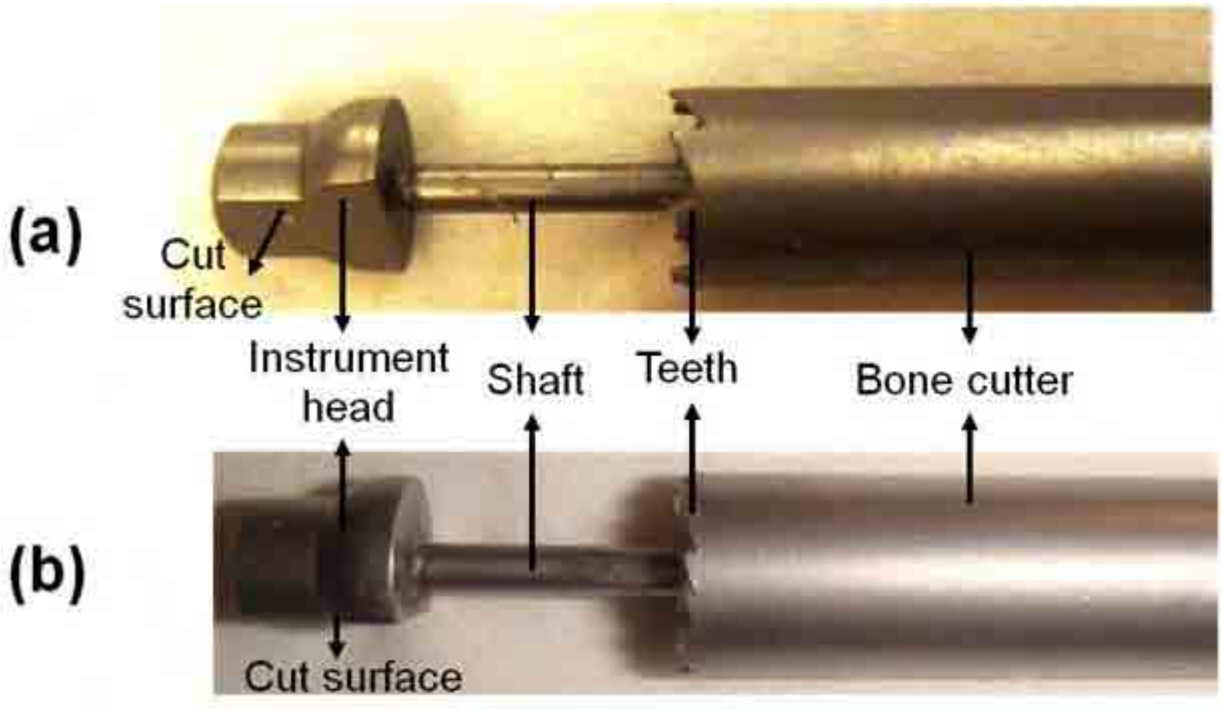

Figure 5. 39. Manufactured concepts. (a) 8 teeth concept. (b) 16 teeth concept.

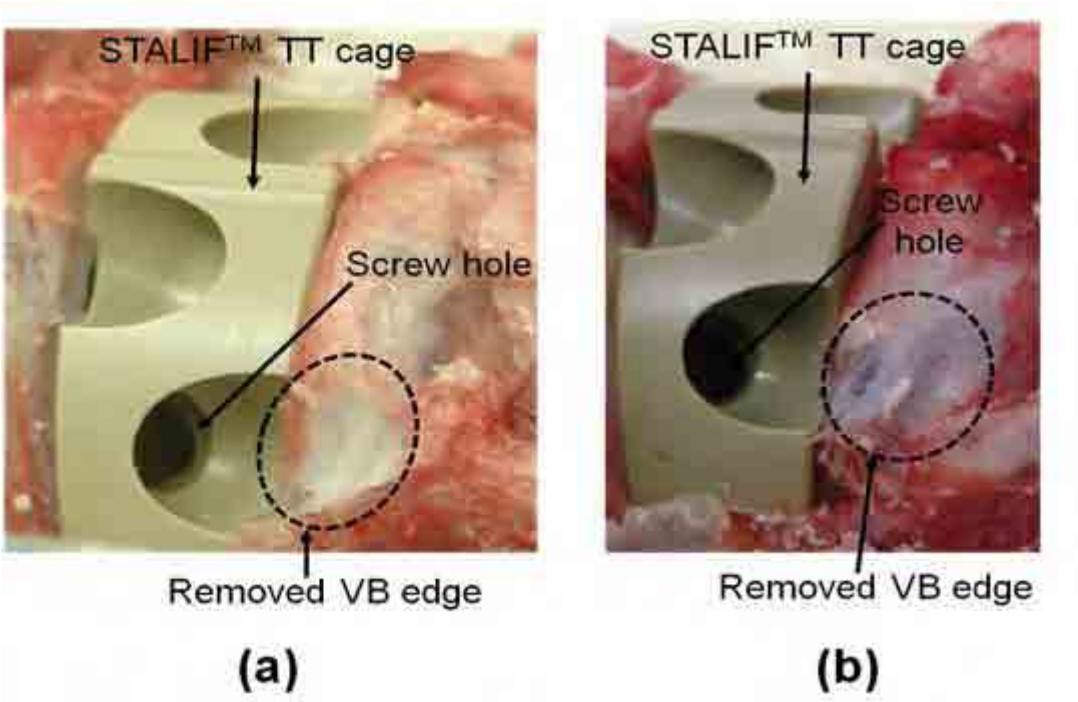

Figure 5. 40. Resultant cuts from functional concepts. (a) Using concept with 8 teeth and (b) using concept with 16 teeth.

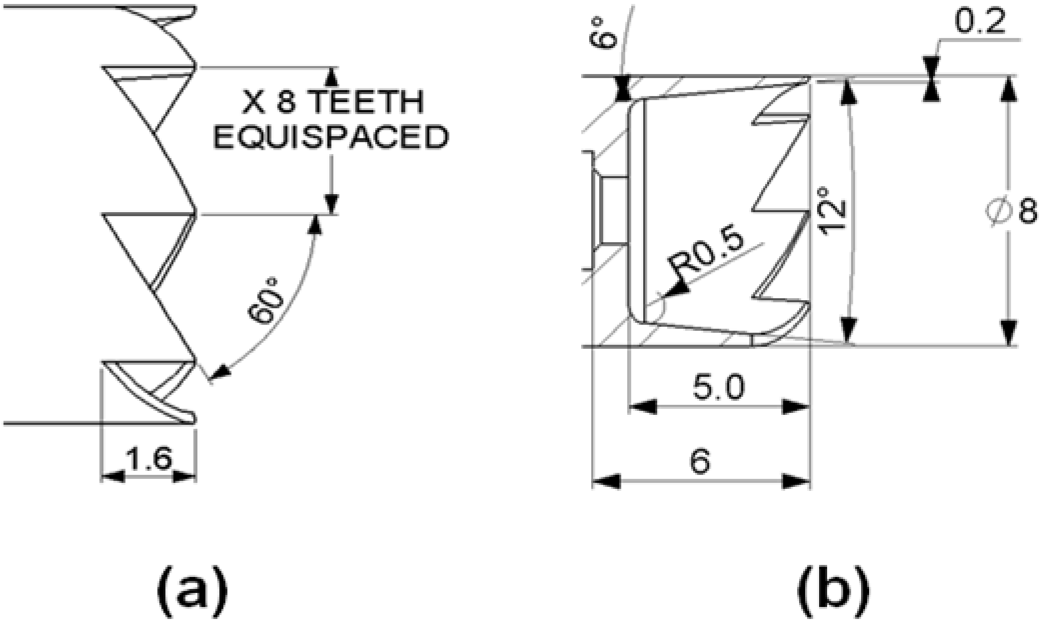

Figure 5. 41. The dimensions of the cutting teeth (final design). (a) Side view of the teeth, (b) the cross-section of the teeth. All dimensions are in millimetres.

5.6.6. Spring

A spring (Figure 5.42) is attached to the shaft (Figures 5.43 a and b). When the spring is in an uncompressed state (Figure 5.42), its length covers all of the STALIF^{TM} TT cage range heights (11, 13, 15 and 17 mm). When it is compressed, there is a 1 mm clearance between the tip of the teeth of the bone cutter and the instrument head (Figure 5.43 c). This clearance was chosen to prevent damage to the teeth of the instrument from touching the surface of the instrument head while ensuring all the targeted VB edge is removed. The spring (LC 018AA 06S316) was purchased from Lee Spring Ltd. (Wokingham, UK). It is made from 316 grade stainless steel and has a stiffness of 1.5 N/mm. The original length of the purchased spring was 16 mm. It was cut down to 14.5 mm to be used in the cutter instrument.

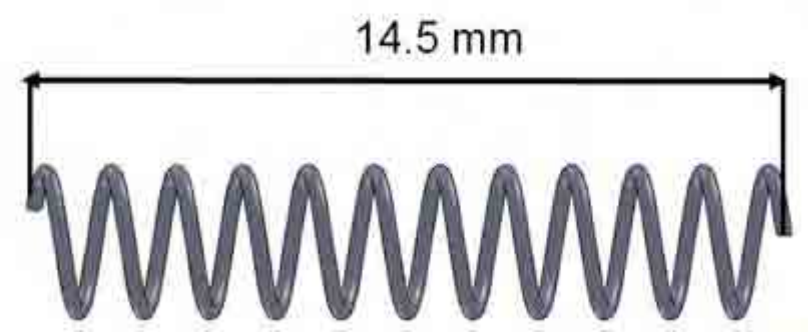

Figure 5. 42. Uncompressed spring (Lee Spring Ltd.). The spring's end coils are closed and ground. When the spring is compressed it has a length of 4.5 mm.

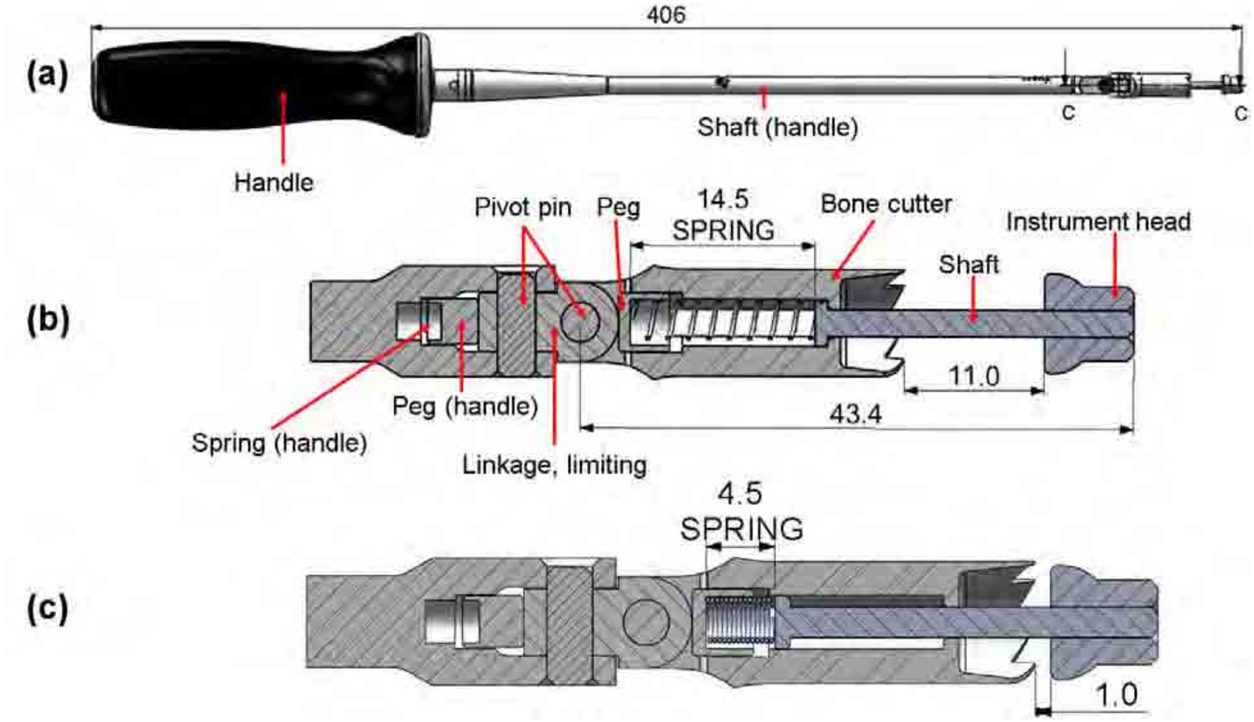

Figure 5. 43. (a) The VB edge cutter instrument attached to the universal joint handle (Surgicraft Ltd.). (b) The cross-section of the VB edge cutter instrument with the universal joint when the spring is uncompressed. (c) The cross-section of the VB edge cutter instrument with the universal joint when the spring is compressed. All dimensions are in millimetres.

5.6.7. Operation of the instrument

The operation of the VB edge cutter instrument is the same as those of the secondary concept designs explained in §5.5.5 and shown in Figures 5.33 and 5.34.

5.6.8. Risk assessment

An important step in the design of a medical instrument is to carry out a risk assessment (Aitchison *et al.,* 2009). Any risk associated with the instrument must be eliminated or reduced as far as possible so the safety of patients and healthcare workers is not compromised (Aitchison *et al.,* 2009). A failure mode and effect analysis (FMEA) (Shepherd, 2002) guided by the British Standard, BS EN ISO 14971:2009, was carried out. FMEA is a method that considers all the potential hazards of each component, sub-assembly and final product assembly (Shepherd, 2002). In this study FMEA was only carried out on the VB edge cutter part of the instrument. This is because the handle with the universal joint (Surgicraft Ltd.) has successfully passed the required analysis and is already commercially available. The potential hazards and harms were identified and then evaluated in terms of their severity (*S*) and probability (*P*). Each of these elements was scored on a scale of 1 to 5. A risk number (*SP*) was then calculated by multiplying the scores for the two elements (*S* and *P*) together (Table 5.1). If *SP* was 10 or greater, the risk was considered to be unacceptably high and had to be reduced. If *SP* was between 5 and 9, the risk was considered as high and had to be reduced where practicable. Any residual risk was to be justified against the device benefits. If the obtained *SP* was between 3 and 4, the risk was considered as medium and had to be reviewed to ensure that it is as low as reasonably practicable. If *SP* was 2 or less, the risk was considered to be safe. The results of the risk analysis are presented in Table 5.1. Subsequent actions were then taken to reduce or eliminate the identified hazards.

Table 5. 1. Results of the risk analysis for the VB edge cutter instrument (severity, *S*, probability, *P*, risk value, *SP*). A score of 1 was given when *S* was considered as negligible harm and *P* was judged to be less than 1%. When minor harm for *S* and up to 5% for *P* was considered, a score of 2 was given. A score of 3 was given when *S* was considered as serious harm and *P* was up to 10%. When critical harm for *S* and up to 25% for *P* was considered, a score of 4 was given. A score of 5 was given when *S* was considered as catastrophic and *P* was up to 50%.

Component	Hazard	Harm	*S*	*P*	*SP*	Action to reduce or eliminate risk
Bone cutter - teeth	Not enough bone to be cut away	Extended surgery	2	1	2	The diameter of the teeth is only 0.2 mm smaller than the cage screw hole allowing the entire targeted VB edge to be removed
Bone cutter - teeth	Too much bone to be cut away	Harm to the patient	1	3	3	The instrument head aligns the teeth with the screw hole axis allowing only the intended VB edge to be cut away The surgeon has to be trained to use the instrument
Bone cutter - teeth	Teeth contacting the cage	Damage to the cage	2	1	2	Tests have been carried out to ensure that the instrument head aligns the teeth with the screw hole axis (§5.6.9.3, cutting test) The surgeon has to be trained to use the instrument
Bone cutter - teeth	Small pieces of the teeth break off	Instrument fragments left in the patient	4	1	4	Durability tests have been carried out on sheep lumbar vertebrae with no signs of fracture (§5.6.9.5, teeth and spring durability) Information on the shape and

						number of the teeth should be available to the surgeon. It is required to check for signs of damage before and after use
Shaft	Instrument shaft bends due to too much force or becomes unseated	Instrument compromised, minor delay to surgery	1	2	2	The instrument is manufactured from 17-4 grade stainless steel which has been heat treated
Spring	The spring gets stuck	Instrument unusable	1	2	2	Durability tests have been carried out on the instrument (§5.6.9.5, teeth and spring durability)
VB edge cutter instrument	Misplacement of the fusion cage due to too much force applied on the instrument	Minor delay to surgery	1	3	3	The cage has to be tightly fitted between the vertebrae The surgeon has to be trained to use the instrument
VB edge cutter instrument - universal joint	Instrument assembly comes apart or loosens	Instrument compromised, minor delay to surgery	1	1	1	Torsion tests have been carried out on the instrument (§5.6.9.4, torsion test)

5.6.9. Testing and validation of the design

5.6.9.1. Test specimens

All tests carried out in this study were performed on sheep lumbar vertebrae (purchased from a local butcher). The mineral density of the sheep lumbar vertebrae was measured using the bone-ashing method (Holmes *et al.,* 1993) and was found to have a mean value of 0.37 g.cm^{-3} (see Appendix K for procedure and Table K.1 for results). This mineral density value was higher than that of human vertebral bodies (0.15 g.cm^{-3}, Holmes *et al.,* 1993). Therefore, it was assumed that if the VB edge cutter can cut away the denser sheep lumbar vertebrae, it can cut away those of humans with more ease.

5.6.9.2. Test set-up

The intervertebral disc between adjacent vertebrae was removed by use of a scalpel and a STALIF^{TM} TT cage (STT39130-12LT) (39 mm × 27 mm × 13 mm) was placed in between the adjacent vertebrae. The vertebrae containing the fusion cage were secured in an open plastic box (30 cm × 20 cm, cross-section) using acrylic cement (WHW Plastics, Hull, UK) to avoid any undesired movements (Figure 5.44).

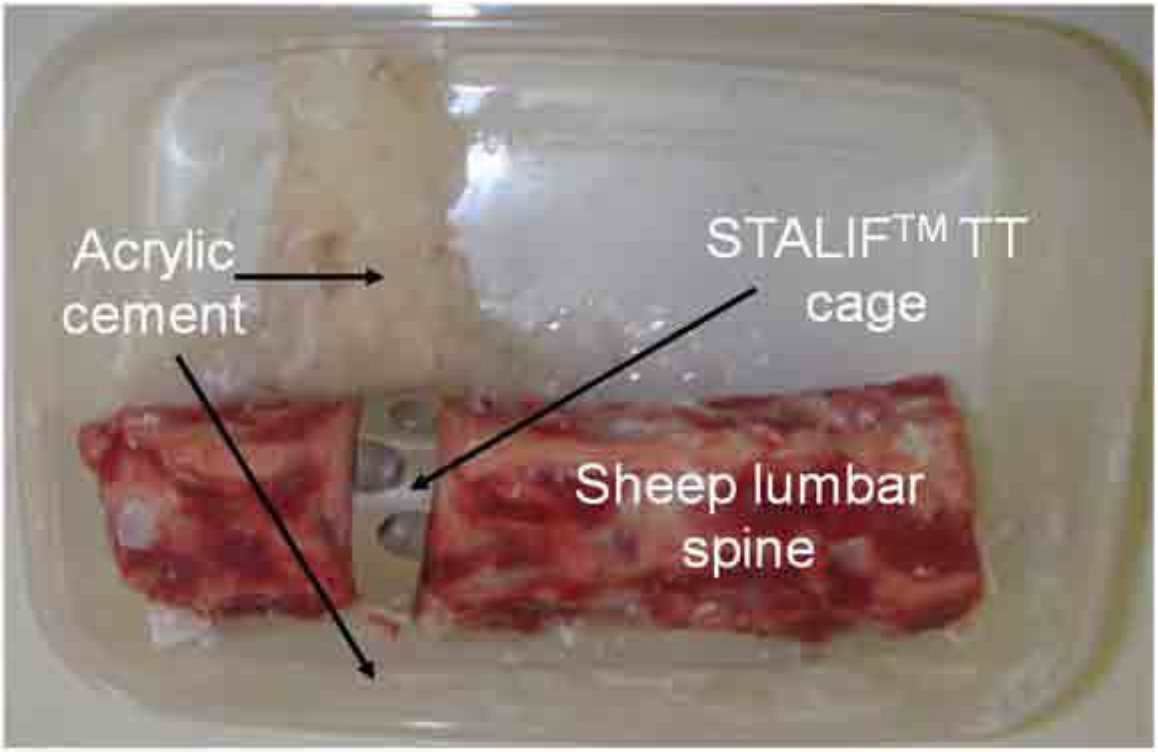

Figure 5. 44. The intervertebral disc was removed by use of a scalpel and a STALIF^{TM} TT cage was placed in between the adjacent vertebrae. The vertebrae containing the fusion cage were secured in an open plastic box using acrylic cement to avoid any undesired movements.

5.6.9.3. Cutting test

The cutting action of the VB edge cutter instrument was compared with that of conventional rongeurs on sheep lumbar vertebrae. The VB edge cutter instrument and rongeurs were used to cut away two separate VB edges adjacent to the cage screw holes. This test was repeated five times on two different sheep vertebrae (10 cuts were produced by each VB edge cutter instrument and rongeurs).

The head of the VB edge cutter instrument was placed within the screw hole which allowed alignment of the cutting teeth with the hole axis (Figures 5.45 and 5.46). This prevented the teeth contacting the cage as well as providing it with full protection (Figures 5.45 and 5.46). The handle was pushed down whilst rotating to allow the teeth to remove the targeted VB edge.

While using the rongeurs, although the specimen was placed in an open box which allowed for more space than would be available during surgery, it was still found difficult to align the tip of the rongeurs with the screw hole axis. In some cases the sharp edges of the rongeurs were in contact with the PEEK cage and caused damage (Figure 5.47).

At the end of the tests, the shape of the cuts and the amount of the removed VB edge resulting from using the VB edge cutter instrument and the rongeurs were compared. In all cases, the VB edge cutter instrument removed only the amount of bone required to enable screw access (Figures 5.48 and 5.49). However, the rongeurs in some cases removed more bone than necessary and in some cases not enough bone (Figure 5.49). Once the targeted VB edge was removed by the VB edge cutter, the fixation screw could be comfortably placed in the screw hole (Figure

5.50). Also, the cage was fully protected while the VB edge was being removed by the VB edge cutter (Figure 5.48), which could not easily be controlled when using rongeurs (Figure 5.47).

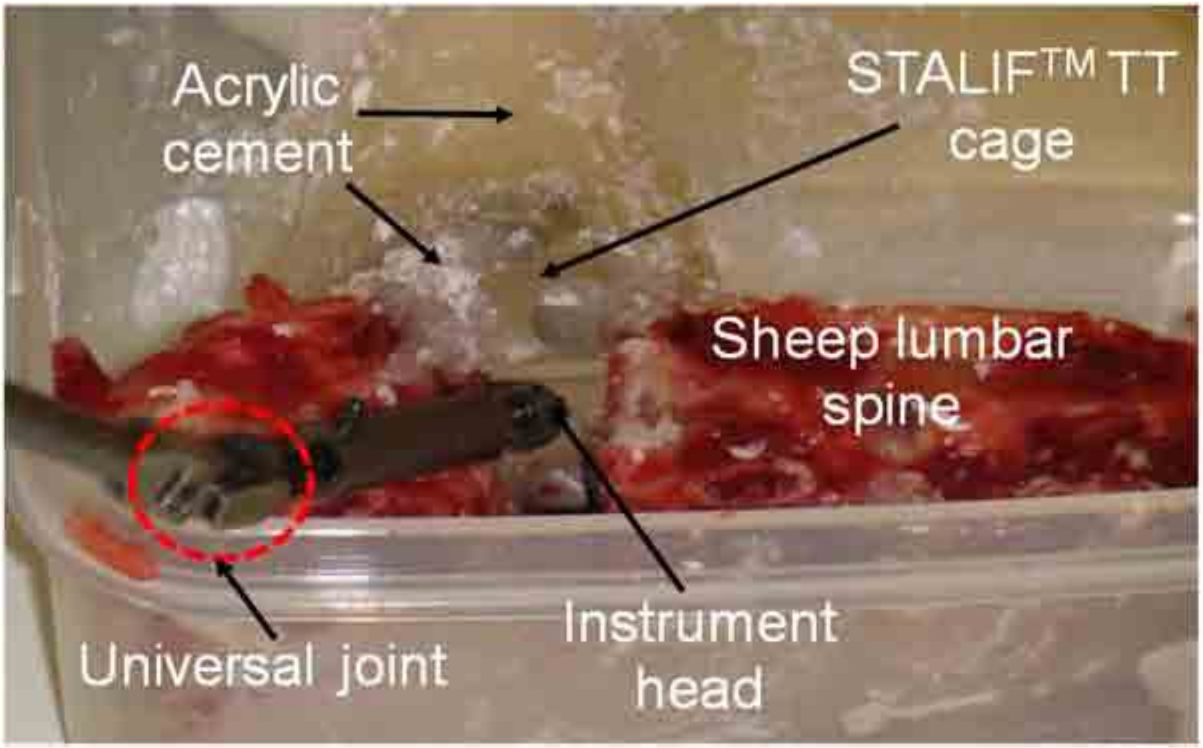

Figure 5. 45. The instrument head was placed within the screw hole which allowed alignment of the cutting teeth with the hole axis.

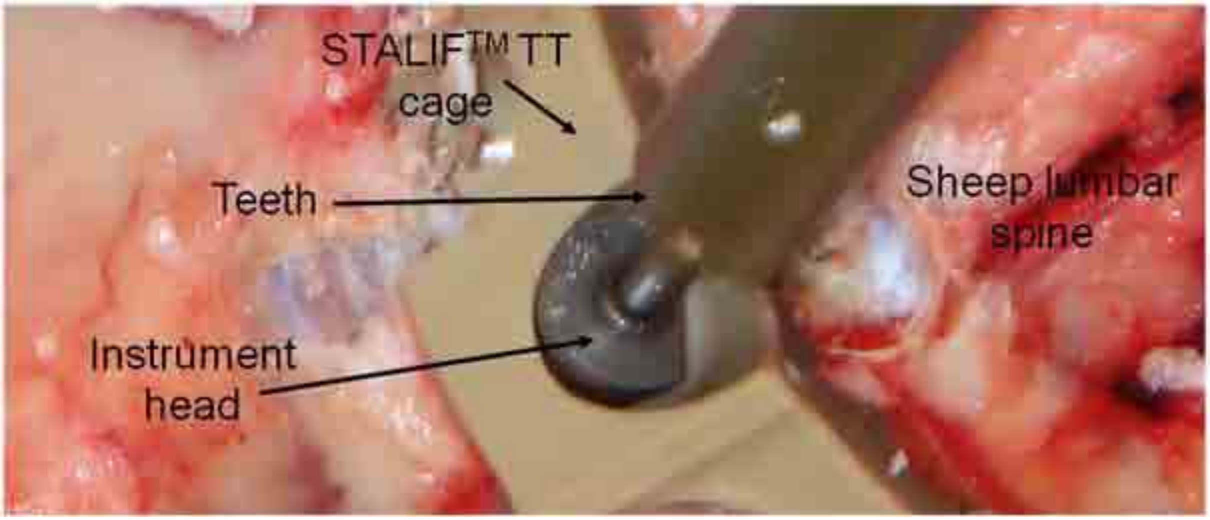

Figure 5. 46. Once the instrument head was placed within the screw hole, the resultant alignment of the cutting teeth with the hole axis prevented the teeth from contacting the cage.

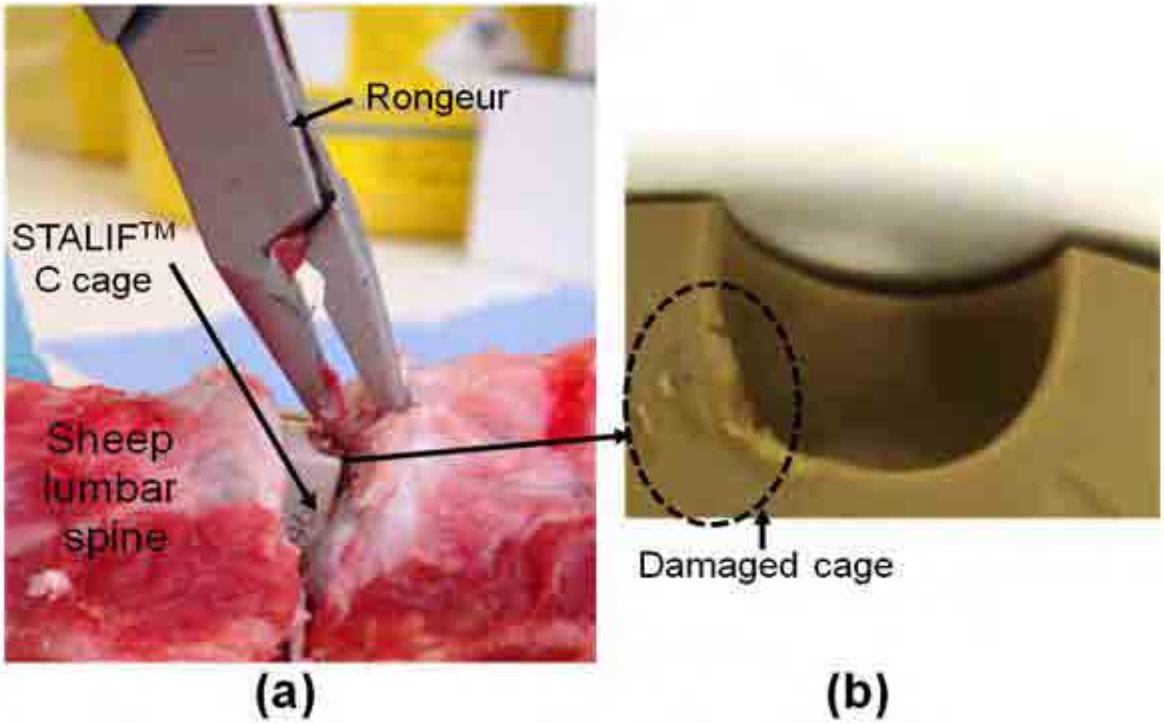

Figure 5. 47. (a) Rongeurs removing the targeted VB edge. (b) Damage to the PEEK cage because the rongeurs' sharp edges were in contact with the cage during the removal of the VB edge. Note, due to shortage of available STLIF^{TM} TT cages, this test was carried out using the STLIF^{TM} C cage (C147561-3T) (16.5 mm × 14 mm × 7.5 mm) on sheep lumbar spine.

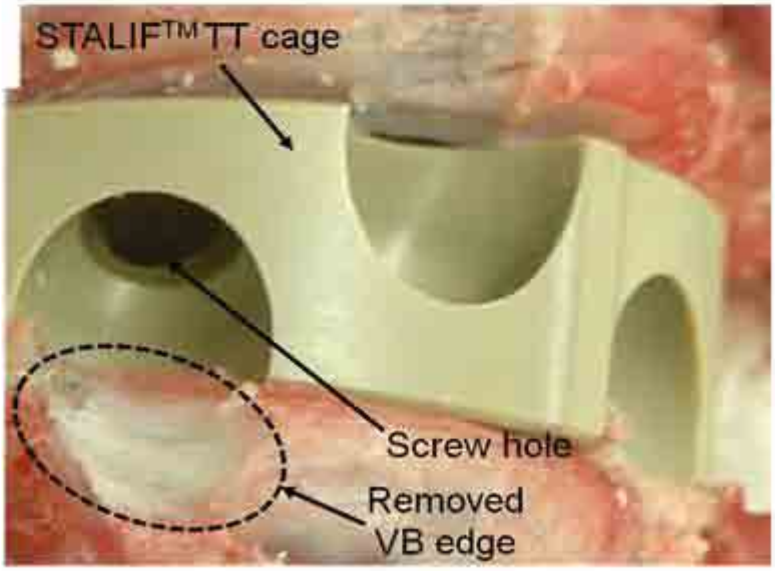

Figure 5. 48. Removed targeted VB edge by VB edge cutter instrument (sheep lumbar spine).

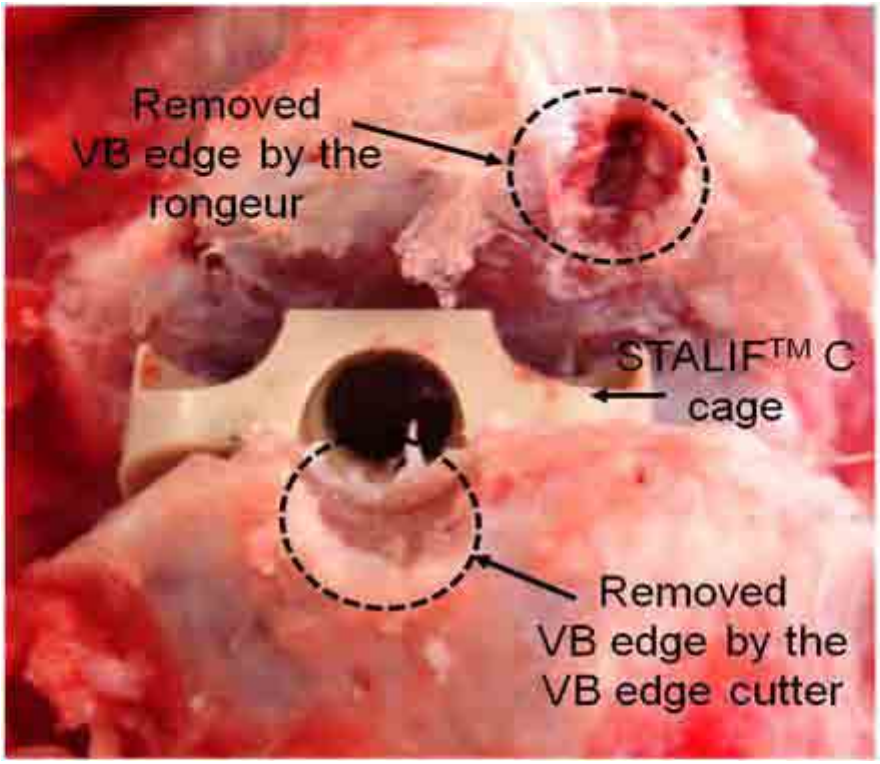

Figure 5. 49. Comparison of the removed VB edge by the rongeurs and the VB edge cutter instrument. Note, due to shortage of available STLIF^{TM} TT cages, this test was carried out using the STLIF^{TM} C cage (C147561-3T) (16.5 mm × 14 mm × 7.5 mm) on sheep lumbar spine.

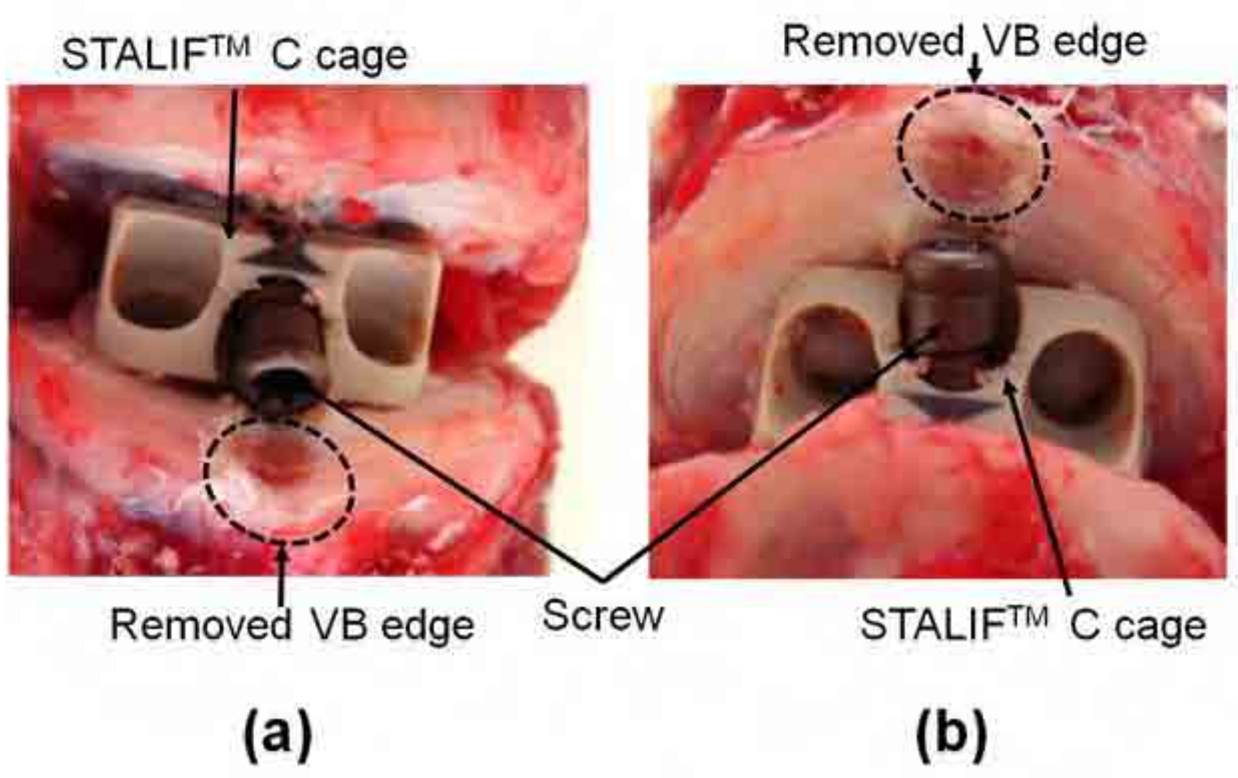

Figure 5. 50. Once the targeted VB edge was removed by the VB edge cutter, the fixation screw could be comfortably placed in the screw hole. Note, due to shortage of available STLIF^{TM} TT cages, this test was carried out using the STLIF^{TM} C cage (C147561-3T) (16.5 mm × 14 mm × 7.5 mm) on sheep lumbar spine.

The VB edge cutter instrument was further tested on a male cadaver specimen by an orthopaedic surgeon (J. S. Thalgott, Valley Hospital Medical Centre, Las Vegas, USA) (Figure 5.51). The levels at which the instrument was operated were L4/L5 and L5/S1. It was concluded that the VB edge cutter instrument removed the targeted VB edge easily and neatly.

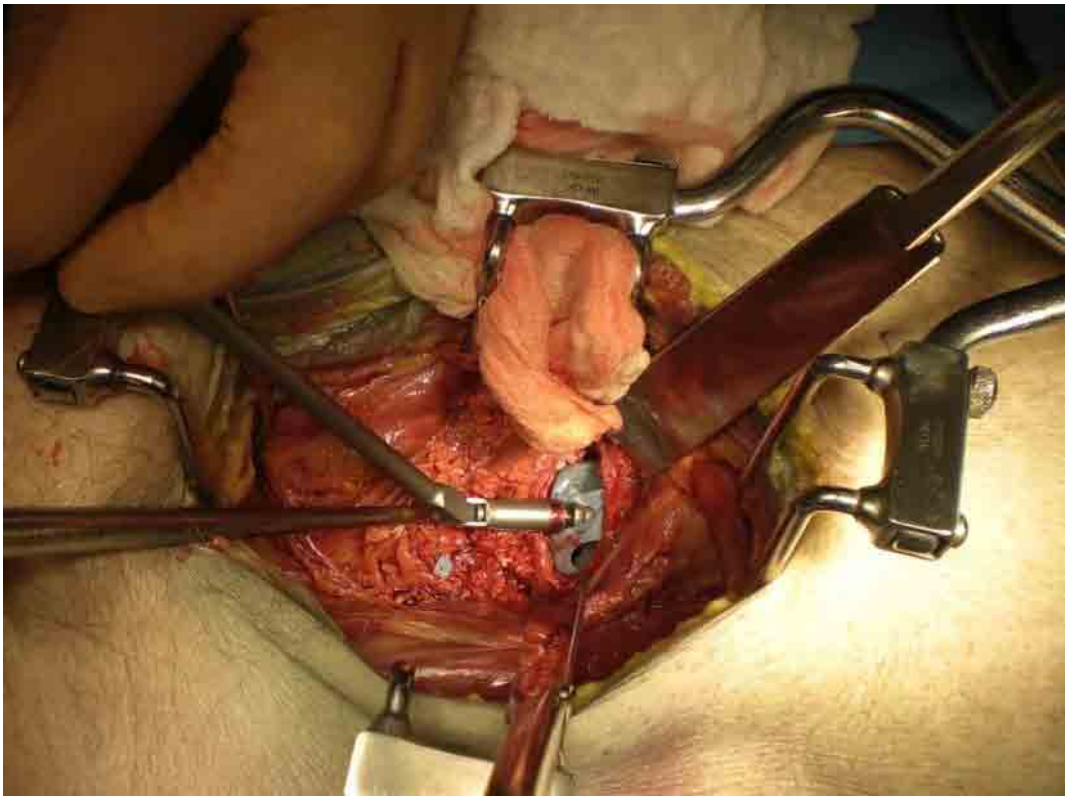

Figure 5. 51. Cadaver test by an orthopaedic surgeon. The instrument head is placed within the screw hole which results in alignment of the cutting teeth with the hole axis allowing the teeth to cut away the VB edge as well as preventing them from contacting the cage.

5.6.9.4. Torsion test

To ensure that the bone cutter does not detach from the handle or loosen, a torque test using a TWD20SB Torqueleader (MHH Engineering Co. Ltd., Guildford, UK) was carried out. The cutter instrument was placed and tightened in between the clamp of the Torqueleader (Figure 5.52) and a torque (5 N.m) was applied to the universal joint that attaches the bone cutter to the handle. The instrument was held by hand while the test was being performed. The joint remained intact.

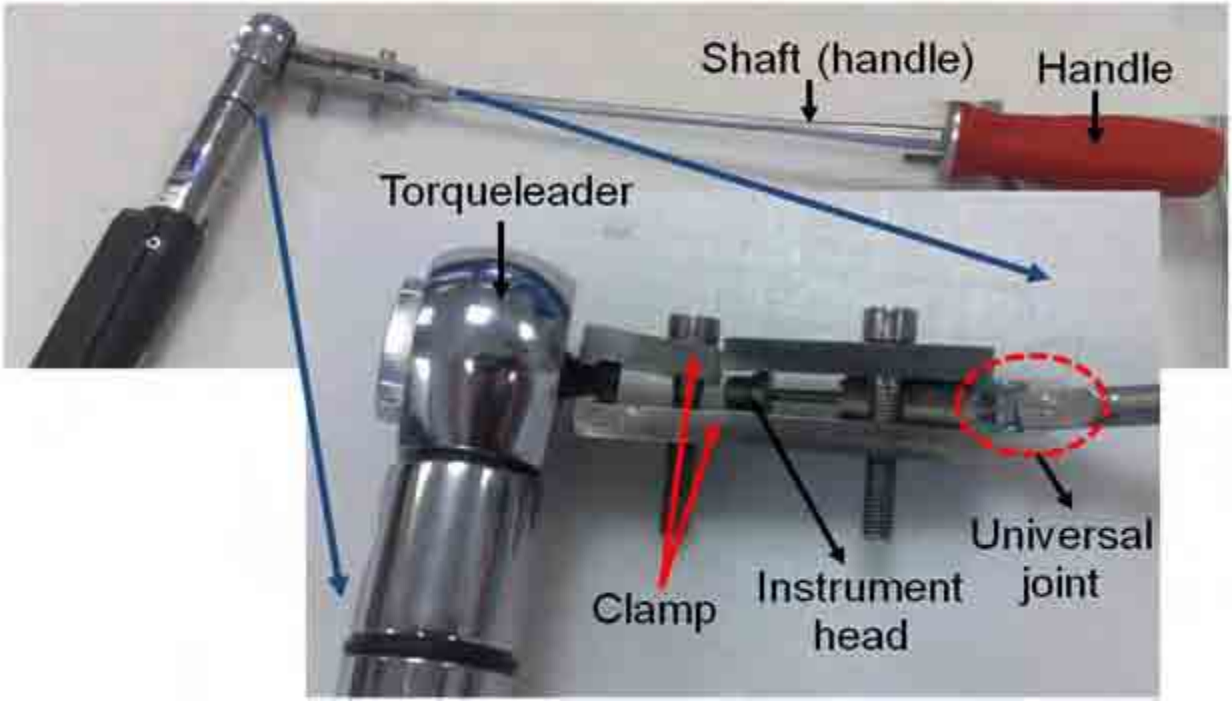

Figure 5. 52. TWD20SB Torqueleader (MHH Engineering Co. Ltd., Guildford, UK). The cutter instrument was placed and tightened in between the clamp of the Torqueleader.

The torque (5 N.m) chosen in this study is assumed to be reasonable as it is much greater than that applied in orthodontic treatments (0.1 N.m, Motoyoshi *et al.*, 2006). Also, this chosen torque (5 N.m) is expected to be greater than the torque applied to the instrument during surgery to remove the VB edge. This expectation was confirmed by setting 5 N.m on the torque-wrench and securing its tip in a vice (Figure 5.53). Attempts to turn the torque-wrench handle were unsuccessful.

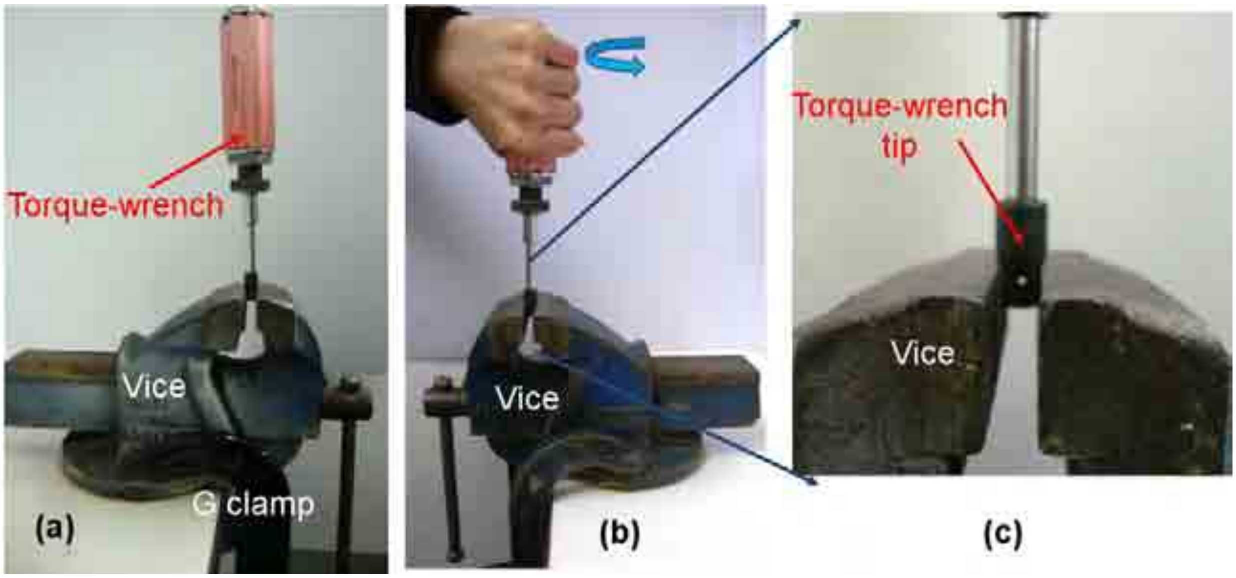

Figure 5. 53. Justification test using quartered screw driver torque-wrench. (a) The tip of the torque-wrench is placed tightly in the vice. (b) Applying force to the torque-wrench. (c) The tip of the torque-wrench did not move.

5.6.9.5. Teeth and spring durability

To determine how many times the instrument could be used before the teeth became too blunt, a durability test was carried out; 150 holes were cut in sheep lumbar vertebrae. In order to speed up the tests and simplify the process, no cage was used in this test and the head of the instrument was removed (Figure 5.54). Five whole sheep lumbar vertebrae were used (purchased from a local butcher). Pilot holes using a crossed tip screw driver were made on the vertebrae (Figure 5.55 a). The tip of the shaft of the instrument was placed in the pilot holes and cuts were made. On average, five rotating actions were made per hole. Micrographs were taken of the teeth before (Figure 5.56) and after (Figure 5.57) the durability test using a Nikon SMZ1500 Stereo microscope (Buhler Centre of Excellence, School of Mechanical Engineering, University of

Birmingham, Birmingham, UK) with magnification of ×19. The sharpness of the teeth after cutting 150 holes was found to be the same as the beginning of the test; the ease with which the bones were cut did not change. Also, the micrographs showed that the teeth were undamaged and intact at the end of the tests (Figure 5.57). While carrying out the durability test, the instrument spring did not get stuck and functioned properly and smoothly.

Figure 5. 54. The instrument head was removed for teeth and spring durability tests.

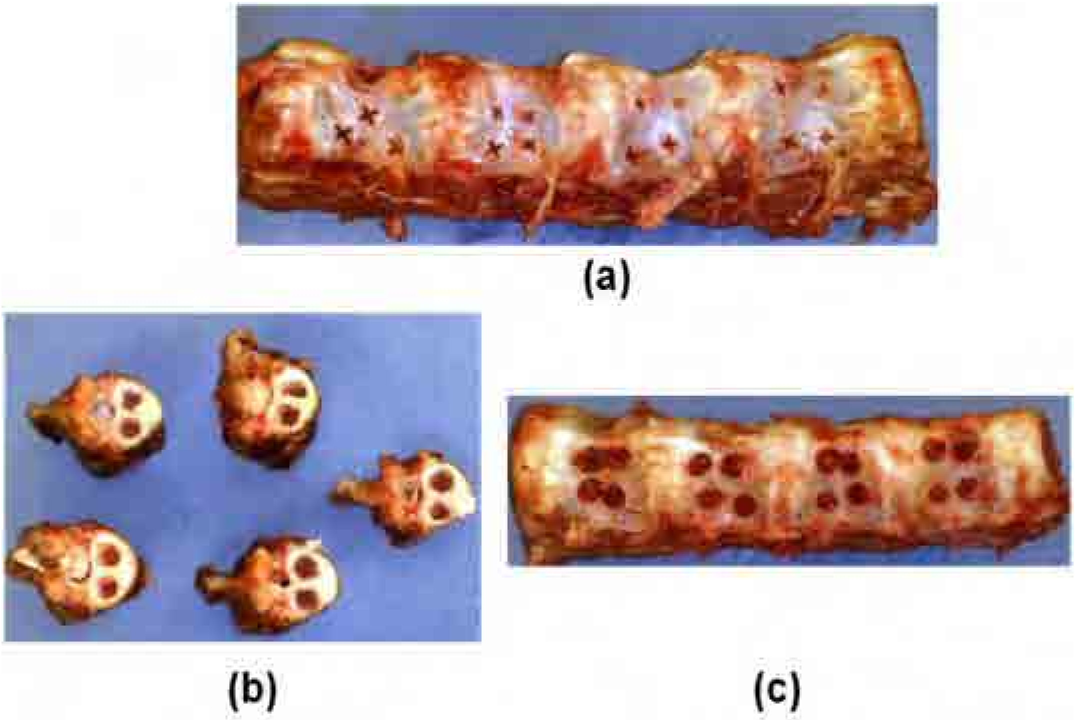

Figure 5. 55. Instrument teeth and spring durability tests on sheep lumbar vertebrae. (a) Pilot holes were made on the vertebrae. (b) and (c) Holes were cut on the vertebrae.

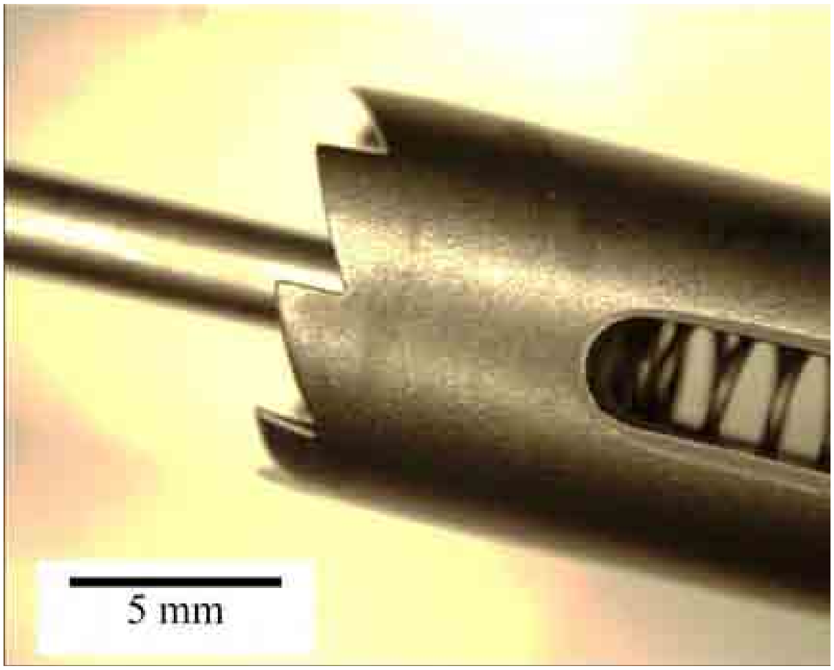

Figure 5. 56. Micrograph (magnification ×19) of the teeth before the durability test had been performed.

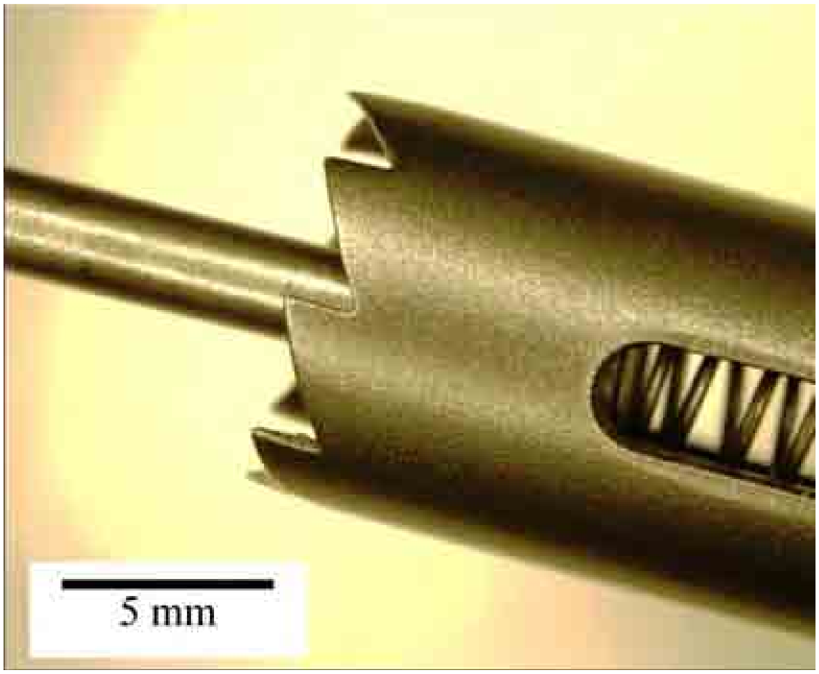

Figure 5. 57. Micrograph (magnification ×19) of the teeth after the durability test had been performed.

5.7. Discussion

This chapter has described the development of a surgical cutting instrument to aid implantation of a range of lumbar fusion cages. Once the cage is in position, between the adjacent vertebrae, the VB edge partially blocks the entrance to the cage screw hole. Also, some of the screw holes of the cage are positioned at an awkward angle. To insert fixation screws to secure the cage between the vertebrae, some parts of the blocking edge have to be removed. The final design of the VB edge cutter instrument was derived after modifications were made to the selected concept. The device as a whole consists of the VB edge cutter instrument and a universal joint handle. The VB edge cutter instrument was manufactured from heat treated 17-4 grade stainless steel to avoid instrument breakage. The VB edge cutter instrument consists of an instrument head, a shaft, a spring and a bone cutter. The instrument is connected to the universal joint handle by the attachment fork of the bone cutter. The universal joint allows free rotation of the instrument which can provide access to all of the screw holes. The length of the VB edge cutter instrument is 43.4 mm in order to meet the requirements of a minimally invasive surgery.

The instrument head of the VB edge cutter instrument acts as a guide; it sits in the cage screw hole and holds the instrument in place. This ensures that the instrument can only follow the desired direction along its centre-line. There is a clearance of 0.2 mm between the diameter of the cutting teeth and the cage screw hole. This and the instrument head (by aligning the cutting teeth with the axis of the screw hole) provide full protection to the cage and allow only the intended targeted VB edge to be cut away. The design characteristics of the VB edge cutter instrument overcome the drawbacks of rongeurs currently in use, which have difficulty in accessing the angled VB edges and may cut away more bone than necessary.

Tests were carried out to assess any potential risks associated with the instrument. The durability test demonstrated that the instrument teeth can stay intact and sharp for as long as required (25 operations). It was also shown that the force required to cut away the targeted VB edge does not bend the instrument shaft. The VB edge cutter instrument remained attached to the handle after applying a torque of 5 N.m. The instrument was tested on sheep lumbar vertebrae and also by a surgeon on a cadaver specimen. The results showed that the VB edge cutter instrument removes the required amount of bone (VB edge) and overcomes the shortcomings of rongeurs.

6. CONCLUSIONS

6.1. Chapter overview

In this thesis, discussion of the results has been included in the relevant chapters. This final chapter summarises the main conclusions of the thesis by relating them to the original aims outlined in Chapter 1. These are addressed in §6.2 to §6.4. The concluding remarks are presented in §6.5.

6.2. Side-holes

In Chapter 3, a cervical fusion cage model was developed. Between 0 and 10 side-holes were incorporated on the lateral side wall of the cage model. These holes may enable fluid to flow into and out of the cage interior which can aid the transportation of nutrients and removal of waste products. The effect of side-holes on the predicted von Mises stress levels in cages subjected to compressive loading was evaluated. FEA was used to simulate compression of the polyetheretherketone (PEEK) cage model between two adjacent vertebrae. The vertebrae were modelled as blocks of cortical bone with Young's modulus values of 12 and 30 GPa. The analyses were validated by experimental tests. In all the models, the von Mises stress was highest at the cage-vertebrae interface. The peak von Mises stress levels were between 14 and 18 MPa with maximum displacements of between 9.4 and 11.2 μm and an average normal compressive stress of 4 MPa (see §3.4.2 for more detail). Increasing the Young's modulus of the vertebrae from 12 to 30 GPa increased the peak von Mises stress on average by 29% and decreased the maximum displacement on average by 14%. The stresses in the models were lower than the compressive strength of PEEK (118 MPa) and are well within the PEEK fatigue strength reported (60 MPa at 10 million cycles). This study suggests that the number of side-holes had a negligible effect on the stress distribution within the cage; the stress magnitudes were fairly constant across all the models and did not change substantially with the number of holes. Hence, a cervical cage with side-holes is unlikely to fail in compression.

Further investigations may involve FEA on the cage models with 10 side-holes under various combinations of load patterns (e.g. combination of compression and bending). The cage model with 10 side-holes should be considered during further investigations as the suitability of such a cage has been demonstrated in Chapter 3 of this thesis. This cage model should be manufactured and be mechanically tested in accordance with standards (e.g. ASTM F 2077-03) before clinical evaluations can be carried out. These would allow the development of a new cage that has the benefits of a large number of side-holes to be completed.

6.3. Bioactive/biodegradable composite

In Chapter 4, the feasibility of using a 45S5 Bioglass/PLDLA composite (see §4.2 for more detail) as a potential cervical spinal fusion cage material was evaluated using FEA. In this study it was assumed that cages made from 45S5 Bioglass/PLDLA composite may overcome the possible long-term risks (e.g. implant loosening, migration, breakage or tissue irritation) associated with cages made from permanent materials (Hojo *et al.,* 2005; Jiya *et al.,* 2009; Lippman *et al.,* 2004; Pietrzak, 2000; Pietrzak and Eppley, 2000; Thomas *et al.*, 2008). A 45S5 Bioglass/PLDLA composite is expected to have potential benefits from both its components. It may degrade over time and may induce localized growth of surrounding tissues (bone formation) (Lowe and Coe, 2002; Rezwan *et al.,* 2006; Stamboulis *et al.,* 2002; Yang *et al.,* 2006; Wuisman and Smit, 2006). As the composite degrades, the load can gradually transfer to the healing bone resulting in a higher fusion rate (Kandziora *et al.,* 2004; Lippman *et al.,* 2004; Smit *et al.,* 2006; Wuisman and Smit, 2006). Reduced stiffness of cages made from this composite may eliminate stress shielding (Kandziora *et al.,* 2004; Wuisman and Smit, 2006) (see §4.2 for more detail).

The cage model with 10 side-holes and vertebrae models with Young's modulus values of 12 and 30 GPa produced in Chapter 3 were used in this study (Chapter 4). A range of Young's modulus values (2 to 13 GPa) for the composite with volume fractions between 0.2 and 0.3 of 45S5 Bioglass were then calculated using Reuss and Voigt models. The von Mises and normal compressive stress levels and displacements were determined using the composite Young's modulus range. In all the models, the von Mises stress was highest at the cage-vertebrae interface with peak stress levels of between 14 and 20 MPa and maximum displacements of between 3.5

and 18.7 µm. The average normal compressive stress for all the models analysed in this study was 4.5 MPa (see §4.4.2 for more detail). Increasing the Young's modulus of the vertebrae from 12 to 30 GPa increased the maximum von Mises stress predicted by 13% and decreased the maximum displacement by 19%. The peak von Mises stress obtained is five times lower than the compressive strength of PLDLA (100 MPa); this suggests that the 45S5 Bioglass/PLDLA composite as a fusion cage material is unlikely to fail in compression.

The next step in investigating the feasibility of a cage made from 45S5 Bioglass/PLDLA would be to manufacture a cage made from this composite and mechanically test it *in vitro* mimicking *in vivo* conditions (i.e. compression test on the cage while it is surrounded by physiological fluid). This will allow evaluation of mechanical performance of this cage while degrading. Although clinical evaluation of a cage made from this composite may be difficult, it is however necessary because as the cage degrades, it loses its mechanical strength. Hence, it is essential to determine that the growth rate of the surrounding tissues matches the degradation rate of the composite.

6.4. Vertebral body edge cutter

A surgical instrument to aid implantation of a range of lumbar spinal fusion cages was developed. This instrument was required to remove parts of the vertebral edge that obscure the screw holes on the cage for fixation screw insertion. The development and evaluation of concept designs were presented and discussed. Potential risks were considered and modifications were performed on the selected concept. Functional prototypes were manufactured and tested on sheep lumbar vertebrae and by an orthopaedic surgeon on a cadaver. The results showed that the newly designed instrument functions as required and removes the required amount of the vertebrae edge (see §5.6 for more detail).

Prior to bringing the instrument to market, more tests need to be performed on cadaveric specimens. Ultimately clinical trials on living people with careful monitoring are required as a continuation of the development process. Development of the instrument may be progressed further in the future, for example for cervical fusion cages. Any further development to the design of the instrument needs to be rigorously tested in accordance with industry regulations and standards (e.g. BS EN ISO 13485:2003, BS EN ISO 9001:2008 and Quality System Regulation 21 CFR 820).

6.5. Concluding remarks

The main conclusions of this thesis are listed below:

- a cervical spinal fusion cage with (up to 10) side-holes is unlikely to fail under compression; the stress levels were fairly constant for all the models and did not change substantially with the number of side-holes. The stress values obtained were also much lower than the compressive strength of the cage material (PEEK);

- a cervical spinal fusion cage made from 45S5 Bioglass/PLDLA composite is unlikely to fail under compression; the stress values obtained were much lower than the compressive strength of pure PLDLA;
- a surgical instrument to aid implantation of a range of lumbar spinal fusion cages was developed; specifically, the instrument removes parts of the vertebrae that obscure the holes for screw insertion.

APPENDIX A. DETAILS OF SIDE-HOLES AND THEIR POSITIONS

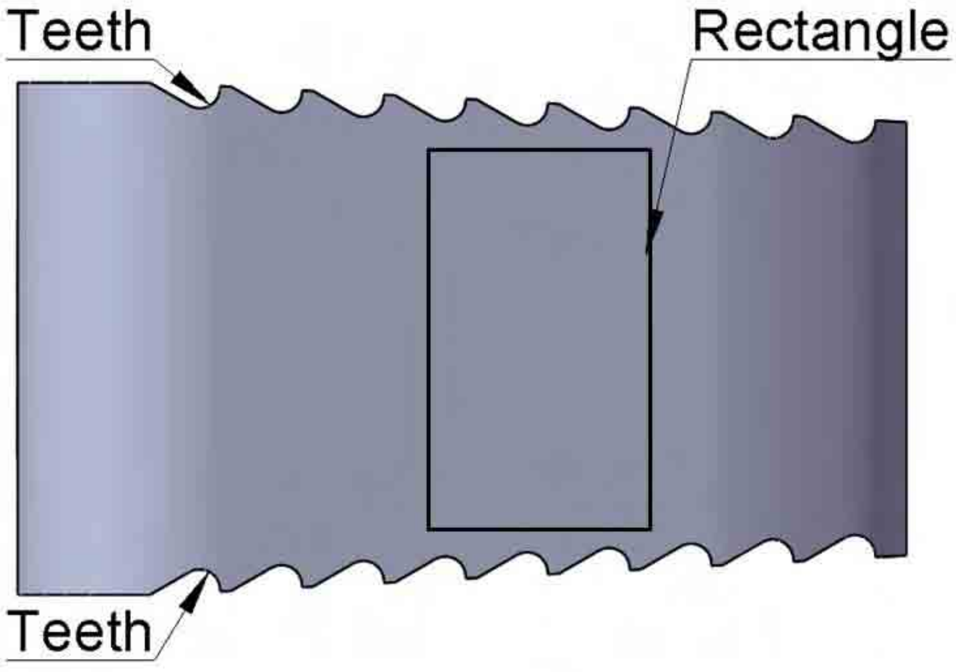

(a)

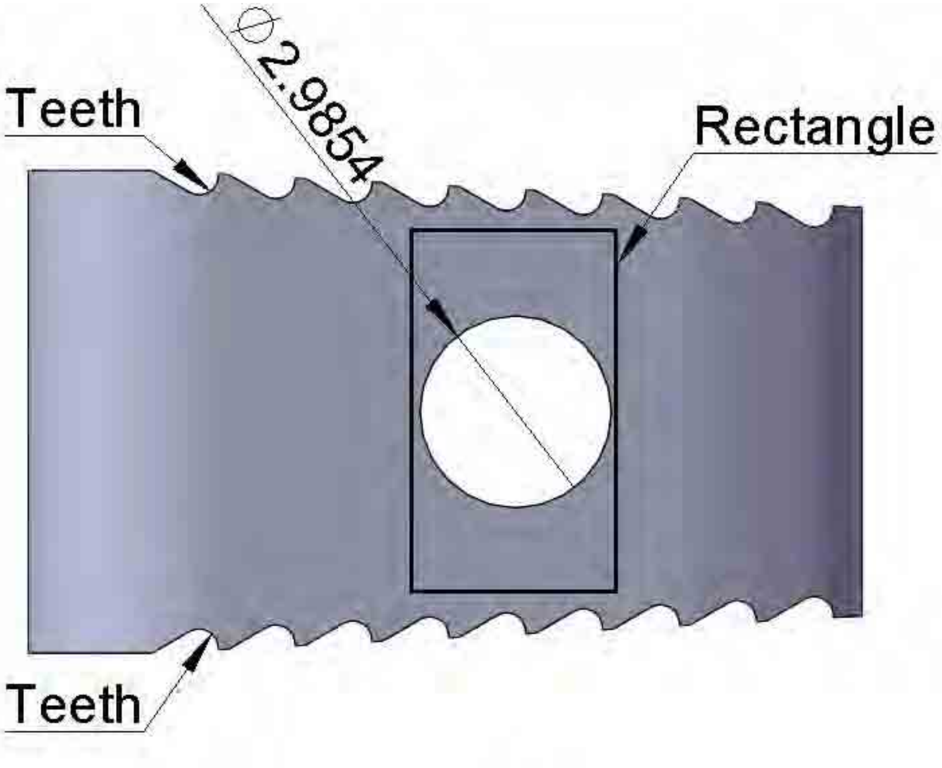

(b)

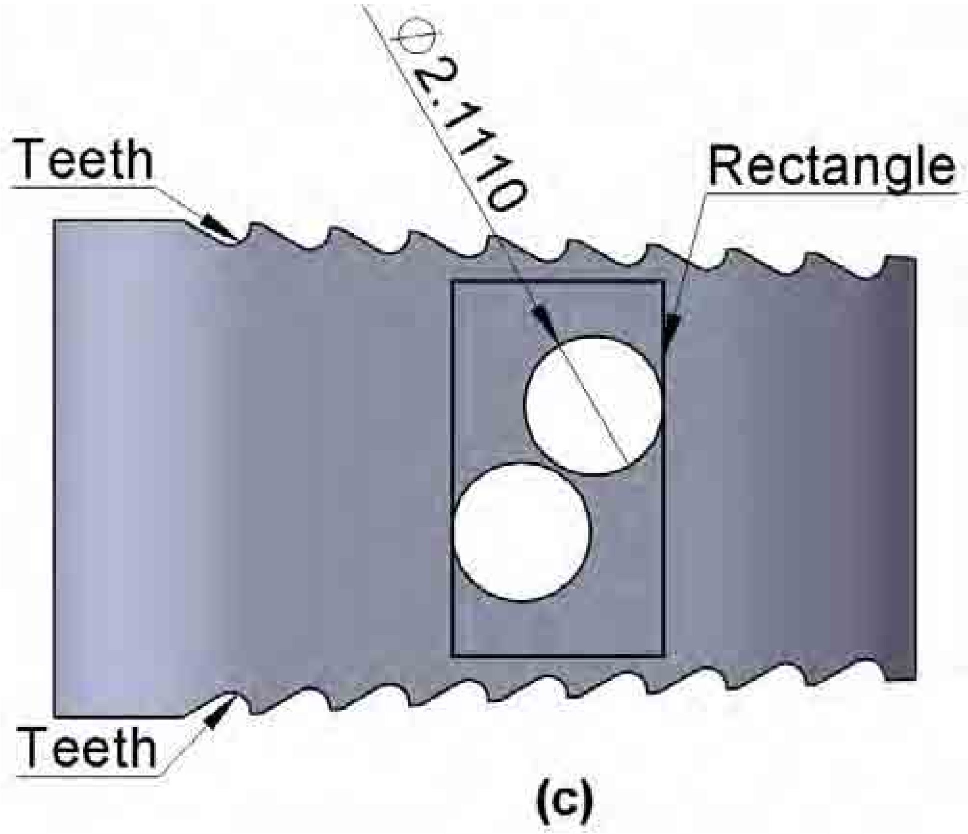
Φ2.1110
Teeth
Rectangle
Teeth
(c)

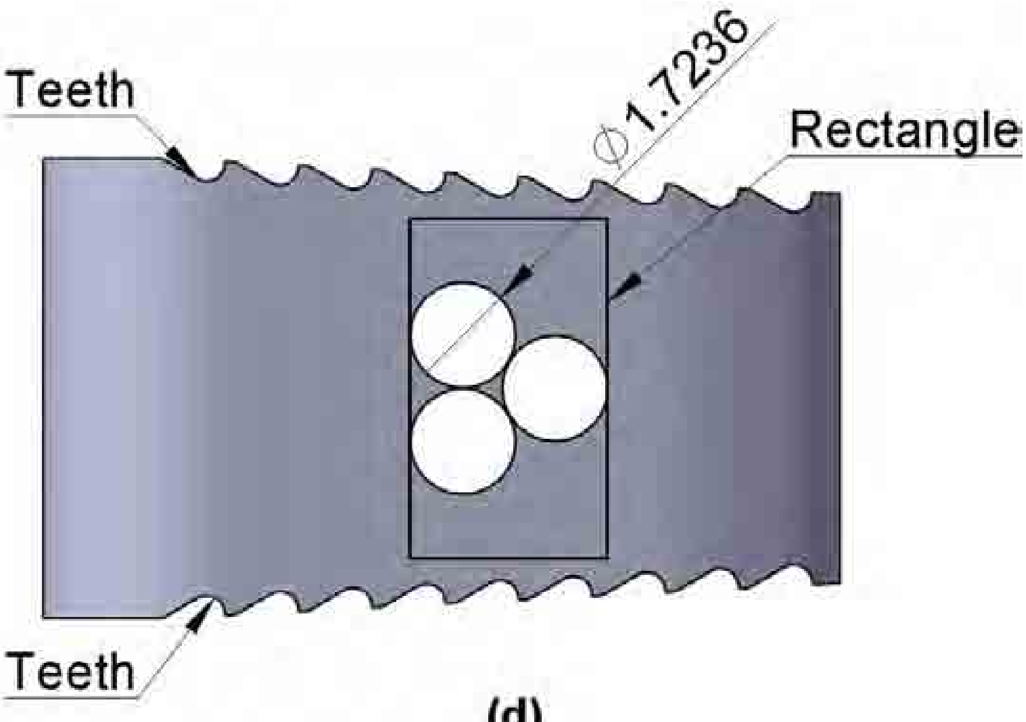

(d)

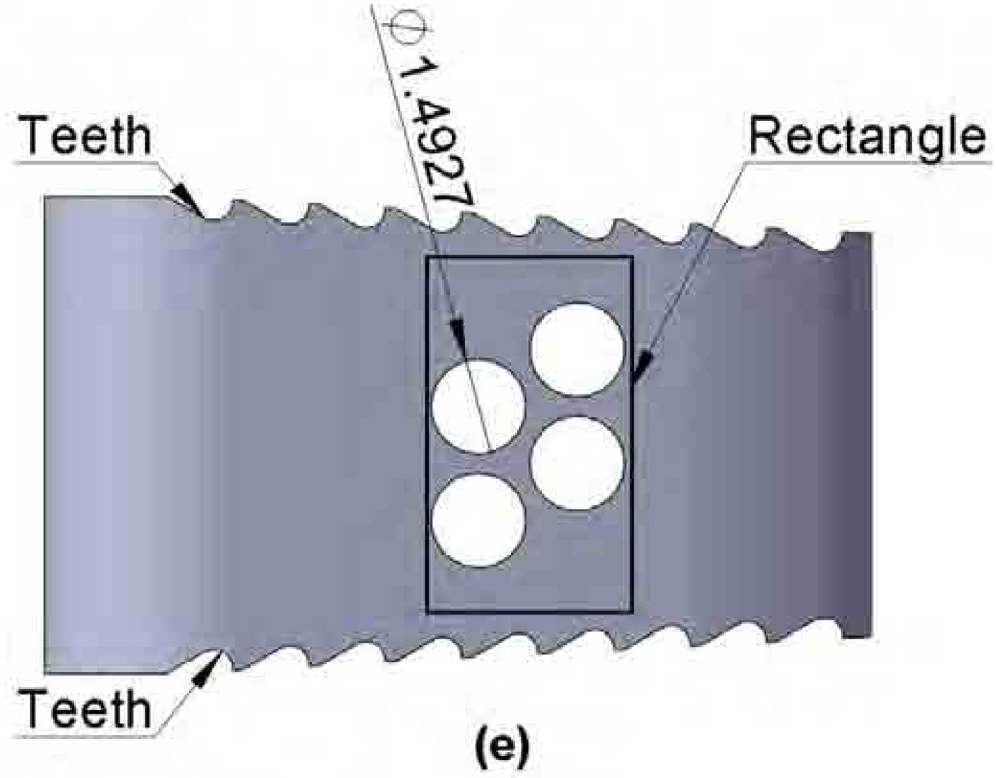

(e)

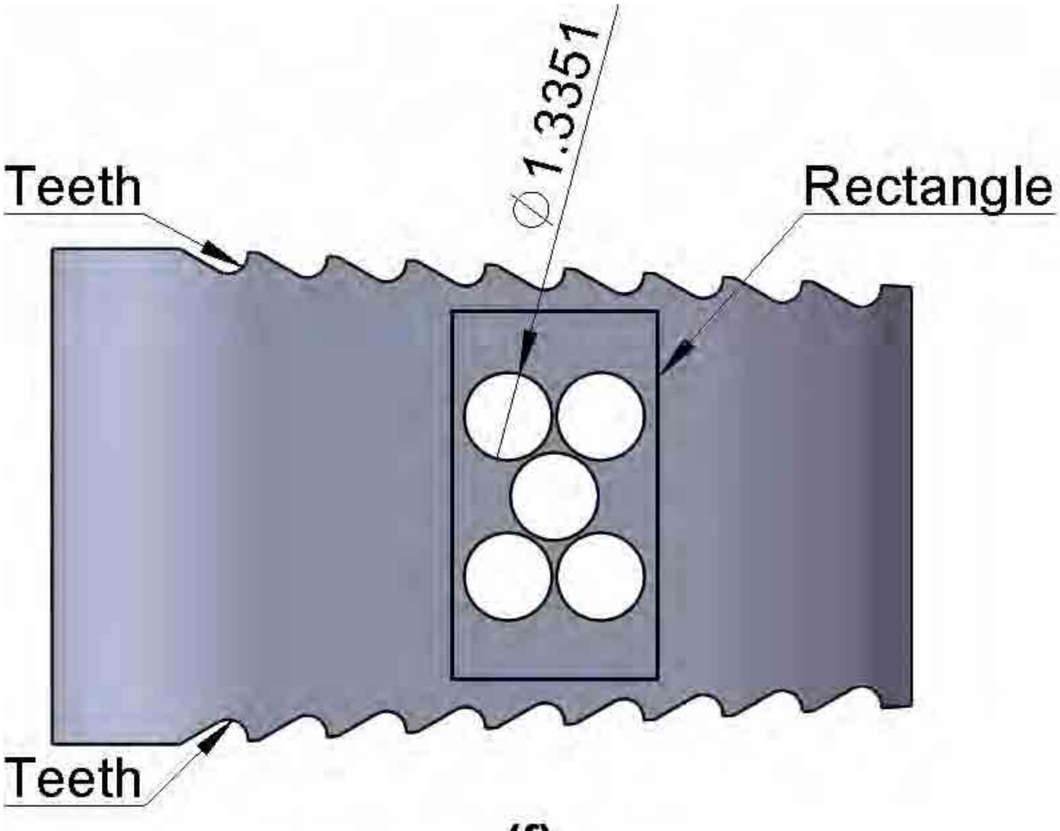

(f)

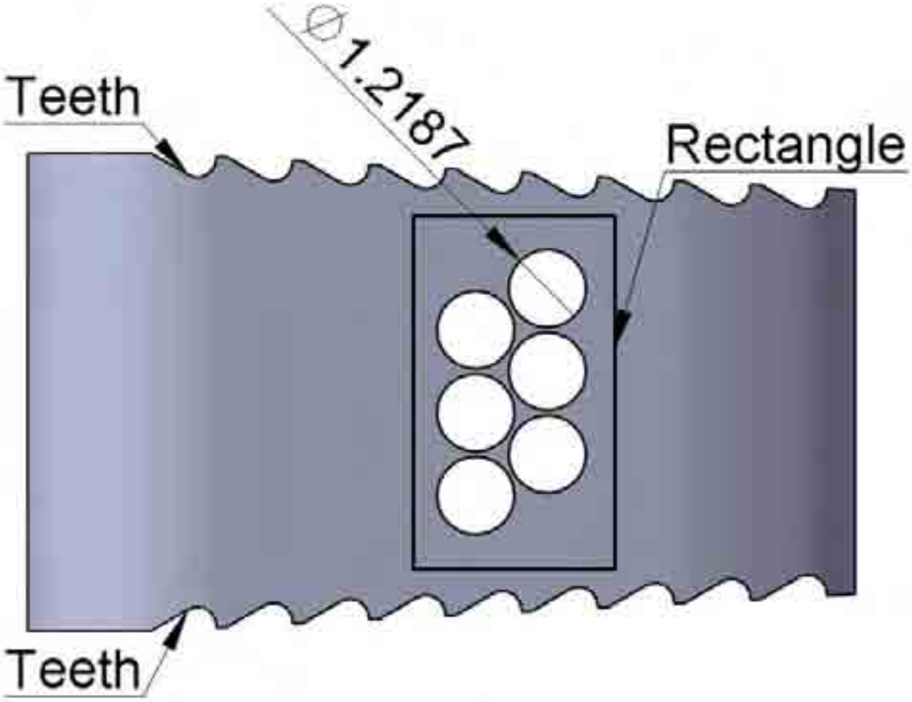

(g)

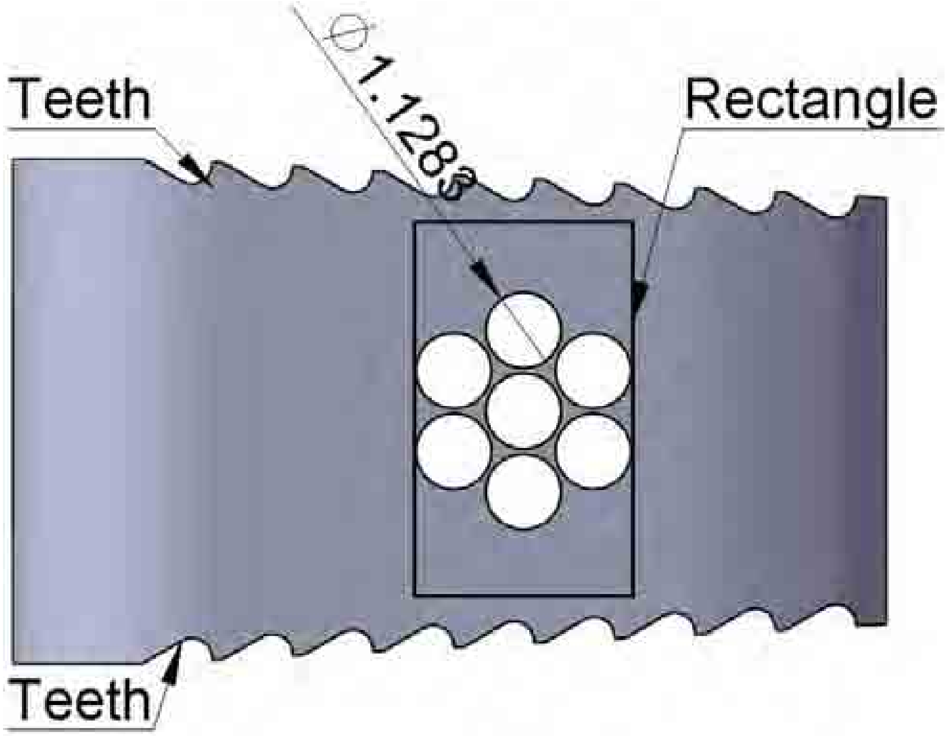

(h)

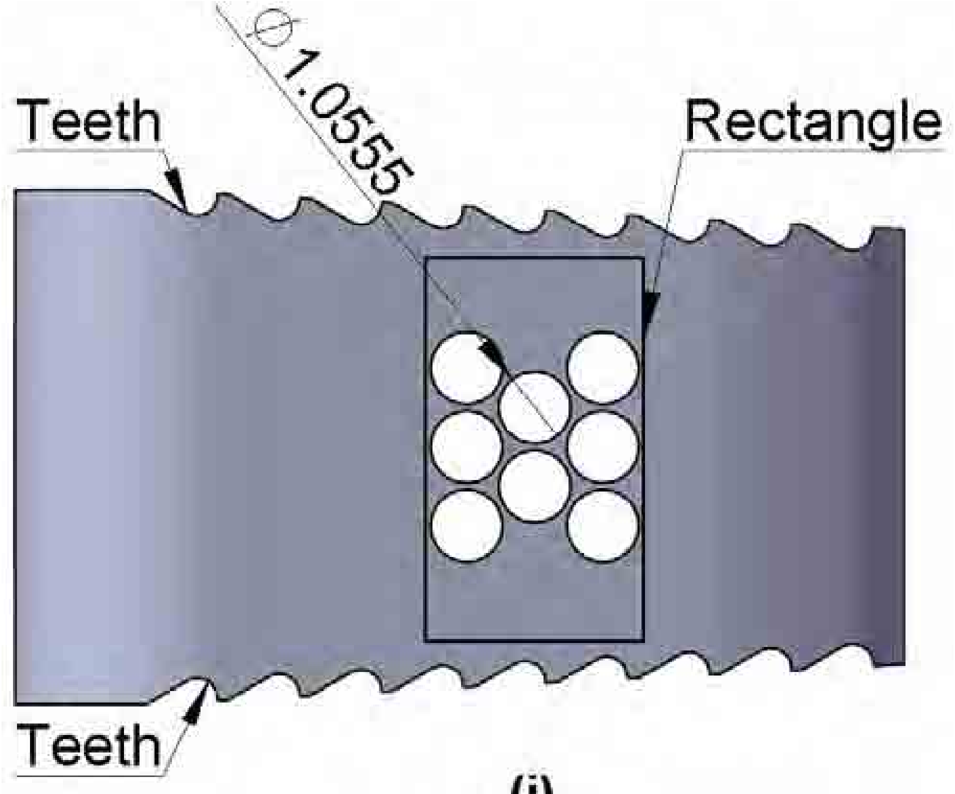

(i)

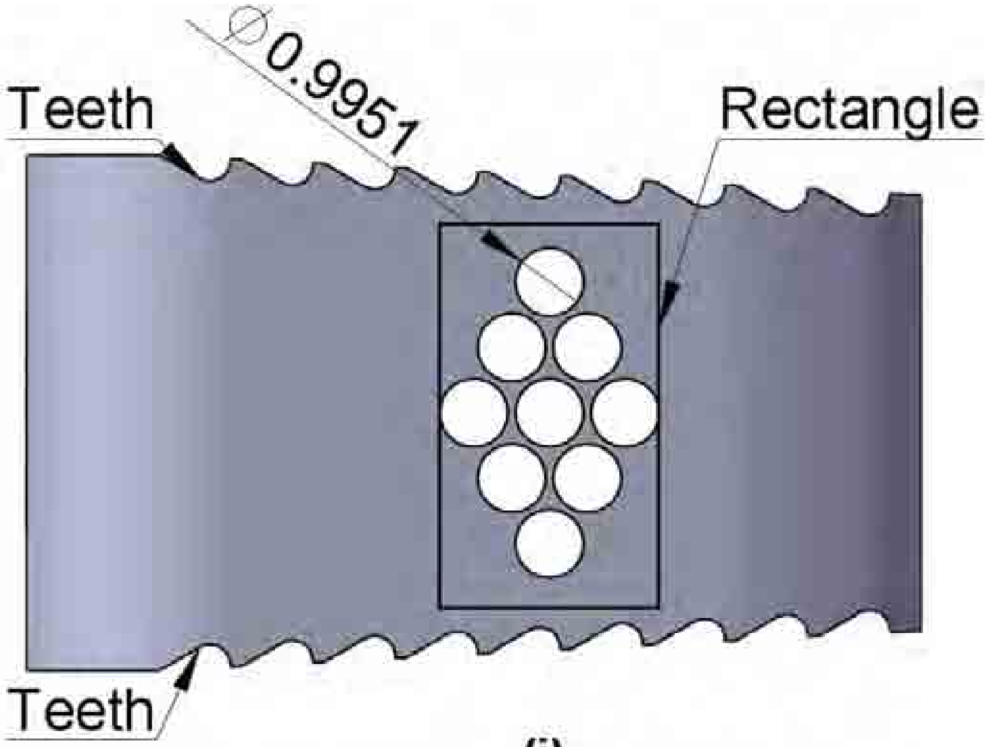

(j)

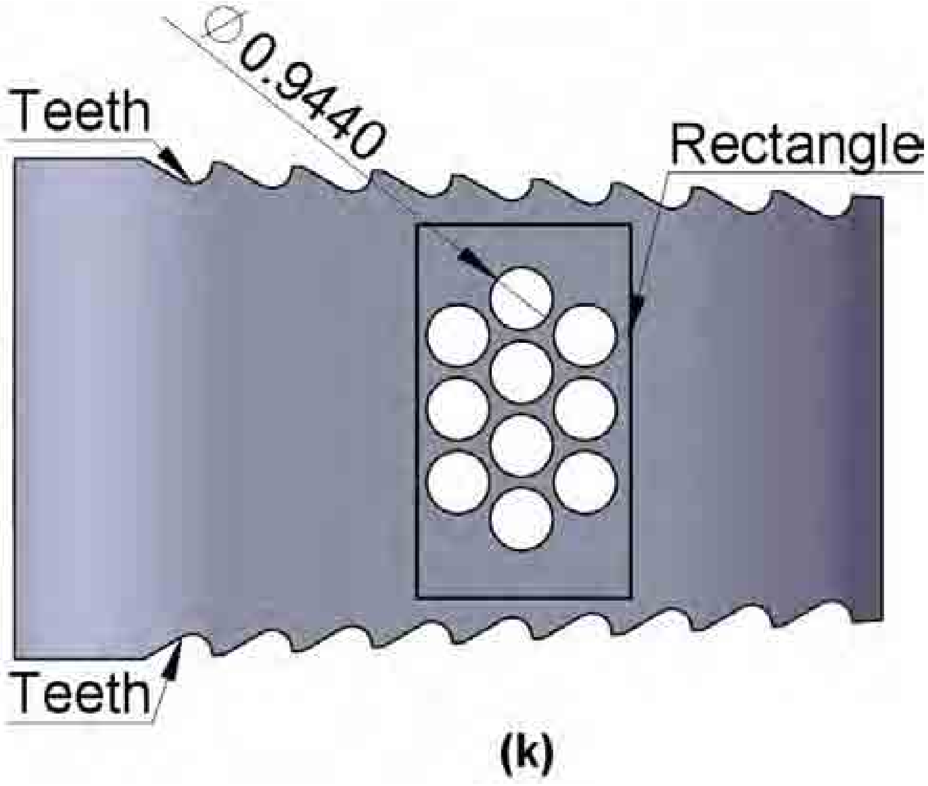

Figure A.1. Details of side-holes and their positions for each cage model with (a) 0, (b) 1, (c) 2, (d) 3, (e), 4, (f) 5, (g) 6, (h) 7, (i) 8, (j) 9 and (k) 10 side-holes.

APPENDIX B. CONVERGENCE TESTS TO DETERMINE THE CAGE MESH SIZE

(see next page)

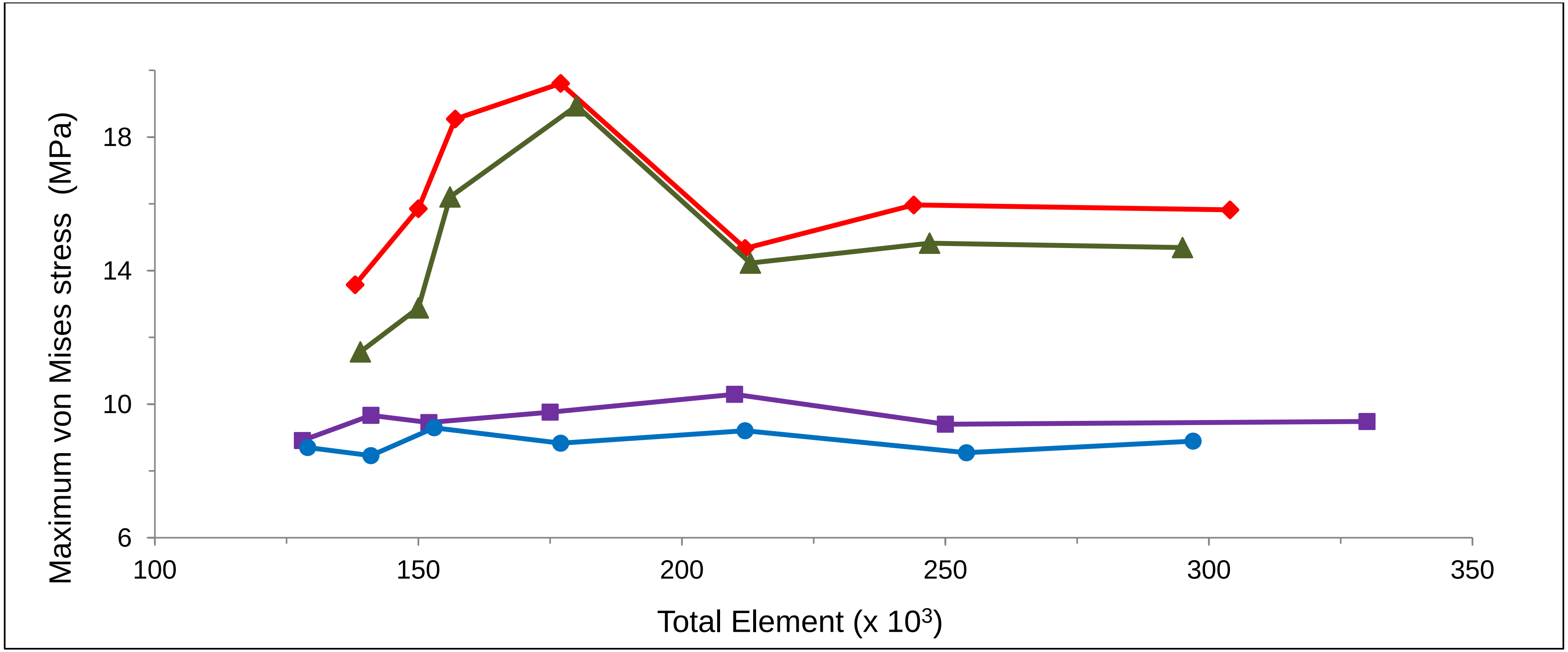

Figure B.1. Graph of maximum von Mises stress plotted against number of elements showing convergence of four models. The lines shown are: cage with no teeth and no side-hole (●), cage with no teeth and one side-hole (■), cage with teeth and no side-hole (▲) and cage with teeth and one side-hole (◆).

APPENDIX C. VALIDATION RESULTS

Table. C.1. E_{ABS} values calculated using the second-order polynomial ($\sigma = 3262.5\varepsilon^2 + 33.843\varepsilon$) from the first ABS experimental block test. These E_{ABS} values were used in the FEA to determine the maximum von Mises stress levels and displacements.

Load (N)	EABS (MPa)	Maximum von Mises stress (MPa)	Maximum displacement (μm)
0	0	0	0
9	45	0	12
20	52	1	23
30	57	1	30
40	63	1	37
50	66	1	44
60	73	2	48
70	76	2	53
80	82	2	57
92	85	2	63
102	89	3	67
110	93	3	69
120	97	3	72
131	101	3	75
139	104	4	78
151	107	4	82

Table. C.2. E_{ABS} values calculated using the second-order polynomial ($\sigma = 3478.5\varepsilon^2 + 28.324\varepsilon$) from the second ABS experimental block test. These E_{ABS} values were used in the FEA to determine the maximum von Mises stress levels and displacements.

Load (N)	E_{ABS} (MPa)	Maximum von Mises stress (MPa)	Maximum displacement (μm)
0	0	0	0
10	42	0	14
21	50	1	24
29	55	1	31
39	60	1	38
50	66	1	44
60	72	2	49
71	76	2	54
81	83	2	57
90	84	2	62
97	89	3	63
109	94	3	68
120	97	3	72
130	103	3	73
141	105	4	78
153	109	4	81

Table. C.3. E_{ABS} values calculated using the second-order polynomial ($\sigma = 3462\varepsilon^2 + 28.515\varepsilon$) from the third ABS experimental block test. These E_{ABS} values were used in the FEA to determine the maximum von Mises stress levels and displacements.

Load (N)	E_{ABS} (MPa)	Maximum von Mises tress (MPa)	Maximum displacement (μm)
0	0	0	0
10	43	0	14
19	48	0	23
31	55	1	32
41	60	1	40
49	65	1	44
60	73	2	48
73	77	2	55
81	81	2	58
92	86	2	62
99	89	3	65
112	93	3	70
121	98	3	72
131	102	3	75
139	105	4	77
150	109	4	80

APPENDIX D. FEA AND EXPERIMENTAL RESULTS

(see next page)

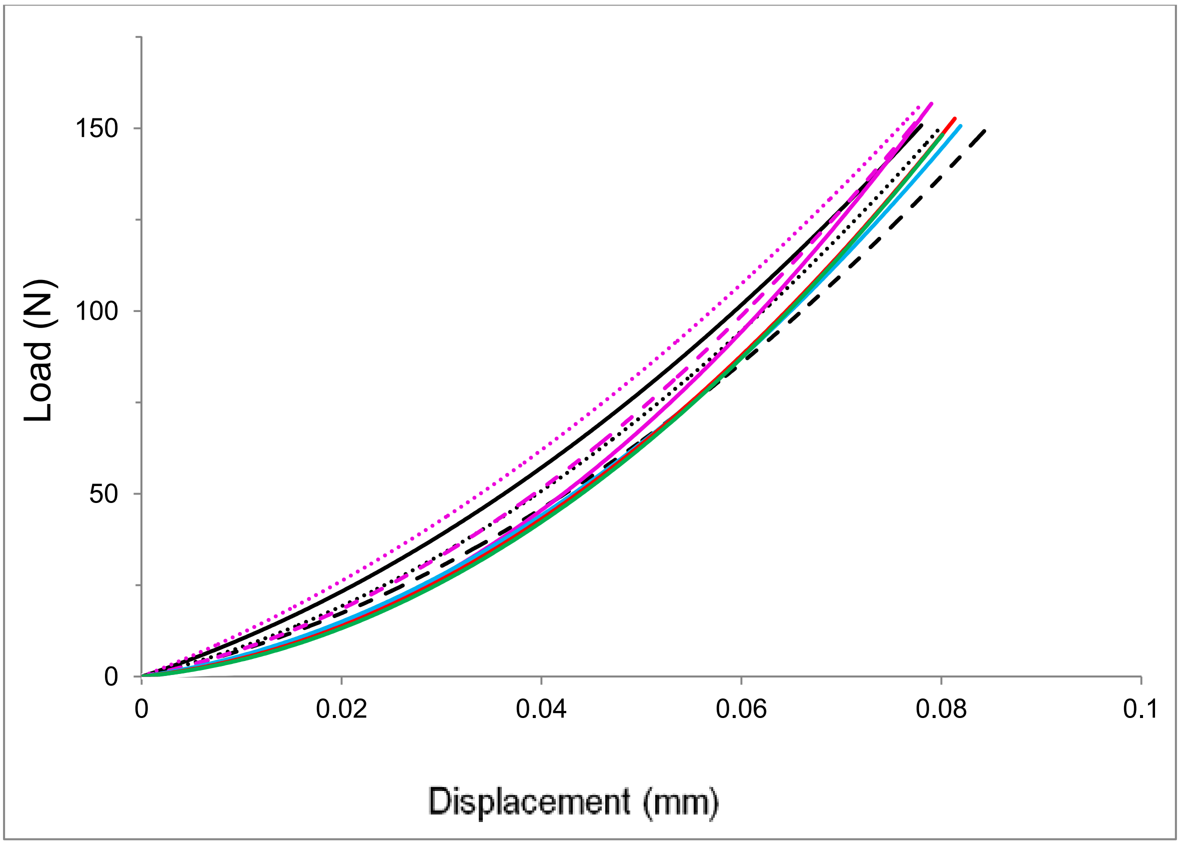

Figure D.1. Load against displacement curves from experimental and FEA tests on ABS cages; in order to calculate the stiffness of the curves, second-order polynomials were fitted to all the graphs. For clarity, the data points are hidden and only the second-order polynomials are shown. The equations derived from polynomials are as follows: Experimental ABS cage 1: test one ($F = 15296x^2 + 657.96x$), test two ($F = 14038x^2 + 587.19x$) and test three ($F = 13264x^2 + 898.52x$). Experimental ABS cage 2: test one ($F = 12034x^2 + 1068.70x$), test two ($F = 17972x^2 + 566.71x$) and test three ($F = 21680x^2 + 271.09x$). FEA from cage model: test one ($F = 17556x^2 + 400.45x$), test two ($F = 19313x^2 + 305.36x$) and test three ($F = 19769x^2 + 266.65x$). In all equations, F and x are load and displacement, respectively. The lines for the experimental tests are: the black curves from the first and the pink curves from the second ABS cages; dotted, dashed and continuous lines are from the first, second and third tests, respectively. The lines for the FEA are: first, second and third tests are shown in blue, red and green, respectively. The equations were differentiated and the stiffness at displacements of 0.04 and 0.07 mm was then determined for both experimental and FEA results (see Table 3.3).

APPENDIX E. RESULTS OF FEA ON A RANGE OF POSSIBLE YOUNG'S MODULUS VALUES FOR THE 45S5 BIOGLASS/PLDLA COMPOSITE

(see next page)

Table E.1. Maximum von Mises stress and displacement of the cage model when analysed with the $E_{Composite}$ values ranging between 2 and 13 GPa and Poisson's ratio of 0.35. The assembled model had a total of 441,350 nodes and 307,722 elements.

$E_{Composite}$ (GPa)	$E_{Cortical}$ = 12 GPa		$E_{Cortical}$ = 30 GPa	
	Maximum von Mises stress (MPa)	Maximum displacement (μm)	Maximum von Mises stress (MPa)	Maximum displacement (μm)
2	16	18.3	19	16.8
3	15	13.1	18	11.5
4	14	10.5	17	8.9
5	13	8.9	16	7.3
6	13	7.9	16	6.3
7	15	5.5	15	5.5
8	15	5.0	15	5.0
9	14	4.5	14	4.5
10	14	4.2	14	4.2
11	14	3.9	14	3.9
12	13	3.7	13	3.7
13	13	3.5	13	3.5
Mean	**14**	**7.4**	**15**	**6.8**

Table E.2. Maximum von Mises stress and displacement of the cage model when analysed with the $E_{Composite}$ ranging between 2 and 13 GPa and Poisson's ratio of 0.4. The assembled model had a total of 441,350 nodes and 307,722 elements.

$E_{Composite}$ (GPa)	$E_{Cortical}$ = 12 GPa		$E_{Cortical}$ = 30 GPa	
	Maximum von Mises stress (MPa)	Maximum displacement (µm)	Maximum von Mises stress (MPa)	Maximum displacement (µm)
2	16	17.9	18	16.3
3	14	12.8	17	11.2
4	13	10.2	16	8.7
5	12	8.7	16	7.1
6	12	7.7	15	6.1
7	12	7.0	14	5.4
8	13	6.4	14	4.9
9	13	6.0	13	4.4
10	14	5.6	13	4.1
11	14	5.4	13	3.8
12	15	5.1	12	3.6
13	15	4.9	12	3.4
Mean	**14**	**8.1**	**15**	**6.6**

Table E.3. Maximum von Mises stress and displacement of the cage model when analysed with the $E_{Composite}$ ranging between 2 and 13 GPa and Poisson's ratio of 0.45. The assembled model had a total of 441,350 nodes and 307,722 elements.

$E_{Composite}$ (GPa)	$E_{Cortical}$ = 12 GPa		$E_{Cortical}$ = 30 GPa	
	Maximum von Mises stress (MPa)	Maximum displacement (μm)	Maximum von Mises stress (MPa)	Maximum displacement (μm)
2	14	17.2	16	15.6
3	13	12.4	15	10.8
4	12	9.9	15	8.3
5	11	8.5	14	6.9
6	12	7.5	13	5.9
7	12	6.8	13	5.2
8	13	6.3	12	4.7
9	13	5.9	12	4.3
10	14	5.5	12	4.0
11	14	5.3	11	3.7
12	15	5.0	11	3.5
13	15	4.8	11	3.3
Mean	**13**	**7.9**	**13**	**6.3**

Table E.4. Maximum von Mises stress and displacement of the cage model when analysed with the $E_{Composite}$ ranging between 2 and 13 GPa and Poisson's ratio of 0.49. The assembled model had a total of 441,350 nodes and 307,722 elements.

$E_{Composite}$ (GPa)	$E_{Cortical}$ = 12 GPa		$E_{Cortical}$ = 30 GPa	
	Maximum von Mises stress (MPa)	Maximum displacement (μm)	Maximum von Mises stress (MPa)	Maximum displacement (μm)
2	13	16.5	14	14.8
3	12	11.9	14	10.2
4	11	9.6	13	8.0
5	11	8.2	13	6.6
6	11	7.3	12	5.7
7	12	6.6	12	5.0
8	12	6.1	12	4.5
9	13	5.7	12	4.1
10	13	5.4	11	3.8
11	14	5.1	11	3.6
12	14	4.9	11	3.4
13	15	4.7	11	3.2
Mean	**13**	**7.7**	**12**	**6.1**

APPENDIX F. ENGINEERING DRAWING OF THE WHOLE INSTRUMENT WITH THE UNIVERSAL JOINT HANDLE

(see next page)

APPENDIX G. ENGINEERING DRAWING OF THE INSTRUMENT HEAD

(see next page)

APPENDIX H. ENGINEERING DRAWING OF THE INSTRUMENT SHAFT

(see next page)

APPENDIX I. ENGINEERING DRAWING OF THE INSTRUMENT BONE CUTTER

(see next page)

APPENDIX J. VB EDGE CUTTER TRAINING GUIDE

(see next page)

APPENDIX K. BONE-ASHING TO DETERMINE THE SHEEP AND PIG LUMBAR BONE MINERAL DENSITY

K.1. Introduction

Animal models such as sheep and pig are usually used in biomechanical tests (Kettler *et al.*, 2007), because the availability of human models is limited. Bone-ashing (Holmes *et al.*, 1993) was used in this study to determine the bone mineral densities of these two animal models. Bone with higher mineral density has a higher mechanical stiffness and hardness (Coats *et al.*, 2003). Hence, the denser animal bone will provide the most strenuous specimens for the cutting tests carried out in Chapter 5 of this thesis.

K.2. Materials and methods

Bone mineral density was determined by ashing the cancellous bone of three different sheep and pig lumbar vertebrae (purchased from a local butcher). Blocks of cancellous bone (~10 mm × 10 mm× 10 mm) were excised from sheep and pig lumbar and the marrow was washed out. The specimens were placed in separate crucibles (the mass of each empty crucible was previously measured) and were dried using a Carbolite natural convection laboratory oven (Carbolite, Hope Valley, UK) for 12 hours at 120˚ C. The dishes containing the specimens were cooled for 4 hours in ambient temperature in a desiccator over silica gel (601-041 silica gel, RS Components Ltd., Corby, UK), which was used to absorb any moisture in the desiccator. The volume of each specimen was then measured by microtomography (SkyScan 1072, SkyScan, Kontich, Belgium). The crucibles containing the specimens (Figure K.1) were heated (ashed) in the Carbolite natural convection laboratory oven (Figure K.2) for 48 hours at 800˚C and then cooled for 4 hours in ambient temperature in a desiccator over silica gel. The mass of the crucibles containing the specimens were then measured and the specimen mass (ash mass) was determined by subtracting the mass of the crucibles from the mass of the crucibles containing the specimens. The bone mineral density was determined by dividing the ash mass by the determined volume. This procedure was carried out on 12 different specimens for each species.

Note, before each test, the crucibles were heated for 48 hours at 800˚ C in the Carbolite oven and were then cooled for 4 hours in ambient temperature in a desiccator over silica gel. The mass of each crucible was measured before and after heating to ensure that it remained unchanged. Each mass measurement throughout the experiment was repeated three times and the mean value was used.

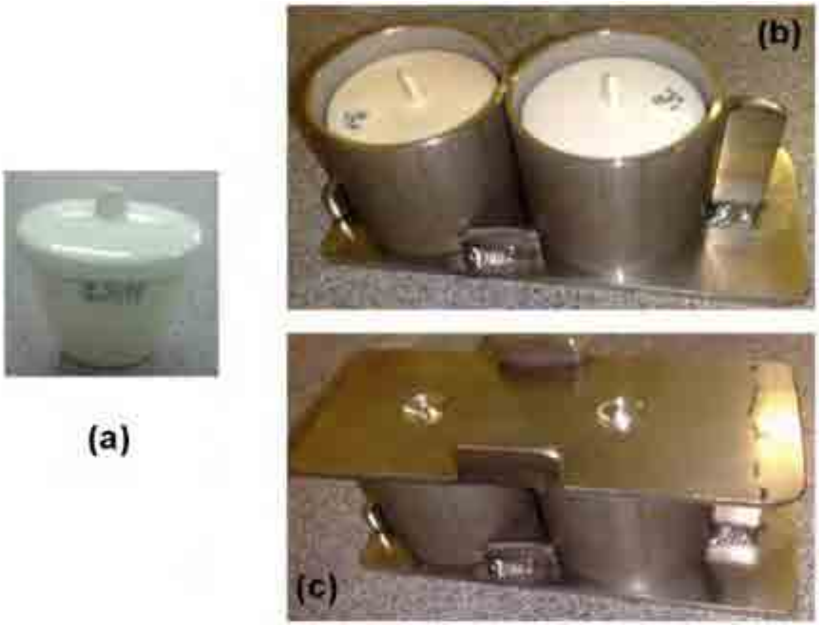

Figure K.1. (a) Crucible. (b) Crucibles were placed in a titanium holder to be placed in the oven. (c) Titanium holder containing the crucibles with the titanium lid.

Figure K.2. (a) Carbolite natural convection laboratory oven. (b) Titanium holder containing the crucibles in the oven.

K.3 Results

Table K.1 shows the bone mineral densities determined for both sheep and pig lumbar vertebrae. The mean bone mineral density values of sheep and pig lumbar spine are 0.37 and 0.33 $g.cm^{-3}$, respectively with standard deviations of 0.06 and 0.03 $g.cm^{-3}$ for sheep and pig lumbar spine, respectively. Two-sample T-tests (Montgomery *et al.,* 2007) (significance level $p < 0.001$) were carried out on the results and showed that mineral densities of the sheep and pig are not significantly different from each other and that both are significantly higher than human (0.15 $g.cm^{-3}$, Holmes *et al.,* 1993).

Table K.1. Bone mineral density of sheep and pig lumbar spine.

Test set	Specimen	Bone mineral density (ash mass/volume) ($g.cm^{-3}$)
1	Sheep	0.24
	Pig	0.32
2	Sheep	0.32
	Pig	0.35
3	Sheep	0.43
	Pig	0.38
4	Sheep	0.28
	Pig	0.34
5	Sheep	0.27
	Pig	0.32
6	Sheep	0.34
	Pig	0.33
7	Sheep	0.44
	Pig	0.30
8	Sheep	0.31
	Pig	0.28
9	Sheep	0.43
	Pig	0.30
10	Sheep	0.42
	Pig	0.39
11	Sheep	0.44
	Pig	0.34
12	Sheep	0.37
	Pig	0.34
Mean mineral density	**Sheep**	**0.37**
	Pig	**0.33**
Standard deviation	**Sheep**	**0.06**
	Pig	**0.03**

LIST OF REFERENCES

Abu Bakar, M. S., Cheng, M. H. W., Tang, S. M., Yu, S. C., Liao, K., Tan, C. T., Khor, K. A. and Cheang, P. (2003) Tensile properties, tension-tension fatigue and biological response of polyetheretherketone-hydroxyapatite composites for load-bearing orthopedic implants. *Biomaterials*, **24**(13), 2245-2250.

Adam, C., Pearcy, M. and McCombe, P. (2003) Stress analysis of interbody fusion - finite element modelling of intervertebral implant and vertebral body. *Clinical Biomechanics*, **18**(4), 265-272.

Aitchison, G. A., Hukins, D. W. L., Parry, J. J., Shepherd, D. E. T. and Trotman, S. G. (2009) A review of the design process for implantable orthopedic medical devices. *The Open Biomedical Engineering Journal*, **3**, 21-27.

Aspden, R. M., Hickey, D. S. and Hukins, D. W. L. (1981) Determination of collagen fibril orientation in the cartilage of vertebral end plates. *Connective Tissue Research*, **9**(2), 83-87.

ASTM F 2077-03: *Standard test methods for intervertebral body fusion devices*. Pennsylvania, American Society for Testing and Materials (ASTM) International.

Axelsson, P., Johnsson, R. and Strömqvist, B. (2009) Stability after anterior lumbar fusion with interbody cages: a radiostereometric evaluation. *The Open Spine Journal*, **1**, 14-17.

Bayraktar, H. H., Adams, M. F., Hoffmann, P. F., Lee, D. C., Gupta, A., Papadopoulos, P. and Keaveny, T. M. (2004) *Micromechanics of the Human Vertebral Body*. Proceedings of the 50th Annual Meeting of the Orthopaedic Research Society, 7-10 March 2004, San Francisco, CA, USA.

Benham, P. P. and Crawford, R. J. (1987) *Mechanics of engineering materials*. New York, John Wiley & Sons, Inc.

Blaker, J. J., Gough, J. E., Maquet, V., Notingher, I. and Boccaccini, A. R. (2003) In vitro evaluation of novel bioactive composites based on Bioglass®-filled polylactide foams for bone tissue engineering scaffolds. *Journal of Biomedical Materials Research, Part A*, **67A**(4), 1401-1411.

Bogduk, N. (2005) *Clinical anatomy of the lumbar spine and sacrum.* 4th edition, Edinburgh, Elsevier Churchill Livingston.

Bryce, R., Aspden, R. M. and Wytch, R. (1995) Stiffening effect of cortical bone on vertebral cancellous bone in situ. *Spine*, **20**(9), 999-1003.

BS EN ISO 9001:2008; *Quality management systems - Requirements.* London, British Standards Institution.

BS EN ISO 13485:2003; *Medical devices - Quality management systems - Requirements for regulatory purposes*. London, British Standards Institution.

BS EN ISO 14971:2009; *Medical devices - Application of risk management to medical devices*. London, British Standards Institution.

BS ISO 18192-1:2011; *Implants for surgery - wear of total intervertebral spinal disc prostheses – part 1*: *Loading and displacement parameters for wear testing and corresponding environmental conditions for test*. London, British Standards Institution.

Chen, J. F. and Lee, S. T. (2006) The polymethyl methacrylate cervical cage for treatment of cervical disk disease Part III. Biomechanical properties. *Surgical Neurology*, **66**(4), 367-370.

Cho, D. Y., Liau, W. R., Lee, W. Y., Liu, J. T., Chiu, C. L. and Sheu, P. C. (2002) Preliminary experience using a polyetheretherketone (PEEK) cage in the treatment of cervical disc disease. *Neurosurgery*, **51**(6), 1343-1349.

Cho, D. Y., Lee, W. Y. and Sheu, P. C. (2004) Treatment of Multilevel Cervical Fusion with Cages. *Surgical Neurology*, **62**(5), 378-386.

Cho, W., Wu, C., Mehbod, A. A. and Transfeldt, E. E. (2008) Comparison of cage designs for transforaminal lumbar interbody fusion: a biomechanical study. *Clinical Biomechanics*, **23**(8), 979-985.

Chou, Y. C., Chen, D. C., Hsieh, W. A., Chen, W. F., Yen, P. S., Harnod, T., Chiou, T. L., Chang, Y. L., Su, C. F., Lin, S. Z. and Chen, S. Y. (2008) Efficacy of anterior cervical fusion: comparison of titanium cages, polyetheretherketone (PEEK) cages and autogenous bone grafts. *Journal of Clinical Neuroscience*, **15**(11), 1240-1245.

Coats, A. M., Zioupos, P. and Aspden, R. M. (2003) Material properties of subchondral bone from patients with osteoporosis or osteoarthritis by microindentation testing and electron probe microanalysis. *Calcified Tissue International*, **73**(1), 66-71.

COSMOSWorks Designer. (2007) *Training Manual, (Document number: PMT0140-ENG)*, SolidWorks, Santa Monica, USA.

Denman, E. E. (1992) *The anatomy of the human skeleton, a question and answer tutorial text*. Edinburgh, Churchill Livingston.

Edwards, W. T., Zheng, Y. and Ferrara, L. A. (2001) Structural features and thickness of the vertebral cortex in the thoracolumbar spine. *Spine*, **26**(2), 218-225.

Epari, D. R., Kandziora, F. and Duda, G. N. (2005) Stress shielding in box and cylinder cervical interbody fusion cage designs. *Spine*, **30**(8), 908-914.

Ferguson, S. J., Visser, J. M. A. and Polikeit, A. (2006) The long-term mechanical integrity of non-reinforced PEEK-OPTIMA polymer for demanding spinal applications: experimental and finite-element analysis. *European Spine Journal*, **15**(2), 149-156.

Galbusera, F., Bellini, C. M., Costa, F., Assietti, R. and Fornari, M. (2008) Anterior cervical fusion: a biomechanical comparison of 4 techniques. *Journal of Neurosurgery Spine*, **9**(5), 444-449.

Hattori, S., Oda, H., Kawai, S. and Ube-Shi. (1981) Cervical intradiscal pressure in movements and traction of the cervical spine. *Zeitschrift fur Orthopadie*, **119**, 568-569.

Hee, H. T. and Kundnani, V. (2010) Rationale for use of polyetheretherketone polymer interbody cage device in cervical spine surgery. *The Spine Journal*, **10**(1), 66-69.

Hench, L. L. (1998) Bioceramics. *Journal of the American Ceram Society*, **81**(7), 1705-1728.

Hibbeler, R C. *Statics and mechanics of materials*. SI edition, Singapore, Prentice-Hall, Inc.

Hickey, D. S. and Hukins, D. W. L. (1980) Relationship between the structure of the annulus fibrosus and the function and failure of the intervertebral disc. *Spine*, **5**(2), 106-116.

Hojo, Y., Kotani, Y., Ito, M., Abumi, K., Kadosawa, T., Shikinami, Y. and Minami, A. (2005) A biomechanical and histological evaluation of a bioresorbable lumbar interbody fusion cage. *Biomaterials*, **26**(15), 2643-2651.

Holmes, A. D., Hukins, D. W. L. and Freemont, A. J. (1993) End-plate displacement during compression of lumbar vertebra-disc-vertebra segments and the mechanism of failure. *Spine*, **18**(1), 128-135.

Hong, Z., Reis, R. L. and Mano, J. F. (2008) Preparation and in vitro characterization of scaffolds of poly(L-lactic acid) containing bioactive glass ceramic nanoparticles. *Acta Biomaterialia*, **4**(5), 1297-1306.

Hukins, D. W. L. (1988) *Disc structure and function.* In *The biology of the intervertebral disc, edited by* **Ghosh, P.** Volume **1**, pp 1-37. Boca Raton, FL: CRC Press.

Hukins, D. W. L., Leahy, J. C. and Mathias, K. J. (1999) Biomaterials: defining the mechanical properties of natural tissues and selection of replacement materials. *Journal of Materials Chemistry*, **9**(3), 629-636.

Jiya, T., Smit, T., Deddens, J. and Mullender, M. (2009) Posterior lumbar interbody fusion using nonresorbable poly-ether-ether-ketone versus resorbable poly-L-lactide-co-D,L-lactide fusion devices: a prospective, randomized study to assess fusion and clinical outcome. *Spine*, **34**(3), 233-237.

Joseph, J. (1986) *Aids to human osteology*. 7th edition, London, Baillière Tindall.

Kandziora, F., Pflugmacher, R., Schäfer, J., Born, C., Duda, G., Haas, N. P. and Mittlmeier, T. (2001) Biomechanical comparison of cervical spine interbody fusion cages. *Spine*, **26**(17), 1850-1857.

Kandziora, F., Pflugmacher, R., Scholz, M., Eindorf, T., Schnake, K. J. and Haas, N. P. (2004) Bioabsorbable interbody cages in a sheep cervical spine fusion model. *Spine*, **29**(17), 1845-1855.

Kettler, A. Liakos, L. Haegele, B. and Wilke, H. J. (2007) Are the spines of calf, pig and sheep suitable models for pre-clinical implant tests? *European Spine Journal*, **16**(12), 2186-2192.

Kuklo, T. R., Rosner, M. K. and Polly, D. W. (2004) Computerized tomography evaluation of a resorbable implant after transforaminal lumbar interbody fusion. *Neurosurgical Focus*, **16**(3), Article 10.

Kumar, N., Judith, M. R., Kumar, A., Mishra, V. and Robert, M. C. (2005) Analysis of stress distribution in lumbar interbody fusion. *Spine*, **30**(15), 1731-1735.

Kurtz, S. M. and Edidin, A. A. (2006) *Spine technology handbook.* Amsterdam, Elsevier Academic Press.

Kurtz, S. M. and Devine, J. N. (2007) PEEK biomaterials in trauma, orthopedic, and spinal implants. *Biomaterials*, **28**(32), 4845-4869.

Leahy, J. C., Stevenson, E. C., Hukins, D. W. L., Mathias, K. J., Shepherd, D. E. T. and Wardlaw, D. (2000) Development of surgical instrumentation for implanting a flexible fixation device for the lumbar spine. *Proceedings of the Institution of Mechanical Engineering Part H-Journal of Engineering in Medicine*, **214**(3), 325-328.

Liebschner, M. A., Kopperdahl, D. L., Rosenberg, W. S. and Keaveny, T. M. (2003) Finite element modeling of the human thoracolumbar spine. *Spine*, **28**(6), 559-565.

Lippman, C. R., Hajjar, M., Abshire, B., Martin, G., Engelman, R. W. and Cahill, D. W. (2004) Cervical spine fusion with bioabsorbable cages. *Neurosurgical Focus*, **16**(3), Article 4.

Lowe, T. G. and Coe, J. D. (2002) Resorbable polymer implants in unilateral transforaminal lumbar interbody fusion. *Journal of Neurosurgery*, **97**(Supplement 4), 464-467.

Maquet, V., Boccaccini, A. R., Pravata, L., Notingher, I. and Jérôme, R. (2003) Preparation, characterization, and in vitro degradation of bioresorbable and bioactive composites based on Bioglass®-filled polylactide foams. *Journal of Biomedical Materials Research*, *Part A*, **66**(2), 335-346.

Maquet, V., Boccaccini, A. R., Pravata, L., Notingher, I. and Jérôme, R. (2004) Porous poly(α-hydroxyacid)/Bioglasss composite scaffolds for bone tissue engineering. I: preparation and in vitro characterization. *Biomaterials*, **25**(18), 4185-4194.

Markolf, K. L. and Morris, J. M. (1974) The structural components of the intervertebral disc. *Journal of Bone and Joint Surgery*, **56**(4), 675-687.

Mastronardi, L., Ducati, A. and Ferrante, L. (2006) Anterior cervical fusion with polyetheretherketone (PEEK) cages in the treatment of degenerative disc disease. Preliminary observations in 36 consecutive cases with a minimum 12-month follow-up. *Acta Neurochirurgica*, **148**(3), 307-312.

McAfee, P. C. and Maryland, T. (1999) Current concepts review - Interbody fusion cages in reconstructive operations on the spine. *The Journal of Bone and Joint Surgery*, **81**(6), 859-880.

Middleditch, A. and Oliver, J. (2005) *Functional anatomy of the spine*. 2nd edition, Edinburgh, Elsevier Butterworth Heinemann.

Middleton, J. C. and Tipton, A. J. (2000) Synthetic biodegradable polymers as orthopedic devices. *Biomaterials*, **21**(23), 2335-2346.

Montgomery, D. C., Runger, G. C. and Hubele, N. F. (2007) *Engineering statistics.* 4th edition, Hoboken, John Wiley & Sons, Inc.

Moroney, S. P., Schultz, A. B. and Miller J. A. A. (1998) Analysis and measurement of neck loads. *Journal of Orthopaedic Research*, **6**(5), 713-720.

Motoyoshi, M., Hirabayashi, M., Uemura, M. and Shimizu, N. (2006) Recommended placement torque when tightening an orthodontic mini-implant. *Clinical Oral Implants Research*, **17**(1), 109-114.

Natarajan, R. N., Chen, B. H., An, H. S. and Andersson, G. B. (2000) Anterior cervical fusion: a finite element model study on motion segment stability including the effect of osteoporosis. *Spine*, **25**(8), 955-961.

Ng, H. W., Teo, E. C., Lee, K. K. and Qiu T. X. (2003) Finite Element Analysis of Cervical Spinal Instability Under physiologic loading. *Journal of Spinal Disorders & Techniques*, **16**(1), 55-65.

Nisitani, H., Noguchi, H. and Kim, Y. H. (1992) Evaluation of fatigue strength of plain and notched specimens of short carbon-fiber reinforced polyetheretherketone in comparison with polyetheretherketone. *Engineering Fracture Mechanics*, **43**(5), 685-705.

Panjabi, M. M., Cholewicki, J., Nibu, K., Grauer, J., Babat, L. B. and Dvorak, J. (1998) Critical load of the human cervical spine: an in vitro experimental study. *Clinical Biomechanics*, **13**(1), 11-17.

Pietrzak, W. S., Sarver, D. and Verstynen, M. (1996) Bioresorbable implants - Practical considerations. *Bone*, **19**(1), S109-S119.

Pietrzak, W. S. (2000) Critical concepts of absorbable internal fixation. *Journal of Craniofacial Surgery*, **11**(4), 335-341.

Pietrzak, W. S. and Eppley, B. L. (2000) Resorbable polymer fixation for craniomaxillofacial surgery; development and engineering paradigms. *Journal of Craniofacial Surgery*, **11**(6), 575-585.

Pitzen, T., Geisler, F., Matthis, D., Müller-Storz, H., Barbier, D., Steudel, W. I. and Feldges, A. (2002a) A finite element model for predicting the biomechanical behaviour of the human lumbar spine. *Control Engineering Practice*, **10**(1), 83-90.

Pitzen, T. R., Matthis, D., Barbier, D. D. and Steudel, W. I. (2002b) Initial stability of cervical spine fixation: predictive value of a finite element model. *Journal of Neurosurgery*, **97**(1), 128-134.

Porter, R. W. (1993) *Management of back pain.* 2nd edition, Edinburgh, Churchill Livingstone.

Quality System Regulation 21 CFR 820 Basic Introduction. Food and Drug Administration, Silver Spring, 20993, USA.

Rezwan, K., Chen, Q. Z., Blaker, J. J. and Boccaccini, A. R. (2006) Biodegradable and bioactive porous polymer/inorganic composite scaffolds for bone tissue engineering. *Biomaterials*, **27**(18), 3413-3431.

Rockoff, S. D., Sweet, E. and Bleustein, J. (1969) The relative contribution of trabecular and cortical bone to the strength of human lumbar vertebrae. *Calcified Tissue Research*, **3**(1), 163-175.

Sagomonyants, K. B., Jarman-Smith, M. L., Devine, J. N., Aronow, M. S. and Gronowicz, G. A. (2008) The in vitro response of human osteoblasts to polyetheretherketone (PEEK) substrates compared to commercially pure titanium. *Biomaterials*, **29**(11), 1563-1572.

Shepherd, D. E. T. (2002) Risk analysis for a radio-carpal joint replacement. *Proceedings of the Institution of Mechanical Engineering Part H- Journal of Engineering in Medicine*, **216**(1), 23-29.

Silva, M. J., Keaveny, T. M. and Hayes. W. C. (1997) Load sharing between the shell and centrum in the lumbar vertebral body. *Spine*, **22**(2), 140-150.

Smit, T. H., Krijnen, M. R., van Dijk, M. and Wuisman, P. I. J. M. (2006) Application of polylactides in spinal cages: studies in a goat model. *Journal of Materials Science - Materials in Medicine*, **17**(12), 1237-1244.

Smit, T. H., Engels, T. A. P., Wuisman, P. I. J. M. and Govaert, L. E. (2008) Time-dependent mechanical strength of 70/30 poly(L,DL-lactide). Shedding light on the premature failure of degradable spinal cages. *Spine*, **33**(1), 14-18.

Smit, T. H., Engels, T. A. P., Söntjens, S. H. M. and Govaert, L. E. (2010) Time-dependent failure in load-bearing polymers: a potential hazard in structural applications of polylactides. *Journal of Materials Science - Materials in Medicine*, **21**(3), 871-878.

Smutz, W. P., Daniels, A. U., Andriano, K. P., France, E. P. and Heller, J. (1991) Mechanical test methodology for environmental exposure testing of biodegradable polymers. *Journal of Applied Biomaterials*, **2**(1), 13-22.

Stamboulis, A., Hench, L. L. and Boccaccini, A. R. (2002) Mechanical properties of biodegradable polymer sutures coated with bioactive glass. *Journal of Materials Science - Materials in Medicine*, **13**(8), 43-48.

Steffen, T., Tsantrizos, A., Fruth, I. and Aebi, M. (2000) Cages: designs and concepts. *European Spine Journal*, **9**(Supplement 1), S89-S94.

Surgicraft Ltd. internal report. (2007) *Dynamic Axial Compression and Torsion Testing of the 2-Hole and 3-Hole cage PEEK Optima Systems.* Redditch, UK.

Thomas, K. A., Toth, J. M., Crawford, N. R., Seim, H. B., Shi, L. L., Harris, M. B. and Turner, A. S. (2008) Bioresorbable polylactide interbody implants in an ovine anterior cervical discectomy and fusion model. *Spine*, **33**(7), 734-742.

Toth, J. M., Estes, B. T., Wang, M., Seim, H. B., Scifert, J. L., Turner, A. S. and Cornwall, G. B. (2002) Evaluation of 70/30 poly (L-lactide-co-D,L-lactide) for use as a resorbable interbody fusion cage. *Journal of Neurosurgery*, **97**(Supplement 4), 423-432.

Toth, J. M., Wang, M., Estes, B. T., Scifert, J. L., Seim, H. B. and Turner, A. S. (2006) Polyetheretherketone as a biomaterial for spinal applications. *Biomaterials*, **27**(3), 324-334.

Totoribe, K., Matsumoto, M., Goel, V. K., Yang, S. J., Tajima, N. and Shikinami, Y. (2003) Comparative biomechanical analysis of a cervical cage made of an unsintered hydroxyapatite particle and poly-L-lactide composite in a cadaver model. *Spine*, **28**(10), 1010-1015.

Tsuang, Y. H., Chiang, Y. F., Hung, C. Y., Wei, H. W., Huang, C. H. and Cheng, C. K. (2009) Comparison of cage application modality in posterior lumbar interbody fusion with posterior instrumentation - A finite element study. *Medical Engineering & Physics*, **31**(5), 565-570.

Vadapalli, S., Sairyo, K., Goel, V. K., Robon, M., Biyani, A., Khandha, A. and Ebraheim, N. A. (2006) Biomechanical rationale for using polyetheretherketone (PEEK) spacers for lumbar interbody fusion - A finite element study. *Spine*, **31**(26), E992-E998.

van Dijk, M., Smit, T. H., Sugihara, S., Burger, E. H. and Wuisman, P. I. (2002) The effect of cage stiffness on the rate of lumbar interbody fusion. An in vivo model using poly(L-lactic acid) and titanium cages. *Spine*, **27**(7), 682-688.

VICTREX PLC - High Performance PEEK Polymers. *Materials Properties Guide*. www.victrex.com, Thornton Cleveleys, UK.

Wicke, L. (1998) *Atlas of radiologic anatomy.* 6th English edition, Baltimore, Williams & Wilkins.

Wuisman, P. I. J. M. and Smit, T. H. (2006) Bioresorbable polymers: heading for a new generation of spinal cages. *European Spine Journal*, **15**(2), 133-148.

Yang, K., Teo, E-C. and Fuss, F. K. (2007) Application of taguchi method in optimization of cervical ring cage. *Journal of Biomechanics*, **40**(14), 3251-3256.

Yang, S., Leong, K. F., Du, Z. and Chua, C. K. (2001) The design of scaffolds for use in tissue engineering. Part I. Traditional factors. *Tissue Engineering*, **7**(6), 679-689.

Yang, X. B., Webb, D., Blaker, J., Boccaccini, A. R., Maquet, V., Cooper, C. and Oreffo, R. O. C. (2006) Evaluation of human bone marrow stromal cell growth on biodegradable polymer/Bioglass® composites. *Biochemical and Biophysical Research Communications*, **342**(4), 1098-1107.

Zhang, D. J., Zhang, L. F., Xiong, Z. C., Bai, W. and Xiong, C. D. (2009) Preparation and characterization of biodegradable poly(D,L-lactide) and surface-modified bioactive glass composites as bone repair materials. *Journal of Materials Science - Materials in Medicine*, **20**(10), 1971-1978.

Zhang, Q. H. and Teo, E. C. (2008) Finite element application in implant research for treatment of lumbar degenerative disc disease. *Medical Engineering &. Physics*, **30**(10), 1246-1256.

Zhong, Z. C., Wei, S. H., Wang, J. P., Feng, C. K., Chen, C. S. and Yu, C. H. (2006) Finite element analysis of the lumbar spine with a new cage using a topology optimization method. *Medical Engineering & Physics*, **28**(1), 90-98.